



Faculty of Science and Technology

MASTER'S THESIS

Study program/ Specialization : Offshore Technology/ Marine and Subsea Technology	Spring semester, 2016 Open / Restricted access
Writer : Rieska Mawarni Putri (Writer's signature)
Faculty Supervisor : Dr. Charlotte Obhrai External supervisor(s):	
Thesis title : A Study of the Coherences of Turbulent Wind on a Floating Offshore Wind Turbine	
Credit (ECTS) : 30	
Keywords : <i>OC3-Hywind, HAWC2, turbulent wind, coherence, Mann Spectral Model, Kaimal Spectra & Exponential Coherence Model, TurbSim, atmospheric stability, floating offshore wind turbine, IEC standards</i>	Pages : 166 +enclosure : 1 CD Stavanger, 15 th June 2016

Abstract

In the development of offshore wind turbine industry, the shift from the use of fixed-substructure wind turbines to the floating wind turbines is expected to maximise the offshore wind power extraction while reducing construction cost and enhancing the structural reliability, particularly in deep waters. Up to the present time, the available floating wind turbine concepts are adopted from the offshore oil and gas industry experiences, namely semi-submersible, tensioned-leg platform (TLP), and deep draft floater (spar). Especially for the latter type (spar), by combining this platform with large turbine rotors, studies had shown that they are susceptible in terms of platform motions when exposed to a turbulent wind. It was hypothesised that the spatial correlation of the occurring turbulence (lateral and vertical coherences) at different points on the floating wind turbine rotor influences the floater motions. The unstable atmospheric stability conditions which occur more frequently offshore, has been hypothesised to cause severe fatigue damages on the wind turbine components. The two recommended models given in the IEC standards to estimate the spatial correlation of the turbulent wind: the Mann Spectral Tensor Model and the Kaimal Spectra & Exponential Coherence Model predict very different coherences, in particular for larger separations. Moreover, the fact that one of the models is unable to capture the effects of varying atmospheric stability, results in the need to select the suitable model for wind turbine design.

This master thesis will investigate the comparison of the influences between the two turbulence models outlined in the IEC standards on a spar-buoy floating wind turbine—the OC3-Hywind—motions and fatigue loadings. The effects of the lateral and the vertical coherences from the synthetic (generated) wind fields from the two turbulence models and fitted-measurements parameter inputs on the OC3-Hywind turbine loadings and motion responses will be studied using HAWC2 aero-hydro-servo-elastic code. In addition, the influences of combined turbulence variation and mean wind profile under different atmospheric stability conditions on a spar-buoy floating wind turbine will also be studied.

In general, it was noted that the OC3-Hywind turbine was rather stiff in terms of yaw motion, but not for the pitch motion. It was found that the IEC Mann Spectral Tensor Model was more conservative when use to quantify damage equivalent loads and platform motions (pitch and yaw) on the OC3-Hywind turbine compared to the IEC Kaimal Spectra & Coherence Model. The given parameters from the IEC standards was found to be more conservative than the fitted-measurements parameters in predicting motions and damage equivalent loads of the OC3-Hywind. The mean wind profile under stable conditions was observed to affect the blade root fatigue damage by up to 5% only. It was also observed that a higher vertical coherence resulted in higher pitch motion of the OC3-Hywind. The influence of the lateral coherence on the OC3-Hywind turbine yaw motion was observed when comparing the coherences from the two IEC turbulent wind models, where lower lateral coherence resulted in higher platform yaw motion. When comparing the coherences from the fitted-measurements parameters, the influence of the lateral coherence on the OC3-Hywind yaw motion was less obvious, but the yaw motion was shown to be influenced by the turbulence levels which was correlated with the parameter $\alpha\epsilon^{2/3}$. Nonetheless, the results obtained were based on limited number of simulations, which should ideally be expanded in a more extensive parametric study.

Keywords: OC3-Hywind, HAWC2, TurbSim, turbulent wind, coherence, Mann Spectral Model, Kaimal Spectra & Exponential Coherence Model, atmospheric stability, floating offshore wind turbine, IEC standards

Acknowledgements

Alhamdulillahirrobbilalamin.

Firstly, I would like to thank Dr. Charlotte Obhrai for being not only my supervisor, but also my mentor and my English teacher, for every advices and guidance through the completion of this master thesis. Also, for the opportunity to write an interesting master thesis topic and for the experiences I had in the past six months.

To Dr. Lene Eliassen for all the helps and advices for HAWC2 and TurbSim as well as for the quick responses whenever I needed. To Mr. Anders Yde and Mr. Torben Larsen from Danmarks Tekniske Universitet for the technical help in HAWC2. To Mr. Abhijit Chougule for the advices and enlightenment concerning my thesis. To Prof. Jasna Bogunovic Jakobsen for taking care of me during the conference in Grimstad. To Prof. Ove Tobias Gudmestad and Mr. Yaaseen Ahmad Amith for the trust and supports.

My mom, my dad, and my little brother to whom I dedicated this master thesis to, thank you for sending me constant prayers, supports, trust, and encouragements so that I could complete this master thesis.

To Dr. Airindy Felisita for the encouragement and making me believe that I can complete this master thesis on time. To Elise Granholt, who always encouraging and wishing me with tons of love and preventing me from being lonely. As I am now writing this acknowledgments and soon we will be apart for a while makes me sad but happy for you. Lykke til med utdanningen din i Australia, vi sees igjen. To Nouman Khalid for convincing me that miracle can happen even within the numbered days if I do not give up. To Kak Reffi for always be there when I needed. To Joakim and Kashif for accompanying me in the D-258 lab and cheering my tough days. To Ahmad for the technical help in the last minutes.

To my Indonesian friends in Stavanger Cendhy, Mas Fikri, Fikri, Kak Ninis, Kak Christy, Mbak Indhira, Mas Hendra, Pahmi, Kevin, Kak Anggi, Kak Arif, Mas Toga, Hafiz, Albert, Amalia, Daisy, Kak Nikka, Madhan, Kak Aam, Bang Sori, and Bang Andri for the togetherness and the laughter.

And to all my friends in Marine & Subsea Technology Study Programme, thank you for the precious memories and lessons.

Stavanger, June 14th 2016

Rieska Mawarni Putri

Table of Contents

Table of Contents.....	i
List of Figures.....	iv
List of Tables.....	vii
Nomenclature.....	ix
Abbreviations.....	xiv
1. Introduction.....	1
1.1 Background.....	1
1.2 Objectives.....	2
1.3 Scope of Work.....	2
1.4 Methodology and Organisation.....	2
2. Basic Theories.....	4
2.1 Wind Boundary Layer.....	4
2.1.1 Wind Speed Profile in Surface Layer.....	6
2.1.2 Atmospheric Stability.....	8
2.2 Turbulent Wind and Turbulence.....	12
2.2.1 Turbulence Intensity.....	12
2.2.2 Wind Spectral Density Function.....	13
2.2.3 Correlation.....	15
2.2.4 Integral Length Scale of Turbulence.....	16
2.2.5 Cross-Spectrum and Coherence.....	17
2.3 Marine Atmospheric Boundary Layer (MABL).....	20
2.4 The Two Turbulence Models.....	23
2.4.1 IEC Kaimal Spectrum and Coherence Model.....	23
2.4.2 Mann Turbulence Model.....	24
2.4.3 Comparison between the Two Turbulence Models.....	27
2.4.4 Influences of Atmospheric Stability on the Two Turbulence Models.....	29
2.4.5 Influences of Atmospheric Stability on the Coherences.....	32
2.5 Wind Turbine Basics.....	33
2.5.1 Parts of an Offshore Wind Turbine.....	33
2.5.2 Wind Turbine Blade Anatomy and Definition.....	34
2.5.3 Wind Turbine Power Curve.....	36
2.6 Structural Responses of Floating Offshore Wind Turbines.....	37

3.	Modelling of a Spar-Buoy Wind Turbine Using HAWC2 Code.....	41
3.1	HAWC2 Software	41
3.1.1	Defining the Structure and Coordinate Systems in HAWC2	41
3.1.2	Rayleigh Damping.....	43
3.1.3	Aerodynamic Modelling in HAWC2.....	44
3.1.3.1.	Rotor Aerodynamics	44
3.1.3.2.	2D Aerofoil Cross Section Aerodynamics	47
3.1.4	Hydrodynamic Modelling in HAWC2	48
3.2	Turbulent Wind Field Input for HAWC2	49
3.2.1.	TurbSim – IEC Kaimal Spectra & Coherence Model Wind Field Simulator	51
3.2.2.	HAWC2 Built-in Mann Model Wind Field Simulator	52
3.3	OC3-Hywind Offshore Wind Turbine Specification	53
3.3.1.	Tower Structural Properties	54
3.3.2.	Floater Properties	55
3.3.3.	Mooring System Properties.....	56
3.4	OC3-Hywind Model in HAWC2	58
3.4.1.	Mooring Model	58
3.4.2.	Defining Constraints (Connection for Each Main Body)	60
3.5.	HAWC2 – The Limitations	61
4.	HAWC2 Simulations for a Spar-Buoy Wind Turbine	64
4.1	Load Cases and Input Parameters	64
4.1.1.	Wind Turbulence Inputs	64
4.1.2.	Waves Input	65
4.2	Setting up Simulations	66
4.2.1.	General.....	66
4.2.2.	Wind and Aerodynamics Input – General.....	66
4.2.3.	Wind Input – Turbulence Box.....	67
4.3	Simulation Results	68
4.3.1.	The Generated Wind Turbulence	70
4.3.2.	Eigen-frequencies	74
4.3.2.1.	Eigen-frequencies of the Rotating Rotor.....	74
4.3.2.2.	Eigen-frequencies of the Environmental Loads	75
4.3.2.3.	Eigen-frequencies Results – OC3-Hywind Modes	75

4.3.3.	Spectral Density	76
4.3.3.1.	Tower Base Fore-Aft Moment	77
4.3.3.2.	Tower Top Yaw Moment.....	79
4.3.3.3.	Blade Root Flap-Wise Moment.....	81
4.3.3.4.	Platform Pitch.....	83
4.3.3.5.	Platform Yaw	85
4.3.3.6.	Mooring Forces (Tensions)	87
4.3.4.	Fatigue Damage Equivalent Load	89
4.3.4.1.	Rainflow Counting Method – Miner Summation Rule.....	89
4.3.4.2.	Damage Equivalent Load – Results.....	92
4.3.4.3.	Damage Equivalent Load – Result Description.....	98
4.3.5.	Motion Responses Result.....	99
4.4	Influence of the Mean Wind Profile Variation on OC3-Hywind Loadings and Responses	102
5.	Discussion and Conclusion	106
5.1	Discussion.....	106
5.1.1	The Simulated Wind Coherences	106
5.1.2	A Note on the Generated Turbulence Properties.....	109
5.1.3	The Case of ‘Constant’ $\alpha\epsilon^{2/3}$ with Variable L_M	110
5.1.4	The Case of ‘Constant’ L_M with Variable $\alpha\epsilon^{2/3}$	111
5.1.5	A Note for the Mooring Lines Tensions Results of the OC3-Hywind	113
5.1.6	A Note on the Pitch/Fore-Aft Modes of the OC3-Hywind.....	113
5.1.7	A Note on the Yaw Modes of the OC3-Hywind.....	116
5.1.8	The IEC Kaimal Spectra & Coherence vs the Mann Spectral Tensor Model from the IEC Standards	118
5.1.9	Influences of the Mean Wind Profile Accounting for Atmospheric Stability on the OC3-Hywind	120
5.2	Conclusion.....	121
5.3	Future Works & Recommendations	122
	References.....	123
	Appendix A. Modelling of the OC3-Hywind in HAWC2.....	A-1
	Appendix B. TurbSim.....	B-1
	Appendix C. Simulation Results.....	C-1

List of Figures

Figure 2.1 Atmosphere vertical structure (ic.galegroup.com, accessed February 2016).	4
Figure 2.2 Boundary layer (Hassan, accessed 2016).	5
Figure 2.3 Roughness length illustration (Dyrbye & Hansen, 1997).	5
Figure 2.4 Wind velocity towards height (Dyrbye & Hansen, 1997).	6
Figure 2.5 Horizontal wind speed spectrum (Gavriluta, 2012).	6
Figure 2.6 Atmospheric stability category.	9
Figure 2.7 Atmospheric stability effect towards mean wind speed profile/wind shear.	10
Figure 2.8 Typical coherence plot.	18
Figure 2.9 Wind velocity profiles over sea surface (Warwick, 2011).	21
Figure 2.10 Stretched eddy taking into account wind shear approaches wind turbine rotor.	26
Figure 2.11 Comparison of the uu-coherence for vertical separations (Obhrai & Eliassen, 2016).	29
Figure 2.12 Comparison of the vv-coherence (left) and ww-coherence (right) for vertical separations (Obhrai & Eliassen, 2016).	29
Figure 2.13 Definition of an offshore wind turbine (IEC, 2009).	33
Figure 2.14 Rotor-nacelle assembly anatomy of a wind turbine (Ayee et al., 2009).	34
Figure 2.15 Definition of 2D aerofoil (DTU, with modification, accessed 2016).	34
Figure 2.16 Definition of blade (Physics Stack Exchange, with modification, 2015).	35
Figure 2.17 Typical wind turbine power-generation curve (STFC, with modification, accessed 2016).	36
Figure 2.18 Offshore wind turbine floater types (U.S. Department of Energy, 2014).	38
Figure 3.1 Multibody system (DTU, accessed 2016).	41
Figure 3.2 Structural definition in HAWC2 (DTU, accessed 2016).	42
Figure 3.3 Coordinate system in HAWC2 (DTU, accessed 2016).	43
Figure 3.4 Blade Element Momentum theory (Ingram, 2011).	44
Figure 3.5 Transient in thrust force with constant wind.	47
Figure 3.6 Drag and lift force on an aerofoil/blade cross section (wikiversity.org, with modification, accessed April 2016).	48
Figure 3.7 3D turbulence box implemented in HAWC2.	50
Figure 3.8 Grid system definition in TurbSim (Jonkman & Kilcher, with modification, 2012).	52
Figure 3.9 Floater of OC3-Hywind.	56
Figure 3.10 Plan view of OC3-Hywind with mooring lines (Jonkman, with modification, 2010).	57
Figure 3.11 3D sketch of OC3-Hywind with mooring lines (Jonkman, with modification, 2010).	58
Figure 3.12 Plan view of OC3-Hywind mooring configuration in HAWC2.	59
Figure 3.13 Load-displacement relation for mooring line tensions computed from Mimosa.	60
Figure 3.14 Illustration of OC3-Hywind model in HAWC2 (side view).	61
Figure 3.15 Error notification due to the use of NHMooringDLL.dll with the HAWC2 version 12.2.	63
Figure 3.16 Visualisation of animation output using Animation.exe.	63
Figure 4.1 Sketch of the inputted 3D turbulence box definition.	68
Figure 4.2 The lateral and vertical coherences of a turbulent wind field.	69
Figure 4.3 The OC3-Hywind six-degree of freedoms (Tran et al., with modification, 2014).	69
Figure 4.4 The blade root bending moments.	70
Figure 4.5 Power spectral density of the along-wind component for 11.4 m/s wind at hub height. ...	71

Figure 4.6 Power spectral density of the cross-wind component for 11.4 m/s wind at hub height. 72

Figure 4.7 Power spectral density of the vertical-wind component for 11.4 m/s wind at hub. 72

Figure 4.8 Turbulence level of the u-component for 40m and 60m lateral separations at rated wind speed..... 73

Figure 4.9 Turbulence level of the u-component for 40m and 60m vertical separations at rated wind speed..... 73

Figure 4.10 Rotor rotational speed for the NREL 5MW Wind Turbine. 74

Figure 4.11 The wave input spectral density..... 75

Figure 4.12 The eigen-frequencies for the OC3-Hywind system (Jonkman & Musial, 2010). 76

Figure 4.13 The tower base fore-aft moment spectral densities at below rated (8m/s) wind speed. ... 77

Figure 4.14 The tower base fore-aft moment spectral densities at rated (11.4m/s) wind speed..... 78

Figure 4.15 The tower base fore-aft moment spectral densities at above rated (15m/s) wind speed. . 78

Figure 4.16 The tower top yaw moment spectral densities at below rated (8m/s) wind speed. 79

Figure 4.17 The tower top yaw moment spectral densities at rated (11.4m/s) wind speed..... 80

Figure 4.18 The tower top yaw moment spectral densities at above rated (15m/s) wind speed. 80

Figure 4.19 The blade root flap-wise moment spectral densities at below rated (8m/s) wind speed. . 81

Figure 4.20 The blade root flap-wise moment spectral densities at rated (11.4m/s) wind speed. 82

Figure 4.21 The blade root flap-wise moment spectral densities at above rated (15m/s) wind speed. 82

Figure 4.22 The platform pitch rotation spectral densities at below rated (8m/s) wind speed. 83

Figure 4.23 The platform pitch rotation spectral densities at rated (11.4m/s) wind speed. 84

Figure 4.24 The platform pitch rotation spectral densities at above rated (15m/s) wind speed. 84

Figure 4.25 The platform yaw rotation spectral densities at below rated (8m/s) wind speed. 85

Figure 4.26 The platform yaw rotation spectral densities at rated (11.4m/s) wind speed..... 86

Figure 4.27 The platform yaw rotation spectral densities at above rated (15m/s) wind speed. 86

Figure 4.28 Mooring line 1 tension spectral densities at below rated (8m/s) wind speed. 87

Figure 4.29 Mooring line 1 tension spectral densities at rated (11.4m/s) wind speed. 88

Figure 4.30 Mooring line 2 tension spectral densities at below rated (8m/s) wind speed. 88

Figure 4.31 Mooring line 2 tension spectral densities at rated (11.4m/s) wind speed. 89

Figure 4.32 Rainflow counting method (DTU, with modification, accessed 2016). 90

Figure 4.33 Damage equivalent load (lower graph) from a given load time series (upper graph). 92

Figure 4.34 Damage equivalent loads for tower base fore-aft moment. 96

Figure 4.35 Damage equivalent loads for tower top yaw moment. 96

Figure 4.36 Damage equivalent loads for blade root flap-wise moment. 97

Figure 4.37 Damage equivalent loads for blade root edge-wise moment. 97

Figure 4.38 Minimum, mean and maximum surge displacement. 99

Figure 4.39 Minimum, mean and maximum pitch rotation. 100

Figure 4.40 Minimum, mean and maximum yaw rotation..... 101

Figure 4.41 Mean wind profile input for LC Group 1 (original case). 102

Figure 4.42 Mean wind profile input for LC Group 1-WP (modified case). 102

Figure 4.43 Comparison of the tower base fore-aft moment damage equivalent loads towards mean wind profile variation..... 103

Figure 4.44 Comparison of the blade root flap-wise moment damage equivalent loads towards mean wind profile variation..... 104

Figure 4.45 Comparison of the blade root edge-wise moment damage equivalent loads towards mean wind profile variation..... 104

Figure 4.46 Comparison of the platform yaw towards mean wind profile variation. 105

Figure 5.1 Lateral coherences of the u-component for different separations at **below rated** wind speed comparing the models given in (IEC, 2005): the Kaimal and the IEC Mann Models. 107

Figure 5.2 Lateral coherences of the u-component for different separations at **rated** wind speed comparing the models given in (IEC, 2005): the Kaimal and the IEC Mann Models. 108

Figure 5.3 Lateral (left) and vertical (right) coherences of the u-component for different separations at **below rated** wind speed comparing the Mann Model with the fitted parameters for neutral and stable conditions..... 108

Figure 5.4 Lateral (left) and vertical (right) coherences of the u-component for different separations at **below rated** wind speed comparing the Mann Model with the fitted parameters for neutral and unstable conditions..... 109

Figure 5.5 Plot of the lateral coherence (left) and vertical coherence (right) of the u-wind component comparing $\alpha \epsilon^{2/3} = 0.0245 \text{ m}^{4/3} \text{ s}^{-2}$ and $\alpha \epsilon^{2/3} = 0.048 \text{ m}^{4/3} \text{ s}^{-2}$ 112

Figure 5.6 Comparison between (a) platform pitch spectral density and (b) u-component vertical coherence at different separations for different LM at the **rated** wind speed. 115

Figure 5.7 Comparison between (a) platform pitch spectral density and (b) u-component vertical coherence at different separations for different LM at **below rated** wind speed. 115

Figure 5.8 OC3-Hywind platform yaw spectral density for 18m/s wind speed (Jonkman & Musial, 2010). 117

Figure 5.9 Platform yaw spectral density at different wind speed (average from all load cases). 117

Figure 5.10 Comparison between (a) platform yaw spectral density and (b) u-component lateral coherence at different separations for different LM at **below rated** wind speed. 118

Figure 5.11 Comparison between (a) platform yaw spectral density and (b) u-component lateral coherence at different separations for different LM at **rated** wind speed..... 118

List of Tables

Table 2.1 The Comparison between Boundary Layer and Free Atmosphere (shodor.org, accessed 2016)	5
Table 2.2 Roughness Length for Different Terrain Type (Dyrbye & Hansen, 1997)	7
Table 2.3 Roughness Length and α for Various Terrain Categories (DNV-RP-C205, 2010).....	7
Table 2.4 Stability Correction Factor (DNV-RP-C205, 2010).....	11
Table 2.5 Atmospheric Stability Class (Gryning et al., 2007).....	12
Table 2.6 Intensity Values According to Wind Turbine Class Turbulence (IEC 61400-1 3 rd edition, 2005)	13
Table 2.7 Non-Dimensional Single Point Spectrum	14
Table 2.8 Integral Length Scales of Turbulence.....	16
Table 2.9 Parameters for Kaimal Spectrum (IEC 61400-1 3 rd edition, 2005).....	24
Table 2.10 Mann Model Parameters from Experiments and Fitting (Mann, 1998).....	26
Table 2.11 Theoretical and Measurement Comparison of u Lateral Coherence (Saranyasontorn & Veers, 2004).....	28
Table 2.12 Theoretical and Measurement Comparison of v Lateral Coherence (Saranyasontorn & Veers, 2004).....	28
Table 2.13 Theoretical and Measurement Comparison of w Lateral Coherence (Saranyasontorn & Veers, 2004).....	28
Table 2.14 Energy Dissipation Rate Parameter at Høvsøre for Reference Height = 90 metre.....	30
Table 2.15 Energy Dissipation Rate Parameter at Høvsøre for Different Wind Speed References	30
Table 2.16 Anisotropic Parameter at Høvsøre for Reference Height = 90 metre	31
Table 2.17 Anisotropic Parameter at Høvsøre for Different Wind Speed References.....	31
Table 2.18 Integral Length Scales of Spectral Velocity Tensor at Høvsøre for Reference Height = 90 metre.....	32
Table 2.19 Integral Length Scales of Spectral Velocity Tensor at Høvsøre for Different Wind Speed References	32
Table 2.20 Integral Length Scales at Høvsøre (DTU, 2013).....	32
Table 2.21 Power Curve Region Definition	37
Table 2.22 General Comparison of the Three Type Offshore Wind Turbine Floater (Jonkman & Matha, 2011).....	38
Table 3.1 General Specification of NREL 5MW Offshore Wind Turbine RNA (Jonkman et al., 2009)	54
Table 3.2 Distributed Tower Properties (Jonkman, 2010)	54
Table 3.3 General Tower Properties (Jonkman, 2010)	55
Table 3.4 Floater Hydrodynamic Properties (Jonkman, 2010).....	55
Table 3.5 General Floater Properties (Jonkman, 2010)	56
Table 3.6 Mooring Line Properties (Jonkman, 2010)	57
Table 3.7 Constraint Definition for OC3-Hywind Model in HAWC2	60
Table 4.1 Mann Turbulence Input Parameters from the Fitted Measurements (Sathe et al., 2013)	64
Table 4.2 Turbulence Input Parameters from IEC Standard for Neutral Conditions (IEC, 2005)	65
Table 4.3 Waves Input Parameters	65
Table 4.4 General Simulation Parameters in HAWC2	66
Table 4.5 General Wind and Aerodynamics Inputs Simulation for LC Group 1	66

Table 4.6 General Wind and Aerodynamics Inputs Simulation for LC Group 2 (Neutral Conditions).....	67
Table 4.7 3D Turbulence Box Input for the 64bit Mann Turbulence Generator	67
Table 4.8 Turbulence Box Input for TurbSim	68
Table 4.9 The Generated Turbulence Standard Deviation	70
Table 4.10 Frequencies of the Rotating Blades for NREL 5MW Wind Turbine	74
Table 4.11 Eigen-frequencies of the First 10 Modes for the OC3-Hywind from the Simulation.....	76
Table 4.12 Fatigue Damage Wöhler Exponent	90
Table 4.13 Tower Base Fore-Aft Moment Damage Equivalent Loads (10^7 cycles) for LC Group 1..	93
Table 4.14 Tower Top Yaw Moment Damage Equivalent Loads (10^7 cycles) for LC Group 1	93
Table 4.15 Blade Root Flap-Wise Moment Damage Equivalent Loads (10^7 cycles) for LC Group 1.....	93
Table 4.16 Blade Root Edge-Wise Moment Damage Equivalent Loads (10^7 cycles) for LC Group 1.....	93
Table 4.17 Tower Base Fore-Aft Moment Damage Equivalent Loads (10^7 cycles) for LC Group 2..	94
Table 4.18 Tower Top Yaw Moment Damage Equivalent Loads (10^7 cycles) for LC Group 2	94
Table 4.19 Blade Root Flap-Wise Moment Damage Equivalent Loads (10^7 cycles) for LC Group 2.....	95
Table 4.20 Blade Root Edge-Wise Moment Damage Equivalent Loads (10^7 cycles) for LC Group 2.....	95
Table 5.1 Energy Dissipation Rate, Length Scale and Anisotropy Degree Parameters for the Load Cases.....	107
Table 5.2 Comparison of the Tower Top Yaw Damage Equivalent Loads for Various $\alpha\epsilon_2/3$	116
Table 5.3 Properties of the Generated Turbulence near the Hub Height	119

Nomenclature

Symbols – Latin characters

a	Induction factor
A	Charnock constant
A	Cross-sectional area
A_r	Structure's peripheral area exposed to displaced water movement
b	Constant for the calculation of σ_1
c	Coherence decay constant
C	Damping matrix
C_a	Hydrodynamic added mass coefficient
C_d	Hydrodynamic drag coefficient
C_D	Aerodynamic drag coefficient
C_L	Aerodynamic lift coefficient
C_m	Hydrodynamic inertia/mass coefficient
c_p	Specific heat of the air at constant temperature
C_P	Betz limit
C_T	Thrust coefficient
c_y	Coherence decay constant in lateral direction
c_z	Coherence decay constant in vertical direction
C_1	ESDU coherence's gradient of decay
C_2	ESDU coherence's coefficient
C_3	ESDU coherence's coefficient
d	Damage
D	Separation distance (lateral or vertical)
D	Rotor diameter
D	Structure's diameter
dt	Time step
dx	Grid spacing in x-direction
dy	Grid spacing in y-direction
dz	Grid spacing in z-direction
E	Modulus of elasticity
f	Frequency
F	Force
F	Prandtl tip loss correction factor
F_D	Drag force
F_L	Lift force
F_M	Moment/tangential force
f_n	Natural frequency of a system/mode/component
f_p	Wave peak frequency
f_r	Reduced frequency
F_T	Thrust force
g	Gravity acceleration
G	Shear modulus
H_s	Significant wave height
I	Second moment of inertia

I_u	Turbulence intensity of the longitudinal/along wind component
I_v	Turbulence intensity of the lateral wind component
I_w	Turbulence intensity of the vertical wind component
I_x	Second moment of inertia with respect to x-axis
I_y	Second moment of inertia with respect to y-axis
I_z	Second moment of inertia with respect to z-axis
I_{ref}	Reference turbulence intensity
k	Shear factor
k	Wave vector
K	Stiffness matrix
K_x	Stiffness-proportional damping with respect to x-axis
K_y	Stiffness-proportional damping with respect to y-axis
K_z	Stiffness-proportional damping with respect to z-axis
k_{Col}	Coleman correction factor
k_i	Polynomial coefficient (for the induction factor)
k_i	Wave number
L	Monin-Obukhov length
L_c	Coherence scale parameter
l_{ch}	Aerofoil length
L_M	Length scale of the spectral velocity tensor
L_{MBL}	Length scale in the middle of boundary layer
$L_{MBL,N}$	Length scale in the middle of boundary layer under neutral condition
L_u^x	Integral length scale of the longitudinal/along wind component in x-direction
L_u^y	Integral length scale of the longitudinal/along wind component in y-direction
L_u^z	Integral length scale of the longitudinal/along wind component in z-direction
L_v^x	Integral length scale of the lateral wind component in x-direction
L_v^y	Integral length scale of the lateral wind component in y-direction
L_v^z	Integral length scale of the lateral wind component in z-direction
L_w^x	Integral length scale of the vertical wind component in x-direction
L_w^y	Integral length scale of the vertical wind component in y-direction
L_w^z	Integral length scale of the vertical wind component in z-direction
L_x	Length of turbulence box in the along wind direction
L_y	Length of turbulence box in the lateral wind direction
L_z	Length of turbulence box in the vertical wind direction
m	Damage (Wöhler exponent)
M	Mass matrix
M_x	Mass-proportional damping with respect to x-axis
M_y	Mass-proportional damping with respect to y-axis
M_z	Mass-proportional damping with respect to z-axis
n	Number of cycle occurrences at the considered stress level
N	Total number of cycles to cause failure at the considered stress level
N_b	Number of blades
n_{bin}	Number of bins (fatigue analysis)
n_{eq}	Equivalent number of cycles
N_p	Number of frequency interest
N_x	Number of grid points in the along wind direction (turbulence box)

N_y	Number of grid points in the cross direction (turbulence box)
N_{yz}	Number of yz-planes (TurbSim)
N_z	Number of grid points in the vertical wind direction (turbulence box)
p	Coherence decay constant (IEC formula)
P	Power production
q	Coherence decay constant (IEC formula)
q	Heat flux
r	Radial position of the rotor
R	Rotor radius
R_i	Richardson Number
$R_{ij}(r)$	Covariance between turbulent velocity fluctuation i and j at separation r (i and j are to be replaced by u , v , or w)
S_{eq}	Damage equivalent load
S_0	The largest load captured in the time series
S_u	Longitudinal/along wind component spectral density
S_v	Lateral wind component spectral density
S_w	Vertical wind component spectral density
t_{ch}	Aerofoil thickness
T	Simulation time length
T_o	Mean temperature of the surface layer
T_p	Wave peak period
T_{use}	Usable simulation time length
TSR	Tip speed ratio
u	Turbulence component in the longitudinal direction
U	Mean wind speed
u_*	Friction velocity
u_{*0}	Friction velocity
$U(z)$	Mean wind speed at height z
U_{hub}	Mean wind speed at wind turbine hub height
U_{ref}	Mean wind speed at a reference height
U_{1hr}	1-hour mean wind speed
\dot{u}	Seawater particle acceleration
\dot{u}_{rel}	Relative seawater particle acceleration
v	Turbulence component in the lateral direction
V_r	Rotor rotational speed
V_{rel}	Relative wind speed
V_{tip}	Blade tip rotational speed
V_1	Undisturbed free flow wind speed
V_2	Wind speed at the rotor (blade)
V_3	Wind speed after the rotor (blade)
V_4	Wind speed at far downstream from the rotor (blade)
v_*	Characteristic velocity scale
w	Turbulence component in the vertical direction
X_G	Global x-axis
x_{mb}	Main body (local) x-axis
Y_G	Global y-axis

y_{mb}	Main body (local) y-axis
z	The considered height
Z_G	Global z-axis
z_{mb}	Main body (local) z-axis
z_i	Boundary layer depth
z_o	Surface roughness length
z_{ref}	Reference height

Symbols – Greek characters

α	Angle of attack
α	Power law profile wind shear exponent
α	Three-dimensional Kolmogorov constant
α_{stall}	Angle of attack on which stall occurs
δ	Deflection
Δy	Separation distance in lateral direction
Δz	Separation distance in vertical direction
ϵ	Turbulent wind kinetic energy dissipation
γ	Coherence
γ	Wave spectrum peak parameter
Γ	Anisotropy parameter
κ	von Kármán constant
λ	Damping constant
λ	Wave length
Λ_1	Parameter of the along wind component length scale
μ	Damping constant
Ω	Azimuth angle
π	Constant = 3.14
φ	Angle between the relative velocity and rotor plane area
φ	Non-dimensional factor for Richardson Number
ϕ	Local flow angle
Φ_{ij}	Spectral velocity tensor, (i and j are to be replaced by u , v , or w)
Φ_y	Rotor skew angle
ρ	Air density
ρ_{sw}	Seawater density
ρ_{cor}	Correlation
σ	Stress level
σ_0	The largest stress in the time series
σ_u	Standard deviation of the longitudinal/along wind component
σ_v	Standard deviation of the lateral wind component
σ_w	Standard deviation of the vertical wind component
σ_1	Standard deviation of the longitudinal/along wind component
σ_u^2	Variance of the longitudinal/along wind component
σ_v^2	Variance of the lateral wind component
σ_w^2	Variance of the vertical wind component

Ψ_m	Stability function
χ	Wake skew angle
χ_{ij}	Cross-spectrum between turbulent velocity fluctuation i and j at separation r (i and j are to be replaced by u , v , or w)

Abbreviations

Definitions

ADAMS	Automatic Dynamic Analysis of Mechanical Systems
A2AD	ADAMS-to-AeroDyn
BEM	Blade Element Momentum
CFD	Computational Fluid Dynamics
CMS	Catenary-Moored Spar
dll	Dynamic Link Library
DNV	Det Norske Veritas
DNV-GL	Det Norske Veritas-Germanischer Lloyd
DTU	Danmark Tekniske Universitet
DU	Delft University
e.g.	exempli gratia (for example)
EAZ	Egmond aan Zee
ESDU	Engineering Sciences Data Unit
etc.	et cetera (and so forth)
ETM	Extreme Turbulence Model
FAST	Fatigue, Aerodynamics, Structures, and Turbulence
FFT	Fast Fourier Transform
FINO	Forschungsplattformen in Nord-und Ostsee
FOWT	Floating Offshore Wind Turbine
HAWC2	Horizontal Axis Wind turbine simulation Code 2 nd generation
i.e.	id est (that is to say; in other words)
IEA	International Energy Agency
IEC	International Electrotechnical Commission
JONSWAP	Joint North Sea Wave Analysis Project
LC	Load Case
LES	Large Eddy Simulation
MABL	Marine Atmospheric Boundary Layer
Matlab	Matrix Laboratory
MIT	Massachusetts Institute of Technology
MW	MegaWatt
NACA	National Advisory Committee for Aeronautics
NORSOK	Norsk Søkkel Konkuranseposisjon
NORSEWInD	Northern Seas Wind Index Database
NREL	National Renewable Energy Laboratory
NTM	Normal Turbulence Model
OC3	Offshore Code Comparison Collaborative
OWT	Offshore Wind Turbine
RIFLEX	Riser System Analysis Program
RNA	Rotor-Nacelle Assembly
rpm	Rotations per Minute
SIMA	Simulation and Engineering Analysis of Marine Operations and Floating Systems
SIMO	Simulation of Marine Operations
SWL	Still Water Level
TI	Turbulence Intensity

TLP	Tensioned-Leg Platform
TSR	Tip Speed Ratio
WAMIT	Wave Analysis at MIT
1D	1-dimensional
2D	2-dimensional
3D	3-dimensional

“The pessimist complains about the wind.

The optimist expects it to change.

*The realist adjusts the **sails.**”*

–William Arthur Ward

1. Introduction

1.1 Background

Renewable energy has gained popularity and attention from many parties over the globe in the recent days. Renewable energy is described as the energy obtained from natural resources available in the surrounding environment. Solar (sunlight), wind, geothermal, and biomass are the most prominent sources of the renewables. This master thesis will focus on the development of the wind energy, in particular offshore wind turbines.

The development of onshore (land-based) wind turbines has several drawbacks compared to offshore, including spatial, visual, and noise issues. As a result, there is now a shift from land-based to offshore-based wind turbines where spatial and noise issues are not a concern. Furthermore, offshore sites have a bigger wind potential than on land due to having less obstacles 'blocking' the airflow. Offshore wind however is still not economically competitive compared to onshore developments due to higher maintenance and installation cost offshore. In order to make offshore wind more competitive there is a trend towards larger wind turbines as this allows the extraction of significantly higher amounts of power. For this reason, larger rotor diameters are starting to be implemented on offshore.

For an offshore site, a larger distance from the coast allows a higher wind potency to be extracted, implying the need for greater water depth regions to be developed. The utilisation of fixed-base substructure offshore (e.g.monopile) in deeper waters is considered ineffective in terms of cost, construction process, and structural reliability. Floating-substructure are offered as an alternative solution enabling cost reduction and installation simplicity compared to conventional fixed-based substructures in the deep waters.

The wind in the atmosphere is composed by two components, the steady and the fluctuating components. The fluctuating component, known as turbulence, is a stochastic random process as a function of space and time. For wind turbines with large rotors, the occurring turbulences at one point on the wind turbine might vary greatly to other points depending on how spatially coherent the turbulence is laterally and vertically. The current standards allows for two different approaches to model the wind field used for engineering estimates: the Mann Spectral Tensor Model and the Kaimal Spectra & Exponential Coherence Model. The point wind spectra generated using these methods are similar, but there is a difference in the correlation between the simulated points. The difference between the two methods is largest for lower frequencies and at large separations between the point wind spectra.

Different atmospheric stability conditions imply different wind profiles—or wind shear, turbulence intensities and wake characteristics, all of which affect the fatigue damage of the rotor blades and the tower. There has been an increased interest in the effects of atmospheric stability conditions and spatial coherence on large offshore wind turbines, both for the power produced and the fatigue damage (Eliassen et al., 2012).

For the above reasons mentioned, this thesis will study the structural responses of a spar-buoy floating wind turbine. The study will investigate differences between the turbulent wind models given in the IEC standards as well as the effect of different atmospheric stability conditions on the wind turbine loadings and motions. The spar-buoy wind turbine model studied was in accordance with the Offshore Code Comparison Collaborative (OC3) Phase IV IEA Task 23, 5MW OC3-Hywind. The hydro-aero-servo-elastic code HAWC2 was utilised as the primary tool to perform the simulations, along with Matlab and TurbSim as the supporting tools.

1.2 Objectives

The main goals of this master thesis enclose the following:

- As the requirement to complete a Master Degree (MSc) in Offshore Technology Programme, specialisation in Marine and Subsea Technology
- Investigating the effects of the lateral and the vertical coherences from synthetic (generated) wind fields from different turbulence models and parameter inputs on a spar-buoy floating wind turbine loadings and motion responses
- A brief study about turbulence coherences
- Comparison of the two turbulence models outlined in the IEC standards: the IEC Kaimal Spectra & Coherence Model and the Mann Spectral Tensor Model
- Investigating the influences of combined turbulence-wind profile under different atmospheric stability towards the spar-buoy floating wind turbine
- Performing analyses and interpretation on the HAWC2 simulation results.

1.3 Scope of Work

The scope of work and limitations of this master thesis encompass the following:

- HAWC2 hydro-aero-servo-elastic code was used for all simulations performed
- The OC3-Hywind model was used in accordance with the IEA Task 23, provided by Risø DTU (HAWC2 developer)
- The two turbulence models adopted in the analyses were the IEC Kaimal Spectra & Coherence Model and Mann Spectral Tensor model
- The loadings and motion responses of the pitch/fore-aft and yaw modes of the spar-buoy wind turbine structure were the primary focus to investigate the influences of the turbulent wind coherences in this study
- The mooring tension forces were quasi-statically computed using the dynamic link library (dll) included in the HAWC2 package which require an input file from Mimoso software i.e. the computed forces are based on the force-displacement relationship
- A constant wave input was considered to acquire the same wave loading condition in all load cases simulated, to highlight only the influences of wind turbulence
- Eigen-frequencies analysis was performed within HAWC2, without performing free-decay tests.

1.4 Methodology and Organisation

The methodology applied in the writing of this thesis comprises of literature study followed by model interpretation and simulation setup prior to the simulation running. The results obtained from the simulations were then analysed and interpreted.

The organisation of this thesis is as follow:

- Chapter 1 (Introduction) – contains general information regarding the background, objectives, and limitations of the study and the organisation of the thesis report.
- Chapter 2 (Basic Theories) – describes all the related theory of turbulent wind, coherences, turbulences (shear and buoyant-generated), turbulence models, and atmospheric stability conditions.

- Chapter 3 (Modelling of a Spar-Buoy Wind Turbine Using HAWC2 Code) – elaborates the spar-buoy wind turbine specifications and the modelling of the turbulence box, as well as the modelling concept using the HAWC2 code.
- Chapter 4 (HAWC2 Simulations for a Spar-Buoy Wind Turbine and Result Descriptions) – explains the simulations performed, the selection of the used parameters, and brief description on the HAWC2 simulations results.
- Chapter 5 (Discussion and Conclusion) – discusses and interprets the simulation results as well as drawing conclusions for the overall study.

2. Basic Theories

2.1 Wind Boundary Layer

The earth's atmosphere is divided into several layers: Troposphere, Stratosphere, Mesosphere, and Thermosphere where can be seen in *Figure 2.1*.

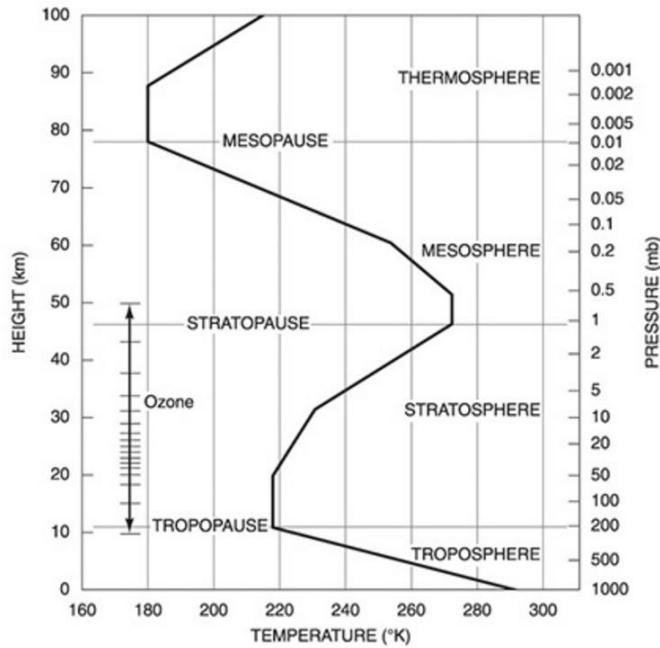


Figure 2.1 Atmosphere vertical structure (ic.galegroup.com, accessed February 2016).

Troposphere Layer is the closest layer to the earth surface, containing most of the atmosphere mass and heighted up to 12km above the ground. This layer is affected by ground roughness and has the warmest temperature due to earth surface temperature radiated by the sun. Consisting of Free Atmosphere and Boundary Layer, this layer is an importance of earth's weather. Moreover, for most wind turbines located both land-based and offshore, boundary layer is the governing atmospheric layer considered.

Boundary Layer can be divided into Surface Layer and Ekman (transition) Layer which is illustrated in *Figure 2.2*, while *Table 2.1* describes the differences for both layers. From *Figure 2.2*, it is noticed that surface layer has contact with the ground (or water in the case of offshore) up to a height of around 40m to 200m depending on the surface roughness and the atmospheric stabilities. The design of wind turbines is dependent on the surface layer since most wind turbines in the present days have the height ranging from 50m to nearly 200m.

Boundary layer thickness varies from one location to another since roughness length value (z_0) is not constant. Surface roughness length z_0 is a parameter describing roughness of the ground or defining the height where the mean wind profile is zero (Dyrbye & Hansen, 1997) as illustrated in *Figure 2.3*. This means, a higher z_0 indicates a higher roughness of the surface and therefore a thicker boundary layer depth. In addition to z_0 , the atmospheric stability also influences the depth of boundary layer, in a way that when the heat flux in the atmosphere is positive, a deeper boundary layer is formed compare to the atmosphere with zero or negative heat flux (North et al., 2014).

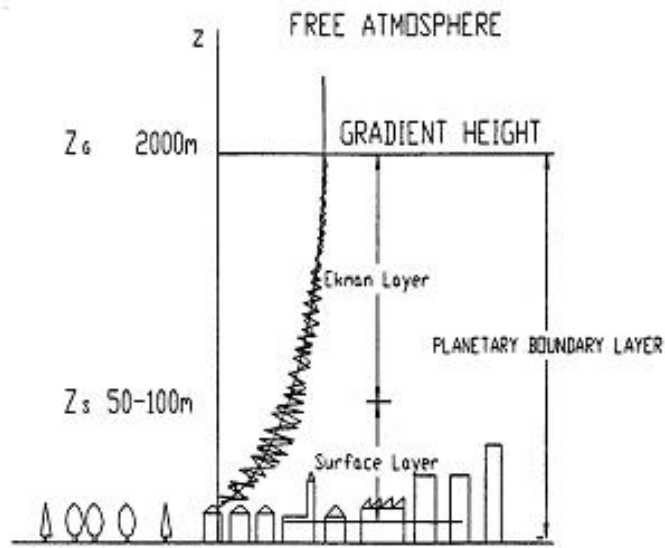


Figure 2.2 Boundary layer (Hassan, accessed 2016).

Table 2.1 The Comparison between Boundary Layer and Free Atmosphere (shodor.org, accessed 2016)

Parameter	Boundary Layer	Free Atmosphere
Thickness	Up to 3000m above the ground (depending on surface roughness at the considered location)	Up to 10km above the ground
Friction	Exposed to large friction (near to the surface) High energy dissipation	Less friction Low energy dissipation
Turbulence	Turbulent almost along the thickness	Only near jet stream and convective clouds
Mixing	Strong mixing both in vertical and horizontal (depends on atmospheric stability)	Low mixing in vertical Mixing in horizontal
Wind	Large vertical variation	Small vertical variation

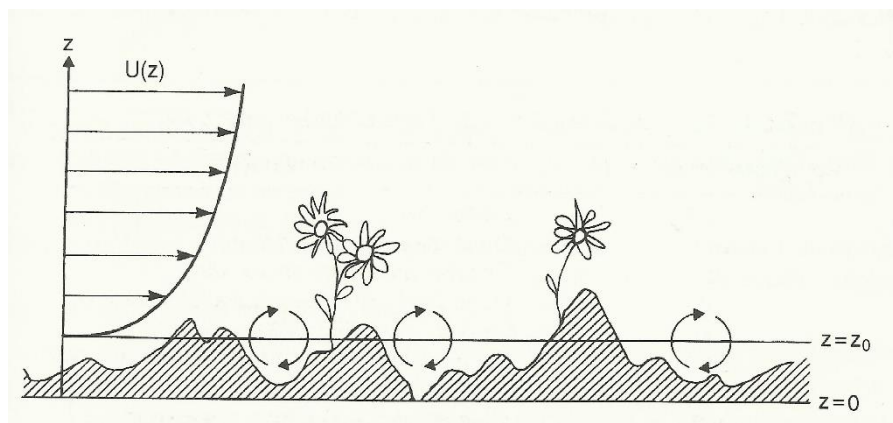


Figure 2.3 Roughness length illustration (Dyrbye & Hansen, 1997).

2.1.1 Wind Speed Profile in Surface Layer

In the surface layer, the wind blows near the surface proximity is influenced by obstacles present, such as buildings, trees, and mountains. These obstructions cause friction to the flowing air and create a ‘sheared’ profile as the airflow gets undisturbed with height. This shear causes turbulence referred as mechanically generated turbulence where its intensity increases with surface roughness z_0 and wind speed, but decreases with height (Harrison, 2001).

The occurring wind in the surface layer is consisted of the mean and the fluctuating part or turbulence as illustrated in **Figure 2.4**. Yet, the representation of wind speed profile in surface layer is generally expressed in terms of the mean wind speed with respect to height indicated as $U(z)$ in **Figure 2.4**. This wind speed profile or variation with respect to height is also called as the *vertical wind shear* or *velocity shear*.

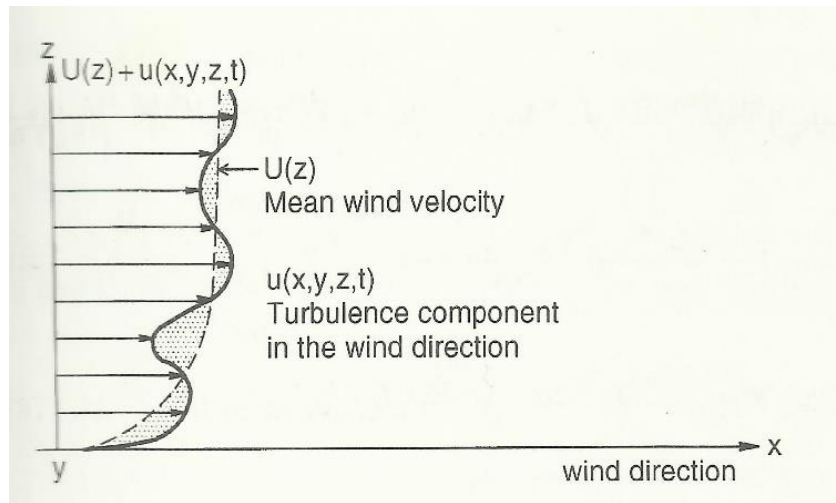


Figure 2.4 Wind velocity towards height (Dyrbye & Hansen, 1997).

The widely used definition of mean wind speed corresponds to either 10-minute-average or 1-hour-average based on the tendency of being ‘stationary’ during the two durations as described in **Figure 2.5**.

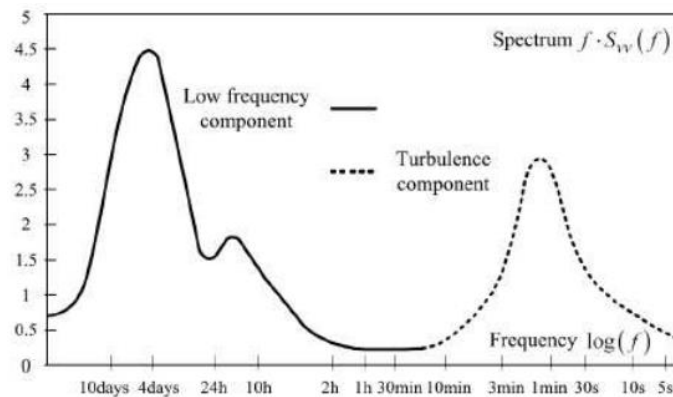


Figure 2.5 Horizontal wind speed spectrum (Gavrilita, 2012).

The gradient of vertical wind profile is varying from one site to another, depending on the surface layer thickness that varies with roughness length z_0 . There are two well-known methods to predict the wind speed profile in the *surface layer*: power law and logarithmic law, on which both methods are highly dependent towards z_0 . Dyrbye & Hansen (1997) recommends the value of roughness length z_0 for different terrain types as given in **Table 2.2** while **Table 2.3** presents the recommended z_0 value according

to (DNV, 2010). As seen from *Table 2.2* and *Table 2.3*, both references give approximately the same value.

Table 2.2 Roughness Length for Different Terrain Type (Dyrbye & Hansen, 1997)

Roughness Length z_o (m)	Terrain Type
10^{-5}	Plane ice
10^{-4}	Open sea without waves
10^{-3}	Coastal area, onshore wind
0.01	Open land with little vegetation and few houses
0.05	Agricultural area with few houses and wind-breaks
0.3	Village and agricultural areas with lots of wind breaks
1 to 10	Urban areas

A. Power Law Wind Profile

This formula only applies for *neutral atmospheric condition* where a power exponent coefficient α is the factor determining the vertical wind shear gradient, although there are studies which give different values of α for different atmospheric stability. The mean wind speed at a particular height z according to this law is computed as:

$$U(z) = U_{ref} \left(\frac{z}{z_{ref}} \right)^\alpha \tag{2.1}$$

where

z_{ref} : reference height

U_{ref} : mean wind velocity at z_{ref}

z : height considered

α : power-law or empirical wind shear exponent given in *Table 2.3*, where a higher value of α implies higher shear and thus higher wind velocity at the same height.

Table 2.3 Roughness Length and α for Various Terrain Categories (DNV-RP-C205, 2010)

Terrain Type	Roughness Length z_o (m)	Power-law Coefficient α
Open sea with waves	0.0001 to 0.01	0.12
Cultivated land with scattered buildings	0.05	0.16
Forests and suburbs	0.3	0.30
City centres	1 to 10	0.40

B. Logarithmic Law Wind Profile

For *neutral atmospheric condition*, the mean wind speed at a height z is defined as:

$$U(z) = \frac{u_*}{\kappa} \ln \left(\frac{z}{z_o} \right) \tag{2.2}$$

where

u_* : friction velocity = $\sqrt{\overline{u'w'} + \overline{v'w'}}$

κ : von Kármán constant = 0.4

z : height considered

z_o : roughness length

If wind speed data at a particular height is known, equation (2.2) can be rearranged as:

$$U(z) = U_{ref} \frac{\ln\left(\frac{z}{z_o}\right)}{\ln\left(\frac{z_{ref}}{z_o}\right)} \quad (2.3)$$

where

z_{ref} : reference height

U_{ref} : mean wind velocity at z_{ref}

z : height considered

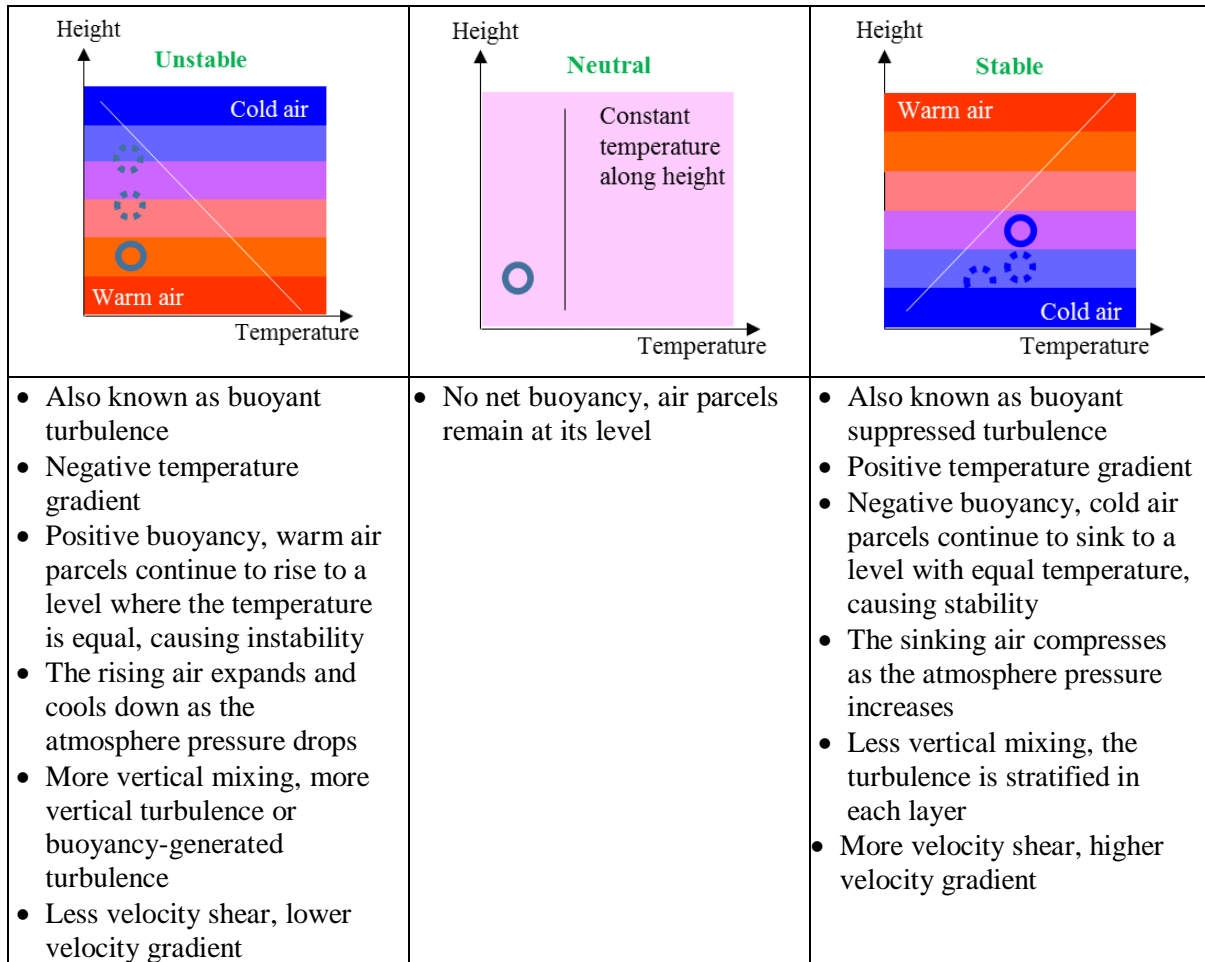
z_o : roughness length

Unlike the power law wind profile, equation (2.3) can account for atmospheric stability effects by introducing a correction factor which detail is given in Subchapter 2.1.2. Despite the various available recommendations for z_o value used in practice, this master thesis considers the values in accordance to DNV as presented in **Table 2.3**.

2.1.2 Atmospheric Stability

The occurring wind turbulence in boundary layer is caused by two mechanisms, one caused by shear friction and the other one is caused by temperature. Aside from the mechanically generated turbulence due to friction as discussed in Subchapter 2.1.1, air temperature also has great impact on wind turbulence known as atmospheric stability. While the mechanically generated turbulence is related to wind shear, atmospheric stability is related to vertical movement of air; that is the tendency of air parcel to either rise or sink depending on its temperature relative to its surroundings. When air parcels have colder temperature than its surroundings, the air parcels will sink, moving downward due to heavier mass. On the other hand, when the air parcels has higher temperature than its surroundings, it rises, moving upward and expands. Based on this tendency of air parcels to either rise or sink, turbulence due to atmospheric stability is often referred as buoyancy-generated turbulence, which can be categorised into three classes: neutral, stable, and unstable. The main differences between the three are further described in **Figure 2.6**. It is also important to note that the term ‘turbulence’ hereafter refers to both (summation of) mechanically and buoyancy-generated turbulence, unless otherwise stated.

Figure 2.6 Atmospheric stability category.



On land, atmospheric stability is a cycle that varies diurnally (daily) where stable conditions occurs at night and unstable conditions occur around midday. The ground propagates heat (through conduction) faster than the air (through radiation) so that during the night, the earth surface is cold and the atmosphere is still warm after heating from the sun at the day. During the day, the earth surface is hot due to sun heating but the atmosphere is still cold after the night.

The type of medium on which heat of the sun travels, affects the cycle of atmospheric stability. This is why at offshore where the surface medium in contact with air is water, the cycle of atmospheric stability occurs seasonally. The ocean has larger heat capacity and volume of energy distribution compared to the ground, so it takes a longer time for the ocean surface to heat up or cool down. Stable conditions take place during summer when sea surface is relatively colder than the summer air. During winter season, unstable conditions occur when sea surface tends to be hotter than the air temperature.

In terms of turbulence, stable atmospheric stability has the least turbulence compared to neutral and unstable conditions, yet has the highest wind shear gradient. Under neutral stability, the occurring turbulence is merely due to contribution of the mechanically generated (shear) turbulence, while unstable stability condition has significant buoyant-generated turbulence. It is important to notice that a larger wind shear gradient does not imply having higher mechanically generated turbulence since mechanically generated turbulence is driven by surface roughness z_0 and wind flow from the large-scale pressure gradients (Gasch & Twele, 2011).

As discussed in *Figure 2.6*, buoyancy-generated turbulence contributes to air parcel mixing between air parcel layers and so it decreases the wind shear gradient as observed in the case of unstable condition. The opposite effect occurs under stable condition: the high wind shear, implying abrupt change in wind speed with respect to height (Roy & Sharp, accessed April 2016). This phenomenon is illustrated in *Figure 2.7*.

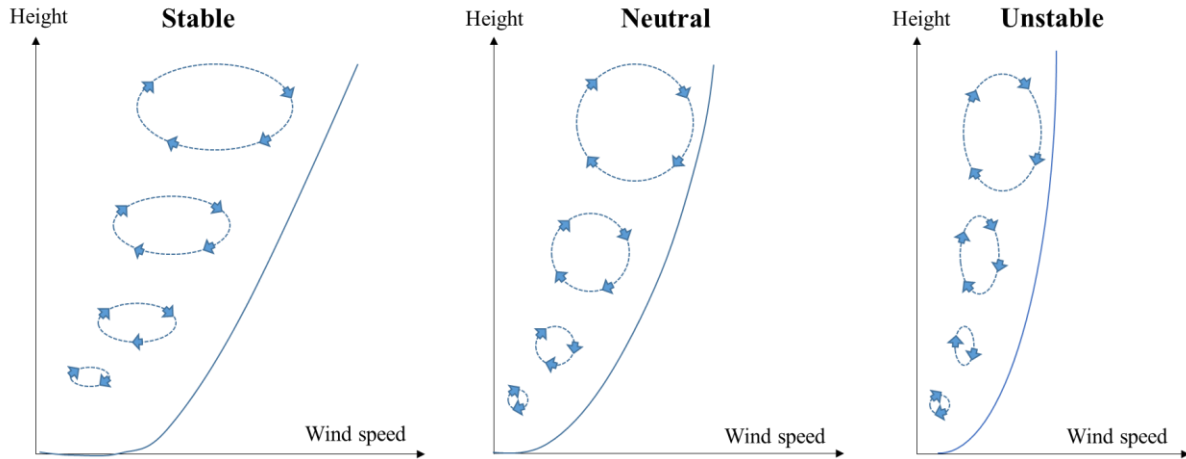


Figure 2.7 Atmospheric stability effect towards mean wind speed profile/wind shear.

From *Figure 2.7*, it is clear to see the influence of different atmospheric stability on the wind speed profile, it is therefore necessary to include a stability correction on the wind profile whenever possible. Motta et al. (2005) highlighted the importance of atmospheric stability correction through comparison of estimation and measurements where they found that in the presence of stability correction, the error was reduced by 50% (for very stable conditions). In addition, Sathe et al. (2011) concluded that without stability correction, the measured and estimated wind profile under stable conditions were over-predicted.

Correction of atmospheric stability on the wind profile can only be made using the logarithmic law wind profile (2.3) but not for power law wind profile (2.1). Taking into account the atmospheric stability, the correction as suggested by DNV (2010) is as follows:

$$U(z) = \frac{\ln(z/z_0) - \Psi_m(z/L)}{\ln(z_{ref}/z_0) - \Psi_m(z_{ref}/L)} U_{ref} \quad (2.4)$$

where

Ψ_m : stability function, depends on height z

L : Monin-Obukhov length (in metre)

Monin-Obukhov length represents the effect of shear friction to buoyancy ratio towards the vertical air movement (Gasch & Twele, 2011). Having three important parameters characterising turbulence in the surface layer, Monin-Obukhov length is mathematically defined as (Monin & Obukhov, 1954):

$$L = - \frac{v_*^3}{\kappa \frac{g}{T_o} \frac{q}{c_p \rho}} \quad (2.5)$$

where

v_* : characteristic velocity scale, normally taken as dynamic velocity = $\sqrt{\tau/\rho}$; τ is the turbulent friction stress and ρ is the density of air

κ : von Karman constant ~ 0.43

g/T_o : dimensional constant; g is the gravity acceleration and T_o is the mean temperature of surface layer

$q/c_p\rho$: temperature flux where q is the heat flux

The sign of L varies depends on the heat flux q . In the case of stable condition, the heat flux is negative $q < 0$ so that L has positive sign, in contrast with unstable condition which heat flux is positive $q > 0$ so L has negative sign (Monin & Obukhov, 1954). In connection with Monin-Obukov length, the measure of air density gradient, the Richarson number R_i is given by (Encyclopædia Britannica, accessed April 2016):

$$R_i = \frac{g}{\rho} \frac{\partial \rho}{\partial z} / \left(\frac{\partial v}{\partial z} \right)^2 \tag{2.6}$$

(2.6) is rearranged into (Monin & Obukhov, 1954):

$$R_i = \frac{z}{L} x \frac{1}{\varphi\left(\frac{z}{L}\right)} \tag{2.7}$$

with $\varphi(z/L)$ is the non-dimensional factor where z is the considered height and should be determined from empirical data, solve-able for $z/L < 1$ (Monin & Obukhov, 1954). When the considered height z is relatively small compared to L , $\varphi(0) = 1$ so the height of dynamic turbulence sublayer L (Monin-Obukhov length) is defined by (Monin & Obukhov, 1954):

$$\frac{1}{L} = \left(\frac{\partial R_i}{\partial z} \right)_{z=0} \tag{2.8}$$

In spite of the complex expression of Monin-Obukhov length L , a simpler form of the two parameters Ψ_m and L are given in **Table 2.4** as recommended by DNV.

Table 2.4 Stability Correction Factor (DNV-RP-C205, 2010)

Parameter	Stability Condition		
	Stable	Neutral	Unstable
Criteria	$z/L > 0$	$z/L = 0$	$z/L < 0$
Richardson Number (Ri)	$0 < Ri < 0.2$	-	$Ri < 0$
Monin Obukhov length (L)	$L = z \left(\frac{1 - 5Ri}{Ri} \right)$	-	$L = \frac{z}{Ri}$
Stability function (Ψ_m)	$\Psi_m \left(\frac{z}{L} \right) = \frac{-4.7z}{L}$	-	$\Psi_m \left(\frac{z}{L} \right) = 2 \ln(1 + x) + \ln(1 + x^2) - 2 \tan^{-1}(x)$ where: $x = (1 - 19.3(z/L))^{1/4}$

Furthermore, atmospheric stability classification might vary from very unstable to very stable, depending on the Monin-Obhukov length as presented in *Table 2.5*. These classification terms will be used throughout the thesis to express different atmospheric stability, unless otherwise stated.

Table 2.5 Atmospheric Stability Class (Gryning et al., 2007)

Obukhov Length (m)	Atmospheric Stability
$-100 \leq L \leq -50$	Very unstable
$-200 \leq L \leq -100$	Unstable
$-500 \leq L \leq -200$	Near unstable
$ L \geq 500$	Neutral
$200 \leq L \leq 500$	Near stable
$50 \leq L \leq 200$	Stable
$10 \leq L \leq 50$	Very stable

2.2 Turbulent Wind and Turbulence

Eddies and gusts generated in a wind field due to turbulence makes wind a random, stochastic process. The mean velocity expressed in (2.1), (2.3), and (2.4) act in the longitudinal along wind direction; however there are also variation in the mean velocity in the cross and vertical directions relative to the along wind direction which correspond to v and w respectively. Normally, these two components do not contribute significantly on the loads on the structure due to much smaller energy content compared to the u -component. Nevertheless, when a flexible structure such as wind turbine is considered, the v and w components might contribute to dynamic resonant of wind turbines, therefore it is necessary to include all three components in the analysis.

Characteristics of turbulent wind field can be assessed through several important parameters including turbulence intensity, spectral density function, integral length scale, correlation, as well as cross-spectrum and coherence.

2.2.1. Turbulence Intensity

Turbulence intensity is a measure of wind speed fluctuation about its mean value, where a higher turbulence intensity means more variation about the mean wind speed. Turbulence intensity is defined as the ratio between standard deviation σ and mean velocity U as a function of height:

$$I_u(z) = \frac{\sigma_u(z)}{U(z)} \quad (2.9)$$

$$I_v(z) = \frac{\sigma_v(z)}{U(z)} \quad (2.10)$$

$$I_w(z) = \frac{\sigma_w(z)}{U(z)} \quad (2.11)$$

where (2.9), (2.10), and (2.11) are turbulence intensities for longitudinal, lateral, and vertical direction respectively. Reference values for turbulence intensity are available in offshore wind turbine guidelines and standards such as NORSOK, DNV and IEC, which serve as the basis for wind turbine classification. The thesis will refer to wind turbine classification according to the IEC standard as given in *Table 2.6*

with the chosen class in this study for offshore wind turbine is Class C. This selection is based on the wind measurements from offshore sites FINO1 (data from 2004-2008 at 91.5m above sea level) and FINO3 (data from November 2009-October 2010 at 90m above sea level) as the average occurring turbulence intensity are below 10% at both locations (Westerhellweg, 2010). It is also important to remember that the value presented in **Table 2.6** refers only to the longitudinal component of the wind (I_u).

Table 2.6 Intensity Values According to Wind Turbine Class Turbulence (IEC 61400-1 3rd edition, 2005)

Wind Turbine Class	I_{ref}^*
A	0.16
B	0.14
C	0.12
S	Specified by the designer

* I_{ref} is the turbulence intensity value at 15m/s mean wind speed

For each wind turbine class mentioned in **Table 2.6**, turbulence intensity value at a given wind speed can be calculated accordingly using (2.9) and standard deviation according to (IEC, 2005):

$$\sigma_1 = I_{ref} (0.75U_{hub} + b) \tag{2.12}$$

where

σ_1 : standard deviation for longitudinal component, assumed to be invariant with *height*

U_{hub} : mean velocity at hub height (m/s)

b : constant, to be taken as 5.6m/s

Equation (2.9), (2.10) and (2.11) show that turbulence intensity value decreases with the increasing mean wind speed, which also implicitly explains why turbulence intensity decreases with height. In addition, unstable conditions have higher turbulence intensity than stable conditions due to larger vertical mixing contributing to more buoyant-generated turbulence (as explained in **Figure 2.6**) and thus the total turbulence. This is observed especially at the low wind speeds where the contribution of atmospheric stability is more pronounced (Gasch & Twele, 2011). Comparing onshore and offshore sites under the same atmospheric stability condition, offshore sites have lower turbulence intensity as the open sea has low roughness length (z_0) causing lower mechanically generated turbulence for the same wind flow. Yet, the influence of the buoyant-generated turbulence (atmospheric stability) is prominent at offshore than onshore due to a more intense heat flux transfers in the vast open ocean water surface (Twidell & Gaudiosi, 2009).

2.2.2. Wind Spectral Density Function

In a turbulent wind field, the occurring turbulence contains a wide range of components with different frequencies. A spectrum –or spectra– or spectral density– describes variation in turbulent wind field and represents the energy contained on the system. In mathematical form, spectral density function is defined as:

$$S_u(f) = \frac{\sigma_u^2}{df} \tag{2.13}$$

So, the variance σ_u^2 can be written as the following:

$$\sigma_u^2 = \int_0^{\infty} S_u(f) df \tag{2.14}$$

Both equations (2.13) and (2.14) are also valid for the v and w wind turbulence components. It is important to note that all spectrums described in this thesis are one-sided spectrum. To mention, there are various spectrums used to describe wind turbulence as summarised in **Table 2.7**, where normalisation is done for the presented spectrums. However, not all spectrums will be studied in detail. Von Kármán and Kaimal Spectra will be elaborated later in Subchapter 2.4, as these two spectrums correspond to the two turbulence models discussed in this thesis.

Within the assumption that length scales (L_i^x) are proportional to height (z) and variances (σ^2) are proportional to u_*^2 , the non-dimensional spectrum as function of frequency f and height z is written as (Mann, 1998):

$$PSD_i(f, z) = \frac{f S_i(f)}{\sigma_i^2(z)} \sim \frac{f S_i(f)}{u_*^2} \tag{2.15}$$

with

$PSD_i(f, z)$: non-dimensional power spectral density

u_* : friction velocity = $\sqrt{u\bar{w} + v\bar{w}}$

f : frequency (Hz)

σ_i^2 : variance

subscript i : u, v, w for each turbulence component

Table 2.7 Non-Dimensional Single Point Spectrum

Spectrum	Parameters	Remark
<p style="text-align: center;">von Kármán</p> $\frac{f S_u(f)}{u_*^2} = 4\hat{f} \frac{\sigma_u^2}{u_*^2} \frac{1}{[1 + 70.8\hat{f}^2]^{5/6}}$ $\frac{f S_v(f)}{u_*^2} = 4\hat{f} \frac{\sigma_v^2}{u_*^2} \frac{1 + 189(2\hat{f})^2}{[1 + 70.8\hat{f}^2]^{5/6}}$ $\frac{f S_w(f)}{u_*^2} = 4\hat{f} \frac{\sigma_w^2}{u_*^2} \frac{1 + 189(2\hat{f})^2}{[1 + 70.8\hat{f}^2]^{5/6}}$ <p>(von Kármán, 1948)</p>	$\hat{f} = \frac{f L_i^x}{U}$ <p>U: mean wind speed</p> <p>L_i^x: turbulent length scale in x-direction</p> <p>Subscript i: u, v, w for each turbulence component</p>	<ul style="list-style-type: none"> Assumes a homogeneous isotropic turbulent field at any time The squared turbulence mean value represents turbulent intensity (von Kármán, 1948).

Spectrum	Parameters	Remark
<p style="text-align: center;">Kaimal</p> $\frac{fS_u(f)}{u_*^2} = \frac{105n}{[1 + 33n]^{5/3}}$ $\frac{fS_v(f)}{u_*^2} = \frac{17n}{[1 + 9.5n]^{5/3}}$ $\frac{fS_w(f)}{u_*^2} = \frac{2n}{1 + 5.3n^{5/3}}$ <p>(Kaimal et al., 1972)</p>	$n = \frac{fz}{U}$ <p>z: the height of interest U: mean wind speed</p>	<p>Derived from measurements in Kansas with stability condition $-2.1 < z/L < +3.3$ (Kaimal et al., 1972).</p>
<p style="text-align: center;">Simiu and Scanlan</p> $\frac{fS_u(f)}{u_*^2} = \frac{200n}{[1 + 50n]^{5/3}}$ $\frac{fS_v(f)}{u_*^2} = \frac{15n}{[1 + 9.5n]^{5/3}}$ $\frac{fS_w(f)}{u_*^2} = \frac{3.36n}{1 + 10n^{5/3}}$ <p>(Simiu & Scanlan, 1996)</p>	$n = \frac{fz}{U}$ <p>z: the height of interest U: mean wind speed</p>	<p>Similar with Kaimal Spectra, only the constants that are different. Used for structural design and overestimate structural response for area with $z_0 > 0.3m$ (Simiu & Scanlan, 1996).</p>
<p style="text-align: center;">Busch-Panofsky</p> $\frac{fS_w(f)}{u_*^2} = \frac{\sigma_w^2}{u_*^2} \frac{2.15n}{1 + 11.16n^{5/3}}$ <p>(Panofsky & Lumley, 1964)</p>	$n = \frac{fz}{U}$ <p>z: the height of interest U: mean wind speed</p>	<p>According to (Cheynet et al., 2015) and (Holmes, 2001), Busch-Panofsky spectra is best describe w-component turbulence; therefore u and v components are not presented.</p>
<p style="text-align: center;">Højstrup</p> $\frac{fS_u(f)}{u_*^2} = \left[\frac{5n_t}{1 + 2.2n_t^{5/3}} + \frac{105n}{(1 + 33n)^{5/3}} \right] \frac{1}{1 + 7.4(z/A)^{2/3}}$ <p>(Højstrup et al., 1989)</p>	<p>$A = 3000m$ (neutral length scale)</p> $n_t = \frac{fA}{U}$ $n = \frac{fz}{U}$ <p>z: the height of interest U: mean wind speed</p>	<p>Kaimal Spectrum presents in the second term inside the brackets. (Mann, 1998) states that v-component spectrum is available but never been compared to data.</p>

Note:

each spectrum in **Table 2.7** correspond for one height z and mean wind speed at z

2.2.3. Correlation

When we consider two points in space exposed to the same stochastic wind, correlation holds an important role, showing the likeness between two spatial points in the turbulent wind field. Correlation is a statistical parameter and is described mathematically as the ratio between covariance of the two points and the multiplication of each point's standard deviation:

$$\rho_{cor} = \frac{cov(u_{z_1}, u_{z_2})}{\sigma_{z_1} \sigma_{z_2}} = \frac{E[\{u_{z_1} - U(z_1)\}\{u_{z_2} - U(z_2)\}]}{\sigma_{z_1} \sigma_{z_2}} = \frac{E[u_{z_1} u_{z_2}]}{\sigma_{z_1} \sigma_{z_2}} \tag{2.16}$$

where

$$-1 < \rho_{cor} < 1$$

$U(z_1)$: mean wind speed at z_1

$U(z_2)$: mean wind speed at z_2

σ_{z_1} : wind speed standard deviation at height z_1

σ_{z_2} : wind speed standard deviation at height z_2

This formula (2.16) refers to vertical correlation (two points at different height), yet it is also possible to have lateral correlation by replacing z with y (horizontal distance between two points). When $\rho_{cor} \sim 1$, it indicates that both points considered are highly correlated or could also mean that both points are on an infinitesimal distance. When ρ approaches 0, both points are not correlated or could be in a very great distance. Other example, $\rho_{cor}=+0.8$ means that if the wind speed at z_1 increases, wind speed at z_2 will also increase. For $\rho_{cor}=-0.8$, both wind speeds at z_1 and z_2 are correlated but on the opposite way i.e. if the wind speed at z_1 increases, wind speed at z_2 will decrease.

2.2.4. Integral Length Scale of Turbulence

The size of vortices (turbulent eddies) in a turbulent wind flow is represented by the integral length scale. Each turbulence component (u, v, w) has its own eddy size in longitudinal, lateral, and vertical direction respectively (Simiu & Scanlan, 1996). For instance, $L_u^x, L_u^y,$ and L_u^z are the measure of eddy size respectively in longitudinal, lateral, and vertical direction of u component. A larger integral length scale implies larger eddies occur in a wind field. These large eddies tend to be unstable and break into smaller eddies while transferring its energy upon the smaller eddies, and continue to break into even smaller eddies until eddies motion is stable (Bakker, 2002). Mathematical expression for integral length scale is given by (Simiu & Scanlan, 1996):

$$L_u^x = \int_0^{\infty} \rho_u(z, r_x) dr_x \tag{2.17}$$

where

$\rho_u(z, r_x)$: cross-correlation function between two u turbulence components separated with the distance r_x in the x-direction

Each turbulence component u, v and w corresponds to measured eddy size in three directions, so there are nine length scales obtained with the similar expression from (2.17) as presented in **Table 2.8**.

Table 2.8 Integral Length Scales of Turbulence

Turbulence Component	Direction		
	Longitudinal	Lateral	Vertical
u	L_u^x	L_u^y	L_u^z
v	L_v^x	L_v^y	L_v^z
w	L_w^x	L_w^y	L_w^z

Integral length scale of turbulence is one of the parameters included in the turbulence model that will be elaborated on Subchapter 2.4. It is important to note, not to confuse L_u^x with the symbol L which defined the Monin-Obukhov length as described in Subchapter 2.1.2.

2.2.5. Cross-Spectrum and Coherence

In the design of offshore wind turbines, at least two-point statistics are needed to describe wind turbulence acting on turbines structures (Sathe et al., 2013). Cross-spectrum is a two-point statistical mean describing wind turbulence and serves as the basis for most of the available turbulence theoretical models (Mann, 1998). Cross-spectrum provides information on how mutually coherent velocity fluctuation at two spatial points, which consists of two parts: real part, known as co-spectrum and imaginary part called quadrature spectrum. Co-spectrum captures different frequency components appearance concurrently (Cheynet et al., 2015) and usually used for structural response calculation. Quadrature spectrum on the other hand, contains information regarding phases. These phases show to which extent the turbulence at –let say point A– leads or lags in time towards turbulence in point B (Chougule et al., 2014). Saranyasontorn & Veers (2004) stated that a phase spectrum is regarded as less important and therefore negligible. In a homogeneous turbulence field, the real part of cross-spectrum is normally more dominant than the imaginary part, so that cross-spectrum can be regarded as co-spectrum or its real part only (Saranyasontorn & Veers, 2004). Chougule et al. (2014) however studied the behaviour of phases for different stability conditions and concluded that there is no significant change of the spectral phases, they behave similarly for the three stability conditions.

Coherence refers to the normalised cross-spectrum, containing both real and imaginary part while the normalised co-spectrum is known as co-coherence. Please note that hereafter; the term ‘coherence’ refers to the co-coherence, which is the normalised form of cross-spectrum’s real part, unless otherwise stated. For two stationary stochastic processes of a and b , the magnitude-squared coherence is mathematically defined as:

$$\gamma^2(f) = \frac{|S_{ab}(f)|^2}{S_{aa}(f) S_{bb}(f)} \quad (2.18)$$

The expression (2.18) can also be expressed in the absolute form (root-coherence), yet the format used in this thesis will be in the form of this magnitude-squared (2.18). A typical theoretical coherence plot is sketched in **Figure 2.8**. It can be seen from **Figure 2.8** that for high frequency turbulence, the coherence decreases significantly, since high frequency turbulence usually has small eddies that only cover a relatively small area (DTU, accessed 2016). The opposite applies to low frequency turbulence as it has large eddies covering wider area than high frequency turbulence.

Coherence on turbulent wind can be expressed in two ways, the horizontal (lateral) and vertical coherence. Lateral coherence is obtained when two points at the same height yet separated horizontally are considered, while vertical coherence is derived when two points separated in vertical distance are considered.

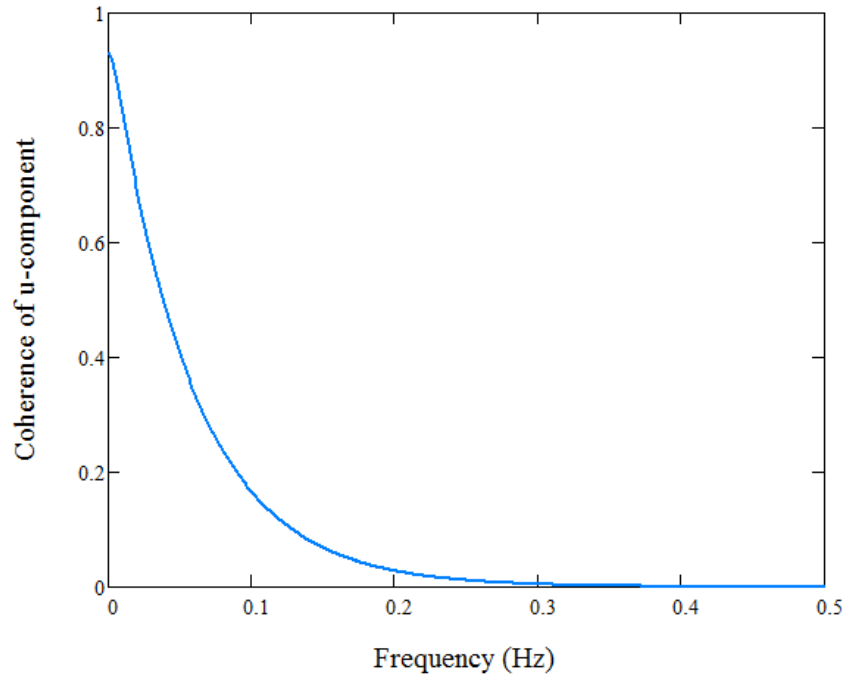


Figure 2.8 Typical coherence plot.

Two widely used empirical coherence models available up to date are the Davenport's Exponential Model and the IEC Modified Exponential Model (Saranyasontorn & Veers, 2004). One additional coherence model is presented here as reference, the ESDU Coherence Model which is less used due to its complexity compared to other empirical coherence models available (Mann, 1998).

A. Davenport's Exponential Coherence Model

A coherence model based on along wind turbulence component is proposed by Davenport (1961) in the exponential form with decay constant c . Viguera-Rodríguez et al. (2012) stated that most of the current coherence models are the modification of decay constant c in (2.19). This model expresses the normalised co-spectrum (the real part of cross-spectrum) and a zero-valued phase-spectrum (imaginary part of cross-spectrum). The model, derived within the assumption that coherence depends only on decay rate and reduced frequency is expressed as follow (Davenport, 1961):

$$\gamma^2(f) = \exp[-c(f_r)] \quad (2.19)$$

where

c : decay constant

$f_r = fD/U$, reduced frequency

f : frequency

D : separation distance

U : mean wind speed at the considered height

Panofsky & Dutton (1984) suggests similar expression of numerical coherence (2.19), yet different decay constant c applicable for both lateral and vertical separation is introduced:

$$c = 6 + 11(D_2 - D_1)/(D_2 + D_1) \quad (2.20)$$

where

D_1 : point 1 considered

D_2 : point 2 considered

For two points with both lateral and vertical separations, the extended Davenport Coherence Model has two decay constants for each direction as shown (Davenport, 1977):

$$\gamma^2(f) = \exp \left[-\frac{f}{U} \sqrt{(c_y D_y)^2 + (c_z D_z)^2} \right] \quad (2.21)$$

where

c_y : decay constant in lateral direction

c_z : decay constant in vertical direction

f : frequency

D_y : separation distance in lateral direction

D_z : separation distance in vertical direction

U : mean wind speed at both considered height = $0.5(U_{z1} + U_{z2})$

The value for decay constants as suggested by Simiu & Scanlan (1996) are $c_y = 32$ and $c_z = 20$. Referring to a study by Saranyasoontorn & Veers (2004), for vertical separation, c_z is increasing as the increment of the separation distance, whereas for lateral separation, there is no consistent dependency of c_y on the separation distance.

Limitations of the Davenport Coherence Model was pointed out by Dyrbye & Hansen (1997) as the following:

- The coherence will always be positive which is inconsistent with the mean of longitudinal turbulence component equals to zero
- As the frequency f goes to zero, the coherence will show unity (resulting '1') in the coherence, which is not logical for large separation distance at low frequency.

Other disadvantages of this model as discussed by Solari (1978) is that the decay constant c does not reflect the stochastic behaviour due to its fixed value, while Viguera-Rodríguez et al. (2006) revealed that the dependence with respect to the incoming wind flow angle is not explained, which is necessary when one consider a wind farm. Moreover, Saranyasoontorn & Veers (2004) indicates that (2.19) is dependent on the reduced frequency and only implicitly dependent towards separation distance, implying the model (2.19) cannot accurately describe the coherence especially in the case of large separation as highlighted by (Dyrbye & Hansen, 1997)

B. IEC Modified Exponential Coherence Model

In response with limitations in Davenport Exponential Coherence Model, modification was made to account for large separations in low frequency range. This modified exponential model having an additional term is currently presented in IEC (2005) guideline, defined as:

$$\gamma^2(f) = \left\{ \exp \left[-p \sqrt{\left(\frac{fD}{U}\right)^2 + \left(\frac{qD}{L_c}\right)^2} \right] \right\}^2 \quad (2.22)$$

where

p : decay constant = 8.8 (equals to 12 for root-coherence)

q : decay constant = 0.12

f : frequency

D : separation distance

L_c : coherence scale parameter, from IEC (2005) to be taken as L_u in **Table 2.9**

U : mean wind speed at the considered height

The formula (2.22) applies for two points with single separation —either lateral or vertical—, which is discussed along with Kaimal spectra (**Table 2.7**) to describe the coherence in a turbulent wind field. Nevertheless, the provided coherence formula (2.22) is valid only for longitudinal wind component u , whereas for lateral v and vertical w components are not stated (Gnanasekaran & Jöckel, 2015).

C. ESDU Coherence Model

One model suggested by Engineering Sciences Data Unit (ESDU) is a coherence exponential model with three parameters, namely C_1 , C_2 , and C_3 (ESDU, 1986):

$$\gamma^2(f) = \left\{ \exp - \left[\frac{D}{U} \sqrt{(C_1 f)^2 + (C_2)^2} \right]^{C_3} \right\} \quad (2.23)$$

where

f : frequency

D : separation distance

U : mean wind speed at the considered

C_1 contributes to gradient of decay, C_2 prevents the coherence value to unity at the low frequency and C_3 gives additional inflection point at low frequency (Cheynet et al., 2015). The values of these parameters can be evaluated by performing fitting from measurement data collected. This coherence model (2.23) is highly dependent on the terrain type since coefficient C_1 , C_2 and C_3 are determined from fitting the turbulence model with the measured data (Krokeborg, 2001).

2.3 Marine Atmospheric Boundary Layer (MABL)

When considering an offshore site, some parameters and characteristics are differ from what occur on onshore. In contrast to the onshore atmospheric boundary layer, MABL is characterised by the non-stationary boundary layer, the variable roughness length, and the seasonal cycle of atmospheric stability.

Non-Stationary Boundary Layer

On land, the ground elevation is fixed, however the sea surface elevation is continuously changing over time due to the wind-wave interaction and so, the surface in contact with the air is a function of time and space. As wind blows over the sea surface, waves are generated and the longer the wind duration, the larger the generated waves. The formed waves give friction to the blowing wind and thus affecting the wind velocity profile as illustrated in **Figure 2.9**. A larger wave implies higher surface roughness z_0 , which mean at high wind speeds, the mechanically generated (shear) turbulence is dominating, indicating a neutral condition. This is in agreement with Twidell & Gaudiosi (2009) who observed the measured wind in Offshore Denmark, Vindeby, at high wind speeds, the atmospheric stability were dominated by neutral conditions. Moreover, a study by Kitaigorodskii et al. (1983) concluded that the

wind-waves interaction affects the generated turbulence in a way that the turbulence's spectrum had the same spectral peak with the waves.

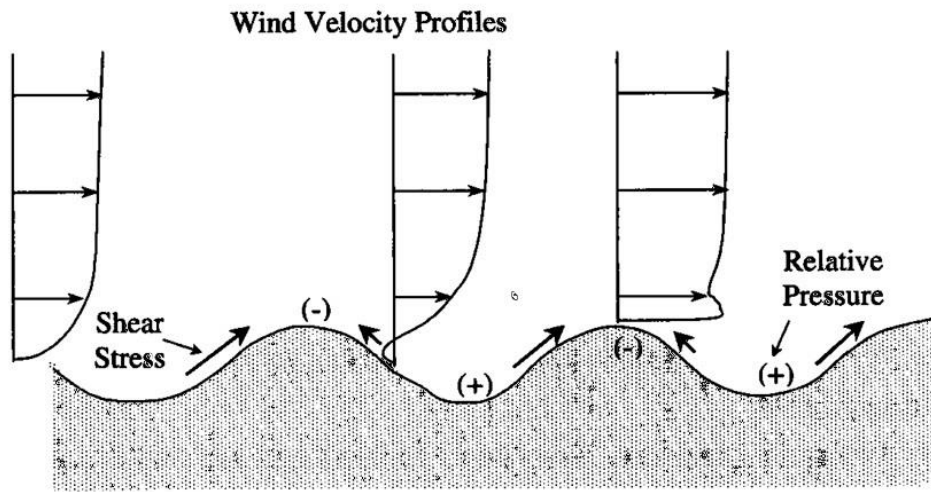


Figure 2.9 Wind velocity profiles over sea surface (Warwick, 2011).

Mann (1998) stated that factors contributing to uncertainty in the velocity fluctuation over sea surface include atmospheric stability, surface currents, wave age, water depth, and the length of wave generation area.

Variable Roughness Length

Over water surface, roughness length is not constant is defined by (Charnock, 1955), due to the fluctuating wind-waves interaction. The roughness length z_0 over a water surface can be solved iteratively and is defined as follows:

$$z_0 = A \frac{u_*^2}{g} \tag{2.24}$$

where

A : Charnock constant (0.0144, as suggested by Garratt over extensive study on ocean data)

u_* : friction velocity = $\sqrt{\overline{u^2} + \overline{v^2}}$ which can be solved iteratively

g : gravity acceleration (9.81m/s^2)

DNV (2010) recommends z_0 value varying from 0.0001m for open sea and 0.001m in coastal regions. This small value of z_0 causes lower thickness of surface layer than on land, meaning the surface layer at offshore could height lower than surface layer on ground. For large rotor turbines at offshore sites, the validity of the mean wind profile is a concern since the surface layer height can be as low as 40m under stable conditions and this is well below the hub height of most modern wind turbines. This means either logarithmic or power-law profile cannot be used since both models are only valid within the surface layer.

Gryning et al. (2007) propose an extended formula to account for wind speed beyond the surface layer. These three formula are correspond to neutral, stable, and unstable atmospheric stability; respectively expressed as:

$$U(z) = \frac{u_{*0}}{\kappa} \left[\ln \left(\frac{z}{z_0} \right) + \frac{z}{L_{MBL,N}} - \frac{z}{z_i} \left(\frac{z}{2L_{MBL,N}} \right) \right] \quad (2.25)$$

$$U(z) = \frac{u_{*0}}{\kappa} \left[\ln \left(\frac{z}{z_0} \right) + \frac{bz}{L} \left(1 - \frac{z}{2z_i} \right) + \frac{z}{L_{MBL}} - \frac{z}{z_i} \left(\frac{z}{2L_{MBL}} \right) \right] \quad (2.26)$$

$$U(z) = u_{*0} \left[\ln \left(\frac{z}{z_0} \right) - \psi \left(\frac{z}{L} \right) + \frac{z}{L_{MBL}} - \frac{z}{z_i} \left(\frac{z}{2L_{MBL}} \right) \right] \quad (2.27)$$

where

u_{*0} : friction velocity

L_{MBL} : length scale in the middle of boundary layer

$L_{MBL,N}$: length scale in the middle of boundary layer in neutral condition

L : Obukhov length scale

b : constant

κ : von Kármán constant = 0.4

z : height considered

z_i : boundary layer depth

z_0 : roughness length

$\psi(z/L)$: stability correction factor (*Table 2.4*)

Further detail of these parameters will not be presented in detail in this thesis, but given in Gryning et al. (2007).

DNV standards recommend Frøya wind profile model for offshore sites in the absence of any information regarding the wind profile. The model enables conversion of the 1-hour mean wind speed at height $H = 10\text{m}$ above sea level, expressed as (DNV, 2010):

$$U(T, z) = U_{1hr} \left\{ 1 + C \ln \frac{z}{H} \right\} \left\{ 1 - 0.41 I_u(z) \ln \frac{T}{T_0} \right\} \quad (2.28)$$

where

H : reference height = 10m

z : considered height (m)

T_0 : reference time, taken as 1 hour

T : considered duration, should be less than T_0 (in hour)

$$C = 0.0573 \sqrt{1 + 0.148U_0}$$

$I_u(z)$: turbulence intensity at height z of the along-wind component

Seasonal Cycle of Atmospheric Stability

The cycle of atmospheric stability is seasonal with unstable conditions dominating during the winter and stable conditions during summer. Motta et al. (2005) found that the hourly stability occurrences at offshore sites are relatively constant whereas the monthly stability occurrences are varying based on measurements. This study also concluded that at Danish Offshore Site, the occurrence of unstable

conditions is the most frequent followed by neutral and very stable atmospheric conditions. Identical finding comes from Sathe et al. (2011) who studied this behaviour in the North Sea. Daily variation of atmospheric stability in the North Sea is very low compared to the significant annual variation. It was also found that unstable and neutral conditions are more dominant in the North Sea.

During unstable conditions, wind turbine loading and performance are affected, in a way that high damage equivalent loads on drivetrains and blades are triggered by sudden bursts of coherent turbulence (Roy & Sharp, accessed April 2016). Sudden bursts of coherent turbulence also causes vibration on wind turbine structure which often lead to shut down and extensive wear & tear for yaw and pitch system (Roy & Sharp, accessed April 2016). During stable conditions, rotors are susceptible to fatigue due to prominent torque over the rotor (Roy & Sharp, accessed April 2016). When considering an offshore site, the access and maintenance is not as simple as on land, therefore an offshore wind turbine should be designed accordingly as the planned lifetime along with a thorough maintenance plan.

2.4 The Two Turbulence Models

A turbulence model is imperative towards loading calculations on wind turbines as it ‘simulates’ the variation of wind with respect to space and time in the form of a generated/synthetic wind field. In this thesis, the generated turbulences are based on two widely used models, the IEC Kaimal Spectra & Coherence Model as well as Mann Spectral Tensor Model. The two models are recommended in the IEC Guideline 61400-1 3rd edition, 2005, even though there are other models available. Nevertheless, it is important to notice that the Mann Tensor Model referred in IEC (2005) has parameters accordingly stated in the standard (IEC, 2005). In addition, there are also fitted parameters available for Mann Tensor Model from different sites which are not included in the IEC (2005) standard which are discussed in Subchapter 2.4.2.

2.4.1. IEC Kaimal Spectrum and Coherence Model

The Kaimal Spectrum is the widely used spectrum to describe energy contained in a turbulent wind field, which derived based on measurement in Kansas under adiabatic (non-neutral) atmospheric stability condition. Except for w component spectra (*Table 2.7*) that fits the neutral condition ($z/L = 0$), u and v components are derived under slightly stable atmospheric stability condition (Kaimal et al., 1972). Yet, the adopted version of Kaimal Spectra in the IEC (2005) equation (2.29) is assumed to be under the influence of neutral atmospheric stability for all three components. The original Kaimal Spectra well-describes energy content of turbulent wind in the range frequency of 0.01Hz to 4Hz under neutral atmospheric stability (Kaimal et al., 1972).

The generated turbulent wind field according to IEC Kaimal Spectra & Coherence Model is computed based on the calculated IEC Kaimal Spectrum (2.29) in the longitudinal, lateral, and vertical directions; respectively u , v , and w components. The computed synthetic wind field is assumed stationary with zero-meaned Gaussian process (IEC, 2005). Based on the single point IEC Kaimal Spectral Density (2.29), the neighbouring points’ variation is calculated depending on the separation distance using the coherence function (2.22). The non-dimensional Kaimal Spectral Density as given in the (IEC, 2005) is defined below:

$$\frac{f S_i(f)}{\sigma_i^2} = \frac{\frac{4fL_i}{U_{hub}}}{\left(1 + \frac{6fL_i}{U_{hub}}\right)^{5/3}} \quad (2.29)$$

where

f : frequency (Hz)

subscript ‘i’ denotes 1, 2, and 3 correspond to longitudinal, lateral, and vertical turbulent component respectively.

S_i : one-sided turbulent component spectrum

σ_i : standard deviation of turbulent component (**Table 2.9**)

L_i : length scale of the turbulent component (**Table 2.9**)

U_{hub} : mean wind speed at hub height (m/s)

Table 2.9 Parameters for Kaimal Spectrum (IEC 61400-1 3rd edition, 2005)

Parameter	Turbulent component (i)		
	1	2	3
Standard deviation σ_i	σ_1	$0.8\sigma_1$	$0.5\sigma_1$
Length scale L_i	$8.1\Lambda_1$	$2.7\Lambda_1$	$0.66\Lambda_1$

σ_1 : along-wind direction turbulence standard deviation (2.12)

$$\Lambda_1 = \begin{cases} 0.7z & z \leq 60m \\ 42m & z \geq 60m \end{cases}$$

z : hub height

Parameter Λ_1 given in **Table 2.9** defines the integral length scale of turbulence for along wind u -component in the longitudinal direction L_u^x (Burton et al., 2001).

2.4.2. Mann Turbulence Model

Unlike the IEC Kaimal Spectra and Coherence Model in which synthetic wind field is calculated using a single point spectra and coherence function, the generated wind field based on Mann tensor model is computed from Large Eddy Simulation (LES) where Taylor’s frozen hypothesis is used (Mann, 1998). This is done by integrating the spectral tensor (2.30) on which the Taylor’s hypothesis allows the velocity variation with respect to space to obtain the ‘velocity relation’ between points within the assumption of homogenous field (stationary within space). The spectral tensor is defined as (Mann, 1998):

$$\Phi_{ij}(k) = \frac{1}{(2\pi)^2} \int R_{ij}(r) \exp(-ik \cdot r) dr \tag{2.30}$$

where

$$\int dr \equiv \int_{-\infty}^{\infty} \int_{-\infty}^{\infty} \int_{-\infty}^{\infty} dr_1 dr_2 dr_3 \tag{2.31}$$

therefore, the velocity variation with respect to space will be:

$$u(x) = \int \exp(ik \cdot x) dZ(k) \tag{2.32}$$

with

$$\langle dZ_i^*(k)dZ_j(k) \rangle = \Phi_{ij}(k)dk_1dk_2dk_3 \quad (2.33)$$

*denotes complex conjugate.

The corresponding cross-spectrum as function of the spectral tensor (2.30) is as follow (Mann, 1998):

$$\chi_{ij}(k_1, \Delta y, \Delta z) = \int_{-\infty}^{\infty} \int_{-\infty}^{\infty} \Phi_{ij}(k) \exp i(k_2 \Delta y + k_3 \Delta z) dk_2 dk_3 \quad (2.34)$$

By replacing $\Delta y = \Delta z = 0$ and $i = j$ into (2.34), the single point spectrum definition is obtained while the coherence can be computed accordingly with (2.18), hence the (vertical) coherence becomes (Chougule, 2013):

$$coh_{ij}(\bar{k}_1, \bar{L}, \bar{\Gamma}, \Delta z) = \frac{|\chi_{ij}(\bar{k}_1, \alpha \epsilon^{2/3}, \bar{L}, \bar{\Gamma}, \Delta z)|^2}{F_i(\bar{k}_1, \alpha \epsilon^{2/3}, \bar{L}, \bar{\Gamma}) F_j(\bar{k}_1, \alpha \epsilon^{2/3}, \bar{L}, \bar{\Gamma})} \quad (2.35)$$

where $F_i = \chi_{ii}(k_1, 0, 0)$ and $F_j = \chi_{jj}(k_1, 0, 0)$ are the single point spectrums, \bar{L} and $\bar{\Gamma}$ are the average of L and Γ values at the two considered points; $\bar{k}_1 = 4\pi f / (U_1 + U_2)$. The lateral coherence is acquired by replacing Δz with Δy .

The Mann spectral tensor implies isotropic von Kármán energy spectrum (**Table 2.7**) as the initial condition in which the isotropic degree is indicated by circular flow structure with constant length scale and variance over time: $\sigma_u^2 = \sigma_v^2 = \sigma_w^2$. The presence of wind shear in the real atmospheric condition is considered in the sheared spectral tensor as postulated by Mann (1998) allowing the isotropic flow transforms into anisotropic flow with time as the circular eddies structure is stretched into oval shape until they break so that $\sigma_u^2 > \sigma_v^2 > \sigma_w^2$ (Mann, 1998). To account for the anisotropic, parameter Γ is added to the Mann tensor model so the model has three parameters in total, namely $\alpha \epsilon^{2/3}$, Γ , and L_M . The anisotropic effect due to wind shear is illustrated in **Figure 2.10**.

Mann Model is originally valid under neutral atmospheric condition, however depending on the atmospheric stability and site conditions, the three parameters can be fitted accordingly (Mann, 1998). Each of the three parameters represents the following:

- $\alpha \epsilon^{2/3}$ has the unit of $m^{4/3} s^{-2}$ where $\alpha \approx 1.7$ is the Kolmogorov constant and ϵ is the turbulent wind kinetic energy dissipation. Together, this parameter is the measure of dissipation rate on which wind turbulence kinetic energy is converted into thermal energy as the large eddies formed and break into smaller eddies (Manwell et al., 2010). This parameter increases with the increment of the occurring mean wind speed (Sathe et al., 2013), where higher $\alpha \epsilon^{2/3}$ value implies higher energy in the turbulence spectrum
- Γ is a non-dimensional sheared spectral tensor parameter indicating the degree of anisotropy in a turbulent eddies due to the effect of shear. When the value $\Gamma=0$, it is an isotropic condition while a high degree of anisotropy (large Γ) results in larger ratio of the three-directions turbulence component variance where $\sigma_u^2 > \sigma_v^2 > \sigma_w^2$ (Mann, 1998)
- L_M is the length scale of the spectral velocity tensor having the unit of m . L_M corresponds to similar definition with parameter described in Subchapter 2.2.4, yet in this context, L_M

represents the eddy size with the most energy in a turbulent wind field (or eddy size belongs to the peak of turbulence spectrum). This parameter characterises the atmospheric stability condition at a specific site as it is greatly influenced by the stability condition. Higher value of L_M implies higher turbulence energy in the low frequency range (Chougule et al., 2015).

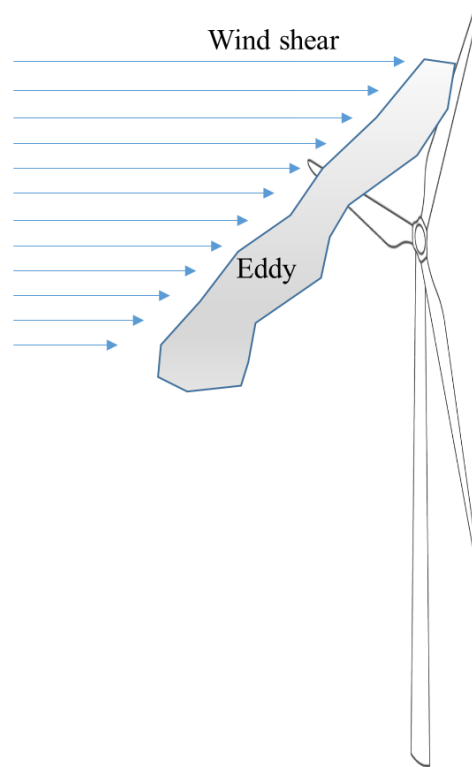


Figure 2.10 Stretched eddy taking into account wind shear approaches wind turbine rotor.

Mann (1998) did some experimental tests to determine the three parameters value for various environmental setup as well as fitting of the spectral tensor model to Kaimal Spectra and Simiu-Scanlan Spectra (*Table 2.7*) as given in *Table 2.10*. In addition, the fitted parameters according to IEC (2005) are also presented in *Table 2.10* where Mann Tensor Model is fitted to the Kaimal Spectra.

Table 2.10 Mann Model Parameters from Experiments and Fitting (Mann, 1998)

Condition	L_M^*		Γ
Atmospheric, over water surface	0.87z		3.2
Atmospheric, over flat terrain	0.91z		2.6
Martin Jensen boundary layer wind tunnel at Danish Maritime Institute (DMI)	0.6z		2.2
DMI's wind tunnel used for bridge section model tests	0.39 meter		0.76
Spectrum	L_M^*	Γ	$\alpha \epsilon^{2/3}$
Kaimal	0.59z	3.9	$3.2 \frac{u_*^2}{z^{2/3}}$
Simiu-Scanlan	0.79z	3.8	$2.8 \frac{u_*^2}{z^{2/3}}$

IEC Standard	L_M^{**}	Γ	$\alpha\epsilon^{2/3}$
61400-1 3 rd edition, 2005	$0.56z \quad z \leq 60m$ $33.6m \quad z \geq 60m$	3.9	$\frac{55}{18}0.4754\sigma_{iso}^2 L_i^{-2/3}$ where $\sigma_{iso} = 0.55\sigma_1$ and σ_1 (2.12) L_i (Table 2.9)

* z is the considered height; ** z is the turbine hub height

2.4.3. Comparison between the Two Turbulence Models

At a glance, the Mann Tensor Model is somewhat more complex and difficult to understand than the IEC Kaimal Spectra & Coherence Model. Yet, one prominent advantage of Mann Model over the IEC Kaimal Spectra & Coherence Model is the possibility to account for atmospheric stability condition on a particular site by performing chi-square fitting of the turbulence spectrum from measurements even though the Mann Model is only valid for neutral atmospheric conditions (Mann, 1994). Nonetheless, this modified Mann Model through ‘forced’ fitting is a drawback and a limitation for the model itself. Another main difference of the two turbulence models is the way the u , v and w turbulence components are treated. The IEC Kaimal Spectra & Coherence Model treats the three components to be independent toward each other, while Mann Model considers the three turbulence components to be correlated, especially the longitudinal u and vertical w components (Burton et al., 2001). This can be seen as the IEC Kaimal Spectra & Coherence Model length scale parameter based only on L_u^x as Λ_1 , neglecting the shear effect while Mann Model length scale parameter L_M does not reflect a specific component of one of the nine length scales available (Table 2.8), but the largest length scale occurs in a turbulent wind flow.

A thorough selection of turbulence model must be done prior to the simulations to obtain correct prediction of wind turbine loads and responses. One way to measure the validity of turbulence model is by performing spatial coherence analysis comparing the analytical model to the real measurements. Previous studies done by Saranyasootorn & Veers (2004) and Obhrai & Eliassen (2016) suggests that Mann Tensor Model describes a turbulent wind field better than IEC Kaimal Spectra & Coherence Model. Both studies were carried out by comparing measurement and analytical result of the coherences using Mann Model and IEC Kaimal Spectra & Coherence Model, with lateral coherence for Saranyasootorn & Veers (2004) and vertical coherence for Obhrai & Eliassen (2016).

A land-based site in Bushland, Texas under slight influence of unstable atmospheric stability was chosen as the study reference by (Saranyasootorn & Veers, 2004). The measured wind was taken at hub height (23m above ground) and four points on the edge of rotor swept area, which then divided into three bins accordingly for three different mean wind speed: (9-11)m/s, (11-13)m/s, and (15-17)m/s. Lateral coherences for u , v , and w components were computed for Mann Model while for the IEC Kaimal Spectra & Coherence Model, only the longitudinal component u is computed. Parameters used for Mann Model is fitted with the measured Kaimal spectra with $\Gamma=3.9$ and $L_M=14m$ were obtained. As for the IEC Kaimal Spectra & Coherence Model, parameters utilised is as given on the standard, Equation (2.22). The comparison result for the three wind speed classes are shown in Table 2.11, Table 2.12 and Table 2.13 respectively for lateral separation of u -component, v -component and w -component. The trends for the three wind speed classes are similar, yet the coherence is slightly increasing with wind speed.

Table 2.11 Theoretical and Measurement Comparison of u Lateral Coherence (Saranyasontorn & Veers, 2004)

Frequency range Separation Distance (lateral) for uu-coherence	Low	Intermediate	High
Small (6m-6.7m)	IEC-Kaimal ⁺ Mann ^u	IEC-Kaimal ⁺ Mann ^u	IEC-Kaimal ⁺ Mann ^u
Intermediate (12.1m-13.4m)	IEC-Kaimal ^u Mann ⁺	IEC-Kaimal ⁺ Mann ⁺	IEC-Kaimal ⁺ Mann ⁺
Large (29.9m-33.2m)	IEC-Kaimal ⁻ Mann ⁺	IEC-Kaimal ⁻ Mann ⁺	IEC-Kaimal ⁻ Mann ⁺

⁺match with the measurement; ⁻not match with the measurement; ^uslightly under-predicts

Table 2.12 Theoretical and Measurement Comparison of v Lateral Coherence (Saranyasontorn & Veers, 2004)

Frequency range Separation Distance (lateral) for vv-coherence	Low	Intermediate	High
Small (6m-6.7m)	Mann ⁺	Mann ⁺	Mann ⁺
Intermediate (12.1m-13.4m)	Mann ^u	Mann ^u	Mann ^u

⁺match with the measurement

^uslightly under-predicts

Table 2.13 Theoretical and Measurement Comparison of w Lateral Coherence (Saranyasontorn & Veers, 2004)

Frequency range Separation Distance (lateral) for ww-coherence	Low	Intermediate	High
Small (6m-6.7m)	Mann ⁺	Mann ⁺	Mann ⁺
Intermediate (12.1m-13.4m)	Mann ⁺	Mann ⁺	Mann ⁺

⁺match with the measurement

The study by Obhrai & Eliassen (2016) was performed using measurement data from offshore site situated in 45km north of Borkum, German island, FINO1 Platform under neutral atmospheric stratification. The measured wind data was collected at three different heights: 40m, 60m, and 80m above sea level, therefore two vertical separations are observed: 20m and 40m. The measured wind speed is classed into three groups: (8-13)m/s, (13-17)m/s, and (17-21)m/s. The result are shown in **Figure 2.11** and **Figure 2.12** where the trends are similar for all three wind-speed classes, only that the coherence value is increasing with wind speed.

From **Figure 2.11**, it can be concluded that the theoretical u -coherences from the IEC Kaimal Spectra & Coherence model for 20m and 40m vertical separations are very close, nearly coincides especially for frequency above 0.05Hz. On the other hand, the calculated coherences by Mann Model show a

difference for 20m and 40m vertical separations. As seen in **Figure 2.11**, the measured u -coherences did not match with both models, where the IEC Kaimal Spectra & Coherence Model depicted lower coherence for small separation (20m) and higher coherence for large separation (40m), while Mann Model captured smaller coherence for small separation and nearly matched the measured coherence for the 40m separation. The computed analytical w -coherences by Mann Model (**Figure 2.12**) showed similar behaviour with the u -coherences, yet the v -coherences were over-predicted for both separation distances.

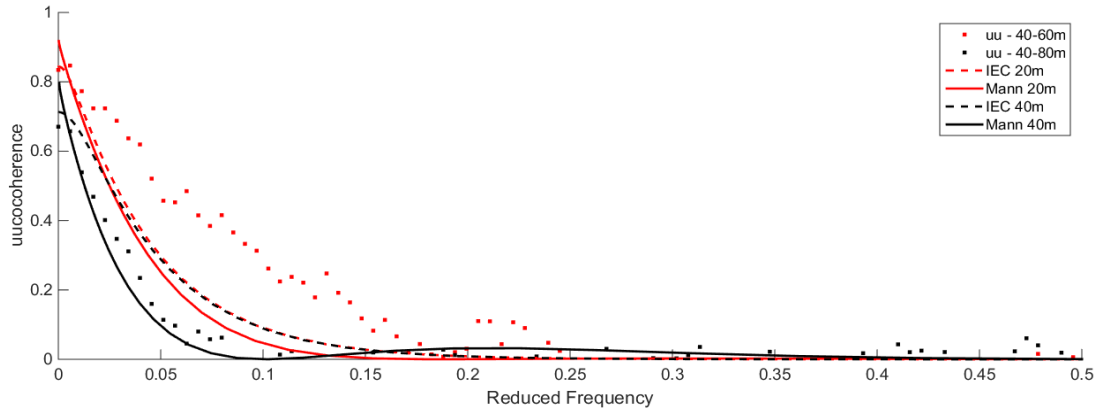


Figure 2.11 Comparison of the uu -coherence for vertical separations (Obhrai & Eliassen, 2016).

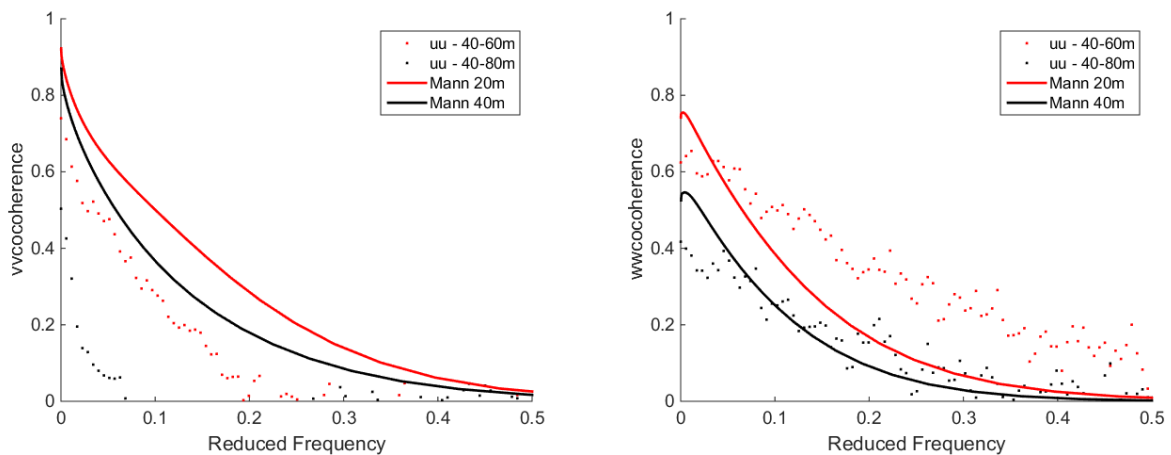


Figure 2.12 Comparison of the vv -coherence (left) and ww -coherence (right) for vertical separations (Obhrai & Eliassen, 2016).

The two previous studies described above can be narrowed to a main conclusion that in general Mann Model describes turbulent wind field better than the IEC Kaimal Spectra & Coherence Model despite the fact that Mann Model is way more complex to compute and demand higher computational tool (Mann, 1998). In addition, Mann Model is able to describe the coherences for v and w components which is another advantage for Mann Model over IEC Kaimal Spectra & Coherence Model.

2.4.4. Influences of Atmospheric Stability on the Two Turbulence Models

Both IEC Kaimal Spectra & Coherence Model and Mann Model are valid only for neutral atmospheric stratification; however the atmospheric stability is not accounted for in the standards and is not site specific. Due to this reason, there might be errors when using of the two models when use to simulate a turbulent wind field under non-neutral atmospheric stability. IEC Kaimal Spectra & Coherence Model in any case is strictly applicable only for neutral atmospheric stability and does not include a stability

correction. Therefore, under non-neutral conditions, the IEC Kaimal Spectra & Coherence Model will lead to inaccurate prediction of the generated/synthetic wind field. On the other hand, the Mann Model can account for stability through fitting with the measured data at a particular location. By fitting the model to acquire the three Mann Model parameters; $\alpha\epsilon^{2/3}$, Γ , and L_M are representing the site specific conditions. The influence of atmospheric stability on parameters $\alpha\epsilon^{2/3}$, Γ , and L_M are discussed below. References available for the three parameters value under different atmospheric conditions are obtained from measurement fitting at Høvsøre site by Pena et al. (2010), Sathe et al. (2013) and Chougule et al. (2015). Even though the site is situated in west coast of Jutland, Denmark, it is taken as offshore reference site for L_M value (in this thesis) due to limited references and data constraints.

Parameter $\alpha\epsilon^{2/3}$

Hypothetically, from very unstable to very stable condition this parameter should decrease since $\alpha\epsilon^{2/3}$ reflects the turbulence energy content where turbulence is decreasing from very unstable to very stable condition. Fitting of the measured wind at Høvsøre obtain $\alpha\epsilon^{2/3}$ values as presented in **Table 2.14** from Pena et al. (2010) and Chougule et al. (2015) as well as **Table 2.15** from Sathe et al. (2013). The fitted values from all references show that in general $\alpha\epsilon^{2/3}$ value for neutral conditions are slightly larger than the values for unstable conditions. Consequently, this implies $\alpha\epsilon^{2/3}_{neutral} > \alpha\epsilon^{2/3}_{unstable} > \alpha\epsilon^{2/3}_{stable}$ which is in contradiction with the outlined hypothesis. According to Chougule et al. (2015), $\alpha\epsilon^{2/3}$ characterises the mechanically generated (shear) turbulence, so when this value increases, the turbulence due to shear is also increasing. Hence, it can be said that under neutral condition, the mechanically generated turbulence dominates than under other stability condition. This is in agreement with Twidell & Gaudiosi (2009) who stated that under near neutral stability, the generated turbulence is purely due to shear (mechanically generated turbulence). Nonetheless, the implication of $\alpha\epsilon^{2/3}_{neutral} > \alpha\epsilon^{2/3}_{unstable}$ is also possible due to the fact that the Mann Model is a best-fit to neutral conditions. Since Mann Model is only valid for neutral conditions, it can only account for changes in mechanically generated (shear) turbulence and not buoyant-generated turbulence which is of importance under non-neutral conditions.

Table 2.14 Energy Dissipation Rate Parameter at Høvsøre for Reference Height = 90 metre

Stability	$\alpha\epsilon^{2/3}$ ($m^{4/3}s^{-2}$) at reference height $z = 90m$	
	(Pena et al., 2010)	(Chougule et al., 2015)
Very unstable	0.0244	not available
Unstable	0.0322	not available
Near unstable	0.0343	0.02278
Neutral	0.04	0.03
Near stable	0.0419	0.03
Stable	0.0329	not available
Very stable	0.0138	not available

Table 2.15 Energy Dissipation Rate Parameter at Høvsøre for Different Wind Speed References

Stability	$\alpha\epsilon^{2/3}$ ($m^{4/3}s^{-2}$) as given by (Sathe et al., 2013)	
	8 m/s	11.4 m/s
Very unstable	0.0305	not available
Unstable	0.0315	0.051
Near unstable	0.033	0.052
Neutral	0.034	0.0685
Near stable	0.034	0.0687
Stable	0.0245	0.048
Very stable	0.0065	0.018

Parameter Γ

Since Γ is a measure of the stretching of eddies due to wind shear, in theory, from very stable to very unstable condition the Γ value should decrease as the wind shear is reduced. Sathe et al. (2013) concluded that in general, neutral stability condition has the largest Γ followed by stable and unstable as presented in **Table 2.17**. Pena et al. (2010) found that stable condition has the largest Γ followed by slight lower value for neutral condition and rather prominent gap towards unstable condition (refer to **Table 2.16**), which is align with the theoretical definition. In short, as the atmosphere stratification tends toward stable conditions, more anisotropic eddies will be generated, implying larger ratio of variance between the three turbulent components where $\sigma_u^2 > \sigma_v^2 > \sigma_w^2$. Yet, deviation is observed from Chougule et al. (2015) indicating that near unstable to near stable the isotropic increases (**Table 2.16**), in contradiction with the theoretical concept and the other two findings by Pena et al. (2010) and Sathe et al. (2013). According to the author, this deviation is caused by the error of the fitting method used, which imply a manual method; while recently a more advanced method was developed, resulting in the highest Γ value for near stable followed by neutral and near unstable conditions (Chougule, 2016).

Table 2.16 Anisotropic Parameter at Høvsøre for Reference Height = 90 metre

Stability	Γ at reference height $z = 90\text{m}$	
	(Pena et al., 2010)	(Chougule et al., 2015)
Very unstable	1.69	not available
Unstable	2.27	not available
Near unstable	2.49	3.2
Neutral	2.63	3.1
Near stable	2.77	2.56
Stable	2.96	not available
Very stable	3.0	not available

Table 2.17 Anisotropic Parameter at Høvsøre for Different Wind Speed References

Stability	Γ as given by (Sathe et al., 2013)	
	8 m/s	11.4 m/s
Very unstable	2.06	not available
Unstable	2.25	2.52
Near unstable	2.71	2.8
Neutral	3.125	3.21
Near stable	3.01	3.05
Stable	2.78	2.7
Very stable	2.74	2.48

Parameter L_M

Unlike $\alpha\epsilon^{2/3}$ and Γ , L_M has distinctive ordered trend with respect to variation in atmospheric stability. From stable-to-neutral-to-unstable atmospheric condition, L_M increases as shown from the three studies discussed by Pena et al. (2010), Sathe et al. (2013) and Chougule et al. (2015) by parameter fitting at Høvsøre. For this reason, Chougule et al. (2015) stated that L_M is the measure of buoyant generated turbulence (atmospheric stability effect) as it is increasing for unstable condition. This also indicates that unstable condition has the largest eddy size on the turbulence spectrum peak than neutral and stable stability condition. Under unstable stratification, the intense vertical mixing causes longer mixing length, hence the stretched eddies can stretch even larger.

From (Pena et al., 2010) and (Chougule et al., 2015), L_M is given as function of height z as presented in **Table 2.18**, while (Sathe et al., 2013) presents L_M as function of the wind speed (**Table 2.19**).

Table 2.18 Integral Length Scales of Spectral Velocity Tensor at Høvsøre for Reference Height = 90 metre

Stability	L_M (m) at reference height $z = 90\text{m}$	
	(Pena et al., 2010)	(Chougule et al., 2015)
Very unstable	73	not available
Unstable	63	not available
Near unstable	47	75
Neutral	31.5	45.5
Near stable	23	35
Stable	11.5	not available
Very stable	8	not available

Table 2.19 Integral Length Scales of Spectral Velocity Tensor at Høvsøre for Different Wind Speed References

Stability	L_M (m) as given by (Sathe et al., 2013)	
	8 m/s	11.4 m/s
Very unstable	114	not available
Unstable	98	107
Near unstable	73	89
Neutral	46	52.5
Near stable	33	33.5
Stable	20	18
Very stable	11.5	8

(DTU, 2013) also suggests reference value for L_M despite the absence of information of the measured site location and the applicability of the data, as shown in **Table 2.20**.

Table 2.20 Integral Length Scales at Høvsøre (DTU, 2013)

Stability	L_M (m)
Very unstable	105.1
Unstable	80
Near unstable	60.7
Neutral	38
Near stable	28
Stable	15.4
Very stable	10.0

2.4.5. Influences of Atmospheric Stability on the Coherences

A recent study by Chougule et al. (2015) who computed vertical coherence from the Høvsøre measurements using Mann Model showed that u, v , and w vertical coherences are affected by atmospheric stability such that from stable to unstable, the coherence is increasing. The vertical coherence of w -component is the most affected while the horizontal component u -vertical coherence is the least affected by variation in atmospheric stability. This is in agreement with the theory that under different atmospheric stability, eddies due to the buoyant-generated turbulence determining the eddies ‘coverage’ in the vertical direction is the most influenced, which imply the vertical coherence for w -component. Another important point is that in the Mann Model, the coherences (both vertical and lateral) are found to be independent with parameter $\alpha\epsilon^{2/3}$ which represents the mechanically generated

(shear) turbulence. This is as seen in the equation (2.35) which show that the coherences are the function of separation distance, L_M , and Γ (Chougule, 2013). This is also supported with the study done by Chougule (2013) who found that the coherences from the measurements at Ryningsnäs and Høvsøre were not dependent on the energy dissipation rate $\alpha\epsilon^{2/3}$.

2.5 Wind Turbine Basics

2.5.1. Parts of an Offshore Wind Turbine

In accordance with IEC 61400-3 1st edition 2009, the parts of an offshore wind turbine can be seen in **Figure 2.13** including the rotor-nacelle assembly (RNA), support structure (tower together with sub-structure) as well as the foundation. An offshore floating wind turbine has no foundation structure, yet mooring lines are deployed while its substructure refers to a floater.

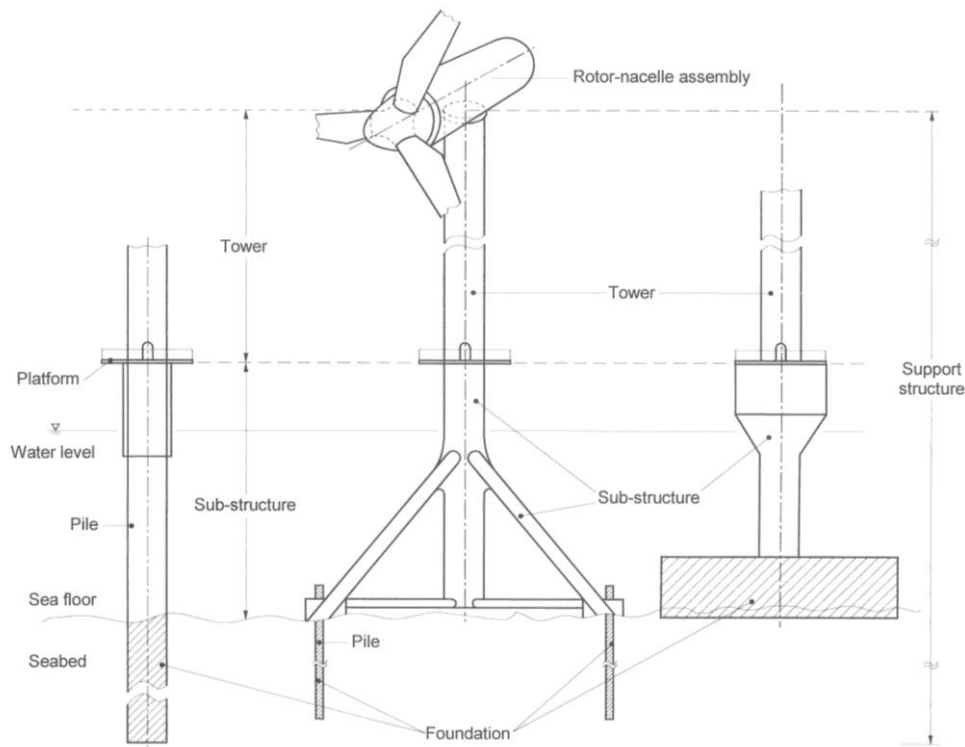


Figure 2.13 Definition of an offshore wind turbine (IEC, 2009).

Rotor-nacelle assembly (RNA) consisted of hub, blades, and nacelle; is the most imperative part of a wind turbine since it is where power generation and control of wind turbine take place. A nacelle contains generator, control system, brake system, and drive-train as well as the blade-pitch regulator. The hub connects the blades and nacelle such that the rotation (kinetic energy) from blades can be converted into electricity by the generator located inside the nacelle. In addition, the yaw bearing is situated below nacelle having the function to adjust RNA orientation towards the incoming wind flow direction through yawing. A sketch of RNA is shown in **Figure 2.14**.

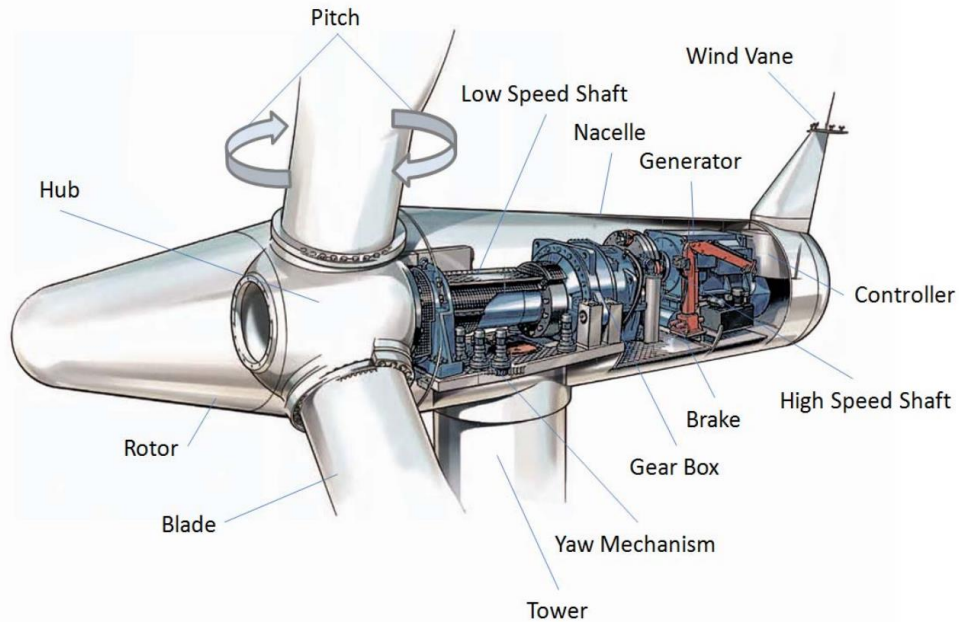


Figure 2.14 Rotor-nacelle assembly anatomy of a wind turbine (Ayee et al., 2009).

2.5.2. Wind Turbine Blade Anatomy and Definition

The blades are a major part of the RNA which ‘receives’ the wind energy and transferring it to the nacelle for further power conversion and extraction. Considering a blade cross section (referred as a 2D aerofoil or just aerofoil) as sketched in *Figure 2.15*, the thickest edge of the aerofoil is called the leading edge where the thinnest edge is called the trailing edge. A straight line connecting trailing edge and leading edge is the chord line, representing aerofoil length (l_{ch}). Thickness t_{ch} of the aerofoil is defined as the farthest distance between upper and lower surface as indicated in *Figure 2.15*. Aerofoil thickness however is usually represented as the ratio between t_{ch} and l_{ch} .

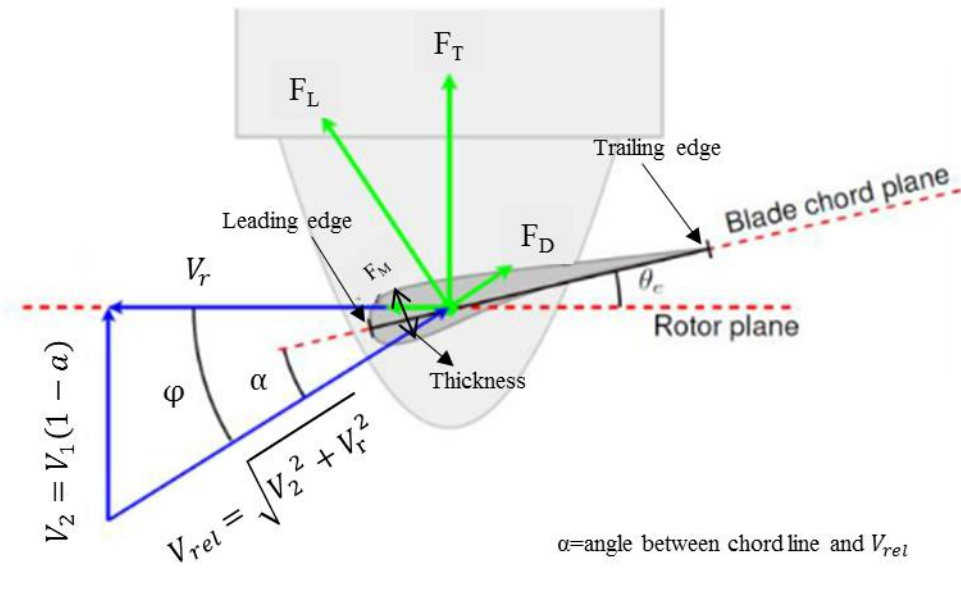


Figure 2.15 Definition of 2D aerofoil (DTU, with modification, accessed 2016).

The incoming undisturbed free wind speed V_1 is reduced to V_2 as it approaches turbine by a factor $(1 - a)$ where a is the induction factor, reflecting the reduction of wind speed on the blades, relative

to the free flow incoming wind speed V_1 . Yet, instead of V_2 , the aerofoil experiences V_{rel} , the relative wind speed at an angle of α° apart from the aerofoil chord line and φ° apart from V_2 is defined as:

$$V_{rel} = \sqrt{V_2^2 + V_r^2} \tag{2.36}$$

where

V_r : rotor rotational speed

V_2 : reduced incoming wind speed = $V_1(1 - a)$

The impact V_{rel} has on the rotor includes drag force (F_D), lift force (F_L), thrust force (F_T) and tangential/moment force (F_M). F_D , parallel with V_{rel} yields load on the rotor while F_L perpendicular with V_{rel} , causes rotation of the blades. The former α is known as angle of attack, on which a maximum lift F_L is determined so that the power output can be determined.

A typical wind turbine blade has various cross sectional sizes and properties from blade root to blade tip as shown in **Figure 2.16**. Normally, the blade root has a relative thick cross section compared to the mid-span and tip of the blade serving as a support for the whole blade length, whereas the tip has thin thickness to minimise bending and shear loads. The rotational speed V_r experienced by a blade varies from blade root to tip with maximum V_r occurs at the tip and minimum at the root. Due to cross sectional size and V_r variation, F_D and F_L along the blade is not constant. To balance the drag over the blade length, the blade is tapered, while twisting of the blade has the purpose to balance the lift as each blade cross section is exposed to different angle of attack α (Gipe, 1995). The blade twist angle is the largest near the blade root and the least at the tip. A detailed explanation regarding F_D and F_L can be found in Subchapter 3.1.3.2.

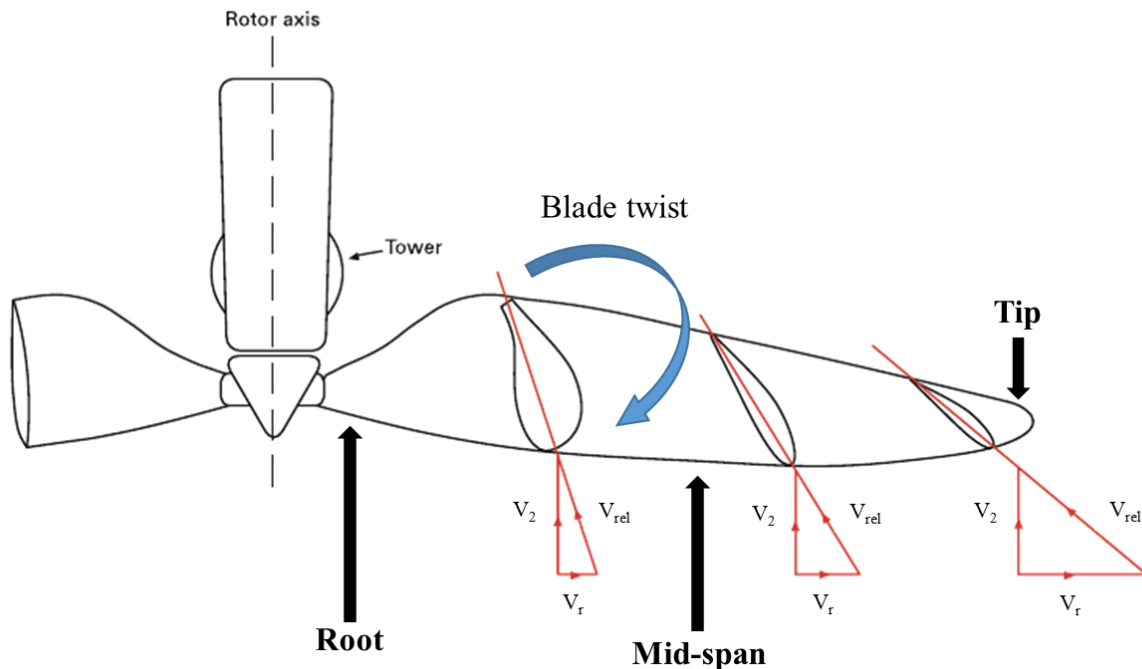


Figure 2.16 Definition of blade (Physics Stack Exchange, with modification, 2015).

The ratio between rotational speed of the blade tip, V_{tip} and V_2 called as tip speed ratio (TSR) is one important parameter determining the power output from a wind turbine, mathematically defined as:

$$TSR = \frac{V_{tip}}{V_2} = \frac{V_r}{V_1(1-a)} \tag{2.37}$$

Apart from angle of attack α , blade rotational speed V_r needs to be preserved at an optimum value in order to optimise the power generation, which can be done through maintaining the TSR. An optimum TSR value for 3-bladed wind turbine for maximum power extraction is around 6 to 8 (Wilson & Lissaman, 1974).

2.5.3. Wind Turbine Power Curve

The wind turbine power-curve is split into four operating regions, where each region applies different approach of the control system and strategy. The division is based on the incoming wind speed: cut-in wind speed, rated wind speed, and cut-out wind speed. Cut-in wind speed is the minimum wind-speed at which the turbine starts to produce power where rated wind speed is the wind speed at which turbine power rating is determined. Cut-out wind speed refers to wind speed if exceeded will lead to shut-down of wind turbine since the high wind speed might cause damage to the turbine.

Region 1 is defined as the area below the cut-in wind speed while Region 2 is the area between cut-in and rated wind speed. Region 3 refers to the area between rated and cut-out wind speed while Region 4 is when the wind speed exceeds cut-out wind speed as shown in **Figure 2.17**. The description for each region is presented in **Table 2.21**. Other wind turbine power-curve definition is according to (DTU, accessed 2016), splitting the power generation curve into four main regions: A, B, C and D which details are summarised in **Table 2.21**.

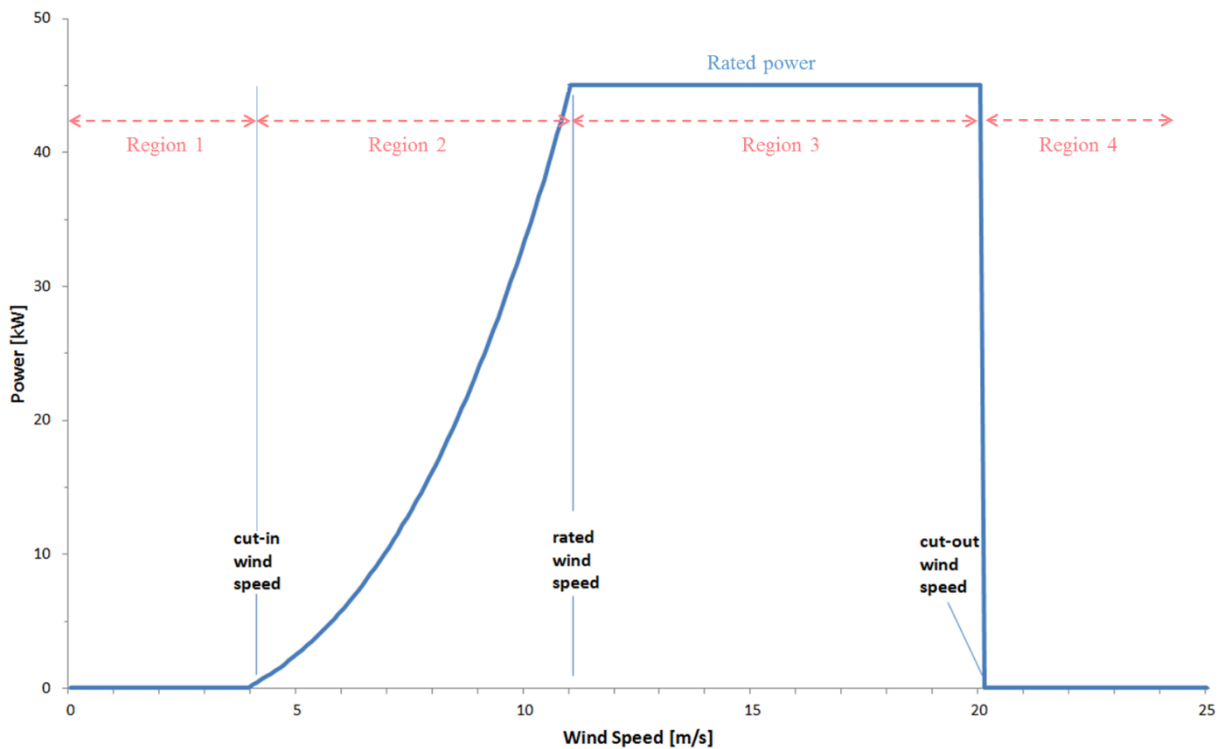


Figure 2.17 Typical wind turbine power-generation curve (STFC, with modification, accessed 2016).

Table 2.21 Power Curve Region Definition

Region	Description and Control Strategy
Region 1	No power production, not enough wind speed to generate power
Region 2	The wind speed is below rated; generator torque is adjusted to optimise power generation. The pitch angle is fixed at constant value capturing maximum lift
Region A	<ul style="list-style-type: none"> • Constant rotor speed at minimum value • Adjusting generator torque to maintain optimum TSR • Constant pitch angle
Region B	<ul style="list-style-type: none"> • Increasing rotational speed to maximise power capture • Adjusting generator torque to maintain optimum TSR • Constant pitch angle
Region C	<ul style="list-style-type: none"> • Constant rotor speed as wind speed approached rated wind speed • Adjusting generator torque as wind speed increases until power production reaches rated power • Constant pitch angle
Region 3 (D)	The wind speed is above rated, thus generator torque is constant to maintain constant production. Pitch angle is adjusted to minimise load on rotor
Region 4	No power production, the wind speed is too high. Wind turbine is exposed to high load and is set to parked/feathered condition to avoid damage (minimise load on rotor)

2.6 Structural Responses of Floating Offshore Wind Turbines

Floating offshore wind turbines (FOWT) are more susceptible to dynamics (motions) than the offshore fixed-substructure wind turbine so that the utilisation of mooring lines is necessary to minimise dynamic motions of the platform. Mainly, the dynamics is caused by wind and waves which in combination influence the loads, motions, and power production of a wind turbine (Jonkman & Buhl Jr, 2007). So far, there has been no specific study concerning the influence of turbulent wind under different atmospheric stability conditions towards FOWT loadings and motion response, yet the effect of wind coherence under neutral conditions on a FOWT was studied by Godvik (2016). The study was done by comparing the effects of the two turbulent wind field models recommended in the IEC standard: the IEC Kaimal Spectra & Coherence Model and Mann Spectral Tensor Model on the 6MW Hywind Scotland spar-buoy wind turbine through SIMA software simulations. It was observed that the coherences from the two models resulted in different estimate of the platform yaw response and mooring line fatigue. The yaw responses for the 6MW Hywind Scotland (70m to 85m draft and 154m rotor diameter) were noticed to be significant where the Mann Turbulence model induced higher maximum yaw than the IEC Kaimal Spectra & Coherence Model (Godvik, 2016), whereas for the mooring line fatigue prediction, the Mann Model was found to be more conservative than the IEC Kaimal Spectra & Coherence Model (Godvik, 2016).

This thesis will mainly focus on the OC3-Hywind spar-buoy floating wind turbine, however responses of three types of floaters are compared in this section as a reference study: barge, tensioned-leg platform (TLP), as well as spar-buoy. Each of these floaters as illustrated in *Figure 2.18* can be distinguished based on its ability to obtain static stability.

The barge type achieves stability by relying on its large water-plane area supported by catenary mooring lines whereas TLP type has tensioned-tendons as its mooring line to stabilise itself. The spar-buoy type or also known as deep-draft floater relies on its concentrated mass (centre of gravity) far below its centre of buoyancy along with catenary mooring lines to gain static stability. To compare these floater concepts

fairly, previous studies performed adopt the 5MW National Renewable Energy Laboratory (NREL) offshore wind turbine specification for rotor nacelle assembly (RNA) and aerodynamics properties as given in the reference (Jonkman et al., 2009). The general qualitative comparison of the three concepts is summarised in *Table 2.22*.

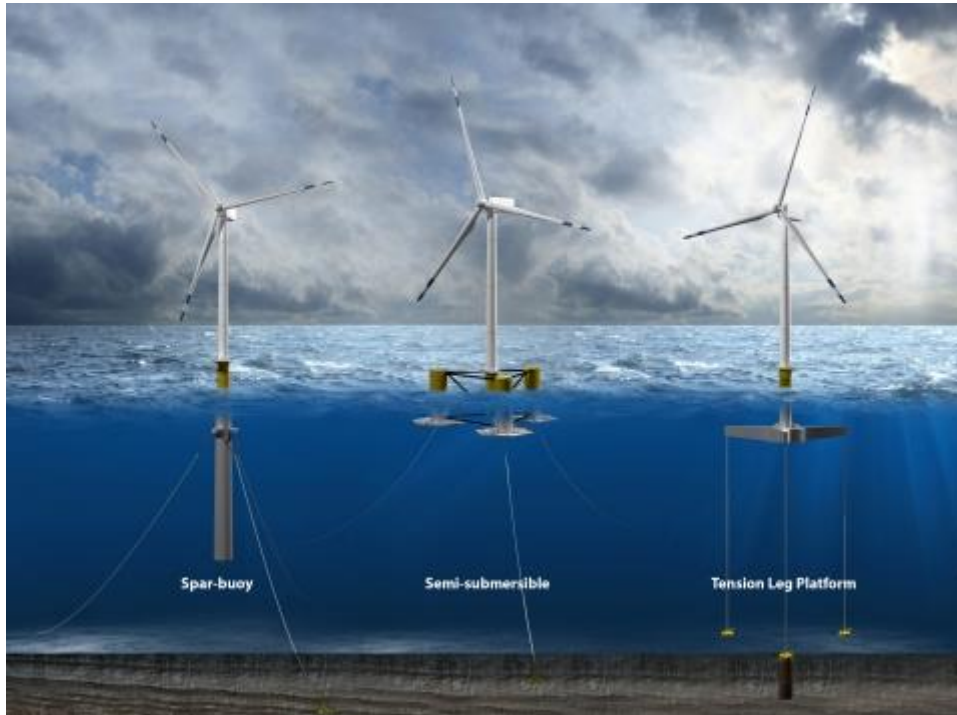


Figure 2.18 Offshore wind turbine floater types (U.S. Department of Energy, 2014).

Table 2.22 General Comparison of the Three Type Offshore Wind Turbine Floater (Jonkman & Matha, 2011)

Parameter	Barge	TLP	Spar-buoy
Stability	Buoyancy	Mooring (tensioned-tendons)	Ballast
Natural periods	-	+	0
Coupled motions	-	+	0
Wave sensitivity	-	0	+
Turbine weight	+	0	-
Moorings	-	+	-
Anchors	+	-	+
Turbine (RNA+tower) weight	+	-	-
Tower-top motion	-	+	-
Controls complexity	-	+	-
Maximum heeling angle	-	+	-

'0' for neutral, '+' for advantages, '-' for disadvantages

Karimirad & Moan (2012) studied the effect of turbulence on a catenary-moored spar (CMS) model through software simulation using coupled HAWC2 – SIMO/RIFLEX. This CMS has the same properties with the OC3-Hywind but with delta connection which was eliminated in the OC3-Hywind. Mann Turbulence Model was used to generate the turbulent wind with 1-hour simulations that were split into 15mins simulations to avoid the repetition of turbulence. The study concluded that motions and responses of CMS (pitch and surge) due to turbulence is not significant, yet a more pronounced effect was observed in the power generation. Furthermore, they found that turbulent wind excited the rigid body pitch and surge natural frequencies but only slightly affect the structural response of CMS (nacelle surge and tower base fore-aft bending) compared to wave-induced effect.

A study conducted by Ma et al. (2015) using FAST code simulation tool where the OC3-Hywind spar-buoy was selected results in a similar conclusion with Karimirad & Moan (2012) that wind-induced loading is in resonance with pitch and surge natural frequencies of OC3-Hywind in the low frequency range. Moreover, wind influence is the most prominent for surge motion (Ma et al., 2015).

Hydro Oil & Energy's Hywind Spar-Buoy remodelling (experiment) and software simulation using coupled HAWC2 – SIMO/RIFLEX was conducted by Nielsen et al. (2006). This study concluded that the deployment of the conventional blade control system on spar-buoy floating wind turbine causes unstable dynamic response, either amplifies or damps wind turbine motions. When the blade is pitched as the wind speed enters above rated, excessive pitching motion of the wind turbine—known as negative damping—occurs (Nielsen et al., 2006). Therefore, a modified control system for wind speed above rated is necessary for spar-buoy floating wind turbines. The proposed control system to reduce negative damping is by adding an active damping to the conventional blade pitch controller where the active damping takes account tower motion during blade pitching (Nielsen et al., 2006). However, more detail with regard to this active damping was not made available for public. In the absence of this active damping system at wind speed above rated, tower pitching angle tends to decay yet remains pitching with notable amplitude afterward.

Wayman et al. (2006) studied both static and dynamic behaviour of MIT/NREL barge-floater adopting the NREL 5MW offshore wind turbine with respect to wind and wave loading. The barge is station-kept with catenary mooring lines. The coupling between Fatigue, Aerodynamics, Structures, and Turbulence (FAST) aerodynamic code and Wave Analysis at MIT (WAMIT) wave simulation code was used for the analysis. The study by Wayman et al. (2006) concluded that roll, pitch, and yaw rotational response as well as sway translation of barge-floater are the highest as the wind enters Region 3 of the power-curve. The reason behind this was in Region 3, when the blades are starting to feather, thus the damping is reduced (Wayman et al., 2006).

Another study using a barge-floater wind turbine was conducted by Jonkman & Buhl Jr (2007) by analysing the ITI Energy Barge with NREL 5MW offshore wind turbine. The barge has eight catenary mooring lines with two lines at each corner of the barge 45° apart from each other. The study utilised coupled FAST with AeroDyn and MSC.ADAMS with A2AD interfaced with WAMIT and TurbSim for turbulent wind simulation. The study showed that with the increasing incoming wind speed, the floater pitch rotation and tower top fore-aft movements are also increasing, where the same manner were observed with the increasing turbulence intensity. Another conclusion was that the mean value of both floater pitch rotation and tower top fore-aft movement was largest at the rated wind speed due to the transition from Region 2 to Region 3 where different control strategy was applied. This conclusion is in contrary to the study from Wayman et al. (2006) who found that the motion response was highest when the turbine was exposed to wind speeds above rated.

Previous studies by Wayman et al. (2006) and Matha (2009) considered the MIT/NREL TLP-type floating wind turbine for analysis. The coupling between FAST code and WAMIT code was utilised by Wayman et al. (2006) who found that at wind speeds near rated, the turbine system was exposed to the maximum surge, sway and yaw motions. The study of Matha (2009) showed that a TLP wind turbine experienced significant aerodynamic instability in platform pitch and roll due to pitching of the blade at wind speeds above rated. Yet, since TLP is stiff in pitch, a more prominent platform surge oscillation was observed instead of pitch oscillations. Furthermore, yaw instabilities were observed in the case where wind turbine is parked (high wind speed) with one blade at 0° pitch and the other two at 90°.

A study by Jonkman & Matha (2011) showed that in general FOWTs are exposed to higher loads than those on land. Barge type floaters were more unstable as the wind increases and towards the rated wind

speed leading to higher rotational motions as well as tower top fore-aft and sway translations. Barge-floaters had the highest loads and responses induced by waves than TLP and spar-buoy (Jonkman & Matha, 2011). A TLP-floater wind turbine starts to experience aerodynamic instability in pitch and roll as the blade pitching at the rated wind speed, however this instability is still less compared to the barge and spar-buoy responses. The TLP stiffness towards pitch rotation results in dominant surge motions which results in enhanced instability. Spar-buoy floater responses were observed when the pitch and surge natural frequencies are excited in low frequencies. Additional active damping on blade controller was required to reduce excessive pitching on spar-buoy, which also reduced the overall loads on the structures as the wind speed increases above the rated wind speed.

3. Modelling of a Spar-Buoy Wind Turbine Using HAWC2 Code

3.1 HAWC2 Software

HAWC2, the abbreviation of Horizontal Axis Wind turbine simulation Code 2nd generation, is an aero-hydro-servo-elastic software to perform wind turbine simulations through modelling. The term ‘aeroelastic’ means to describe elastic or flexible structures—e.g. wind turbine—responses when subjected to aerodynamic forces. HAWC2 is capable of simulating coupled circumstances between wind turbine deformations and aerodynamic forces since the two terms are correspond to each other (DTU, accessed 2016). HAWC2 implements flexible multibody framework structural model where each body is constrained to each other with different type of ‘connection’ as illustrated in **Figure 3.1**.

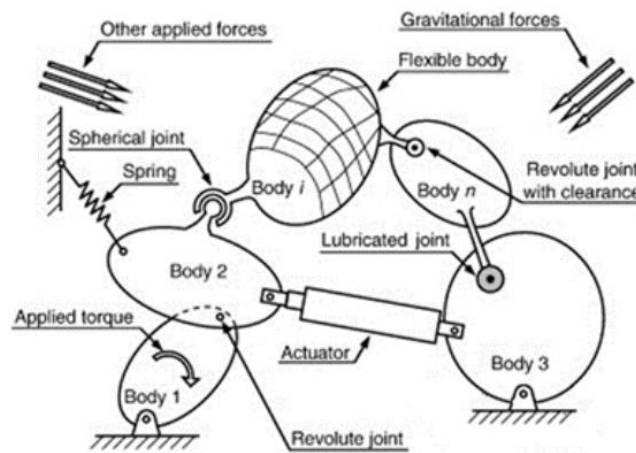


Figure 3.1 Multibody system (DTU, accessed 2016).

3.1.1 Defining the Structure and Coordinate Systems in HAWC2

In HAWC2, a wind turbine structural definition is divided into components (main bodies), bodies (or sub-bodies) and beam elements (DTU, accessed 2016). Blade, hub, generator shaft, nacelle, tower, and substructure are included on the components level referred as the main bodies (DTU, accessed 2016). Depending on the main bodies’ dimensional complexity, it can be broken down into several sub-bodies to account a more accurate displacement and forces, e.g. a blade main body can be divided into several blade sub-bodies (DTU, accessed 2016). Each sub-body having its own reference system, is composed by nodes which can be either evenly distributed or unevenly distributed along the main body (DTU, accessed 2016). The definition of main body and sub-bodies is illustrated in **Figure 3.2** with the upper and lower figures showing the unevenly distributed and evenly distributed nodes respectively. It is important to distinguish the terms ‘main body’ and ‘sub-body’ or simplified as ‘body’ in the modelling, as the two definitions have different physical meanings.

Each two-node structure is referred to a beam element (**Figure 3.2**), where each element is considered as flexible; yet the stiffness, inertia, and mass properties for each beam element can be defined along the element (DTU, accessed 2016). The beam element in HAWC2 adopts the 6 degree-of-freedom Timoshenko Beam structural elements theory (DTU, accessed 2016).

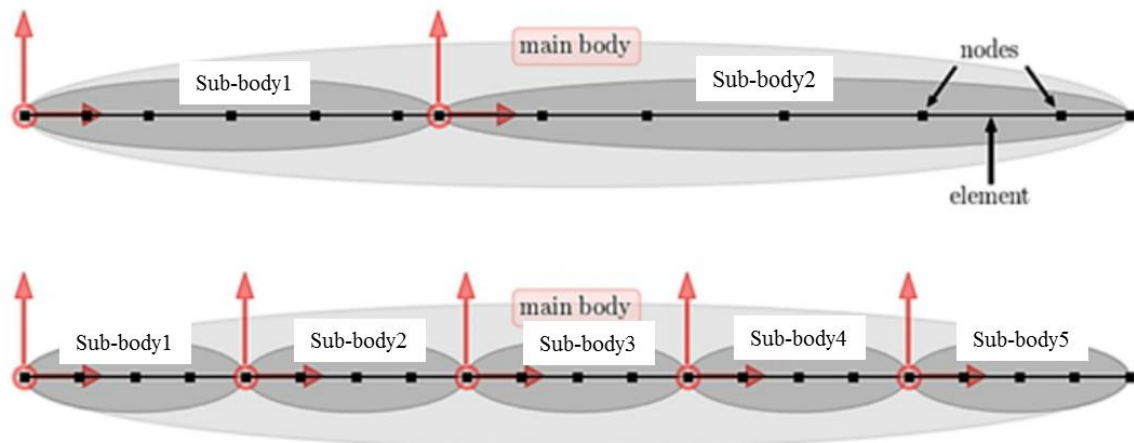


Figure 3.2 Structural definition in HAWC2 (DTU, accessed 2016).

Main bodies must be connected to one another in order to construct the whole wind turbine structure using ‘connectors’ called as constraints. Several constraint types are available in HAWC2 such as fixed to ground, fixed connection, fixed to ground allowing translation, fixed to ground allowing translation, and rotation free (DTU, accessed 2016). Special constraints (bearings) are available for the RNA, allowing—for instance—frictionless yaw rotation of the nacelle to adjust with the incoming wind speed direction. Other example of bearing constraint is allowing blade pitching with respect to the hub.

Coordinate systems used in HAWC2 include the global coordinates, meteorological (wind) coordinates, and main body (local) coordinates as illustrated in *Figure 3.3*, where each of the coordinate system follows the right-hand-rule (DTU, accessed 2016). In *Figure 3.3*, the global coordinate system corresponds to $(x=0, y=0, z=0)$ where the gravity forces work in the positive global Z-axis (Z_G) direction (DTU, accessed 2016). Main bodies have their own coordinate systems (referred as local coordinate system) and orientations as seen in *Figure 3.3* for the tower, tower top, shaft, hub, and blade. Moreover, user should notice since HAWC2 defines different coordinate system for meteorological (wind).

For an onshore wind turbine, the global coordinate system starting point usually coincides with the tower base. For a fixed-substructure offshore wind turbine, the global coordinate system ($x=0, y=0$) could be set to coincide with the lowest part of the pile substructure or the floater in the case of FOWT; while $z=0$ represent the sea surface water level. Any main body coincides with the global coordinate is called the base, while other main bodies’ local coordinate systems are defined as ‘relative’ to the base body coordinate by adding a relative distance or rotation angle (DTU, accessed 2016).

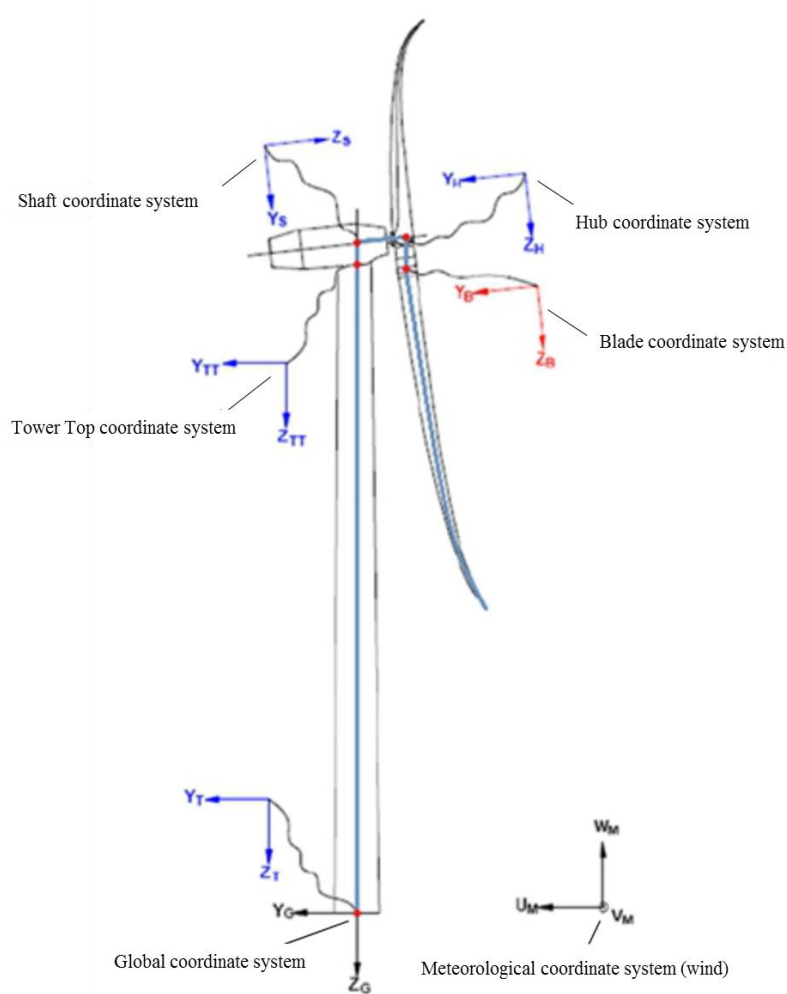


Figure 3.3 Coordinate system in HAWC2 (DTU, accessed 2016).

3.1.2 Rayleigh Damping

In all structural designs, damping is one important parameter affecting the responses of a structure, in a way that the structure's motion is reduced or 'damped' with time. The determination of a structure's natural frequency depends on damping value inputted in the model. Structural damping in HAWC2 implements the Rayleigh damping, which is proportional to combination of mass and stiffness (DTU, accessed 2016). In mathematical form, the Rayleigh damping is written as (Orcina, accessed April 2016):

$$C = \mu M + \lambda K \tag{3.1}$$

with

C : damping matrix

M : mass matrix

K : stiffness matrix

μ : constant

λ : constant

Despite it is used widely for structural numerical modelling, Rayleigh damping has one disadvantage, that is the dependency towards response frequency resulting in variable/inconstant damping ratio

(Orcina, accessed April 2016). The input of Rayleigh damping in HAWC2 comprises of six parameters, three of which are the mass-proportional damping (M_x, M_y, M_z) and the other three are the stiffness-proportional damping, namely K_x, K_y, K_z (DTU, accessed 2016). These damping parameters can be set differently for each main body, so subscript $x, y,$ and $z,$ is referred to each direction relative to the local main body coordinate (DTU, accessed 2016).

3.1.3 Aerodynamic Modelling in HAWC2

Aerodynamic simulations to solve the forces acting on wind turbine rotors in HAWC2 comprises of two levels, the rotor as a-whole (the rotor aerodynamics) and the blade segments (2D aerofoil section aerodynamics). Rotor aerodynamics is related to the power generation of wind turbines, while the 2D aerofoil aerodynamics describes how the blades produce aerodynamic forces to revolve the rotor. HAWC2 implements the Blade Element Momentum (BEM) theory to assess the rotor aerodynamic model where the 2D aerofoil theory is deployed to assess blade segments aerodynamics (DTU, accessed 2016).

3.1.3.1. Rotor Aerodynamics

The BEM theory assumes an ideal rotor with infinite number of blades, constantly loaded and frictionless (DTU, accessed 2016). As illustrated in **Figure 3.4**, BEM theory allows partition of the whole rotor area into several annular uniformly loaded cross sections in the along-wind direction where each annular cross-section is assumed independent to each other.

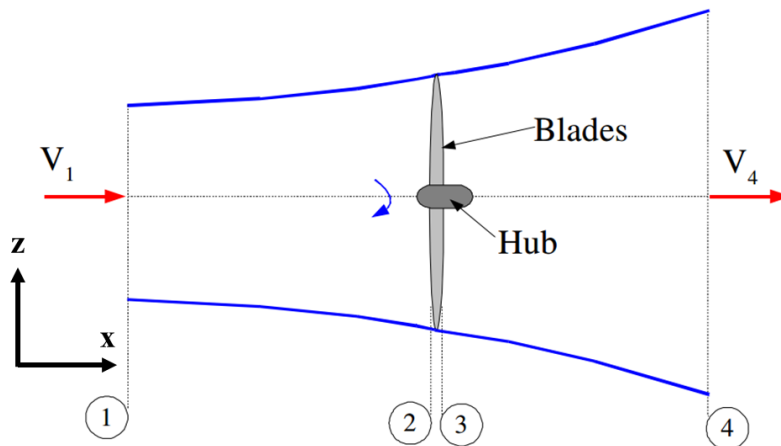


Figure 3.4 Blade Element Momentum theory (Ingram, 2011).

The discretization is done relative to the rotor position, namely area 1, 2, 3, and 4 which are exposed to different wind speed due to the presence of the rotor itself. Area 1 represents the undisturbed incoming wind velocity, the upstream region; while area 2 describes the region when the wind is right about to ‘hit’ the rotor and the wind is slightly perturbed. Area 3 is the region right after the wind hit the rotor causing disruption of wind flow, whereas area 4 is far away downstream where the wind condition is starting to recover after ‘hitting’ the rotor.

The power generated from the incoming wind speed V_1 is computed as:

$$P = \rho_{air} A_{rotor} V_1^3 \quad (3.2)$$

with

ρ_{air} : density of air, normally 1.225kg/m^3

A_{rotor} : blade/rotor swept area = $0.25\pi D^2$ and D is the rotor diameter.

The increment in the wind speed leads to greater power extraction, which also implies the increase of the thrust force F_T (**Figure 2.15**), causing a decrement in the power production after reaching a certain maximum point even though the incoming wind speed is increasing. Theoretically, the maximum power that can be generated corresponds to $(16/27)P$ where P is the generated power as indicated in (3.2). The theoretical value $16/27$ is known as Betz limit (Burton et al., 2001), symbolised by C_P so that (3.2) is corrected to:

$$P_{max} = C_P \rho_{air} A_{rotor} V_1^3 = \frac{16}{27} \rho_{air} A_{rotor} V_1^3 \quad (3.3)$$

The above equation (3.3) is valid within the assumption of constant induction a and thrust coefficient C_T along the blade length. In HAWC2, a and C_T are computed as variable at each radial and azimuthal position of the blade element to obtain a more accurate calculation in the case of non-uniform wind flow caused by either wind shear or turbulence (DTU, accessed 2016). The induction factor a is a function of C_T polynomial third order, expressed as (DTU, accessed 2016):

$$a = k_0 + k_1 C_T + k_2 C_T^2 + k_3 C_T^3 \quad (3.4)$$

with k_i is the polynomial coefficients as function of radial position.

Nevertheless, the deployment of BEM method in HAWC2 has several limitations, yet can be overcome with the use of the tip-loss correction, the skewed inflow model, and the rotor wake transient dynamic (DTU, accessed 2016).

A tip loss correction is implemented to correct the infinite number of blades becomes finite. Prandtl tip loss correction is used in HAWC2 by introducing a correction factor F by Wilson and Lissaman (DTU, accessed 2016):

$$F = \frac{2}{\pi} \cos^{-1} \left\{ \exp \left[-\frac{N_b}{2} \frac{\left(1 - \frac{r}{R}\right)}{\left(\frac{r}{R}\right) \sin \phi} \right] \right\} \quad (3.5)$$

where

$0 \leq F \leq 1$: correction factor, 0 at blade tip and 1 at blade root

N_b : number of blades

r : radial position of rotor

R : radius of rotor

ϕ : local flow angle

This correction factor is applied to the thrust coefficient C_T in (3.4) so that the corrected induction factor $a_{tip-loss}$ can be calculated using:

$$a_{tip-loss} = k_0 + k_1 C_T^* + k_2 C_T^{*2} + k_3 C_T^{*3} \quad (3.6)$$

where C_T^* is the corrected thrust coefficient.

The utilisation of the skewed inflow model takes into account variation of the induction factor $a_{tip-loss}$ due to non-uniform flow. As the rotor is yawed or tilted, the skewed wind flow influences induction factor $a_{tip-loss}$ in two manners: (i) variation within azimuthal position and (ii) decrement in the mean value. (DTU, accessed 2016). Reduction in the mean value of $a_{tip-loss}$ is accounted by reduction factor K_a in accordance with Glauerts's model. Therefore, we get the following definition to compute the induction factor (DTU, accessed 2016):

$$a_{corrected} = a_{tip-loss} K_a \quad (3.7)$$

with:

$$K_a = k_1 C_t + k_2 C_t^2 + k_3 C_t^3 \quad (3.8)$$

where coefficients k is a function of the rotor skew angle (Φ_y): $k_i = f(\Phi_y)$ and C_t is the thrust coefficient. Variation of the induction factor within azimuthal position is corrected by applying Coleman correction factor (DTU, accessed 2016):

$$k_{col} = \tan(0.4\chi) \quad (3.9)$$

where χ is the wake skew angle. The final form to compute the induction factor as a function of azimuthal position is (DTU, accessed 2016):

$$a^* = a_{tip-loss} \left(1 + k_{col} \frac{r}{R} \cos \Omega \right) \quad (3.10)$$

where

a^* : corrected induction factor

$a_{tip-loss}$: induction factor taking into account tip-loss correction (3.7)

k_{col} : Coleman correction factor (3.9)

r : radial position of rotor

R : radius of rotor

Ω : azimuth angle

A correction is also made for the rotor wake transient dynamics, which is done by introducing an additional dynamic inflow model (DTU, accessed 2016). This model allows the correction on the transient period (**Figure 3.5**) which is important for large rotor wind turbine, since lower wind speed implies longer transient period due to slower development of the transient state.

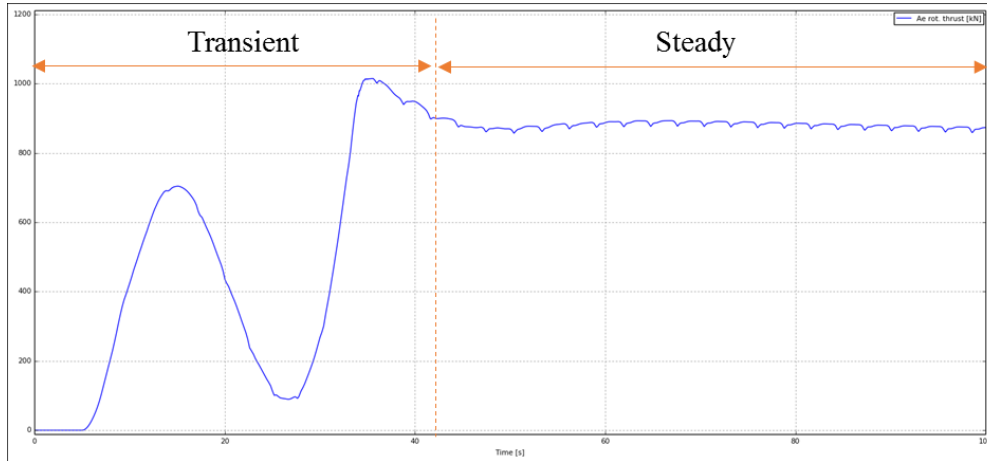


Figure 3.5 Transient in thrust force with constant wind.

3.1.3.2. 2D Aerofoil Cross Section Aerodynamics

The aerofoil aerodynamics is represented by drag and lift forces of the blades. The blade aerodynamic behaviour is important when performing load calculations and analyses on the whole turbine structure since the loads experienced by the blades will affect the tower response, and thus the floater/platform response.

As mentioned in Subchapter 2.5.2, if a blade is discretised into sections, one will observe variation of cross sectional size and rotational velocity V_{rel} , causing variable drag force F_D and lift force F_L along the blade. The drag force experienced by the blades is defined as:

$$F_D = \frac{1}{2} \rho_{air} C_D A_{ref} V_2^2 \quad (3.11)$$

where

ρ_{air} : air density

C_D : drag coefficient

A_{ref} : projection area which is ‘hit’ by the wind flow

V_2 : $V_1(1 - a)$; a is the induction factor

While the lift force acting on the blades is:

$$F_L = \frac{1}{2} \rho_{air} C_L A_{ref} V_2^2 \quad (3.12)$$

with C_L : lift coefficient.

Since (3.11) and (3.12) are identical, except for C_D in (3.11) and C_L in (3.12), the terms ‘drag capacity’ and ‘lift capacity’ on an aerofoil are usually represented by the magnitude of C_D and C_L successively. In principal, the drag force F_D induces load on the rotor, while the lift force F_L causes the rotor to revolve, therefore in the aerodynamics design, an aerofoil is desired to have less drag but more lift, so the desired ratio C_L/C_D is high. Consider an aerofoil section as described in **Figure 3.6**, F_D acts in parallel with V_{rel} whereas F_L acts perpendicular towards V_{rel} .

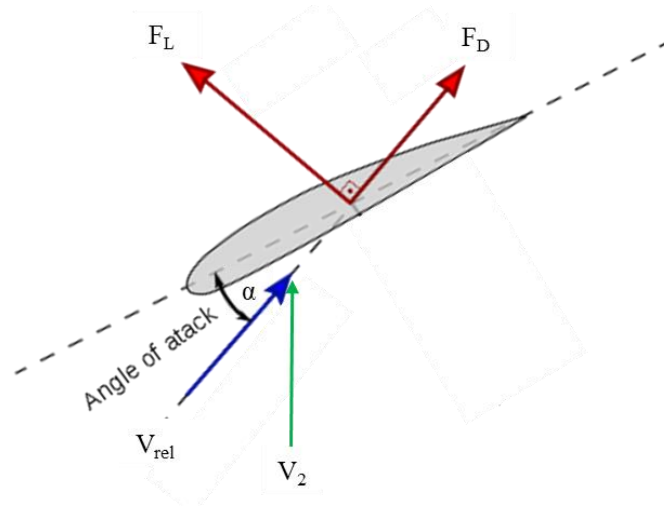


Figure 3.6 Drag and lift force on an aerofoil/blade cross section (wikiversity.org, with modification, accessed April 2016).

For an ideal flat plate, F_L is increasing with the increment of the angle of attack α , however for an aerofoil, F_L is increasing until at a certain value of angle of attack α_{stall} , the lift force is then decreases while the drag force is increasing significantly. This α_{stall} value differs for one aerofoil type to another depending on the aerofoil's aerodynamic characteristics. In the design of wind turbines, the optimum angle of attack $\alpha_{optimum}$ is determined so that it has slight less, almost equal value to α_{stall} resulting in maximum C_L/C_D .

HAWC2 considers three different aerodynamic effects: dynamics in the attached flow region, stalled flow region, as well as the added mass effect due to the motion of aerofoil (DTU, accessed 2016). In the region of the attached flow, the aerodynamics is computed by superposing indicial step responses on which the transient effect is accounted (DTU, accessed 2016). For stalled region, HAWC2 implements Beddoes-Leishmann dynamic stall model, which sums the two lift components, during the fully attached and fully separated conditions, that are weighted differently (DTU, accessed 2016). In the transition of stalled to attached flow, it takes some time for the flow to re-attached (transient period), that is also considered in the HAWC2 (DTU, accessed 2016).

3.1.4 Hydrodynamic Modelling in HAWC2

To model the hydrodynamics in HAWC2, the water kinematics are computed through the utilisation of an external dll called wkin.dll (DTU, accessed 2016). The water kinematics are related to wave's characteristics, including the seawater surface elevation, the dynamic pressure, as well as the wave-induced particle velocity and acceleration. The wkin.dll is able to generate 2D wave field for different wave model such as regular airy waves, irregular airy waves, stream function waves, and deterministic waves—or user defined (DTU, accessed 2016). The 2D wave field is represented as a time series of either wave surface elevation, wave-induced particle velocity or acceleration. A 3D wave field is generated by using a Fourier summation when considering wave spreading, which can be applied *only* if irregular waves are chosen. Moreover, wheeler stretching, wave directional spreading, and current can also be added into the hydrodynamic model (DTU, accessed 2016).

Hydrodynamic forces in HAWC2 are computed using the Morison equation, valid for slender structures, that is the diameter-to-wave length ratio less than 0.2: ($D/\lambda < 0.2$). In case of a spar-buoy structure, this assumption is valid, and the Morison force acting on the spar-buoy floater is consisted of three terms: Froude-Krylov force, inertia/mass force, and drag force (DTU, accessed 2016). Froude-Krylov force

accounts for unsteady pressure due to the undisturbed waves and disregards the wave diffraction. The inertia term considers mass force due to the displaced water's movement, while drag force describes the force due to fluid flow passing the structure's peripheral. The Morison force acting on a flexible slender structure per unit length is computed using (DTU, accessed 2016):

$$f = \rho_{sw} A \ddot{u} + \rho_{sw} C_a A_r \dot{u}_{rel} + \frac{1}{2} \rho_{sw} C_d D u_{rel} |u_{rel}| \quad (3.13)$$

where

ρ_{sw} : seawater density

A : structure's submerged peripheral area

\dot{u} : water particle acceleration

C_a : added mass coefficient

A_r : structure's peripheral area exposed to displaced water movement

\dot{u}_{rel} : relative water particle acceleration towards moving structure

C_d : drag coefficient (not to confused with drag coefficient in (3.11))

u_{rel} : relative water particle velocity towards moving structure

D : structure's diameter

Within the assumption of *stiff* slender structures, then both Froude-Krylov and inertia terms in (3.13) are combined so (3.13) is rearranged into (DTU, accessed 2016):

$$f = \rho_{seawater} C_m \frac{\pi D^2}{4} \dot{u}_{rel} + \frac{1}{2} \rho_{seawater} C_d D u_{rel} |u_{rel}| \quad (3.14)$$

where

C_m : mass coefficient = $1 + C_a$

3.2 Turbulent Wind Field Input for HAWC2

The generated synthetic turbulent wind field represents the 'real condition' of wind field in the HAWC2 simulations and needs to be generated prior to running the simulation. This pre-generated input can be generated either inside or outside HAWC2 by the use of external program to reduce computational time as well as due to the limited capacity of HAWC2. The synthetic wind field is represented as a 3D box of vector field consisting of grid points. Each grid point represents a spatial location on the box and provides information regarding the local wind speed for u , v and w components as well as its direction. **Figure 3.7** illustrates the 3D vector field box (or referred as turbulence box) system implemented in HAWC2. The turbulence box covers only the rotor swept area so that the rest part of the wind turbine—e.g. tower—is not accounted for the turbulence wind exposure. This is a reasonable assumption since the rotor swept area is the largest part of the wind turbine that is exposed to turbulent wind field relative to the tower. During the simulation, the 3D box vector field will approach the wind turbine's rotor with the same speed as mean wind speed defined at the wind turbine's hub (DTU, accessed 2016). A good representation of the turbulent wind field requires an adequate number of grid and grid-spacing.

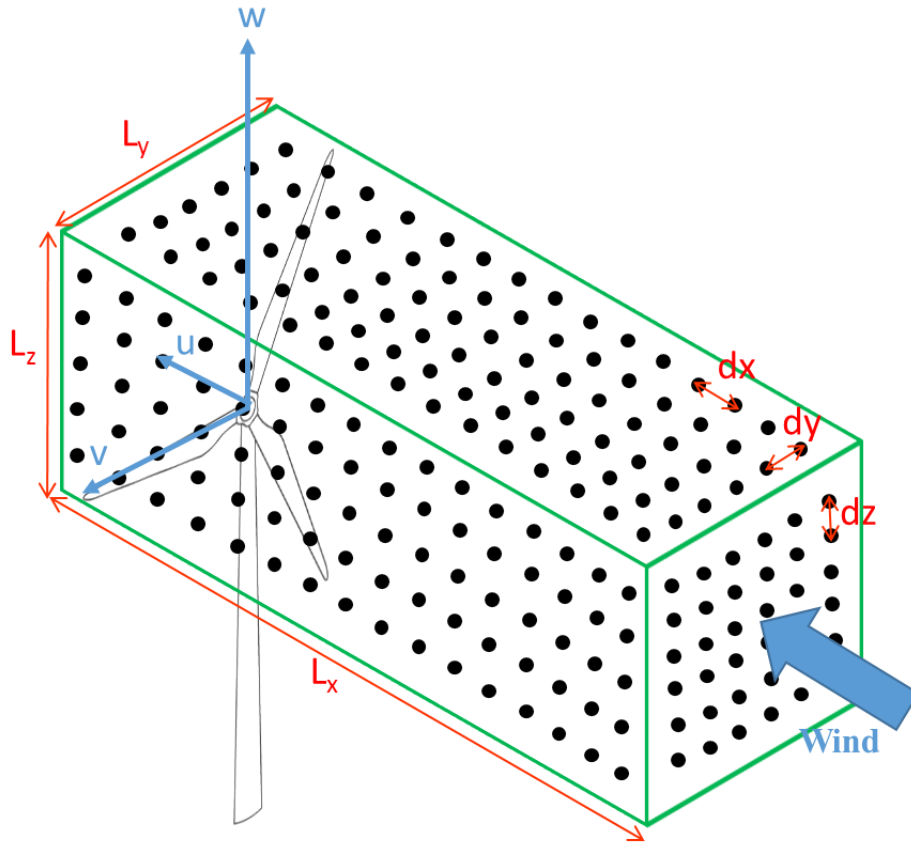


Figure 3.7 3D turbulence box implemented in HAWC2.

To set up a 3D turbulence box in HAWC2, the required parameters are:

- Number of grid points in the along wind direction (N_x)
- Number of grid points in the cross wind direction (N_y)
- Number of grid points in the vertical wind direction (N_z)
- Grid spacing in the along wind direction (dx)
- Grid spacing in the cross wind direction (dy)
- Grid spacing in the vertical wind direction (dz)
- Length of turbulence box in the long wind direction ($L_x = N_x \times dx$)
- Length of turbulence box in the cross wind direction ($L_y = N_y \times dy$)
- Length of turbulence box in the vertical wind direction ($L_z = N_z \times dz$)

The number of grid points in the turbulence box must be $\sim 2^n$ (DTU, accessed 2016) so $N_x = 2^{n_x}$, $N_y = 2^{n_y}$, and $N_z = 2^{n_z}$ where n_x , n_y , and n_z are real, positive float numbers. The grid spacing dx is computed as a function of the occurring mean wind speed defined at hub height U_{hub} and simulation time length T , that is (DTU, accessed 2016):

$$dx = \frac{T U_{hub}}{N_x} \quad (3.15)$$

where

T : simulation time length

U_{hub} : mean wind speed at wind turbine's hub

N_x : number of grid points in the along wind direction

In HAWC2 two turbulence models can be utilised, the Veers Model, implementing the inverse Shinozuka model in polar grid; and the Mann Model, generating velocity vector field in Cartesian coordinate (HAWC2, accessed 2016). The IEC Kaimal Spectra & Coherence Model turbulence generation is based on the Veers Model utilising the TurbSim Program while the Mann Model turbulence is generated using a separate 64-bit Mann Turbulence Generator included in the HAWC2 package.

3.2.1. TurbSim – IEC Kaimal Spectra & Coherence Model Wind Field Simulator

TurbSim is a stochastic inflow turbulence simulator used to generate turbulent wind field or full-field flow developed by National Renewable Energy Laboratory (NREL). The deployment of the Veers Model allows velocity time series of the u , v and w wind components to be generated for different spatial points N in a fixed two-dimensional (2D) rectangular yz -plane implying Taylor's frozen hypothesis (Jonkman & Kilcher, 2012). This fixed plane represents the rotor swept area as sketched in *Figure 3.8*. The Veers Model calculates the IEC Kaimal wind spectra (on frequency domain) for the three wind components at a point in the rotor where later Fast Fourier Transform (FFT) is applied to the calculated spectrum to obtain the turbulence time series (Veers, 1988). Shinozuka Method handles the computation of the turbulence time series for the remaining grid points using the coherence function (Veers, 1988) assuming the three turbulence components are independent towards each other.

TurbSim input file has the extension of '.inp' and contains five sections, each describes different boundaries: Runtime Options, Turbine/Model Specifications, Meteorological Boundary Conditions, Non-IEC Meteorological Boundary Conditions, and Coherent Turbulence Scaling Parameters. An example of TurbSim input file is given in the Appendix B.

TurbSim is capable to generate different types of simulated wind field such as turbulent and uniform field that are stored in different output file extensions, namely '.sum'; '.bin'; '.dat'; '.hh'; '.bts'; '.wnd'; '.twr'; and '.cts' (Jonkman & Kilcher, 2012). Some of these files are human-readable as it can be read with ASCII-based programs, while others are machine-readable that needs a specific program such as Matlab to access. The '.sum' output file is a human-readable file that is always generated, containing summary information of the simulation and its result. Despite the various types of output files, only '.bts' file that is chosen to be generated as this file is the relevance of the turbulence input for the IEC Kaimal Spectra & Coherence Model in HAWC2.

User should notice that the turbulence box model definition in TurbSim is slightly different from the HAWC2 turbulence box. In TurbSim, the grid points are defined at the end point, so to acquire the same grids position as HAWC2 3D turbulence box (which grid points are defined in the middle), the length defined on 'GridHeight' L_z and 'GridWidth' L_y should be reduced by one spacing distance dz and dy respectively from the desired height and width of the HAWC2 3D turbulence box.

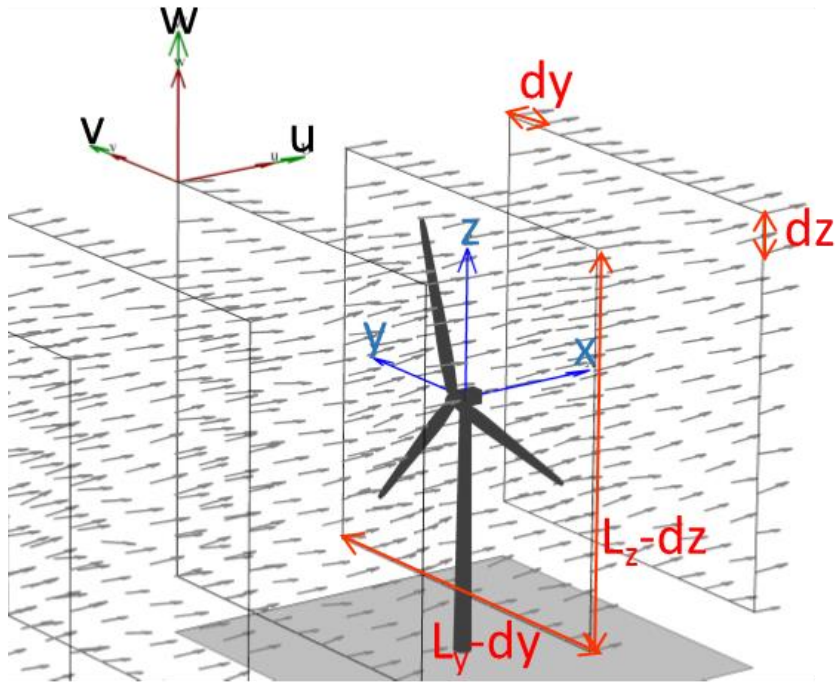


Figure 3.8 Grid system definition in TurbSim (Jonkman & Kilcher, with modification, 2012).

The total number of grids in the rotor plane N equals to $(N_y \times N_z)$, each with dy and dz spacing distance as indicated in **Figure 3.8**. Since TurbSim's 'turbulence box' is 2D, instead of having number of points in the longitudinal direction N_x , number of yz -planes N_{yz} approaching rotor area are considered, implying $N_{yz} = N_x$ in the HAWC2 3D turbulence box definition and must follow $N_{yz} \sim 2^{nx}$. The longitudinal spacing distance dx in the 3D turbulence box is interpreted as time step dt in TurbSim so when we consider a simulation length time T and N_{yz} number of yz -planes, the time step input will be:

$$dt = \frac{T}{N_{yz}} \quad (3.16)$$

Moreover, the useable time is computed as (Jonkman & Kilcher, 2012):

$$T_{use} = T - \frac{L_y'}{U_{hub}} \quad (3.17)$$

where

T : analysis time/simulation time length

$L_y' = (L_y - dy)$: length of the rectangular yz -plane in y -direction

U_{hub} : mean wind speed at the wind turbine's hub

3.2.2. HAWC2 Built-in Mann Model Wind Field Simulator

Generation of the Mann Turbulence input file in HAWC2 could be done in two ways, using the built-in 32bit generator as part of HAWC2 dll or utilising a separate program 64-bit Mann Turbulence

Generator. Both methods are based on the same exact principle, except for storage handling capacity as the dll is limited up to 32bit resulting in $nx + ny + nz < 32$, whereas the separate program 64-bit Mann Turbulence Generator allows $nx + ny + nz < 64$ (DTU, accessed 2016). For this thesis, the 64-bit Mann Turbulence Generator was used, with a sample input file is presented in the Appendix A.

Mann's turbulent wind field generated by the Mann turbulence generator is computed from the isotropic von Karman turbulence spectrum where wind shear effect is later added by introducing anisotropic parameter Γ as the eddies stretch with time. Aside from 3D turbulence box dimensional input as elaborated in Subchapter 3.2, other input parameters are required to model the Mann turbulent wind field in HAWC2 (DTU, accessed 2016):

- $\alpha\epsilon^{2/3}$
- Γ
- L_M
- High-frequency compensator, used to avoid u -component low pass filtering effect, can be set to either on or off (DTU, accessed 2016)
- Turbulence scaling factor: to manually adjust the generated turbulence level of the three components u , v , and w as required by user in the absence of parameter $\alpha\epsilon^{2/3}$ value (DTU, accessed 2016). For the implementation of simulations in this thesis, this function is set to off because the values of parameter $\alpha\epsilon^{2/3}$ are known (for the Mann Model). As a result, the generated turbulences (both from TurbSim and the 64-bit Mann Turbulence Generator) are used with no scaling adjustment in HAWC2 so the generated turbulence level ratio between u , v , and w wind components as the generated values from TurbSim and the 64-bit Mann Turbulence Generator.

Parameters $\alpha\epsilon^{2/3}$, Γ , and L_M are to be inputted accordingly to conform each atmospheric stability condition as explained in Subchapter 2.4.2.

3.3 OC3-Hywind Offshore Wind Turbine Specification

A spar-buoy FOWT was chosen as the substructure to study in this thesis as this type of FOWT has been found in previous studies to be sensitive to changes in coherence which is a key topic for this study. The model used for the analysis was based on the IEA Annex 23, the 5MW NREL fictive wind turbine; also known as the OC3 Project. The Offshore Code Comparison Collaboration (OC3) project serves as a standard to verify the validity of offshore wind turbine structure models by comparing several aero-hydro-servo-elastic codes (Jonkman & Musial, 2010), consisting of four phases. The four phases of OC3 project is divided according to the substructure's type, in which spar-buoy concept was defined during Phase IV.

The OC3 – Phase IV spar-buoy concept was developed based on Statoil's "Hywind" wind turbine substructure structural properties along with the 5MW NREL, yet with a slight different control system (Jonkman, 2010). The adopted structural properties of the 5MW NREL turbine includes the tower and the RNA (blades, hub, and nacelle). To distinguish between the real Hywind wind turbine and the fictive model, the term 'OC3-Hywind' will be used to refer OC3 – Phase IV concept model in this thesis. The general specification of the NREL 5MW offshore wind turbine is presented in *Table 3.1*, while other structural properties of the OC3-Hywind is given in Subchapter 3.3.1 to 3.3.3 and Appendix A. The OC3-Hywind structural model used in this study was based on the model provided by Risø DTU (HAWC2 developer).

Table 3.1 General Specification of NREL 5MW Offshore Wind Turbine RNA (Jonkman et al., 2009)

Parameter	Value
Power production rating	5 MW
Rotor orientation, Rotor configuration	Upwind, 3 blades
Control	Variable Speed and Collective Pitch
Drivetrain	High Speed and Multiple-Stage Gearbox
Rotor diameter, Hub diameter	126m, 3m
Hub height	90m
(Cut-in, Rated, Cut-out) wind speed	3m/s, 11.4m/s, 25m/s
Cut-in rotor speed, Rated rotor speed	6.9rpm, 12.1rpm
Rated tip speed	80m/s
Overhang, Shaft tilt, Precone	5m, 5°, 2.5°
Rotor mass	110,000kg
Nacelle mass	240,000kg
Tower mass	347,460kg
Rotor-nacelle-tower centre of gravity (x,y,z)*	(-0.2m, 0.0m, 64.0m)

3.3.1. Tower Structural Properties

OC3-Hywind’s tower structure has a bottom diameter of 6.5m and 27mm thickness, linearly decreased to 3.87m at the tower top with 19mm thickness (Jonkman, 2010). The tower height is 77.6m with tower base located at 10m above still water level (SWL) relative to the original or un-displaced position of the tower. The detailed distributed tower structural properties are given in *Table 3.2* while the general properties of the tower are given in *Table 3.3*.

Table 3.2 Distributed Tower Properties (Jonkman, 2010)

Elevation Above SWL (m)	Mass per length (kg/m)	Fore-Aft stiffness (GNm ²)	Side-Side stiffness (GNm ²)	Torsional stiffness (GNm ²)	Longitudinal stiffness (GN)	Fore-Aft inertia (kg m)	Side-Side inertia (kg m)
10.00	4667.00	603.903	603.903	464.718	115.302	24443.7	24443.7
17.76	4345.28	517.644	517.644	398.339	107.354	20952.2	20952.2
25.52	4034.76	440.925	440.925	339.303	99.682	17847.0	17847.0
33.28	3735.44	373.022	373.022	287.049	92.287	15098.5	15098.5
41.04	3447.32	313.236	313.236	241.043	85.169	12678.6	12678.6
48.80	3170.40	260.897	260.897	200.767	78.328	10560.1	10560.1
56.56	2904.69	215.365	215.365	165.729	71.763	8717.2	8717.2
64.32	2650.18	176.028	176.028	135.458	65.475	7124.9	7124.9
72.08	2406.88	142.301	142.301	109.504	59.464	5759.8	5759.8
79.84	2174.77	113.630	113.630	87.441	53.730	4599.3	4599.3
87.60	1953.87	89.488	89.488	68.863	48.272	3622.1	3622.1

Table 3.3 General Tower Properties (Jonkman, 2010)

Parameter	Value	Unit
Tower base elevation relative to SWL	+10	m
Tower base elevation relative to SWL	+87.6	m
Total tower mass	249,718	kg
Centre of mass location along centre line relative to SWL	+43.4	m
Tower steel density	7850	kg/m ³
Tower steel modulus of elasticity	210	GPa
Tower steel shear modulus	80.8	GPa

3.3.2. Floater Properties

OC3-Hywind floater is a spar-buoy, a ballasted cylindrical mono-hull substructure where the centre of gravity is much lower than its centre of buoyancy. The floater top is connected to the tower base at an elevation of 10m above SWL. The mono-hull substructure comprises of three parts: the upper part interfacing the tower base, the middle part connecting upper and lower part, as well as the lowest part where the mooring connection is attached.

The upper part is a cylinder with diameter of 6.5m, having the same diameter size with the tower base. The lowest part is a cylinder with diameter of 9.4m running from elevation 12m to 120m below SWL. The middle part is a linearly tapered cone (as it connects the upper and lowest part which size is different) located at 4m to 12m below SWL. The purpose of having a varying cylinder diameter is to reduce hydrodynamic loads acting in the splash zone, hence the smaller cylinder diameter is used in this zone (Jonkman, 2010). The OC3-Hywind’s floater is illustrated in *Figure 3.9* where the coordinates are relative to the original or un-displaced position of the floater.

The floater hydrodynamic parameters are presented in *Table 3.4* whereas its general properties are given in *Table 3.5*. Parameters that are not presented in *Table 3.4*—e.g. the hydrostatic restoring force of surge, sway, and yaw—are to be taken as zero (Jonkman, 2010).

Table 3.4 Floater Hydrodynamic Properties (Jonkman, 2010)

Parameter	Value	Unit
Sea water density ρ_{sw}	1,025	kg/m ³
Water depth	320	m
Draft	120	m
Buoyancy force relative to original position of floater ($\rho_{sw}gV_0$)	80,708,100	N
Hydrostatic restoring force (heave)	332,941	N/m
Hydrostatic restoring force (roll)	-4,999,180,000*	N/m
Hydrostatic restoring force (pitch)	-4,999,180,000*	N/m
Added mass coefficient C_a	0.969954	-
Drag coefficient C_D	0.6	-
Additional linear damping (surge)	100,000	Ns/m
Additional linear damping (sway)	100,000	Ns/m
Additional linear damping (heave)	130,000	Ns/m
Additional linear damping (yaw)	13,000,000	Nm/(rad s)

*negative value due to centre of buoyancy is located far below SWL

Table 3.5 General Floater Properties (Jonkman, 2010)

Parameter	Value	Unit
Total floater mass (including ballast)	7,466,330	kg
Centre of mass location along centre line relative to SWL	-89.9155	m
Roll inertia about centre of mass	4,229,230,000	kg m ²
Pitch inertia about centre of mass	4,229,230,000	kg m ²
Yaw inertia about centre of mass	164,230,000	kg m ²

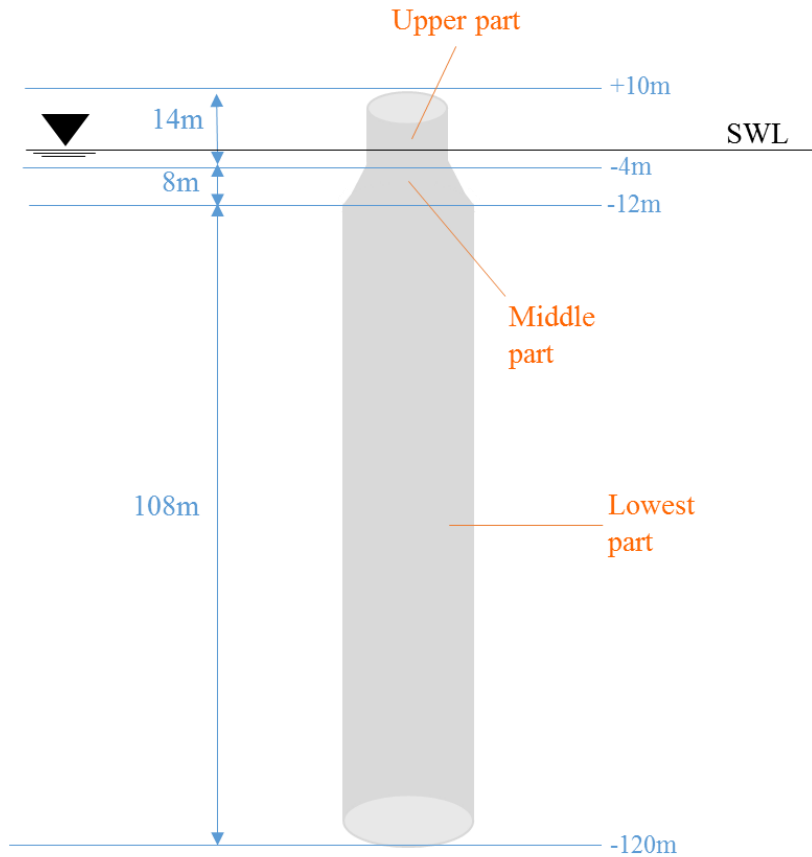


Figure 3.9 Floater of OC3-Hywind.

3.3.3. Mooring System Properties

OC3-Hywind deploys three catenary mooring lines where each of the line is located 120° adjacent to each other as illustrated in **Figure 3.10**. One of the lines is in the direction of along wind coordinate (u -component) or global y -coordinate Y_G in HAWC2. In the real Hywind, each mooring line has delta connections having the purpose to improve mooring yaw stiffness. Moreover, each mooring line has variable distributed properties along its length depending on the segments considered; yet, this segmentation and the delta connections are eliminated in the OC3-Hywind for simplicity purposes (Jonkman, 2010).

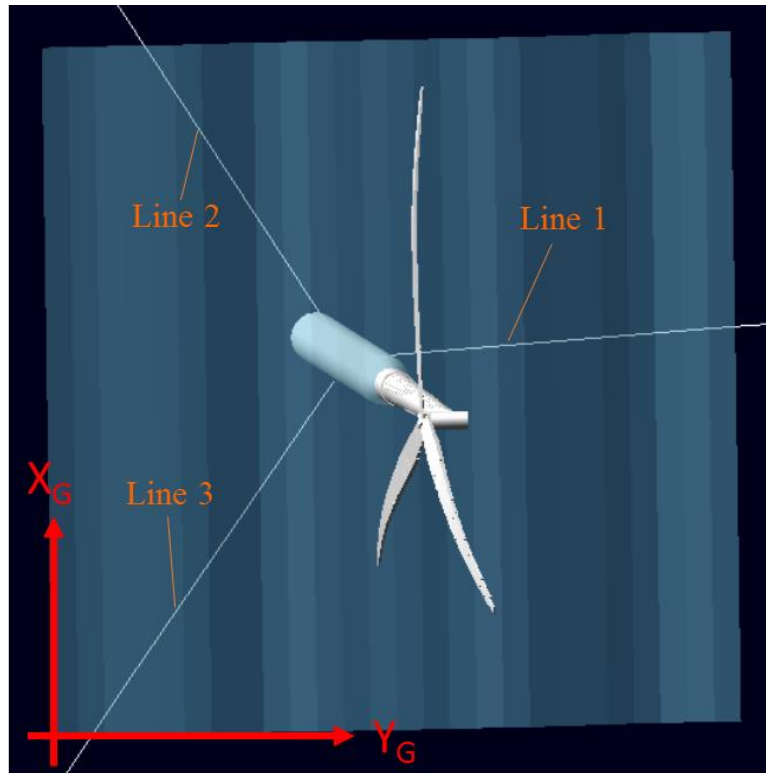


Figure 3.10 Plan view of OC3-Hywind with mooring lines (Jonkman, with modification, 2010).

Considering the static condition where the floater is un-displaced, the fairlead is located 70m below SWL at 5.2m radius from floater centre line, while the anchors are situated 320m below SWL at 853.87m radius from floater centre line (Jonkman, 2010). *Figure 3.11* shows the sketch of the three-dimensional view of OC3-Hywind mooring lines. General description of OC3-Hywind mooring line properties are presented in *Table 3.6*.

Table 3.6 Mooring Line Properties (Jonkman, 2010)

Parameter	Value	Unit
Un-stretched mooring line length	902.2	m
Mooring line diameter	0.09	m
Equivalent mooring line mass density	77.7066	kg/m
Equivalent mooring line submerged weight	698.094	N/m
Equivalent mooring line longitudinal stiffness	384,234,000	N
Additional yaw spring stiffness	98,340,000	Nm/rad

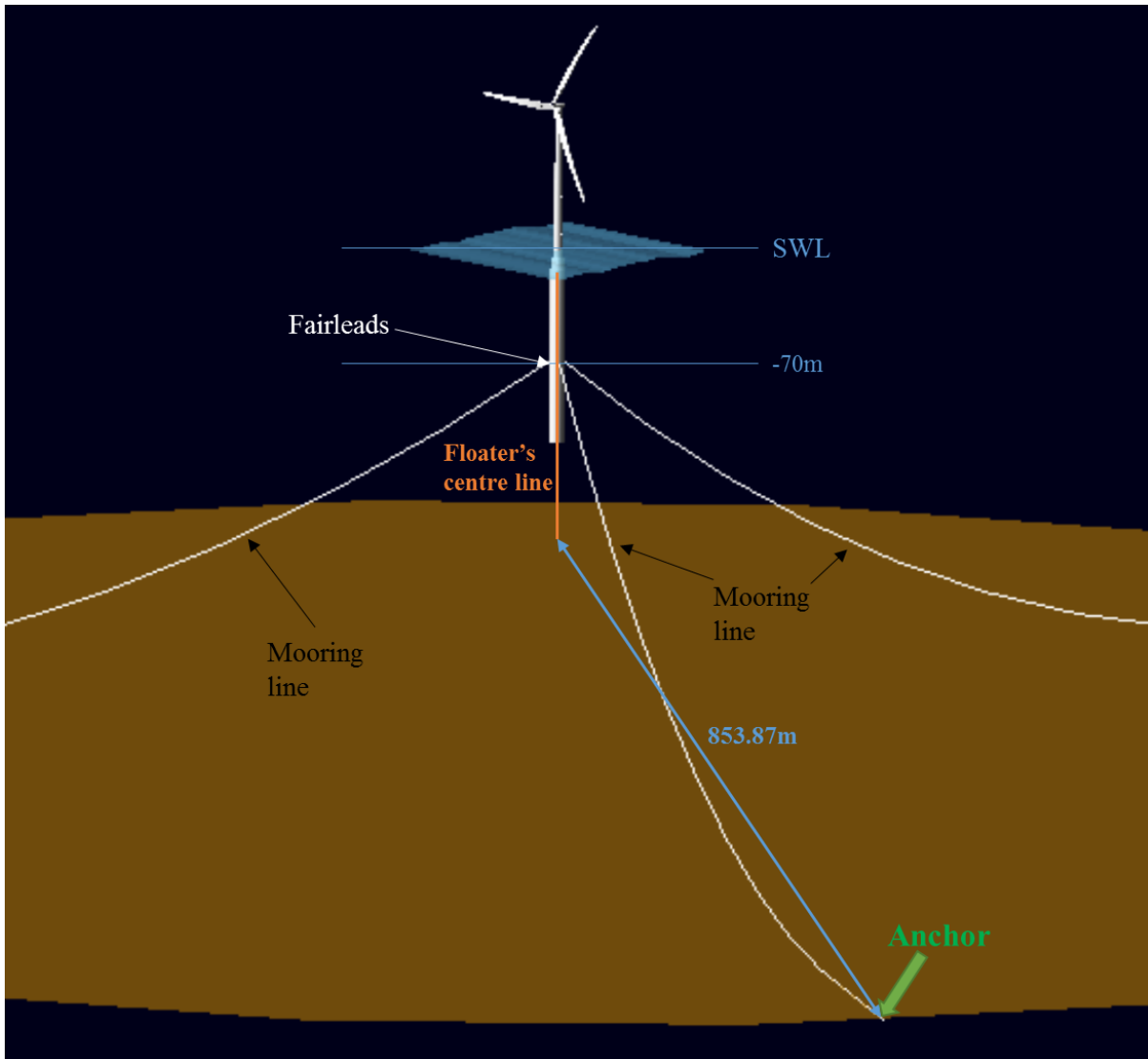


Figure 3.11 3D sketch of OC3-Hywind with mooring lines (Jonkman, with modification, 2010).

3.4 OC3-Hywind Model in HAWC2

The implementation of the given structural properties to the model definition in HAWC2 might have slight adjustments to fit the HAWC2 modelling format. The adjustments however, is still compliant and does not change the structural properties and specification given for the OC3-Hywind. To build the OC3-Hywind model using HAWC2, the overall structure is separated into several main bodies: floater, tower, tower top (nacelle), shaft, hub, and blades. This subchapter will focus on the mooring model and the connector of the main bodies. The floater, tower, RNA and blades modelling in HAWC2 is described in the HAWC2 main input file—the htc file—in the Appendix A.

3.4.1. Mooring Model

The three catenary mooring lines are modelled quasi-statically in the HAWC2 and implemented in the NHMooringDLL.dll as well as the add_MCK.dll, which computes mooring line forces and taking into account the added linear damping.

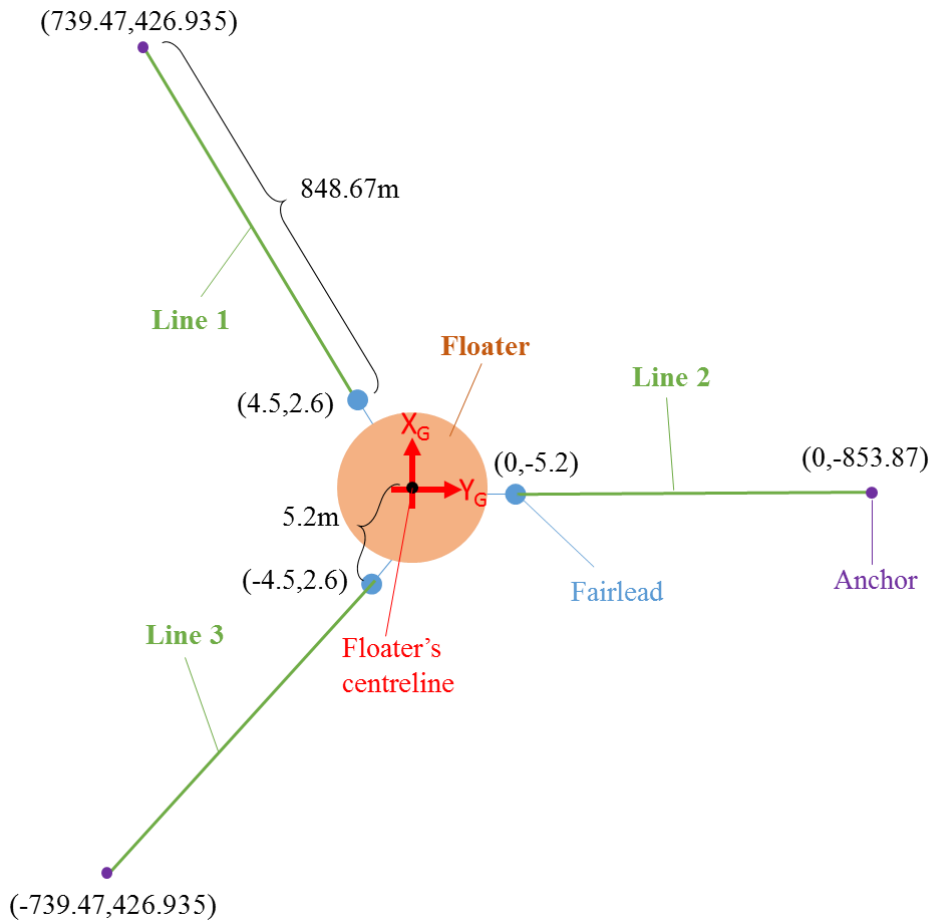


Figure 3.12 Plan view of OC3-Hywind mooring configuration in HAWC2.

The mooring lines adopted in the dll have a slightly different configuration than the one shown in **Figure 3.10**, as illustrated in **Figure 3.12**. The difference covers the naming of the mooring lines, that is line 1 as defined in OC3-Hywind specification becomes line 2 in the HAWC2 model and vice versa. Note that this configuration difference *does not influence* the physical meaning of the system, yet it is just a sorting to get an ordered configuration.

Mooring line forces computations through NHMooringDLL.dll requires an input which will be used as a reference, serving as a look-up table relating a specific horizontal distance of the floater (fairlead) to the anchor and the tension force (DTU, accessed 2016). The available input file from the HAWC2 package is generated from Mimosa software developed by DNV-GL, containing the quasi-statically computed tensions which was also mentioned in the OC3-Hywind specification report by Jonkman (2010). This input file is attached in the Appendix A.

The mooring tension forces are returned as an external force in HAWC2 acting on the floater node no. 3 (fairlead point) by NHMooringDLL.dll, whereas the additional linear damping is added to the system by add_MCK.dll on floater node no.7 (at the SWL). The use of quasi-static analysis from Mimosa allows the load-displacement relation as shown in **Figure 3.13**, which is plotted in accordance with the OC3-Hywind report by Jonkman (2010).

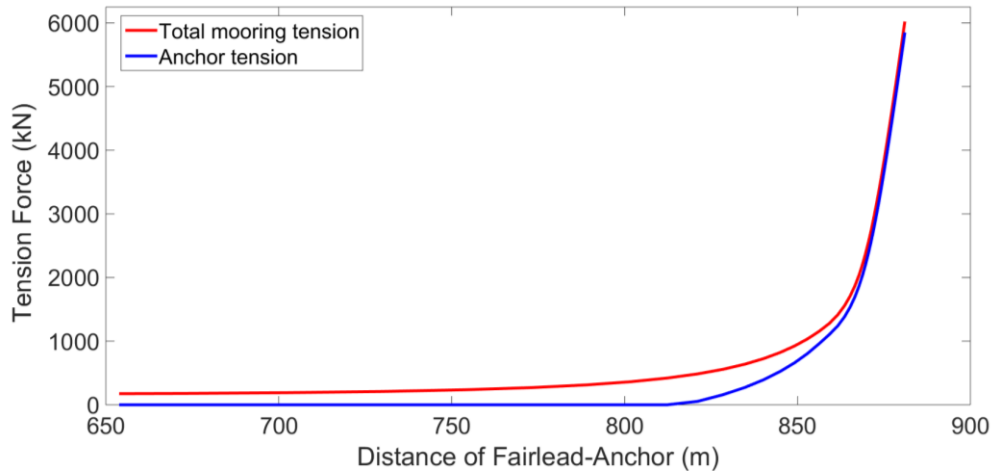


Figure 3.13 Load-displacement relation for mooring line tensions computed from Mimosa.

3.4.2. Defining Constraints (Connection for Each Main Body)

All main bodies defined in the htc main input file are connected to form the entire OC3-Hywind structure using the orientation and constraint commands (DTU, accessed 2016). Orientation command allows the locally defined main body coordinates to adjust with the global coordinate, as each main body is connected to the adjacent corresponding structure. The constructed OC3-Hywind model composed by nodal points for HAWC2 simulations as seen in *Figure 3.14*. Furthermore, the constraint commands describe the connection types between the main bodies’ interfaces and the connections are summarised in *Table 3.7*.

Table 3.7 Constraint Definition for OC3-Hywind Model in HAWC2

No.	Constraint Type	Connecting		Remark
		Main body 1	Main body 2	
1	fix1	Floater	Tower	Fixed connection between floater and tower, relative to each other body translation and rotation
2	fix1	Tower	Tower top	Fixed connection between tower and tower top, relative to each other body translation and rotation
3	bearing1	Tower top	Shaft	Frictionless bearing, to allow yaw bearing (shaft rotation)
4	fix1	Shaft	Hub	Fixed connection between shaft and hub, relative to each other body translation and rotation
5	bearing2	Hub	Blade	Pitch bearing, allowing the blades to pitched when wind speed is above rated; connected to bladed2hawc.dll

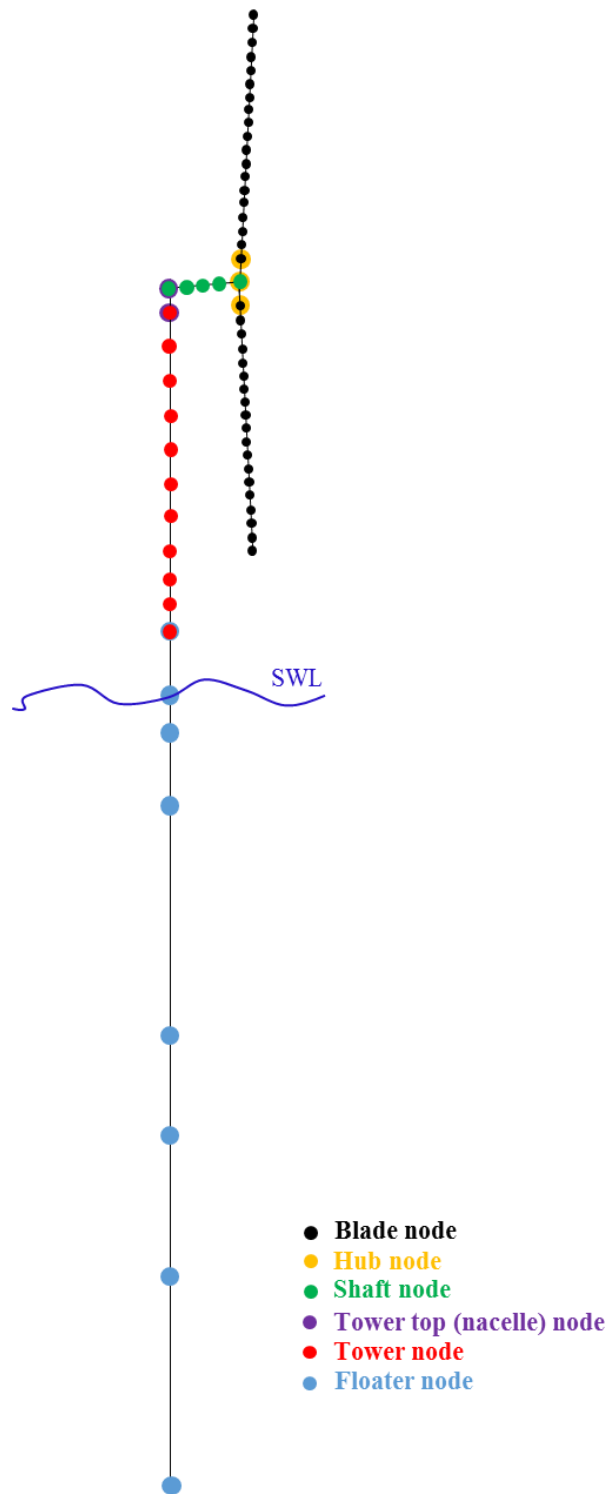


Figure 3.14 Illustration of OC3-Hywind model in HAWC2 (side view).

3.5. HAWC2 – The Limitations

Prior the simulation running, it is useful to acknowledge some limitations of the OC3-Hywind modelling using HAWC2 as listed below.

Atmospheric-Stability-Corrected Mean Wind Shear Profile

In HAWC2, five wind shear profile options are available: no wind shear $U(z)=0$, constant wind shear $U(z)=\text{constant}$, logarithmic law profile (equation 2.1), power law wind profile (equation 2.3), and linear profile $U(z) = U_{ref} dU/dz$. The five available wind shear profiles are unable to account for atmospheric stability correction, however, in this study correction on the wind profiles will be performed and elaborated in Subchapter 4.2.

Damping for multiple bodies

The Rayleigh damping implemented in HAWC2 does not perform well when used for main bodies that are split into several sub-bodies (e.g. blades), and main bodies that are not fixed to the ground i.e. floater of floating wind turbines (DTU, accessed 2016). As consequence result, to define Rayleigh damping for these bodies, it is recommended to set only the value of stiffness-proportional damping (K_x, K_y, K_z) while mass-proportional damping (M_x, M_y, M_z) are set to zero (DTU, accessed 2016).

Another issue related to the damping is the performance of the eigen-frequencies computations. For a very stiff and/or light structure, a warning error appears during the computation of the eigen-frequencies, which indicate either the structure is too stiff or the inputted damping is too high (DTU, accessed 2016). In any case, the stiffness input can be adjusted accordingly to eliminate the warning error as long as the inputted value are within a reasonable range (DTU, accessed 2016).

Static mooring analysis for OC3-Hywind through dynamic link library (dll)

The NHMooringDLL.dll computing mooring tension forces has one significant drawback: the dependency on the Mimosa output result serving as a look-up reference for the mooring tension calculations. Even though this method is described in the OC3-Hywind report by Jonkman (2010), this method requires the user to define the force-displacement relationship (*Figure 3.13*). By using this relationship, the tension force is computed depending on the relative distance of the platform displaced position from the anchors. In other words, regardless the considered load cases, when the platform-to-anchor distance is the same between two load cases, the computed mooring tension forces will be the same. For this reason, different load cases will result in similar computed mooring tension forces.

Compliant issues of some HAWC2 versions with the dynamic link library (dll)

HAWC2 has several published versions and available to be used, from the older HAWC2 version 10.9 to the latest HAWC2 version 12.3 Beta, which update the Intel compiler and has fixed several bugs. Nonetheless, these updates in the internal system prevent some of the dll's working and result in error occurrences in the simulation log. For instance, the use of NHMooringDLL.dll in HAWC2 version 12.x prohibits the writing of mooring forces output, causing termination of the simulation due to "Program Exception – access violation", which give an unclear indication of what might be the error root cause, as seen in *Figure 3.15*. For this reason, user should be aware when selecting the 'right' version of HAWC2, that the relevant dll's are compatible.

```

C:\windows\system32\cmd.exe
r_buoy_phase_4_me.htc
HAWC2MB version: HAWC2MB 12.2
License verified - OK
Opening main command file: \htc\oc3_floating_spar_buoy_phase_4_me.htc
Continue on no convergence = true
Logfile: ./log/oc3_floating_spar_buoy.log is open for log outputs
Blade2Hawc.dll loaded and initialized!
The DLL pitchservo.dll is loaded with succes
Initialization of pitchservo parameters
The DLL damper.dll is loaded with succes
In wkin_dll init, inputfile: ./htc_hydro/reg_airy_h6_t10.inp
Wkin_dll version2-0
Reg_airy input commands read with succes
Wkin_dll input commands read with succes
forrtl: severe (157): Program Exception - access violation
Image      PC          Routine      Line      Source
nhmooringdll.dll 100087AD Unknown      Unknown   Unknown
HAWC2MB.exe    004C4762 Unknown      Unknown   Unknown
HAWC2MB.exe    004CD7F7 Unknown      Unknown   Unknown
HAWC2MB.exe    006230F1 Unknown      Unknown   Unknown
HAWC2MB.exe    00622E96 Unknown      Unknown   Unknown
HAWC2MB.exe    00647605 Unknown      Unknown   Unknown
HAWC2MB.exe    0064C7D0 Unknown      Unknown   Unknown
HAWC2MB.exe    0132B903 Unknown      Unknown   Unknown
HAWC2MB.exe    0081A165 Unknown      Unknown   Unknown
kerne132.dll   76F1338A Unknown      Unknown   Unknown
ntdll.dll     77AC9882 Unknown      Unknown   Unknown
ntdll.dll     77AC9855 Unknown      Unknown   Unknown

C:\Users\Rieska Mawarni Putri\Desktop\HAWC222>

```

Figure 3.15 Error notification due to the use of NHMooringDLL.dll with the HAWC2 version 12.2.

Limited animation and visualisation ability

During the running of simulations, HAWC2 is unable to visualise the real-time running progress, even though a visualisation of simulation will be written and saved after the running has been completed. This means user must wait until the whole simulation is completed to examine the physical appearance of the wind turbine model as well as the model responses, which is somewhat ineffective. In addition, the available supporting animation-reader program (Animation.exe) visualises a very simple sketch, as shown in *Figure 3.16* for the OC3-Hywind model. It is not possible to distinguish between the floater and the tower structure as well as the mooring line which are not shown.

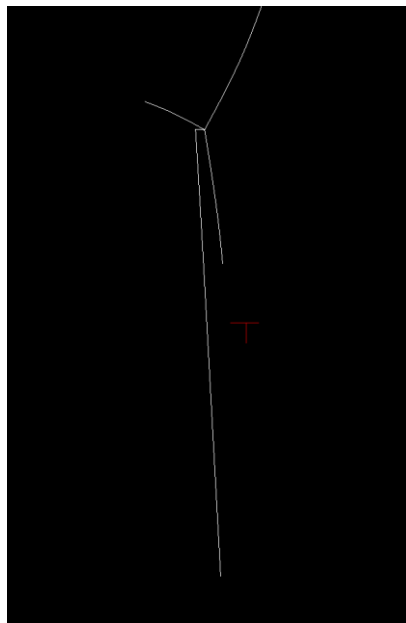


Figure 3.16 Visualisation of animation output using Animation.exe.

4. HAWC2 Simulations for a Spar-Buoy Wind Turbine

4.1 Load Cases and Input Parameters

The load cases performed in this study were distinguished by varying the wind turbulence input based on different atmospheric stability conditions using the IEC Kaimal Spectra & Coherence Model and the Mann Spectral Tensor Model. Each of the load cases were run six times with six different random seed numbers upon the recommendation from IEC (2005) to minimise the uncertainty. Each simulation was performed for 1-hour to account for the wave stationarity (DNV, 2010) as well as allowing the lowest mode frequency to occur within a considerable number of cycles. The eigen-frequency (analysis) was also performed to determine the natural frequencies (modes) of the OC3-Hywind systems.

The simulation load cases results were split into two main groups: (i) load cases from the *fitted-Mann parameters* at Høvsøre site by Sathe et al. (2013) and (ii) load cases for *neutral atmospheric stability conditions* comparing both Kaimal and Mann parameters provided in the IEC standards and the Mann neutral fitted-measurement (Sathe et al., 2013). From hereafter, the two group will be referred as LC Group 1 and LC Group 2 respectively for the fitted-Mann parameters and the neutral atmospheric conditions.

4.1.1. Wind Turbulence Inputs

The IEC Kaimal Spectra & Coherence Model turbulences were generated only for neutral condition while the Mann Model turbulences were generated for stable, neutral, and unstable conditions (according to the stability definition given in **Table 2.5**) from the fitted-Mann parameter values by Sathe et al. (2013). In addition, the Mann Model turbulences for neutral conditions were generated using the parameters given in the standard IEC (2005) computed using formulas given in **Table 2.10**.

Three wind speed cases used in this study correspond to different operational regions of the wind turbine which include: 8m/s (below rated), 11.4m/s (rated), and 15m/s (above rated); however due to data constraints at Høvsøre there were no available fitted-Mann parameter for the above rated case for stable and unstable conditions (Sathe et al., 2013). The turbulence input parameters are summarised in **Table 4.1** for the fitted-Mann parameters and in **Table 4.2** for the parameters of the Model in accordance with IEC standards under neutral conditions. The required input parameter for the IEC Kaimal Spectra & Coherence Model in TurbSim are the turbulence intensity and two random seed numbers for each simulation as shown in **Table 4.2**. The seed numbers were selected randomly and set as constant for different stability cases.

Table 4.1 Mann Turbulence Input Parameters from the Fitted Measurements (Sathe et al., 2013)

Parameter	Below rated (8m/s)			Rated (11.4m/s)			Above rated (15m/s)
	Neutral	Stable	Unstable	Neutral	Stable	Unstable	Neutral
$\alpha \epsilon^{2/3}$ ($m^{4/3}s^{-2}$)	0.034	0.0245	0.0325	0.0685	0.048	0.051	0.099
L_M (m)	46	20	98	52.5	18	107	59
Γ	3.125	2.78	2.25	3.21	2.7	2.52	3.3
Seed no.1	1027						
Seed no.2	2703						
Seed no.3	1992						
Seed no.4	227638						
Seed no.5	8797						
Seed no.6	15509022						

Table 4.2 Turbulence Input Parameters from IEC Standard for Neutral Conditions (IEC, 2005)

Parameter	Below rated (8m/s)		Rated (11.4m/s)		Above rated (15m/s)	
	IEC Kaimal Spectra & Coherence Model	IEC Mann Model	IEC Kaimal Spectra & Coherence Model	IEC Mann Model	IEC Kaimal Spectra & Coherence Model	IEC Mann Model
Turbulence intensity (%)	Class C (12)	Class C (12)	Class C (12)	Class C (12)	Class C (12)	Class C (12)
$\alpha \epsilon^{2/3}$ ($m^{4/3} s^{-2}$)	-	0.0817	-	0.1216	-	0.172
L_M (m)	-	33.6	-	33.6	-	33.6
Γ	-	3.9	-	3.9	-	3.9
Seed no.1	227638, RanLux*	1027	227638, RanLux*	1027	227638, RanLux*	1027
Seed no.2	2703, 1992	2703	2703, 1992	2703	2703, 1992	2703
Seed no.3	8797, 15509022	1992	8797, 15509022	1992	8797, 15509022	1992
Seed no.4	1027, 856	227638	1027, 856	227638	1027, 856	227638
Seed no.5	934, 79759	8797	934, 79759	8797	934, 79759	8797
Seed no.6	1970, 977	15509022	1970, 977	15509022	1970, 977	15509022

* refers to the Lüscher’s level 3 “Luxury Pseudorandom Numbers”, detailed info is given in reference (Jonkman & Kilcher, 2012)

4.1.2. Waves Input

The waves input parameters were constant for all simulations performed, as presented in **Table 4.3**. The selection of the wave theory, wave spectrum and significant wave height H_s was based on the OC3 report by Jonkman & Musial (2010). The value of the wave peak period T_p was taken as the recommended value in the DNV (2010) for a specified H_s and the chosen wave spectrum, computed as follow:

$$3.6 < \frac{T_p}{\sqrt{H_s}} < 5 \tag{4.1}$$

where H_s is the significant wave height.

Table 4.3 Waves Input Parameters

Parameter	Value	Unit
Wave type/theory	Irregular Airy wave	-
Significant wave height (H_s)	6	meter
Wave peak period (T_p)	12	second
Peak parameter (γ)	3.3	-
Spectrum	JONSWAP	-
Wave direction	0*	degree
Seed number	27	-

* the waves approaching direction is in the same direction with the along wind

4.2 Setting up Simulations

This subchapter covers the simulation settings inputted in the HAWC2 and TurbSim for all load cases performed.

4.2.1. General

The following general setups presented in **Table 4.4** were applied in HAWC2 for all load cases run.

Table 4.4 General Simulation Parameters in HAWC2

Parameter	Value	Unit
Simulation length	3600	second
Simulation time step	0.02*	second
Convergence limit (for internal-external forces)	10*	N
Convergence limit (for residual on increment)	1.0*	-
Convergence limit (for residual on constraint equations)	10 ⁻⁷ *	%

*recommended values by DTU (HAWC2 developer)

4.2.2. Wind and Aerodynamics Input – General

Aside from the wind turbulence input, general properties of the wind and the aerodynamic methods used in the simulations for the two load cases LC Group 1 and LC Group 2 are presented in **Table 4.5** and **Table 4.6** respectively. As outlined previously (Subchapter 3.5), the stability corrections to the mean wind profile cannot be inputted directly. As a result, adjustment to the wind profile was achieved by varying the power law exponent α for stable and unstable conditions using values taken from the NORSEWInD Project by Diaz et al. (2012). The α values were fitted from measurements at Egmond aan Zee (EAZ), situated in the Dutch North Sea, 15km away from Dutch coast during July 2005 until December 2008. The values are shown in **Table 4.5**.

Table 4.5 General Wind and Aerodynamics Inputs Simulation for LC Group 1

Parameter	Below rated (8m/s)			Rated (11.4m/s)		
	Neutral	Stable	Unstable	Neutral	Stable	Unstable
Air density ρ (kg/m ³)	1.225					
Mean wind speed (m/s)	8	8	8	11.4	11.4	11.4
TI	0.12 ¹					
Wind shear profile	Power law					
Power law exponent α	0.12*	0.18**	0.04**	0.12*	0.18**	0.04**
Tower shadow method	Potential flow ²					
Scaling ratio for the generated turbulence	No scaling ¹					
Induction method	BEM					
Tip loss method	Prandtl					
Dynamic stall method	Beddoes-Leishmann					

¹When “no scaling” option is chosen, the generated turbulences from the 64bit Mann Turbulence Generator are used with no scaling adjustment to achieve the given (target) turbulence intensity input. Nonetheless, a TI value is still need to be inputted for HAWC2 to account for the turbulence (i.e. if TI is left empty or set as zero, a constant wind will be considered by HAWC2).

²This method allows the calculation of drag force on the tower, where the displaced position of the tower with respect to the incoming wind direction is accounted for.

*Recommended value from the DNV-RP-C205, October 2010

**Taken from the EAZ measurement by Diaz et al. (2012)

Table 4.6 General Wind and Aerodynamics Inputs Simulation for LC Group 2 (Neutral Conditions)

Parameter	Below rated (8m/s)			Rated (11.4m/s)			Above rated (15m/s)		
	Fitted-Mann	IEC Kaimal	IEC Mann	Fitted-Mann	IEC Kaimal	IEC Mann	Fitted-Mann	IEC Kaimal	IEC Mann
Air density ρ (kg/m ³)	1.225								
Mean wind speed (m/s)	8	8	8	11.4	11.4	11.4	15	15	15
TI	0.12 ¹								
Wind shear profile	Power law								
Power law exponent α	0.12*								
Tower shadow method	Potential flow ²								
Scaling ratio for the generated turbulence	No scaling ¹								
Induction method	BEM								
Tip loss method	Prandtl								
Dynamic stall method	Beddoes-Leishmann								

¹When “no scaling” option is chosen, the generated turbulences from the 64bit Mann Turbulence Generator are used with no scaling adjustment to achieve the given (target) turbulence intensity input. Nonetheless, a TI value is still need to be inputted for HAWC2 to account for the turbulence (i.e. if TI is left empty or set as zero, a constant wind will be considered by HAWC2).

²This method allows the calculation of drag force on the tower, where the displaced position of the tower with respect to the incoming wind direction is accounted for.

*Recommended value from the DNV-RP-C205, October 2010

4.2.3. Wind Input – Turbulence Box

As recommended in the TurbSim manual (Jonkman & Kilcher, 2012) and DTU (accessed 2016), the grid box sizes (L_y and L_z) should be added at least 10% of the rotor swept area diameter (as indicated by the dashed green line in *Figure 4.1*) or even larger for FOWT to account for excessive structural movement of the turbine. Thus, in this study, an addition about 20% of the rotor swept diameter area was added in the turbulence box sizes (L_y and L_z).

The inputs of the turbulence box for the Mann Model (generated by 64bit Mann Turbulence Generator) and the IEC Kaimal Spectra & Coherence Model (generated by TurbSim) are presented in *Table 4.7* and *Table 4.8* respectively.

Table 4.7 3D Turbulence Box Input for the 64bit Mann Turbulence Generator

Case	Mean wind speed at hub (m/s)	N_x	dx (m)	N_y	dy (m)	N_z	dz (m)
Below rated	8	32768	0.8789	32*	5*	32*	5*
Rated	11.4		1.2524				
Above rated	15		1.6479				

*as recommended by DTU (HAWC2 developer)

Table 4.8 Turbulence Box Input for TurbSim

Case	Mean wind speed at hub (m/s)	N_y	N_z	dt (sec)	Analysis time (sec)	Useable time (s)	L'_y (m)	L'_z (m)
Below rated	8	32	32	0.10986	3600	3580.62	155	155
Rated	11.4					3586.40		
Above rated	15					3589.67		

In the given turbulence box dimensional input, the rotor centre hub (blue dot in *Figure 4.1*) does not coincide with any of the grid points, yet it is enclosed by four grid points as indicated by the red dots in *Figure 4.1*. As a result, in HAWC2, the generated turbulence at the rotor centre hub is interpolated from the four grid points (red dots), so the generated turbulence at the rotor centre will have lower standard deviation than the four surrounding points. This also applies for other area inside the turbulence box that is not coinciding with the turbulence box grid points.

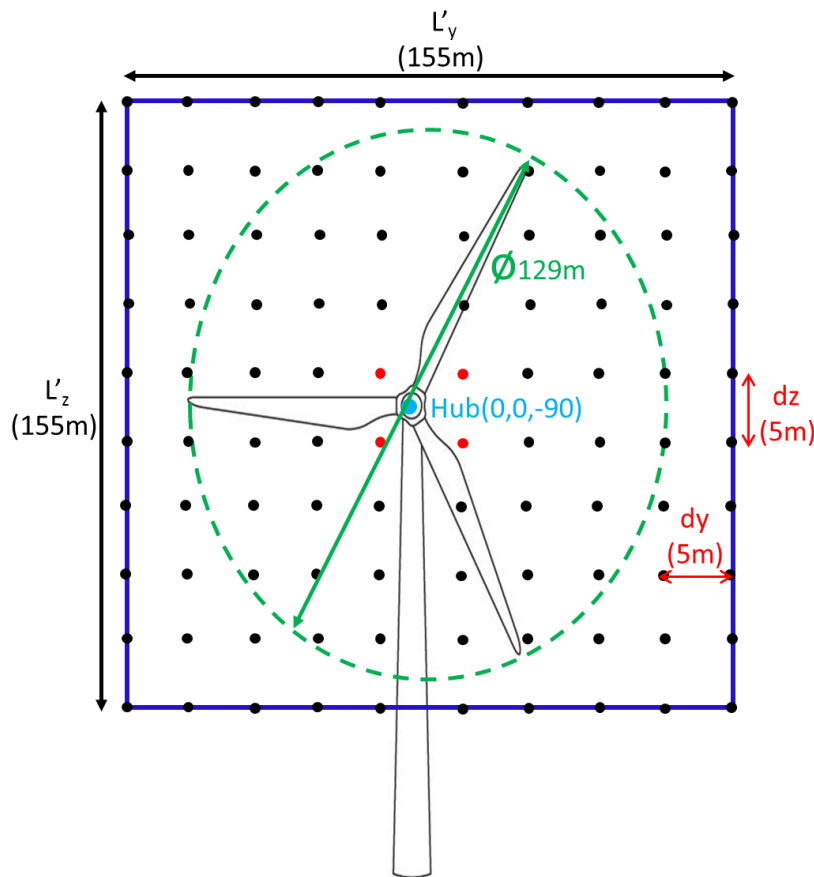


Figure 4.1 Sketch of the inputted 3D turbulence box definition.

4.3 Simulation Results

Since the objective of this thesis is to study the influences of turbulent wind and spatial coherences on the OC3-Hywind turbine, the results presented will focus on the following components of the wind turbine: tower base fore-aft, tower top yaw, platform pitch, platform yaw, and blade root flap-wise bending moments. The definition of spatial coherences are illustrated in *Figure 4.2*, where point A-B

expresses vertical coherence and point C-D represents lateral coherence. The vertical coherence is hypothesised to influence the fore-aft/pitch while the lateral coherence is hypothesised to influence the yaw of the OC3-Hywind. In addition, the effect of the coherences with respect to the blades loading will also be discussed. *Figure 4.3* describes the definition of the OC3-Hywind degree of freedoms, while *Figure 4.4* illustrates the blade root bending moments.

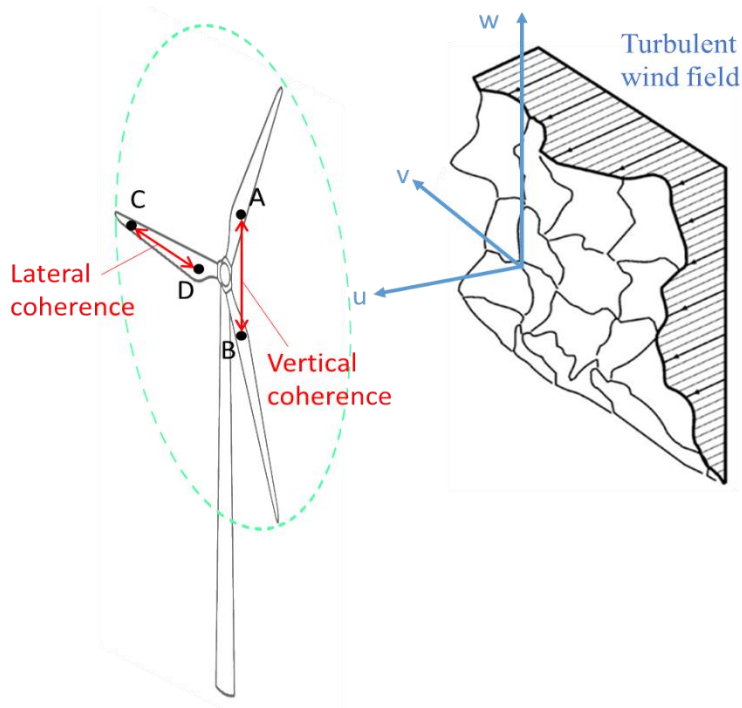


Figure 4.2 The lateral and vertical coherences of a turbulent wind field.

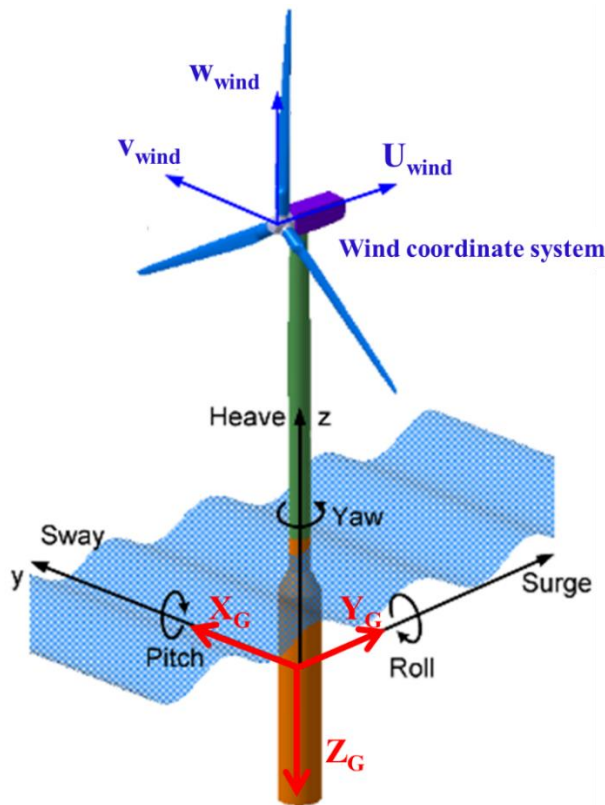


Figure 4.3 The OC3-Hywind six-degree of freedoms (Tran et al., with modification, 2014).

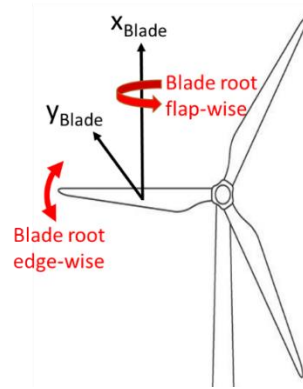


Figure 4.4 The blade root bending moments.

The simulation results are presented within the two defined main groups, LC Group 1 and LC Group 2 (as defined in Table 4.5 and Table 4.6) and categorised into eigen-frequency, power spectral density, fatigue damage, and motion responses. All given results are the average of the six simulations of each load cases, except for the motion responses which also consider the maximum and minimum value from the six simulations.

4.3.1. The Generated Wind Turbulence

Prior to discussing the simulations results, analysis on the properties of the generated wind turbulence (represented by statistical parameter standard deviation σ) is performed here. Table 4.9 shows the standard deviation values of the wind component u from each load cases at the hub height elevation from the generated turbulence box (red box represents LC Group 1, blue box for LC Group 2).

Table 4.9 The Generated Turbulence Standard Deviation

Parameter	Below rated (8m/s)				
	IEC		Fitted Parameters (Sathe et al., 2013)		
	Kaimal (Neutral)	Mann (Neutral)	Mann (Neutral)	Mann (Stable)	Mann (Unstable)
Turbulence intensity (%)	Class C (12)	Class C (12)	-	-	-
$\alpha\epsilon^{2/3} (m^{4/3}s^{-2})$	-	0.0817	0.034	0.0245	0.0325
L_M (m)	-	33.6	46	20	98
Γ	-	3.9	3.125	2.78	2.25
σ_u (m/s)	0.957	1.385	0.871	0.521	0.914
Parameter	Rated (11.4m/s)				
Turbulence intensity (%)	Class C (12)	Class C (12)	-	-	-
$\alpha\epsilon^{2/3} (m^{4/3}s^{-2})$	-	0.1216	0.0685	0.048	0.051
L_M (m)	-	33.6	52.5	18	107
Γ	-	3.9	3.21	2.7	2.52
σ_u (m/s)	1.358	1.674	1.303	0.687	1.264
Parameter	Above rated (15m/s)				
Turbulence intensity (%)	Class C (12)	Class C (12)	-	-	-
$\alpha\epsilon^{2/3} (m^{4/3}s^{-2})$	-	0.172	0.099	not available	not available
L_M (m)	-	33.6	59	not available	not available
Γ	-	3.9	3.3	not available	not available
σ_u (m/s)	1.781	1.985	1.650	not available	not available

Table 4.9 informs that the turbulence standard deviation is increasing as the wind speed increases, indicating a higher level of turbulence, which is align with the study done by Sathe et al. (2013). **Figure 4.5**, **Figure 4.6** and **Figure 4.7** give the interpolated power spectral density plots of the average six simulations for rated wind speed (11.4m/s) at the hub height, respectively for U -component, v -component, and w -component.

Furthermore, in the case of Mann Model, it can be observed that there was a general tendency of σ_u towards the parameter $\alpha\epsilon^{2/3}$ which higher $\alpha\epsilon^{2/3}$ results in higher σ_u . Comparing the fitted parameters within various atmospheric stability conditions (LC Group 1, **Table 4.9** red box), neutral conditions have the highest turbulence (σ_u) followed by unstable and stable conditions. Theoretically, unstable conditions should have the highest turbulence levels as the vertical mixing is more significant; however the results showing that neutral conditions has the highest turbulent energy is related to the increasing mechanically generated (shear) turbulence. This tendency however is not observed for the v and w wind components as the unstable conditions result in the highest σ_v and σ_w (**Table C.1**). The calculated $\alpha\epsilon^{2/3}$ parameters from the IEC standard (neutral condition) at each wind speed cases are the highest among all Mann Turbulence load cases, resulting in the highest turbulence levels σ_u , which was also noted by Sathe et al. (2013).

Comparing LC Group 2 (**Table 4.9** blue box), despite the generated IEC Kaimal turbulence gives smaller values of σ_u than the IEC Mann Turbulence; it has close values with the fitted Mann (neutral), which is the largest among the other fitted $\alpha\epsilon^{2/3}$ parameter at different stability conditions.

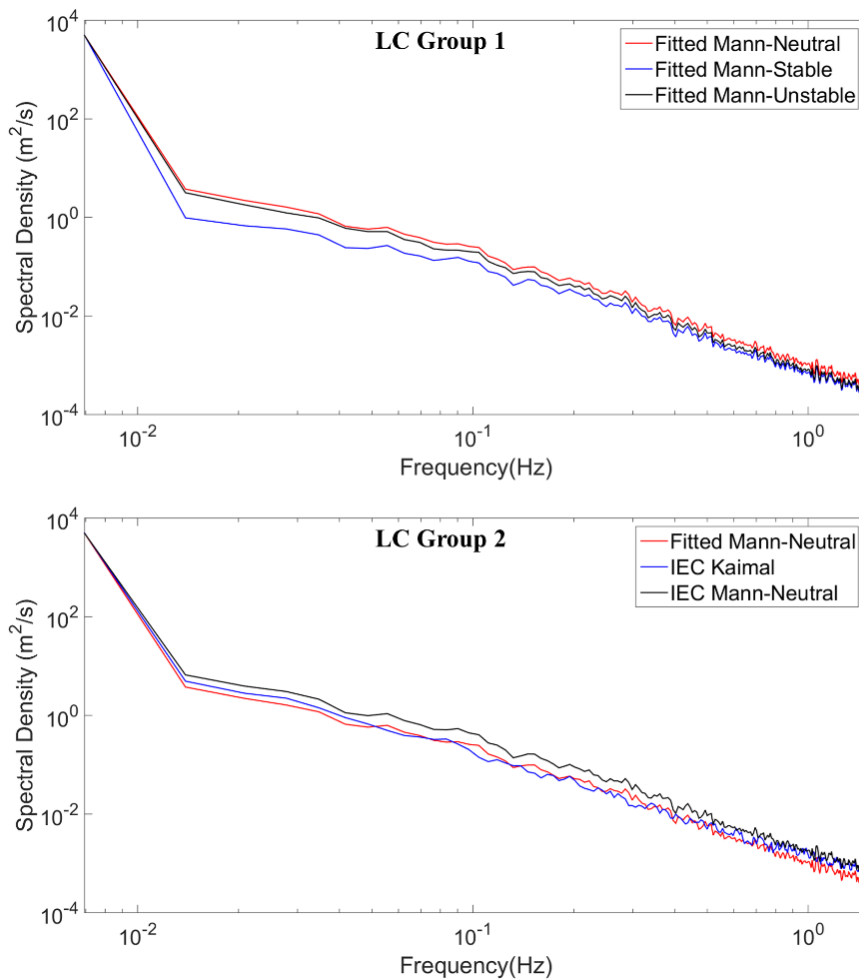


Figure 4.5 Power spectral density of the along-wind component for 11.4 m/s wind at hub height.

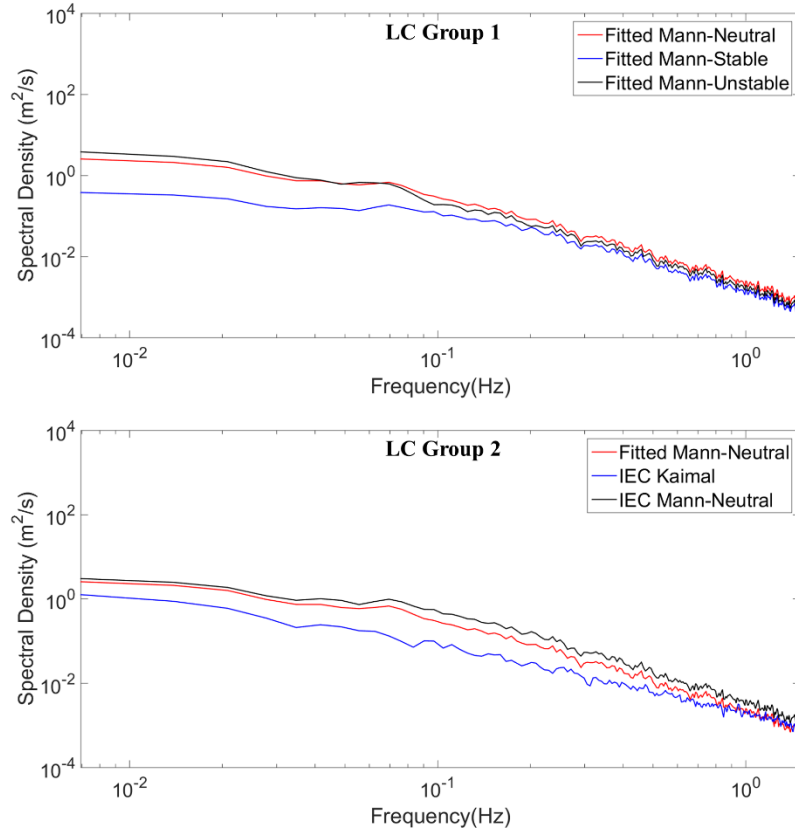


Figure 4.6 Power spectral density of the cross-wind component for 11.4 m/s wind at hub height.

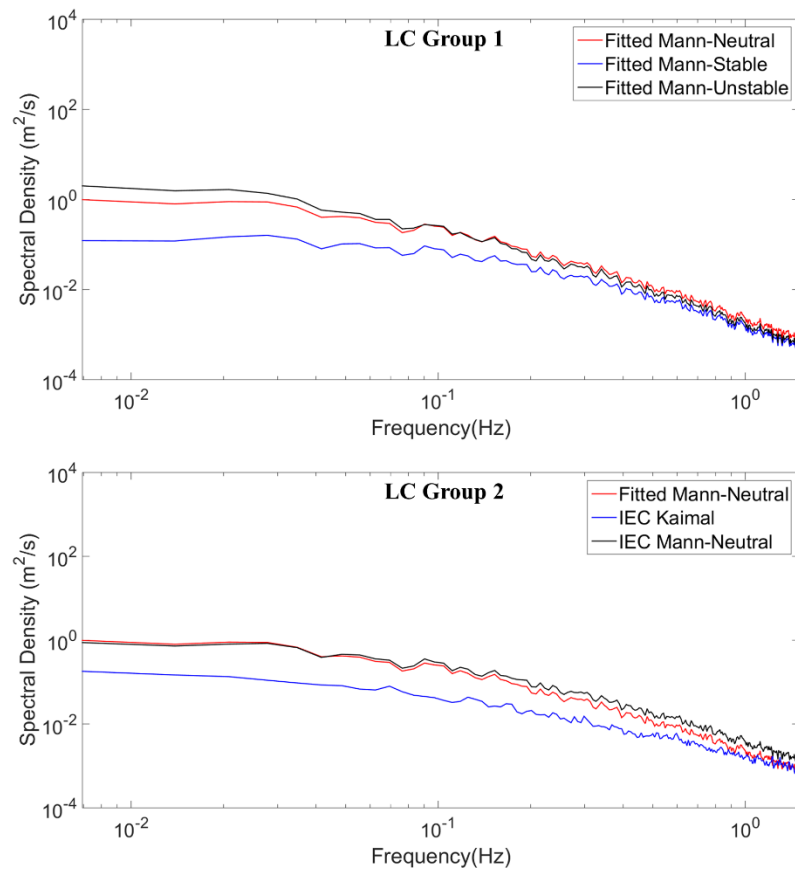


Figure 4.7 Power spectral density of the vertical-wind component for 11.4 m/s wind at hub.

Considering spatial variation (lateral and vertical direction), it is observed that the turbulence level σ_u is invariant with respect to lateral and vertical spatial variation (*Figure 4.8* and *Figure 4.9*, respectively). This also applies for wind speed at below and above rated, where the plots are given in the Appendix C. The same manner is also observed for σ_v and σ_w for all wind speeds that are tends to be invariant with lateral and vertical direction where the plots are also provided in the Appendix C.

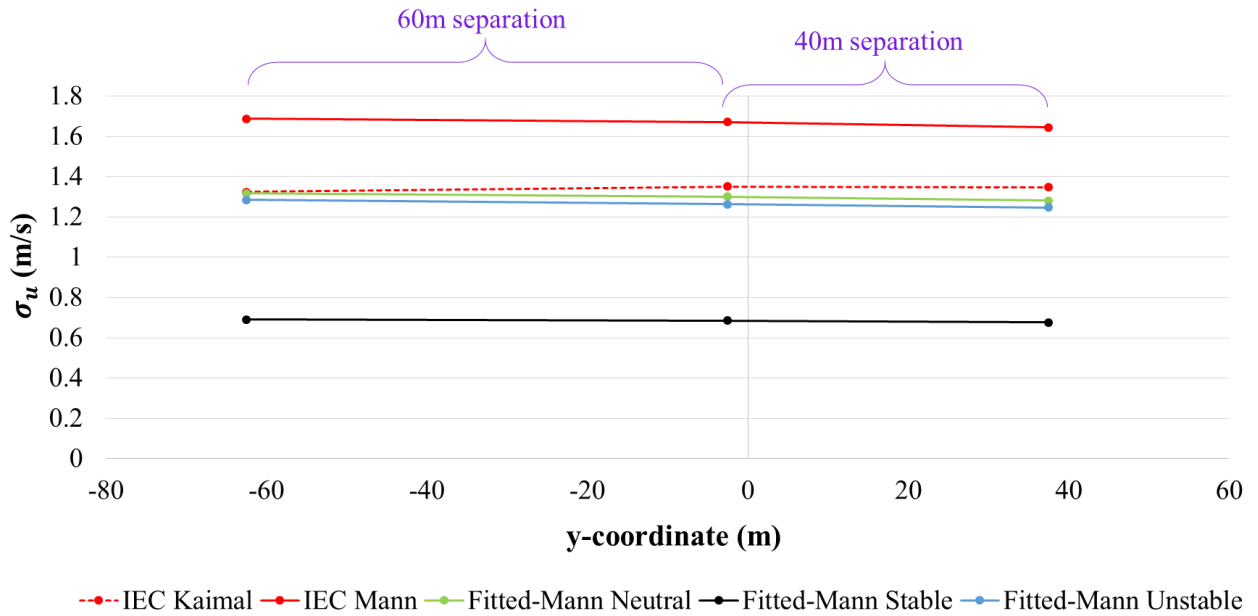


Figure 4.8 Turbulence level of the u -component for 40m and 60m lateral separations at rated wind speed.

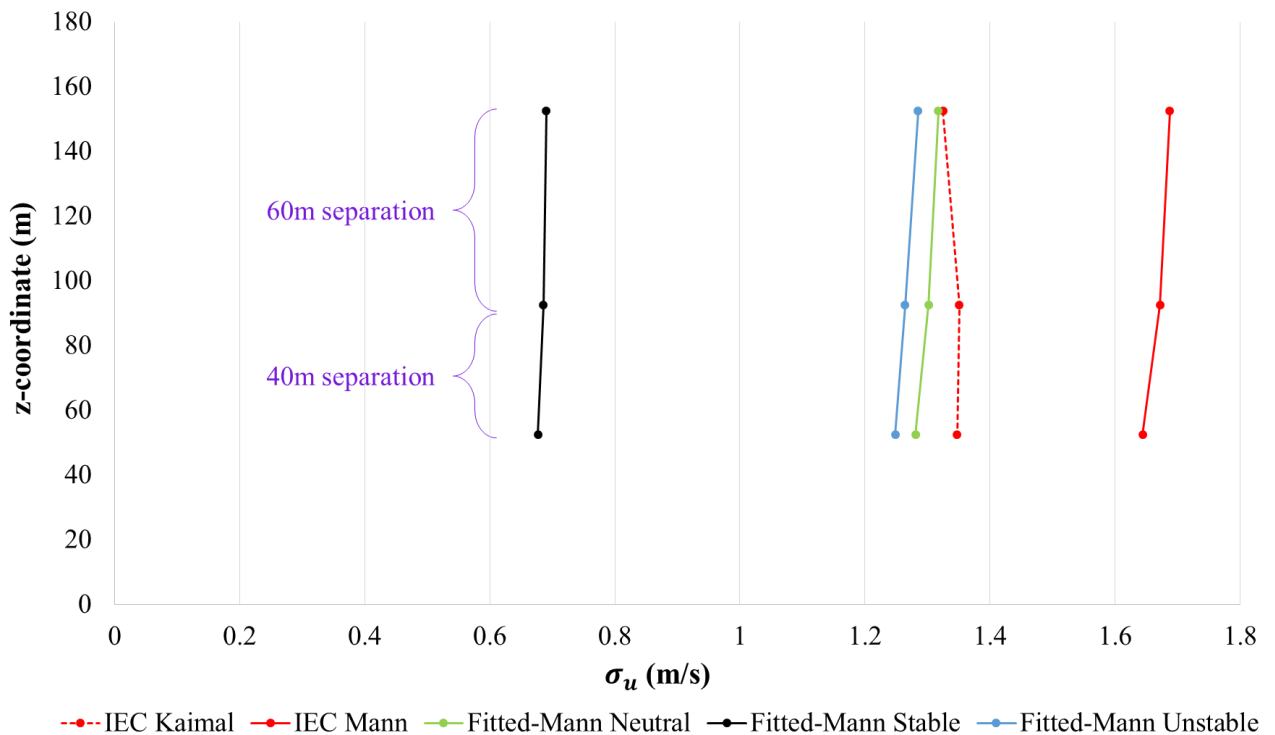


Figure 4.9 Turbulence level of the u -component for 40m and 60m vertical separations at rated wind speed.

4.3.2. Eigen-frequencies

The dynamics of the OC3-Hywind depends both on the excitations (wind and waves) acting on the structure as well as its natural frequencies. It is then important to check the eigen-frequencies of the excitations (waves and wind) and the modes (natural frequencies/ f_n) of the OC3-Hywind system.

4.3.2.1. Eigen-frequencies of the Rotating Rotor

The frequencies of the rotating blades are one of the important parameters determining the dynamic response of the OC3-Hywind, aside from the wind & waves excitations. There are two main frequencies related to the rotating blades: the constant rotor rotational speed (known as 1P) and the blade passing frequency (N_bP) where N_b is the number of blades (van der Tempel & Molenaar, 2002). In the case of the 3-bladed OC3-Hywind, the blade passing frequency is 3P. The 1P and 3P frequencies for the OC3-Hywind were computed from the rotor rotational speeds given from **Table 3.1**, as plotted on **Figure 4.10**. **Table 4.10** presents for the 1P and 3P frequencies at each wind speed cases considered.

Table 4.10 Frequencies of the Rotating Blades for NREL 5MW Wind Turbine

Operating region	Wind speed (m/s)	Rotor rotational frequency (rpm)	1P Frequency (Hz)	2P Frequency (Hz)	3P Frequency (Hz)
Below rated	8	9.995	0.16	0.33	0.48
Rated	11.4	12.1	0.20	0.40	0.60
Above rated	15	12.1	0.20	0.40	0.60

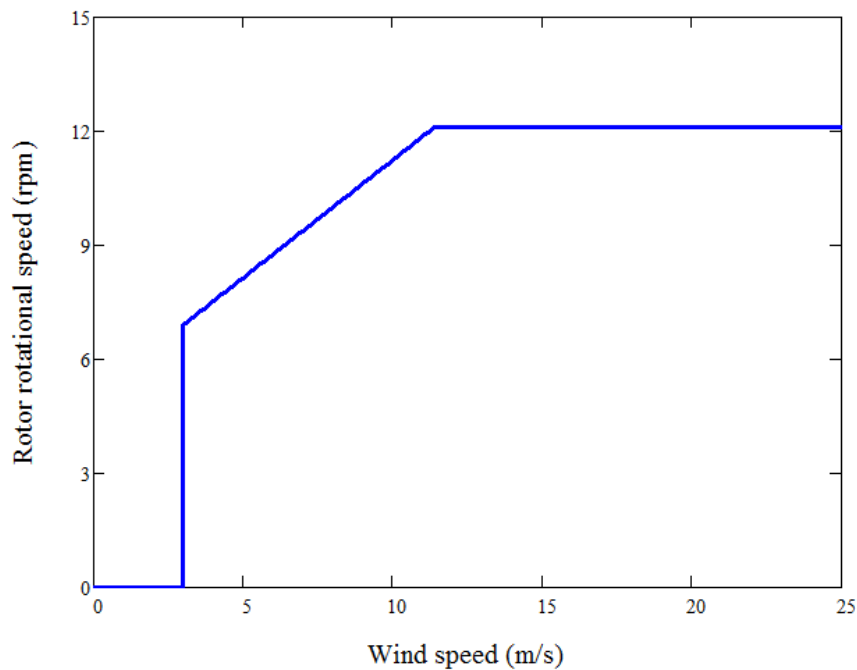


Figure 4.10 Rotor rotational speed for the NREL 5MW Wind Turbine.

The value of other rotational 4P, 5P up to N_pP frequencies are not presented in **Table 4.10** but can be computed using the following formula:

$$N_pP = N_p \times 1P \tag{4.2}$$

where

N_p : the number of considered frequency (e.g. 4, 6, etc.)

$1P$: constant rotor rotational speed (*Table 4.10*)

4.3.2.2. Eigen-frequencies of the Environmental Loads

The environmental loadings included in this study are the turbulent wind and the waves. Excitations from the turbulent wind are presented in *Figure 4.5* to *Figure 4.7* for the rated wind speed at the hub height respectively for u , v , and w wind components. The generated power spectral densities for the turbulent wind at below rated and above rated wind speeds are provided in the Appendix C.

Figure 4.11 presents the wave power spectral density for the given input parameters described in *Table 4.3*. The highest wave excitation is at the wave peak frequency f_p (0.083Hz), corresponding to the wave peak period $T_p=12$ second.

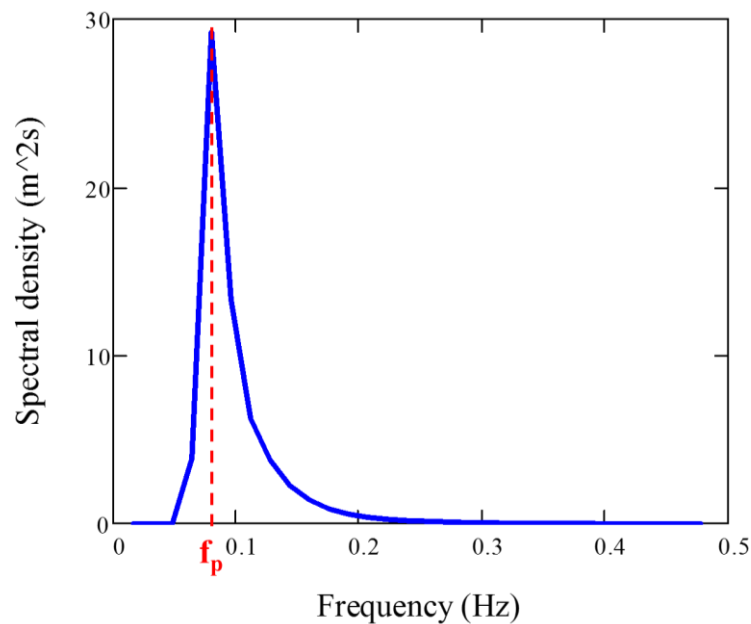


Figure 4.11 The wave input spectral density.

4.3.2.3. Eigen-frequencies Results – OC3-Hywind Modes

The values presented in *Table 4.11* are obtained from the simulation result for the first 10 eigen modes, while *Figure 4.12* shows the computed values from the OC3-Hywind Report by Jonkman & Musial (2010). The values obtained from the simulation were computed using the recommended (given) stiffness and damping from the OC3-Hywind model provided by DTU (HAWC2 developer). Moreover, the model was run by disabling the wave kinematics (still water condition) and setting the air density as zero (no air) to match the eigen-frequency load case as given by (Jonkman & Musial, 2010).

In general, both sets of values match well even though some deviations are observed, which most likely caused by the limitations within the HAWC2. Firstly, for a main body (structure) not fixedly attached to the ground (i.e. floater), some issues related with the Rayleigh damping model have been observed (DTU, accessed 2016). Secondly, the mooring lines system could not be handled correctly when the normal method of eigen-frequencies computation in HAWC2 is adopted (Yde, 2016). Nonetheless, the correct eigen-frequencies value can be obtained with free-decay tests in HAWC2 which were not performed in this study, as it is a limitation of this study. A significant difference is observed in the platform heave natural frequency as well as the roll and pitch natural frequencies. It is stated in the OC3-Hywind report that the pitch and roll natural frequencies computed from HAWC2 were having higher values due to the handling of the gravity term in the linearization of the model as the spar floater

roll and pitch restoring are significantly affected by gravity (Jonkman & Musial, 2010). According to Jonkman (2010) in ‘The Definition of OC3-Hywind’, the actual platform pitch natural frequency of OC3-Hywind is about 0.21rad/s (0.03Hz). This reference value of the pitch natural frequency will be considered later for the spectral density analysis (Subchapter 4.3.3), instead of using the simulation result due to the previously mentioned reason.

The eigen-frequencies values differences from the simulation results on the OC3-Hywind Report provided by Jonkman & Musial (2010) were also observed from the study of Saccoman (2015) who stated that the system eigen-frequencies analysis should be assessed cautiously due to its current implementation in HAWC2.

Table 4.11 Eigen-frequencies of the First 10 Modes for the OC3-Hywind from the Simulation

Mode No.	Simulation Result	
	Mode Description	Frequency (Hz)
1	Heave	0.0025
2	Surge	0.0109
3	Sway	0.0109
4	Roll	0.053
5	Pitch	0.06
6	Yaw	0.121
7	1 st Tower fore-aft	0.43
8	1 st Tower side-side	0.442
9	Blade flapwise	0.63
10	Drivetrain torsion	0.642

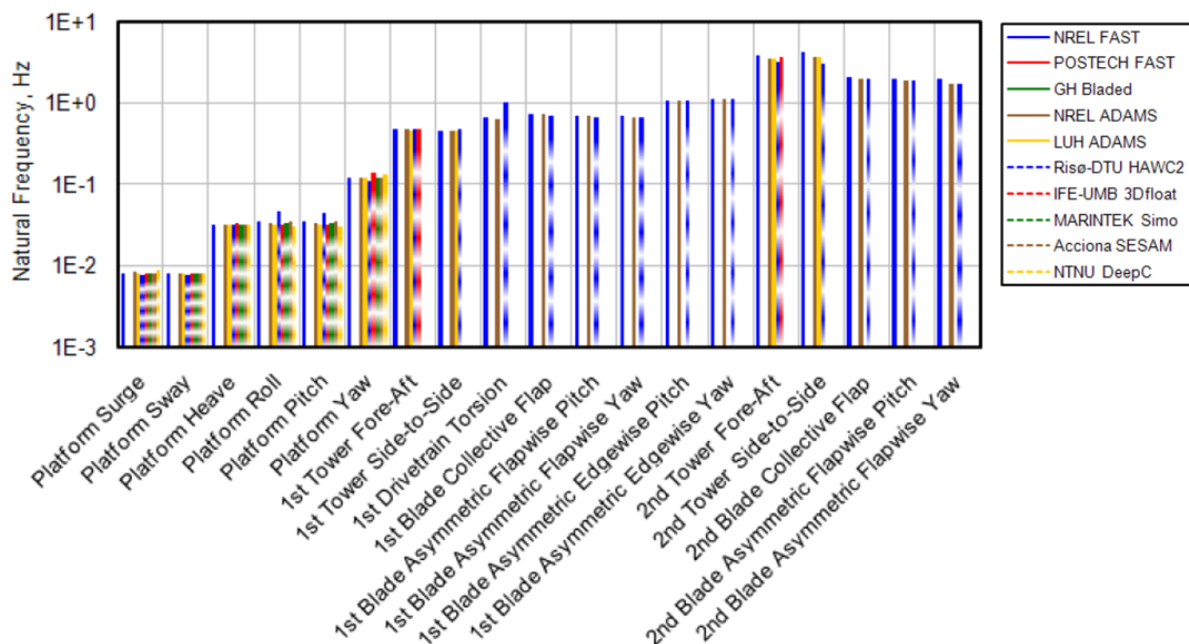


Figure 4.12 The eigen-frequencies for the OC3-Hywind system (Jonkman & Musial, 2010).

4.3.3. Spectral Density

The spectral density analysis is performed to examine the primary excitations governing the spar-buoy wind turbine components responses. The spectral density analyses are limited only to the small frequencies range, where the wave excitations and the main platform degree of freedom modes are captured. For analysis purpose, the spectral density results will be focused on the tower base fore-aft

moment, tower top yaw moment, blade root flap-wise, pitch and yaw rotations of the platform, as well as the mooring forces.

It is important to notice that the excitation from the 1st tower fore-aft in this spectral density result (0.47Hz) was not precisely lie in the computed frequency as given in *Table 4.11* (0.43Hz). The 1st tower fore-aft natural frequency from the OC3-Hywind report (*Figure 4.12*) is roughly near 0.46Hz. In addition, the platform pitch frequency is taken as 0.03Hz as outlined previously.

4.3.3.1. Tower Base Fore-Aft Moment

The tower base fore-aft moment spectral densities at below rated, rated, and above rated wind speed are shown in *Figure 4.13* to *Figure 4.15* respectively. We observe that there is negligible difference in the energy content between each load cases, suggesting that the tower base fore-aft moment is not significantly influenced by variation in the atmospheric stability or the variation in turbulence input. The increment of wind speed only slightly increases the tower base fore-aft moment energy. At below rated wind speed (*Figure 4.13*), the main excitations are at the frequencies of the wave spectral peak, 6P and the 1st tower fore-aft. As the wind speed enters the rated (*Figure 4.14*) and above (*Figure 4.15*), an additional excitation is observed, coming from the platform pitch frequency. The wave spectral peak induces the highest tower base fore-aft moment energy content amongst all other primary excitations for all load cases. The excitation at the 6P frequency was also observed by Eliassen (2016) for a fixed-monopile 10MW OWT. The study (Eliassen, 2016) also showed that the tower base fore-aft moments were excited in the 3P frequency which was not observed in this study since the OC3-Hywind 1st tower fore-aft natural frequency (0.47Hz) which is adjacent to the 3P frequency (0.48Hz for below rated wind speed, 0.6Hz for the rated wind speed and above).

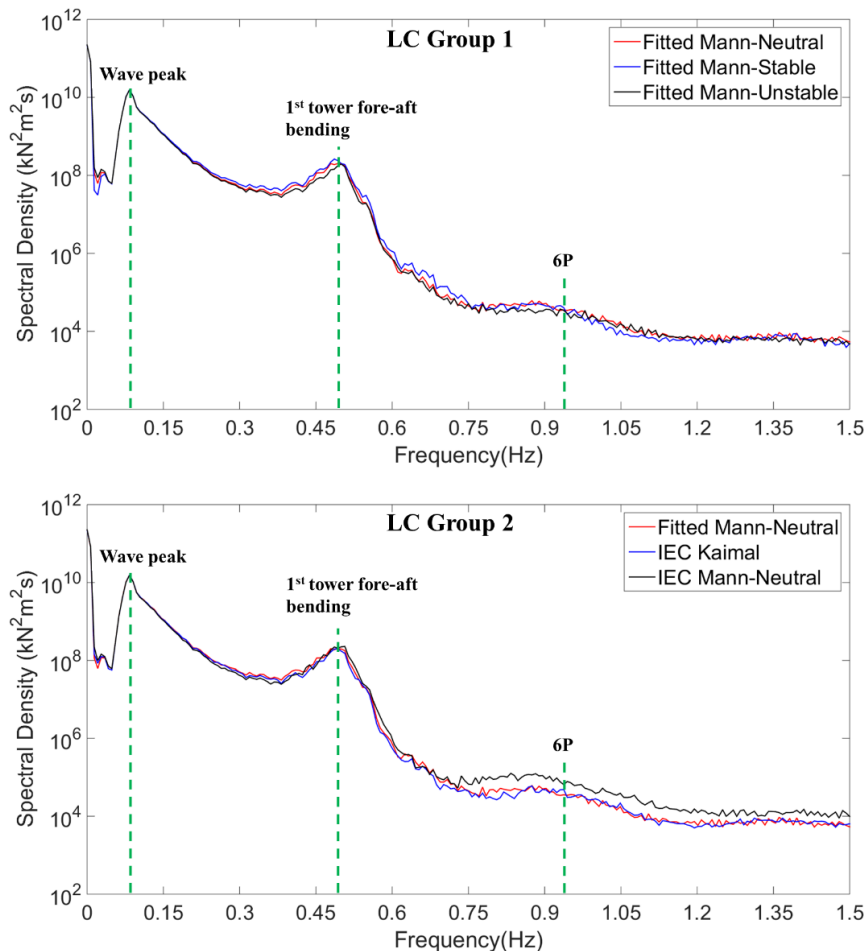


Figure 4.13 The tower base fore-aft moment spectral densities at below rated (8m/s) wind speed.

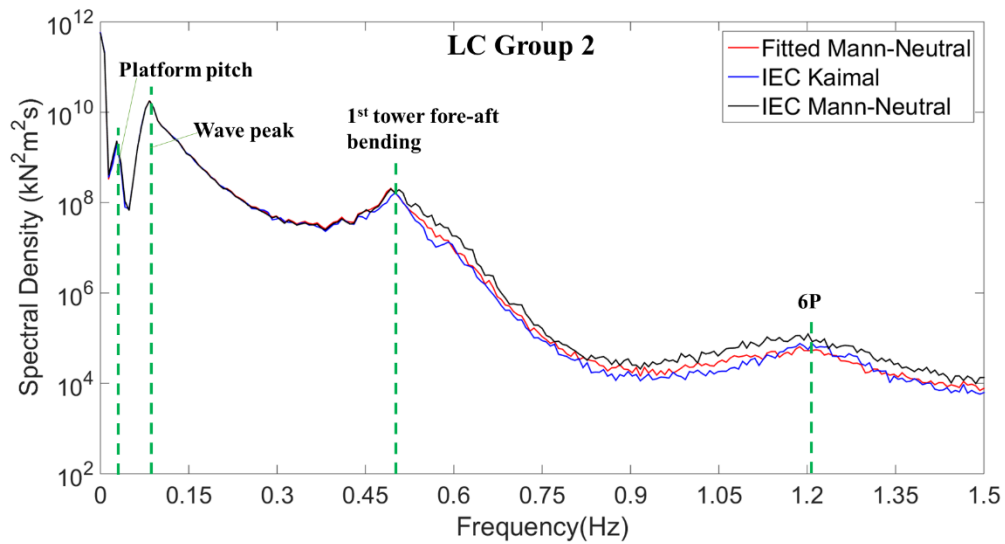
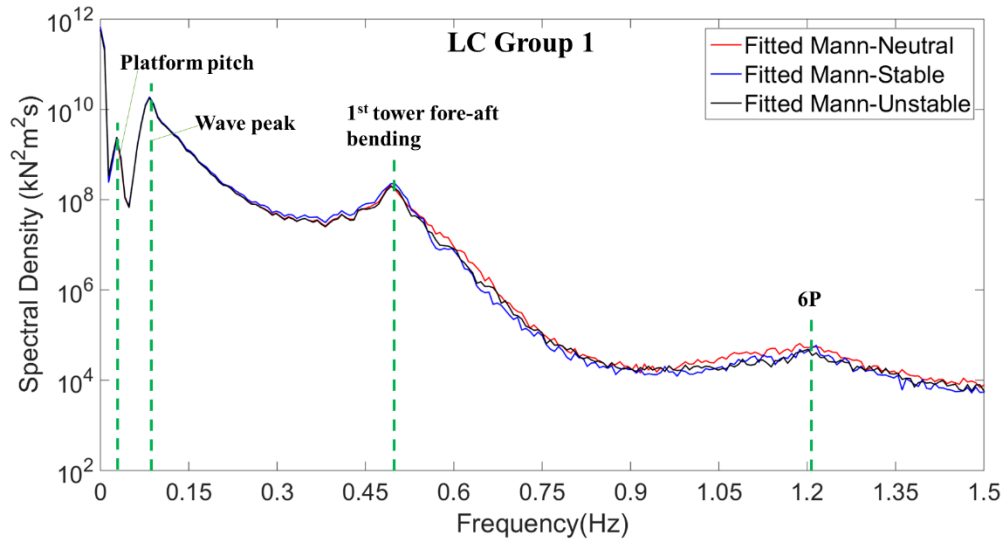


Figure 4.14 The tower base fore-aft moment spectral densities at rated (11.4m/s) wind speed.

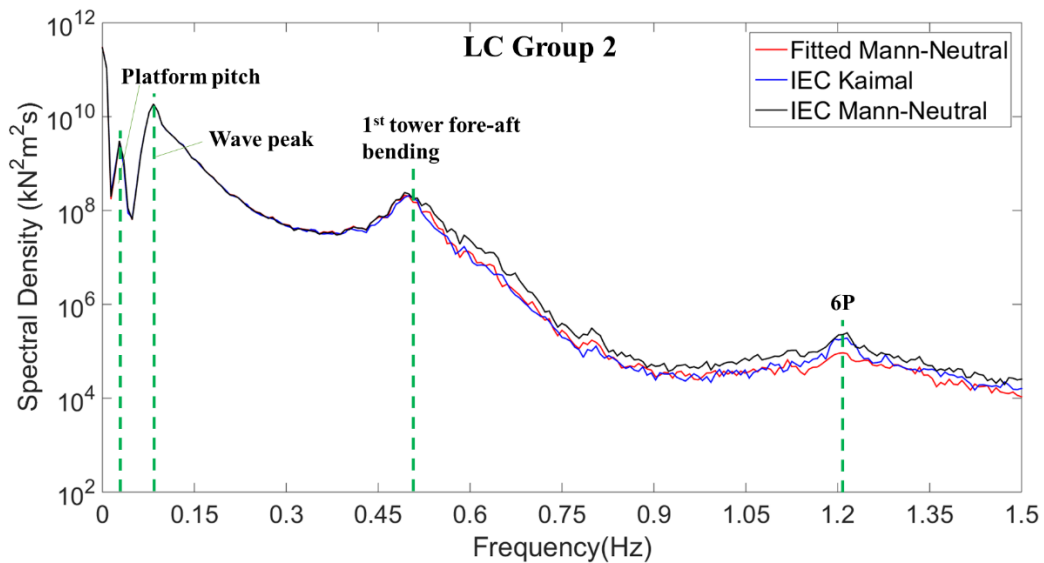


Figure 4.15 The tower base fore-aft moment spectral densities at above rated (15m/s) wind speed.

4.3.3.2. Tower Top Yaw Moment

Figure 4.16 to Figure 4.18 present the tower top yaw moment spectral densities at below rated, rated, and above rated wind speed respectively. The differences between each turbulence load case is more significant for the tower top yaw and it is following the tendency of the generated turbulence intensity σ_u . The highest energy is observed in the cases with the highest generated σ_u (Table 4.9) that is the fitted-Mann neutral condition for LC Group 1 and the IEC-Mann for LC Group 2. Comparing LC Group 1 and 2, the overall highest energy content comes from the IEC-Mann.

There is an increase in the energy content as the wind speed increases especially from below rated (Figure 4.16) to the rated wind speed (Figure 4.17). For all wind speed cases, the main excitations are observed at the frequencies of the wave spectral peak, 3P, and 6P; except at above rated wind speed (Figure 4.18) where there is additional energy content at lower frequencies than the wave spectral peak. The excitations from the rotational frequencies (3P and 6P) for the tower top yaw were also observed for a fixed-monopile 10MW OWT from the study by Eliassen (2016). Overall, the wave spectral peak gives the highest excitation of the tower top yaw for all load cases.

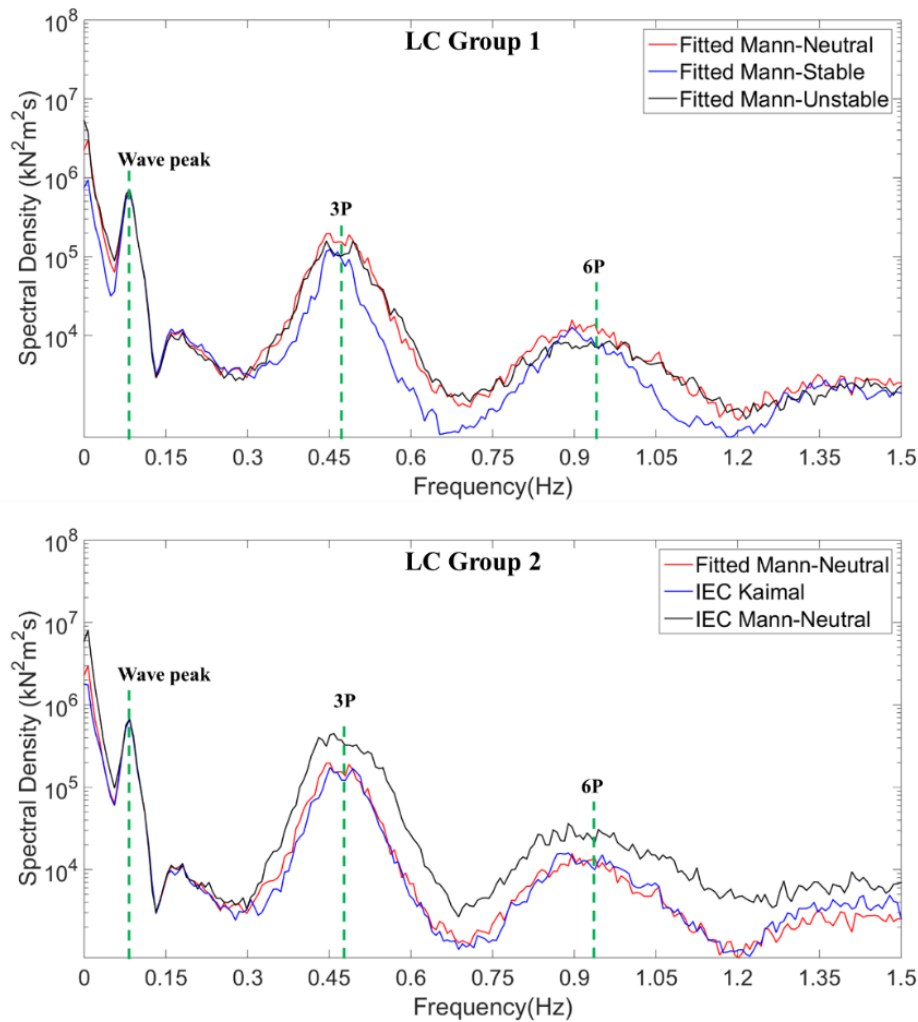


Figure 4.16 The tower top yaw moment spectral densities at below rated (8m/s) wind speed.

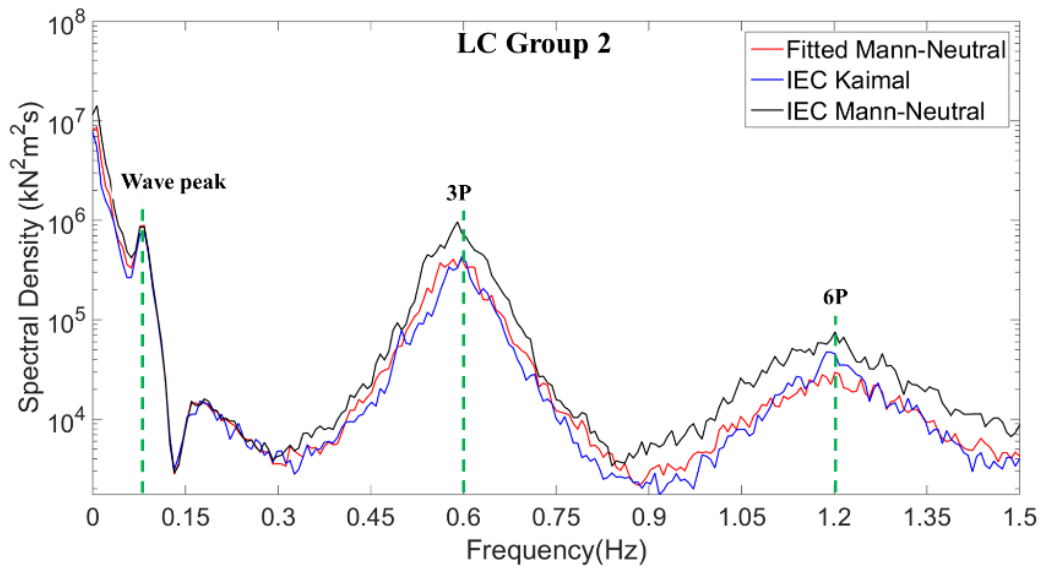
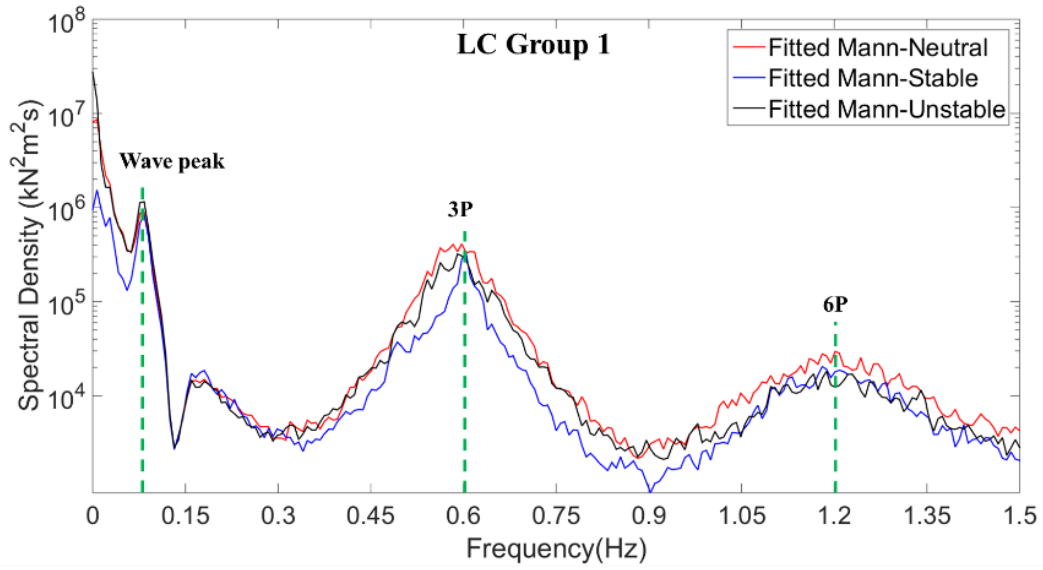


Figure 4.17 The tower top yaw moment spectral densities at rated (11.4m/s) wind speed.

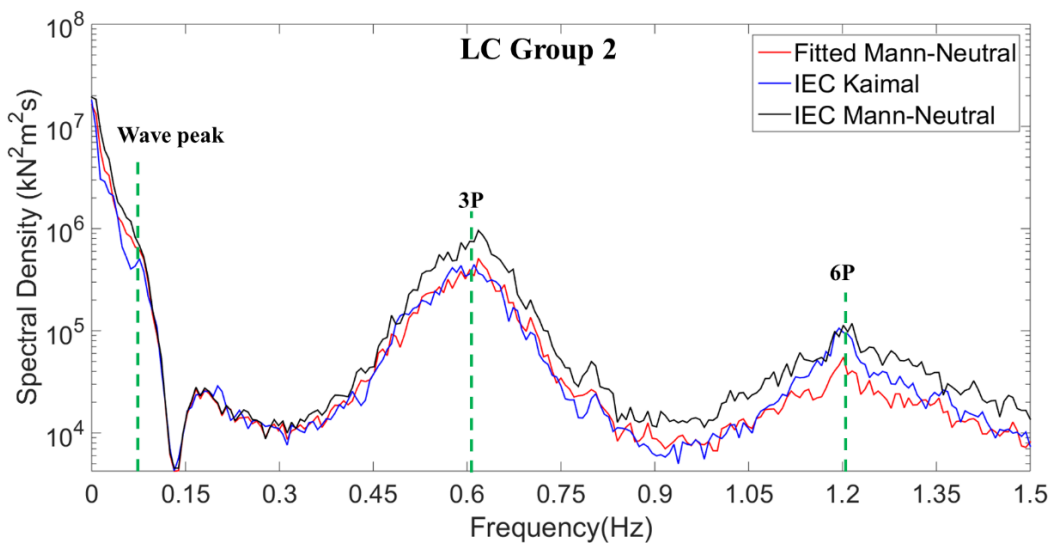


Figure 4.18 The tower top yaw moment spectral densities at above rated (15m/s) wind speed.

4.3.3.3. Blade Root Flap-Wise Moment

The spectral densities for the blade root flap-wise moment at below rated, rated, and above rated wind speed are shown in the **Figure 4.19** to **Figure 4.21** respectively. In general, the main excitations for the blade root flap-wise bending moment are the wave spectral peak, 1P, 2P, and 3P rotational frequencies. The 4P frequency is observed at below rated wind speed; however, at the rated wind speed (**Figure 4.20**) and above (**Figure 4.21**), this frequency starts to vanish while the platform pitch excitation is increasing. The wave provide the highest excitation of the blade root flap-wise mode for all load cases.

A noticeable increment in the energy contents for the blade root flap-wise moment (particularly at the rotational frequencies) is observed as the wind speed increases, especially from below rated (**Figure 4.19**) to the rated wind speed. Nonetheless, at above rated wind speed these peak values are began to decrease. For rated and above rated wind speeds, additional excitation at the platform pitch frequency is observed which most likely due to the influence of the blade-pitch controller activity. The differences between each turbulence cases is slightly visible in LC Group 1 where the highest energy content is seen from the fitted-Mann neutral case. For LC Group 2, the IEC-Mann gives the highest energy content, following the tendency of the generated σ_u values (**Table 4.9**). Comparing LC Group 1 and 2, overall the IEC-Mann yields in the highest energy content.

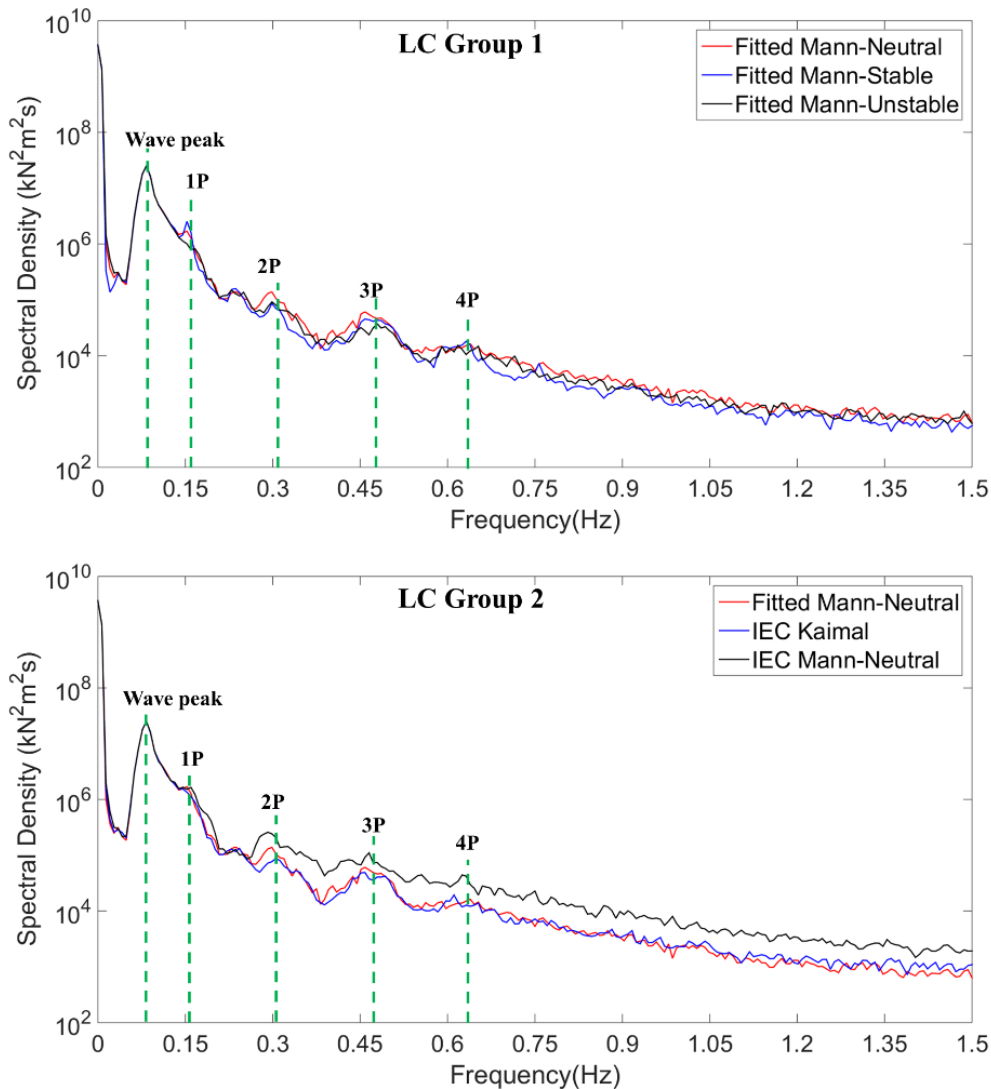


Figure 4.19 The blade root flap-wise moment spectral densities at below rated (8m/s) wind speed.

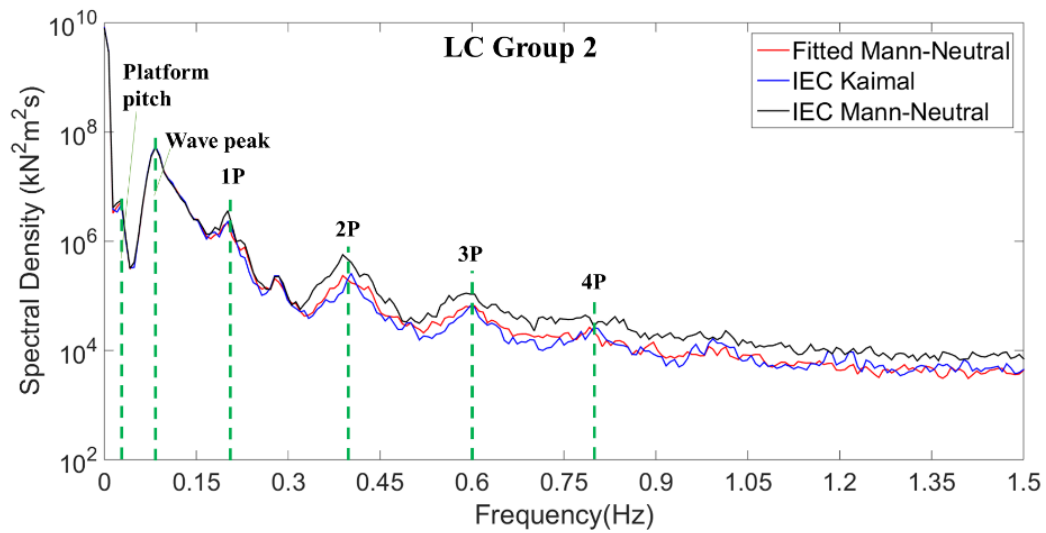
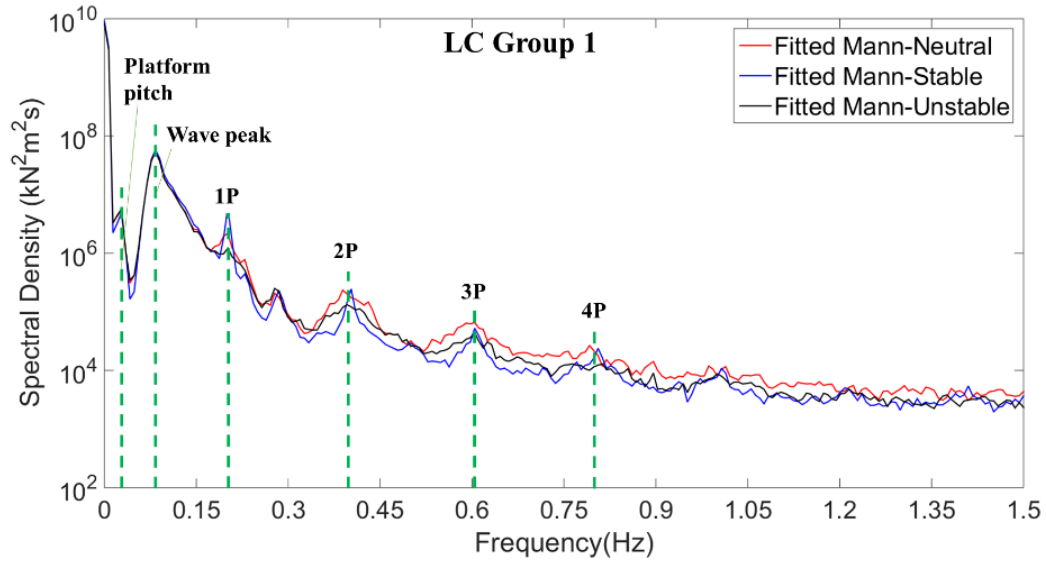


Figure 4.20 The blade root flap-wise moment spectral densities at rated (11.4m/s) wind speed.

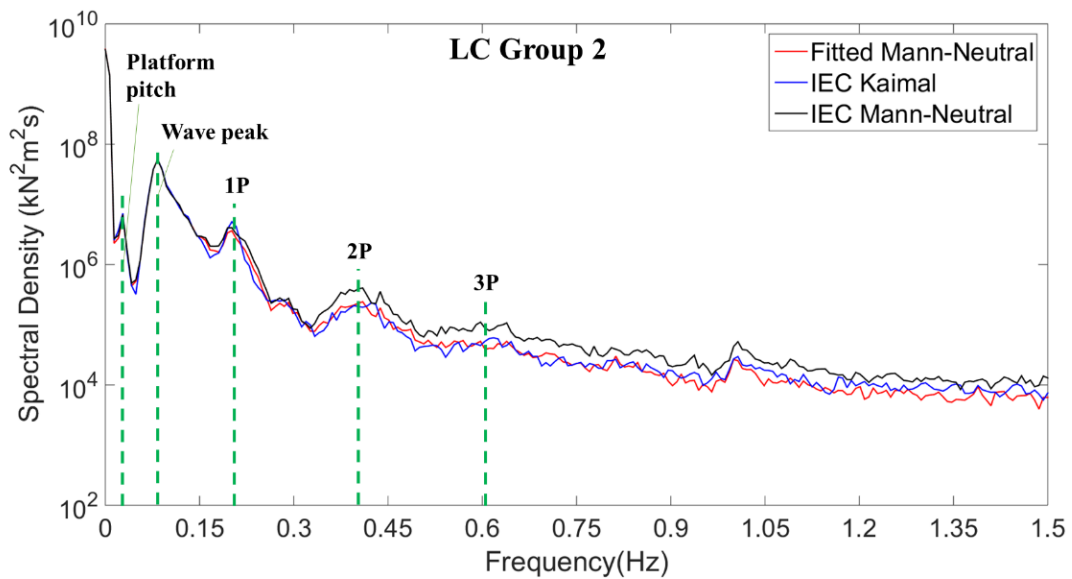


Figure 4.21 The blade root flap-wise moment spectral densities at above rated (15m/s) wind speed.

4.3.3.4. Platform Pitch

For platform pitch rotation, the spectral density plots are given in *Figure 4.22* to *Figure 4.24* for below rated, rated, and above rated wind speeds respectively. It is seen that the energy content for the platform pitch rotation is not appear to be affected by the different load cases as very little differences are observed (*Figure 4.22* to *Figure 4.24*). The main excitations for the platform pitch rotation are the platform pitch rotation itself, wave spectral peak, and the 1st tower fore-aft bending. The wind speed increment enhances the platform pitch rotation energy, in particular at the platform pitch rotation frequency, where the highest energy content is observed for rated and above rated wind speed. At below rated wind speed, the wave spectral peak induces the highest excitation amongst all other governing excitations.

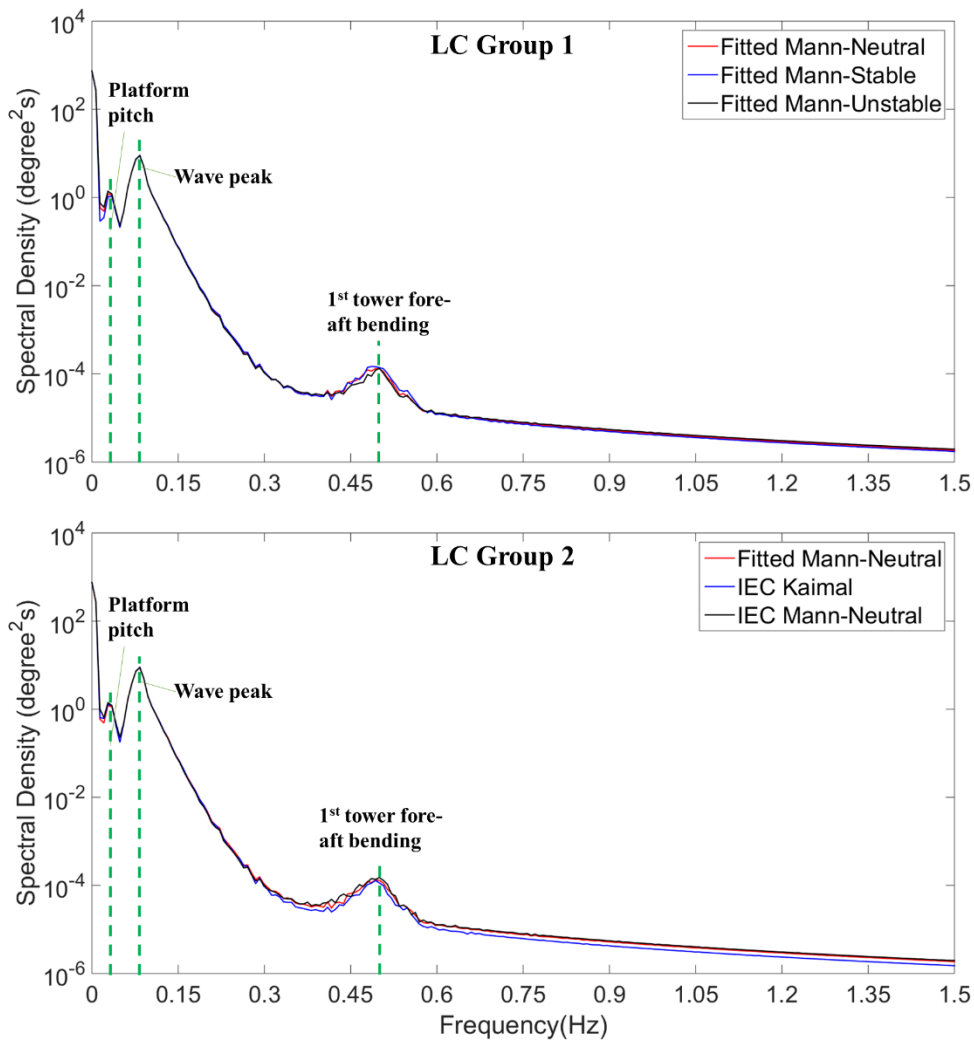


Figure 4.22 The platform pitch rotation spectral densities at below rated (8m/s) wind speed.

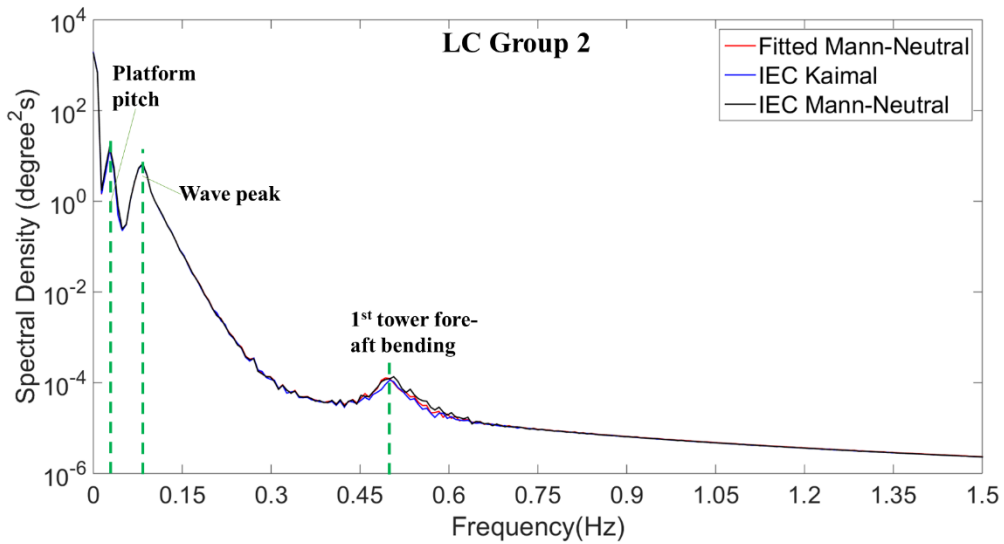
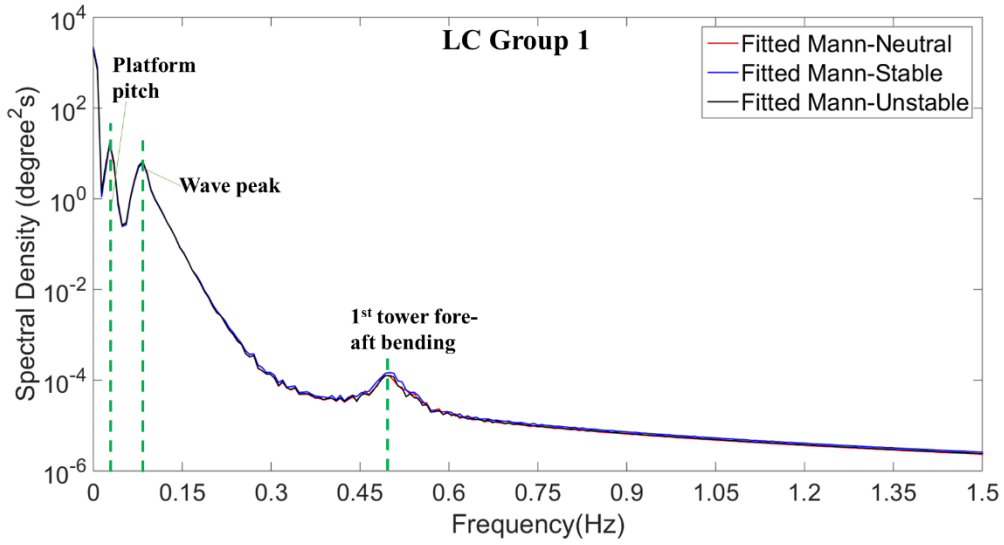


Figure 4.23 The platform pitch rotation spectral densities at rated (11.4m/s) wind speed.

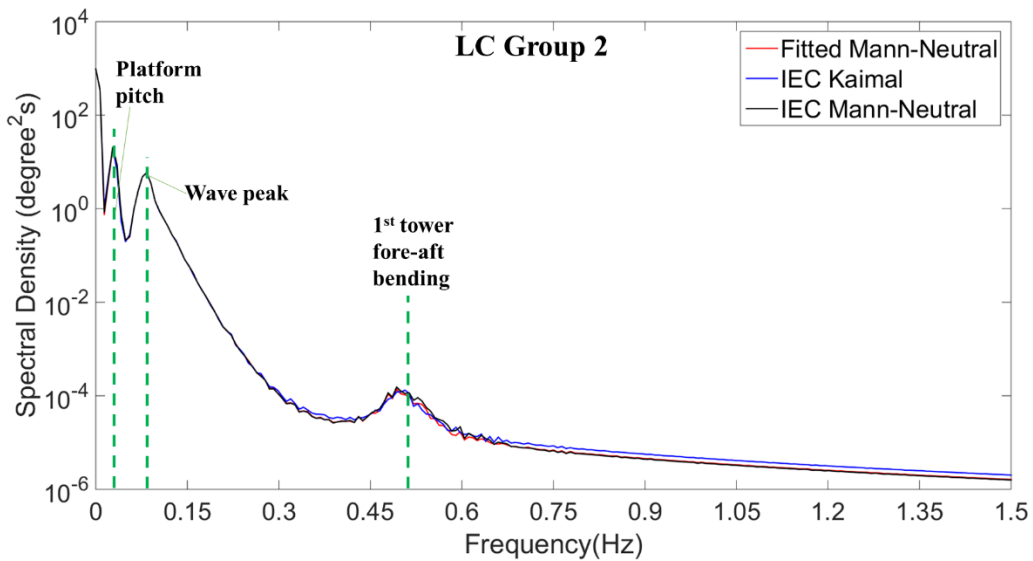


Figure 4.24 The platform pitch rotation spectral densities at above rated (15m/s) wind speed.

4.3.3.5. Platform Yaw

Figure 4.25 to Figure 4.27 show the platform yaw rotation spectral densities for below rated, rated, and above rated wind speeds respectively. The primary excitations for the platform yaw rotation are the wave spectral peak, 3P and 6P frequencies, where the induced energy from the wave spectral peak is the highest. The tendency of the platform yaw rotation energy density follows the generated values of σ_u (Table 4.9) which is observed for all wind speed cases, where the highest energy in LC Group 1 is from the fitted-Mann neutral and the IEC-Mann for LC Group 2, each has the highest σ_u . The differences between the load cases are apparent for both LC Groups, which the IEC-Mann generates the highest energy content. The platform yaw energy content is increasing as the wind speed increases, notably for the lower frequencies as the wind speed goes from rated (Figure 4.26) to above rated wind speed (Figure 4.27).

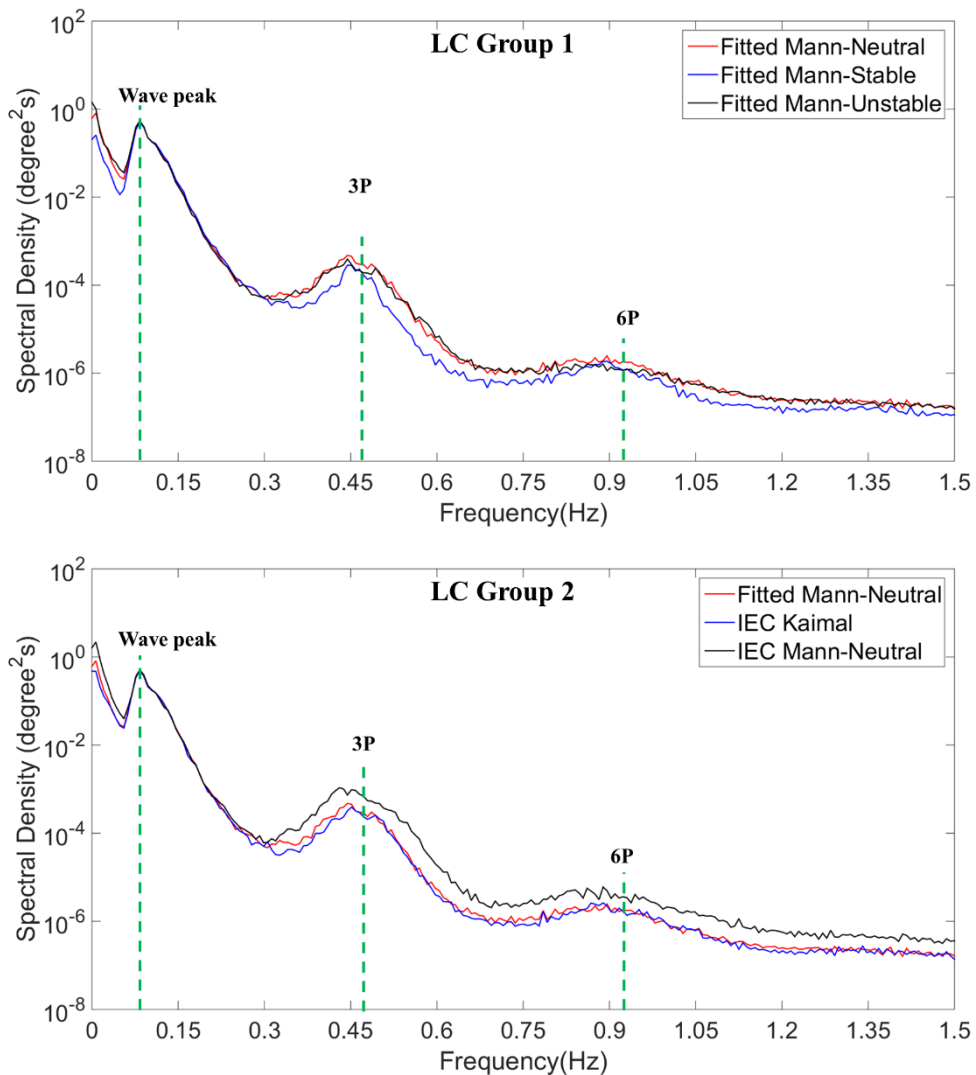


Figure 4.25 The platform yaw rotation spectral densities at below rated (8m/s) wind speed.

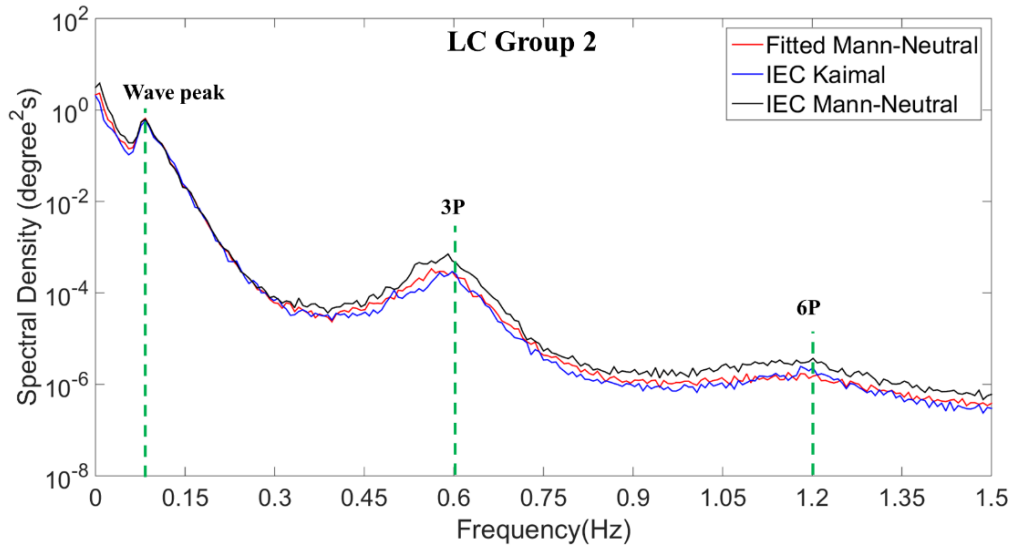
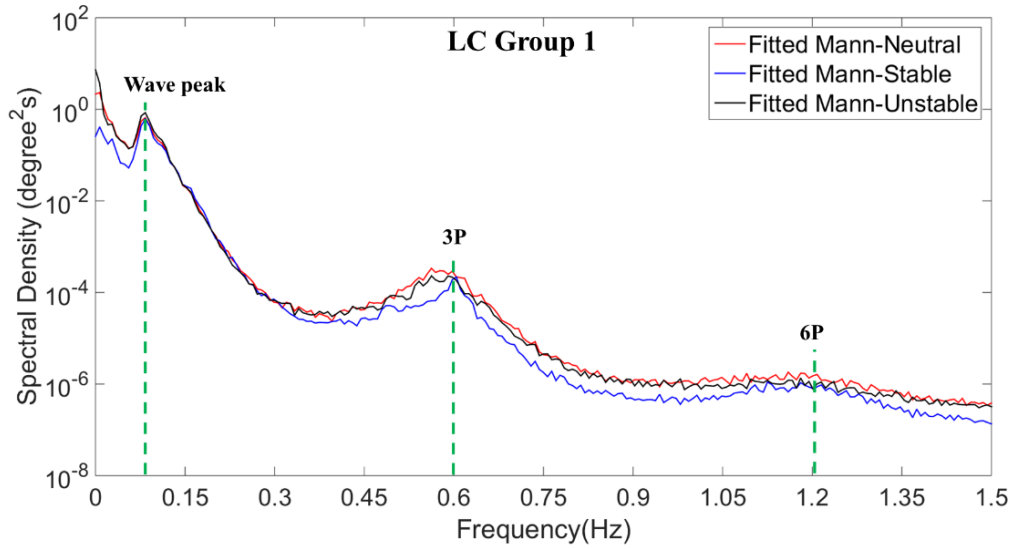


Figure 4.26 The platform yaw rotation spectral densities at rated (11.4m/s) wind speed.

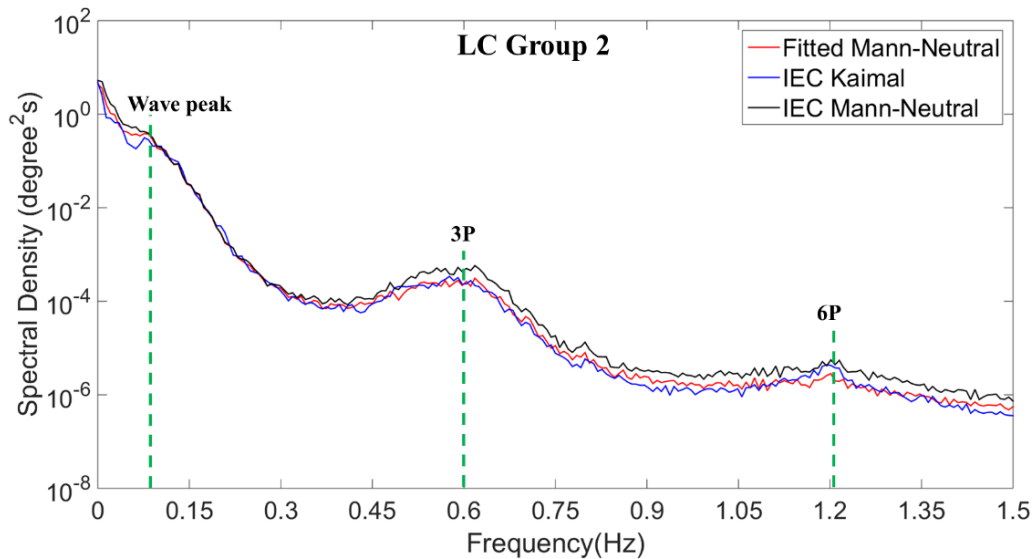


Figure 4.27 The platform yaw rotation spectral densities at above rated (15m/s) wind speed.

4.3.3.6. Mooring Forces (Tensions)

Figure 4.28 and Figure 4.29 show the mooring tension spectral densities for line 1 at below rated and rated wind speed respectively, whereas Figure 4.30 and Figure 4.31 relate to line 2. The spectral densities for mooring line 3 as well as for mooring line 1 and 2 at above rated wind speed are attached in the Appendix C. Figure 4.28 to Figure 4.31 show that the only primary excitation of the mooring lines tensions is the wave spectral peak. The generated mooring tension spectral density for line 1 and line 2 for different turbulence cases have very close values. Moreover, the increase in the wind speed does not affect the mooring tension energy content. Further explanation for the mooring lines tensions is discussed in Chapter 5.

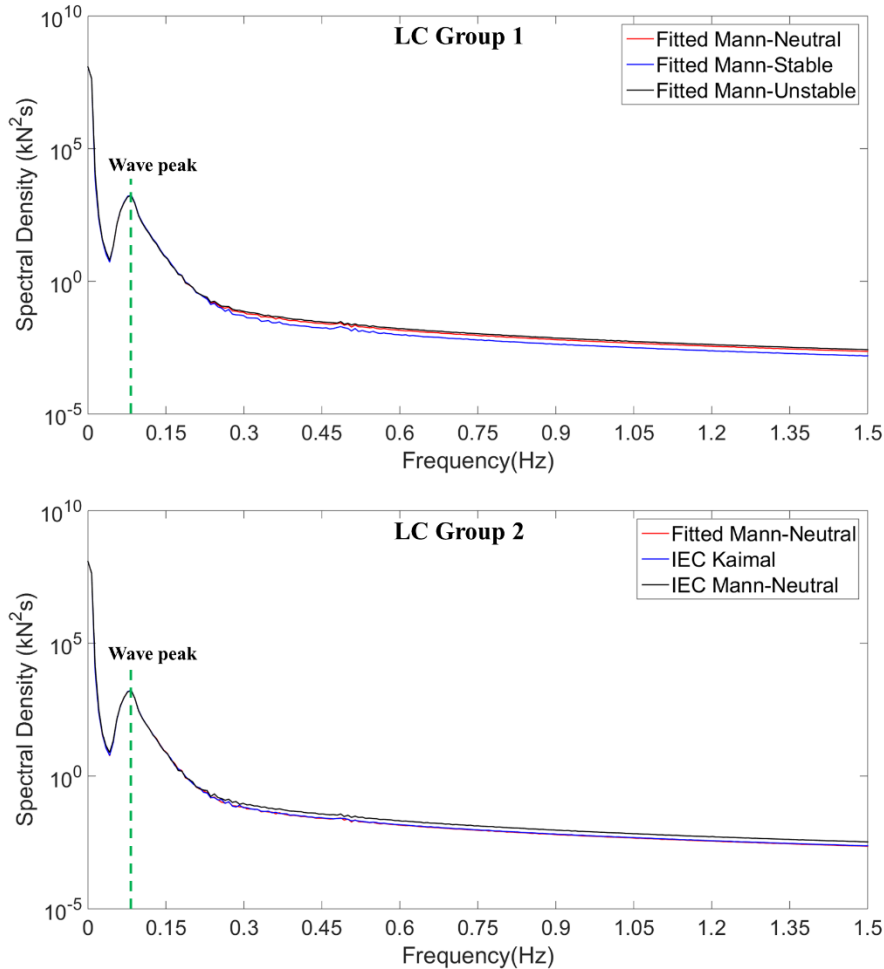


Figure 4.28 Mooring line 1 tension spectral densities at below rated (8m/s) wind speed.

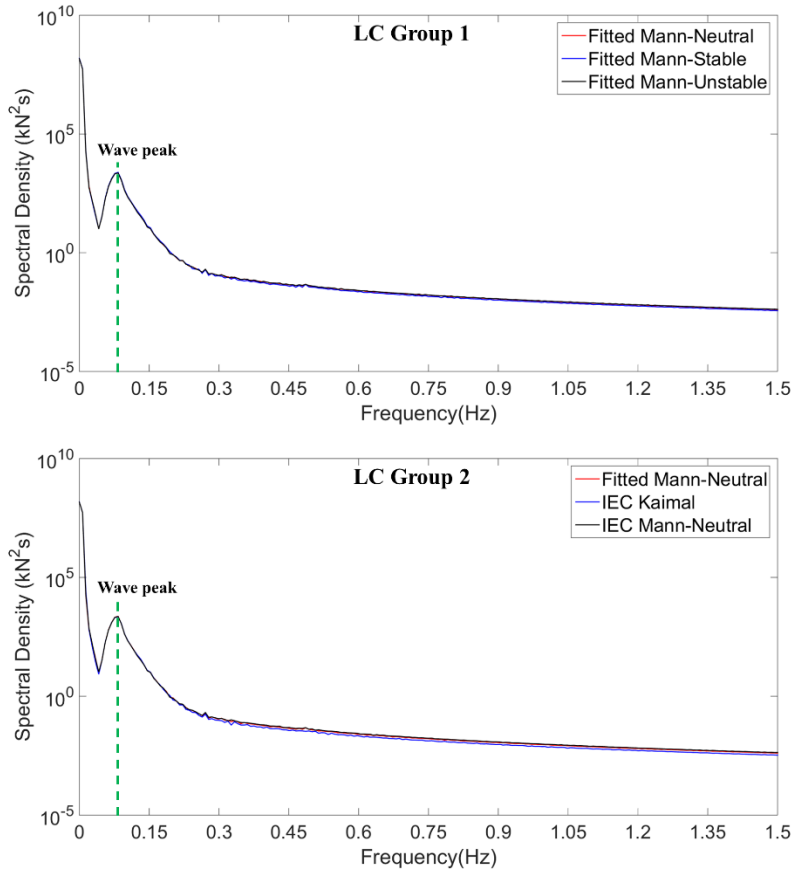


Figure 4.29 Mooring line 1 tension spectral densities at rated (11.4m/s) wind speed.

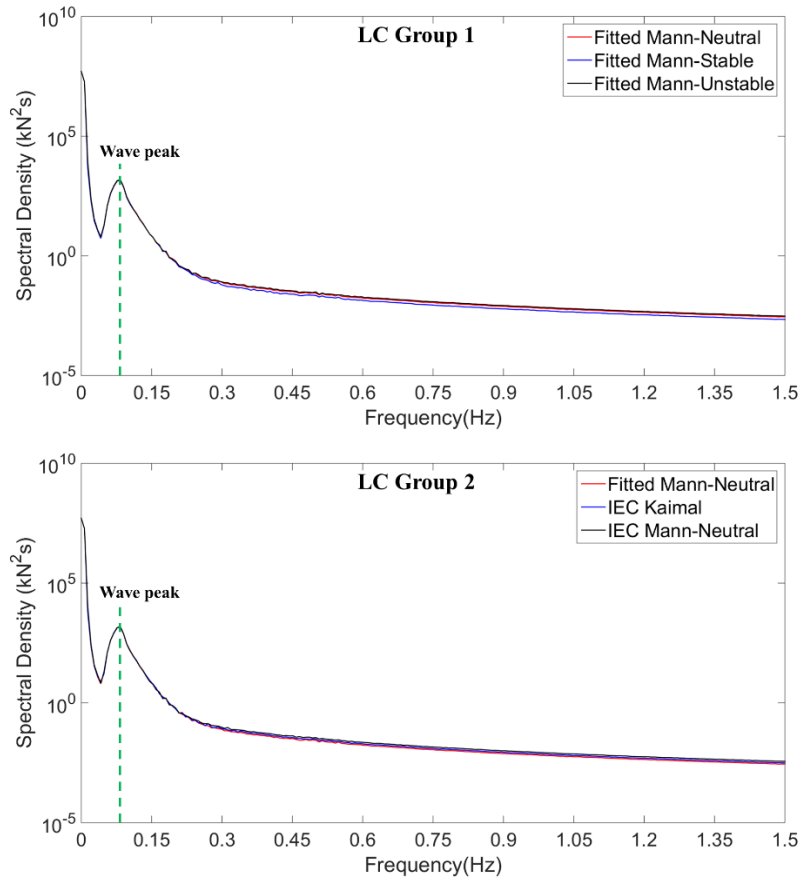


Figure 4.30 Mooring line 2 tension spectral densities at below rated (8m/s) wind speed.

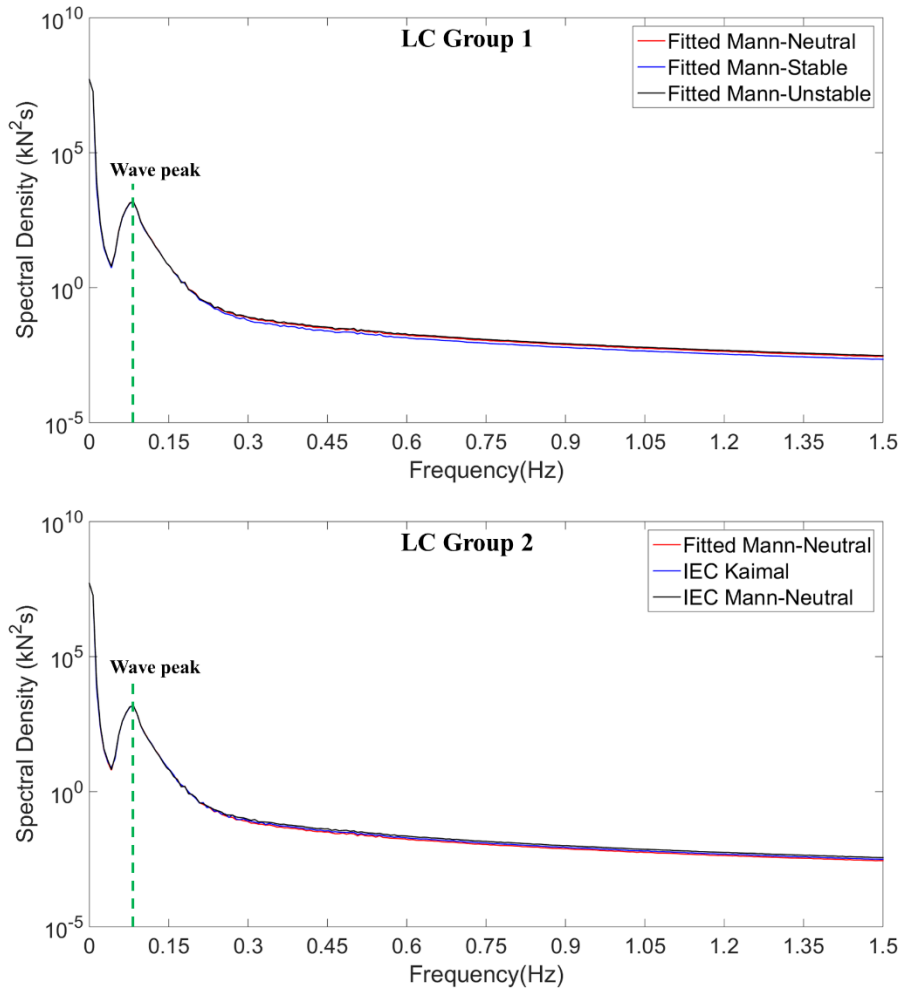


Figure 4.31 Mooring line 2 tension spectral densities at rated (11.4m/s) wind speed.

4.3.4. Fatigue Damage Equivalent Load

The fatigue damage analysis is carried out to observe the accumulated damage caused by repetitive (cyclic) loadings on the wind turbine. This is one way to measure the effects of turbulent loadings on the spar-buoy wind turbine loadings.

4.3.4.1. Rainflow Counting Method – Miner Summation Rule

In order to compute the accumulated equivalent fatigue loads, the Miner’s Rule is used with the rainflow counting method to specify the load ranges and the corresponding number of cycles (stress range histogram). Despite many methods of stress ranges filter available, the rainflow counting method is often chosen since the method predicts the most reliable result of the accumulated fatigue prediction under irregular loading (Lalanne, 2010). The rainflow counting implies conversion of the load time series into bins of load ranges occurrences by ‘imagining’ a raindrop flow over the load time series. This is done by ‘rotating’ the axes of load time series (*Figure 4.32 (a)*) so that the vertical axis represents the time while the horizontal axis represents the loads as illustrated in *Figure 4.32 (b)*. The horizontal distance travelled by each ‘raindrop’ from the starting point to the stopping point will be a *half-cycle having a constant amplitude* (Lalanne, 2010); for instance as shown in *Figure 4.32 (b)*, the indicated ‘horizontal distance’ belongs to the rainflow from point 1 to 8.

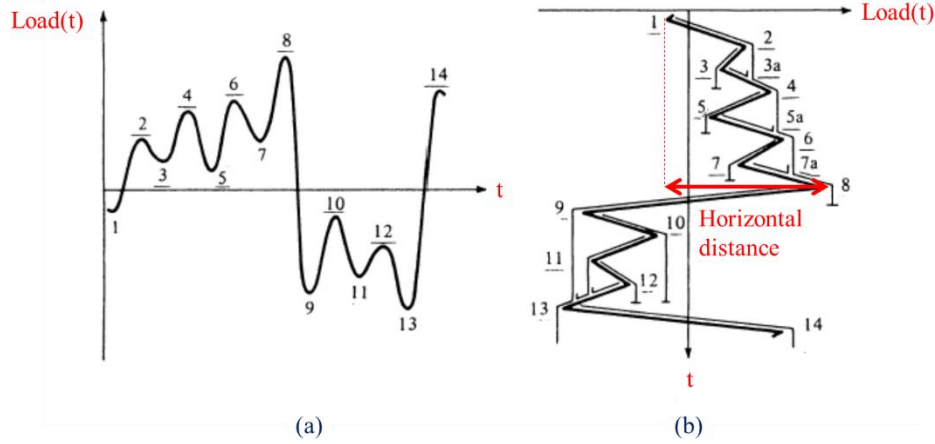


Figure 4.32 Rainflow counting method (DTU, with modification, accessed 2016).

After the number of cycles for each stress level (σ) are acquired, the stress range histogram is processed to determine the occurring damage by applying the Miner’s Summation Rule, within the assumption that the stress σ is a sinusoidal function (Lalanne, 2010):

$$d = \frac{n}{N} \tag{4.3}$$

where

d : damage

n : number of cycle occurrences for the considered stress level σ (from the computed stress range histogram)

N : total number of cycles to cause failure at the considered stress level σ , which is determined from the experimentally defined S-N (stress – number of cycles curve)

In the absence of the S-N curve, the number of cycles resulting in failure (N) can be quantified using a log-log relation. Instead of looking at a specific stress level σ , a stress range (classed into n_{bin} number of bins) is considered so the total number of cycles N_i to cause failure at a specific stress range σ_i can be determined using the following formula (DTU, accessed 2016):

$$N_i = \left(\frac{\sigma_0}{\sigma_i}\right)^m \tag{4.4}$$

where

σ_0 : the largest stress in the time series

σ_i : the considered stress range class

m : damage exponent or Wöhler exponent (Table 4.12)

Table 4.12 Fatigue Damage Wöhler Exponent

m	Material
3	Steel
3	Aluminium
3.3	Nickel
5	Titanium
12	Fiberglass

Note that the term ‘stress’ considered in the equation (4.4) is applicable for other type of loadings such as force or bending moment. To make an easier interpretation of the accumulated loads, normally a quantified equivalent damage for a given number of cycle n_{eq} is considered. The total damage is computed as (DTU, accessed 2016):

$$D_{total} = n_{eq} \frac{S_{eq}^m}{S_0^m} \quad (4.5)$$

where

n_{eq} : equivalent number of cycles

S_0 : the largest load in the time series

S_{eq} : damage equivalent load

m : damage exponent or Wöhler exponent

The damage equivalent load S_{eq} is then computed by rearranging equation (4.5) (DTU, accessed 2016):

$$S_{eq} = \left(\frac{\sum n_i S_i^m}{n_{eq}} \right)^{1/m} \quad (4.6)$$

where

n_i : number of cycle occurrences for the considered load range class (from the computed load range histogram)

n_{eq} : equivalent number of cycles

S_i : the considered load range class

S_{eq} : damage equivalent load

m : damage exponent or Wöhler exponent

The physical interpretation of the damage equivalent load (4.6) is as illustrated in **Figure 4.33** that is the conversion of a load time series with variable load amplitudes into a sinusoidal load time series with a constant amplitude, S_{eq} .

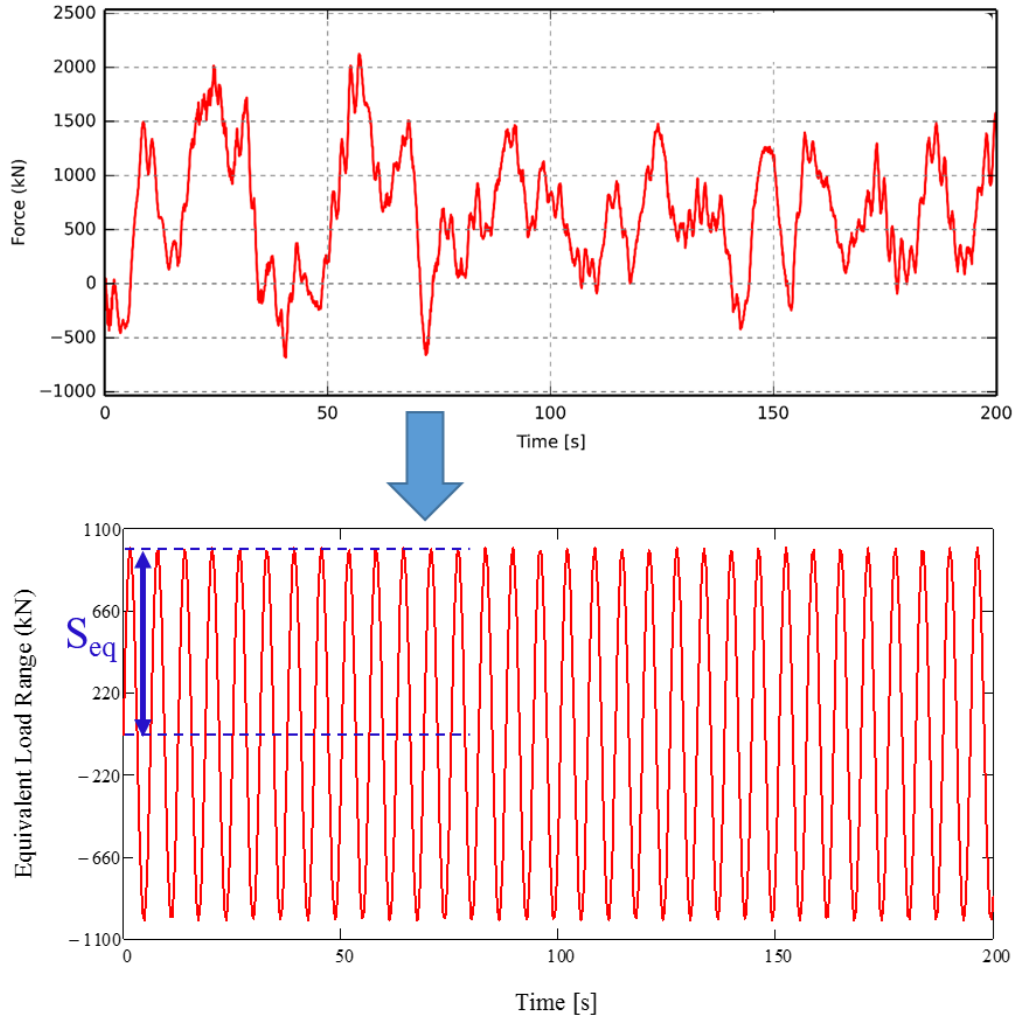


Figure 4.33 Damage equivalent load (lower graph) from a given load time series (upper graph).

4.3.4.2. Damage Equivalent Load – Results

The damage equivalent load analysis is performed for the tower base fore-aft moment, tower top yaw moment, blade root flap-wise bending moment, as well as blade root edge-wise bending moment. The calculated damage equivalent loads assumed the wind turbine will operate for 20 years (175200 hours) and correspond to number of cycles $n_{eq}=10^7$ where the selection is based on the physical meaning that $n_{eq}=10^7$ is near the fatigue limit for typical steel material types (Lalanne, 2010). The Wöhler exponent was taken as $m=3$ for both the tower and tower top which were made from steel, whereas $m=12$ was taken for the blades which are made from fiberglass (Sathe et al., 2013). The number of bins selected for the rainflow counting analysis is $N_{bin}=46$ as recommended in the HAWC2 manual.

Table 4.13 to **Table 4.20** present the calculated result for the damage equivalent loads of the tower base fore-aft moment, tower top yaw moment as well as blade root flap-wise and edge-wise bending moments respectively, for each of the LC groups. **Figure 4.34** to **Figure 4.37** show the normalised damage equivalent loads relative to the fitted-Mann neutral conditions, where the dots at each wind speed cases represent the six simulation seeds.

Table 4.13 Tower Base Fore-Aft Moment Damage Equivalent Loads (10^7 cycles) for LC Group 1

No.	Below Rated (8m/s)			Rated (11.4m/s)		
	Neutral (kNm)	Stable (kNm)	Unstable (kNm)	Neutral (kNm)	Stable (kNm)	Unstable (kNm)
1	151747.1	147044.8	151403.4	165105.3	160136.4	164655.2
2	153445.5	148549.4	151213.9	165518	159779.4	163130
3	151938.4	148429.4	151461	163867.7	159245.5	162575.5
4	154785.7	148340.3	152341.7	165643.8	159085	162409.6
5	153109.7	147622	151642.1	162954.4	158117.9	161606.7
6	152987.5	148540	151222.2	165163.9	159596.8	163342.8

Table 4.14 Tower Top Yaw Moment Damage Equivalent Loads (10^7 cycles) for LC Group 1

No.	Below Rated (8m/s)			Rated (11.4m/s)		
	Neutral (kNm)	Stable (kNm)	Unstable (kNm)	Neutral (kNm)	Stable (kNm)	Unstable (kNm)
1	4301.602	3154.603	4068.603	7565.969	5202.38	6396.166
2	4318.488	3183.511	4017.529	7600.623	5246.12	6336.443
3	4270.228	3169.628	4011.226	7530.963	5237.001	6354.26
4	4385.957	3167.115	4099.887	7523.343	5169.924	6320.218
5	4368.92	3146.362	4132.295	7604.829	5161.051	6407.35
6	4461.879	3197.126	4191.599	7795.591	5262.875	6545.056

Table 4.15 Blade Root Flap-Wise Moment Damage Equivalent Loads (10^7 cycles) for LC Group 1

No.	Below Rated (8m/s)			Rated (11.4m/s)		
	Neutral (kNm)	Stable (kNm)	Unstable (kNm)	Neutral (kNm)	Stable (kNm)	Unstable (kNm)
1	7249.426	6649.923	7533.821	10595.51	10173.62	10177.86
2	7582.853	6708.968	7850.226	10045.14	10027.55	9887.755
3	7447.003	6679.299	7925.017	9930.177	9935.936	9843.181
4	7393.058	6625.974	7850.228	10326.83	10177.33	10011.87
5	7365.338	6589.574	7556.975	10449.42	10023.3	10121.61
6	7661.84	6724.131	8131.603	10500.43	10163.99	10388.33

Table 4.16 Blade Root Edge-Wise Moment Damage Equivalent Loads (10^7 cycles) for LC Group 1

No.	Below Rated (8m/s)			Rated (11.4m/s)		
	Neutral (kNm)	Stable (kNm)	Unstable (kNm)	Neutral (kNm)	Stable (kNm)	Unstable (kNm)
1	8863.884	8854.003	8820.711	9435.243	9293.773	9234.127
2	8873.822	8859.978	8808.522	9436.712	9303.260	9221.393
3	8835.714	8835.301	8777.89	9336.509	9289.699	9164.502
4	8900.897	8853.526	8849.641	9437.043	9309.774	9244.948
5	8852.453	8846.754	8807.431	9417.017	9313.613	9216.066
6	8893.149	8844.972	8830.652	9403.234	9287.111	9216.472

Table 4.17 Tower Base Fore-Aft Moment Damage Equivalent Loads (10^7 cycles) for LC Group 2

No.	Below Rated (8m/s)			Rated (11.4m/s)			Above Rated (15m/s)		
	Fitted-Neutral (kNm)	IEC Kaimal (kNm)	IEC Mann (kNm)	Fitted-Neutral (kNm)	IEC Kaimal (kNm)	IEC Mann (kNm)	Fitted-Neutral (kNm)	IEC Kaimal (kNm)	IEC Mann (kNm)
1	151747.1	151671.1	166895	165105.3	161901.2	171923.2	171030.7	172511.8	179010.4
2	153445.5	151433.5	165232.5	165518	164253.5	175234.8	170799.5	170807	184553.2
3	151938.4	152250.2	161450.3	163867.7	163202.8	170779.1	172111.2	174509.2	180189.4
4	154785.7	152421.9	167453.9	165643.8	163749.8	174256.1	170664	170639.3	179209.7
5	153109.7	153061.9	165180.3	162954.4	163701.1	172416	171939.2	172037.2	180011.8
6	152987.5	152906.2	163478.8	165163.9	163769.7	173657.8	173058.5	172247.1	182215.4

Table 4.18 Tower Top Yaw Moment Damage Equivalent Loads (10^7 cycles) for LC Group 2

No.	Below Rated (8m/s)			Rated (11.4m/s)			Above Rated (15m/s)		
	Fitted-Neutral (kNm)	IEC Kaimal (kNm)	IEC Mann (kNm)	Fitted-Neutral (kNm)	IEC Kaimal (kNm)	IEC Mann (kNm)	Fitted-Neutral (kNm)	IEC Kaimal (kNm)	IEC Mann (kNm)
1	4301.602	4400.087	6984.588	7565.969	7393.755	10332.48	9243.893	9545.803	12273.49
2	4318.489	4267.445	6962.925	7600.623	7217.048	10360.607	9174.435	9278.719	12177.84
3	4270.228	4323.552	6847.025	7530.963	7146.389	10239.09	9103.317	9343.159	12036.94
4	4385.957	4226.283	7132.831	7523.343	7095.383	10244.98	9153.451	9208.166	12095.44
5	4368.92	4318.813	6984.009	7604.829	7323.218	10209.17	9242.348	9473.468	12137.48
6	4461.879	4319.763	7271.549	7795.591	7239.618	10597.14	9475.29	9485.655	12569.66

Table 4.19 Blade Root Flap-Wise Moment Damage Equivalent Loads (10^7 cycles) for LC Group 2

No.	Below Rated (8m/s)			Rated (11.4m/s)			Above Rated (15m/s)		
	Fitted-Neutral (kNm)	IEC Kaimal (kNm)	IEC Mann (kNm)	Fitted-Neutral (kNm)	IEC Kaimal (kNm)	IEC Mann (kNm)	Fitted-Neutral (kNm)	IEC Kaimal (kNm)	IEC Mann (kNm)
1	7249.426	7986.164	8706.869	10595.51	10337.22	11266.85	10774.94	10996.88	11696.1
2	7582.853	7299.257	8352.714	10045.14	10460.74	10860.81	11265.7	10643.94	12039.15
3	7447.003	7713.484	8696.773	9930.177	10398.48	10552.34	11598.44	11229.53	12397.93
4	7393.058	7688.824	8779.207	10326.83	10385.96	11349.7	11327.26	10648.25	12511.59
5	7365.338	7252.448	8365.911	10449.42	10280.06	11186.36	10366.41	10942.84	11432.03
6	7661.84	7788.82	9062.64	10500.43	10486.9	11124.67	11903.75	10841.59	12607.84

Table 4.20 Blade Root Edge-Wise Moment Damage Equivalent Loads (10^7 cycles) for LC Group 2

No.	Below Rated (8m/s)			Rated (11.4m/s)			Above Rated (15m/s)		
	Fitted-Neutral (kNm)	IEC Kaimal (kNm)	IEC Mann (kNm)	Fitted-Neutral (kNm)	IEC Kaimal (kNm)	IEC Mann (kNm)	Fitted-Neutral (kNm)	IEC Kaimal (kNm)	IEC Mann (kNm)
1	8863.884	8894.33	9035.23	9435.243	9367.706	9682.342	9849.211	9797.047	10403.16
2	8873.823	8859.437	9053.339	9436.712	9334.239	9666.438	9838.151	9761.457	10303.93
3	8835.714	8878.686	8986.036	9336.509	9362.8	9551.83	9717.891	9755.161	10176.26
4	8900.897	8873.591	9083.247	9437.043	9355.123	9654.96	9854.443	9704.505	10313.4
5	8852.453	8857.455	9034.621	9417.017	9362.003	9683.458	9815.707	9765.661	10330.17
6	8893.149	8872.922	9077.347	9403.234	9355.517	9633.645	9861	9821.841	10350.04

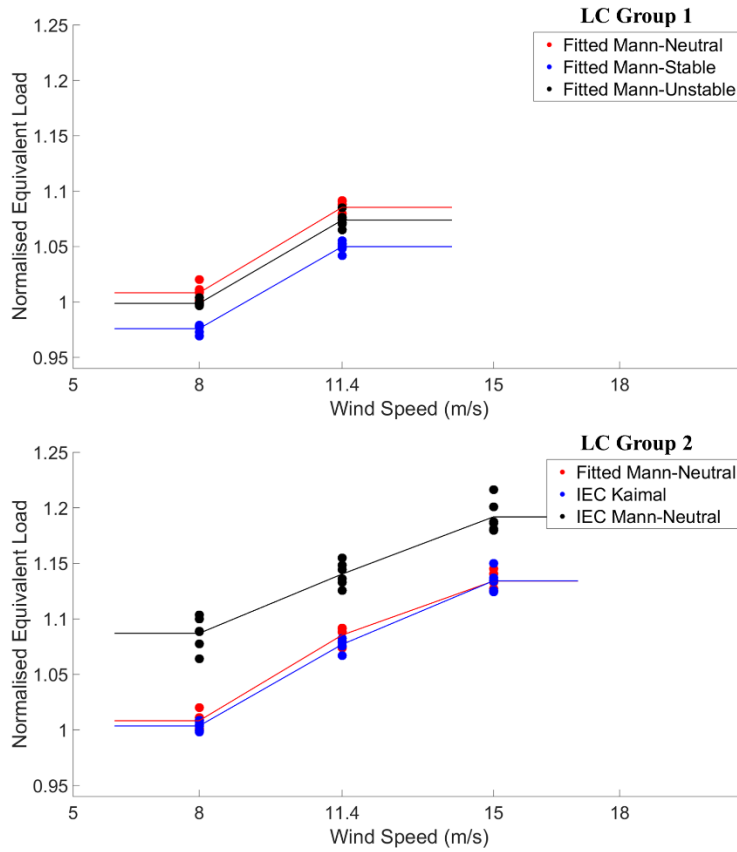


Figure 4.34 Damage equivalent loads for tower base fore-aft moment.

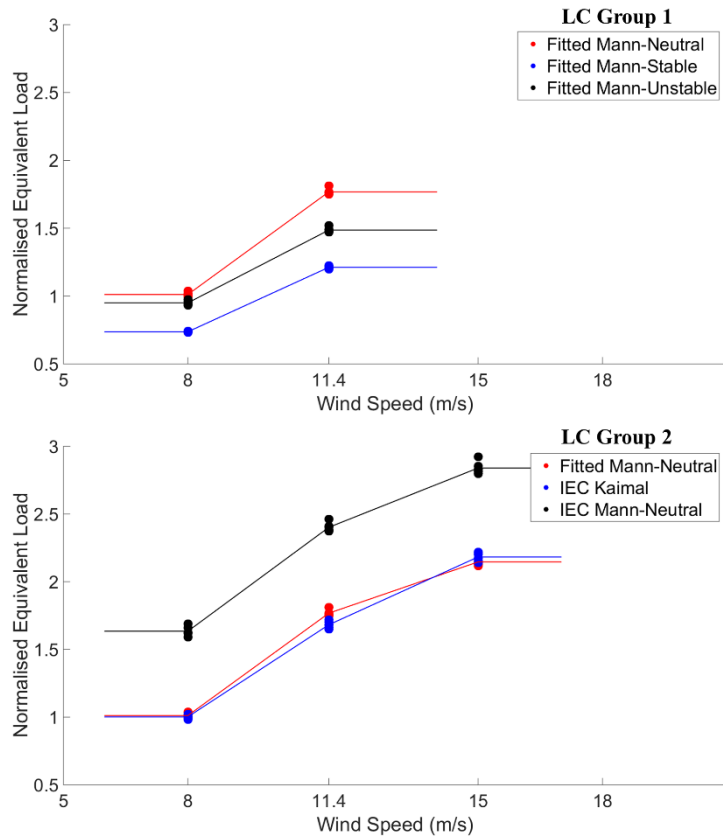


Figure 4.35 Damage equivalent loads for tower top yaw moment.

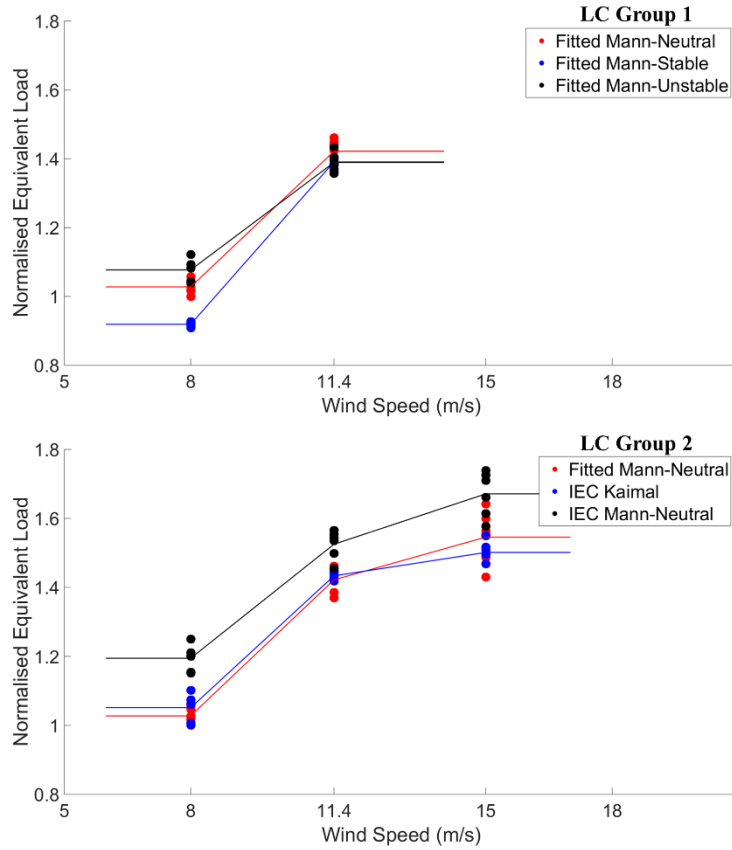


Figure 4.36 Damage equivalent loads for blade root flap-wise moment.

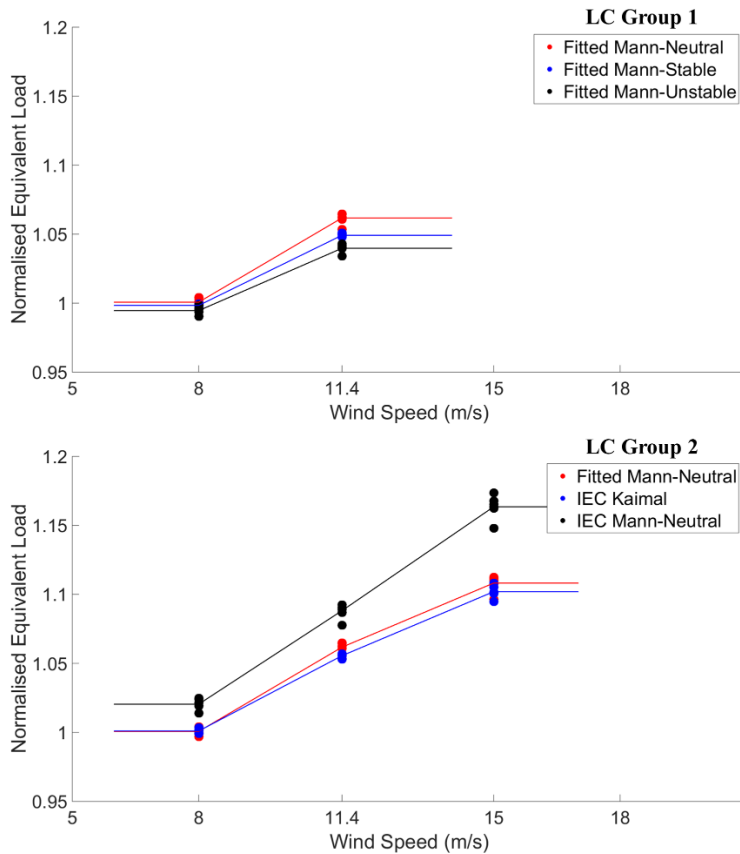


Figure 4.37 Damage equivalent loads for blade root edge-wise moment.

4.3.4.3. Damage Equivalent Load – Result Description

From **Table 4.13** to **Table 4.20**, it is shown that the magnitude of the tower base fore-aft damage equivalent loads are the highest, followed by the blade root flap-wise, edge-wise, and the tower top yaw bending moments. Nonetheless, from **Figure 4.34** to **Figure 4.37**, we see that the tower top yaw damage equivalent loads are the most affected by different turbulence cases followed by the blade root flap-wise, tower base fore-aft and blade root edge-wise damage equivalent loads. In the normalised equivalent load graphs (**Figure 4.34** to **Figure 4.37**), it is observed that the increment of wind speed results in higher damage equivalent loads for all considered moments. In general, there is a trend of the computed accumulated damage equivalent loads to follow the σ_u values (**Table 4.9**), where larger σ_u generates higher accumulated damage equivalent loads. This implies that the fitted-Mann neutral conditions yield in the highest damage equivalent loads for LC Group 1 and the IEC-Mann for LC Group 2.

The tower base fore-aft moment (**Figure 4.34**) has the highest damage equivalent loads obtained from the IEC-Mann (comparing both LC Groups), also corresponds to the highest σ_u values for all wind speed cases. In LC Group 1, the fitted-Mann neutral results in the highest damage equivalent loads followed by unstable and stable conditions respectively. From LC Group 2, it is noticed that the IEC-Kaimal and the fitted-Mann neutral result in very similar damage equivalent loads. Overall, the effect of the variation in turbulence for the tower base fore-aft damage equivalent load is rather small with the maximum difference is about 7.5% (considering the same wind speed).

For tower top yaw moment loads (**Figure 4.35**), similar trends with the tower base fore-aft moment are observed, however the differences between the load cases are more significant with maximum differences up to 70% (considering the same wind speed). The highest damage equivalent loads for each wind are obtained from the IEC-Mann, which has the highest σ_u . The fitted-Mann neutral has the highest equivalent loads followed by unstable and stable conditions for LC Group 1, while for LC Group 2, the fitted-Mann neutral generates very close damage equivalent loads with the IEC-Kaimal.

The damage equivalent loads for blade root flap-wise moment (**Figure 4.36**) has the highest values from the IEC-Mann case when comparing both LC Groups for all wind speed cases. This again follows that the parameter σ_u which is the highest for the IEC-Mann. At rated wind speed for both LC Groups, the differences in the equivalent loads are reduced, while at above rated wind speed the differences are increasing. For LC Group 2, the IEC-Kaimal and the fitted-Mann neutral are again giving similar results. The maximum difference between the turbulence load cases is at the level of 18.5% (considering the same wind speed).

Generally, the variation in the turbulent load cases does not significantly affect the blade root edge-wise moment damage equivalent loads (**Figure 4.37**) with a maximum difference of only 6.5% (considering the same wind speed). The main reason for this was due to the prominent effect of the gravity (Sathe et al., 2013) compared to the wind turbulence. The damage equivalent loads from the IEC-Mann are the highest comparing both LC Groups at each wind speeds. For LC Group 2, the IEC-Kaimal and the fitted-Mann neutral are again giving very similar results. Unlike the blade root flap-wise moment loads which show that differences between each load cases are minimised at the rated wind speed, the difference between load cases for blade root edge-wise moment are increasing with wind speed. Another important observation is for LC Group 1, the equivalent damage from the fitted-Mann neutral is the highest, followed by the fitted-Mann stable and unstable, which is not following the order of the generated turbulence level (σ_u).

4.3.5. Motion Responses Result

Since OC3-Hywind is a floating wind turbine, the impact of waves and turbulent wind loadings on the structure will induce six-degree of freedom motions, as illustrated in *Figure 4.3*. The result of the platform surge displacement as well as the pitch and yaw rotations are presented as the average mean as well as maximum positive & negative values from the six simulations in *Figure 4.38* to *Figure 4.40* for both LC Groups respectively. Before interpreting the simulation result, it is important to remember that the results shown in *Figure 4.38* to *Figure 4.40* are based *only* from six simulations for each load cases. Generally, the induced pitch and yaw motions distribution of the maximum positive & negative values are increasing with the wind speed for both LC Groups, but not for the surge displacement.

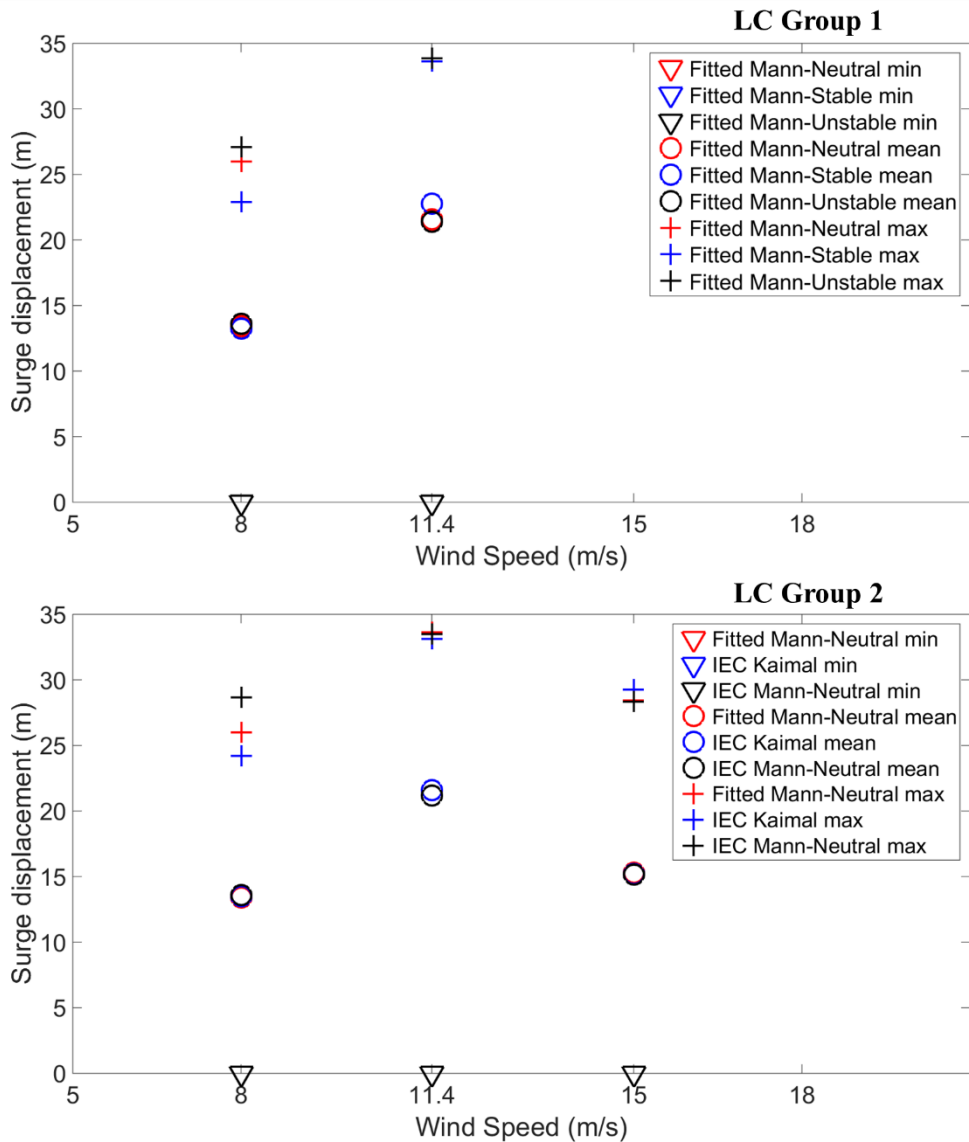


Figure 4.38 Minimum, mean and maximum surge displacement.

From *Figure 4.38* we notice that the mean surge displacement experienced by the platform was significant (up to 22.5 m at the rated wind speed) which means that the incoming wind is ‘pushing’ the wind turbine backward so the platform is displaced longitudinally from its original position. This is in accordance with reference (Jonkman & Musial, 2010) that when constant wind is introduced, the mean platform surge reached about +15m. In LC Group 1, the fitted-Mann (unstable) conditions induce the largest positive displacement followed by the fitted-Mann (neutral) and the fitted-Mann (stable). This

effect is observed especially at below rated wind speed, while at the rated wind speed, the maximum positive displacement is the same for the fitted-Mann neutral, stable and unstable. For LC Group 2 at below rated wind speed, the IEC-Mann induces the largest positive displacements. The maximum difference between the load cases for the platform surge is about 4 metre when considering the same wind speed (*Figure 4.38*). The reduced values of the mean and the maximum distribution of the platform surge at above rated wind speed (compared to at rated) as shown in *Figure 4.38* might be due to the blade-pitching activity that reduce the drag loads on the rotor and thus reduce the thrust force ‘pushing’ the wind turbine backward.

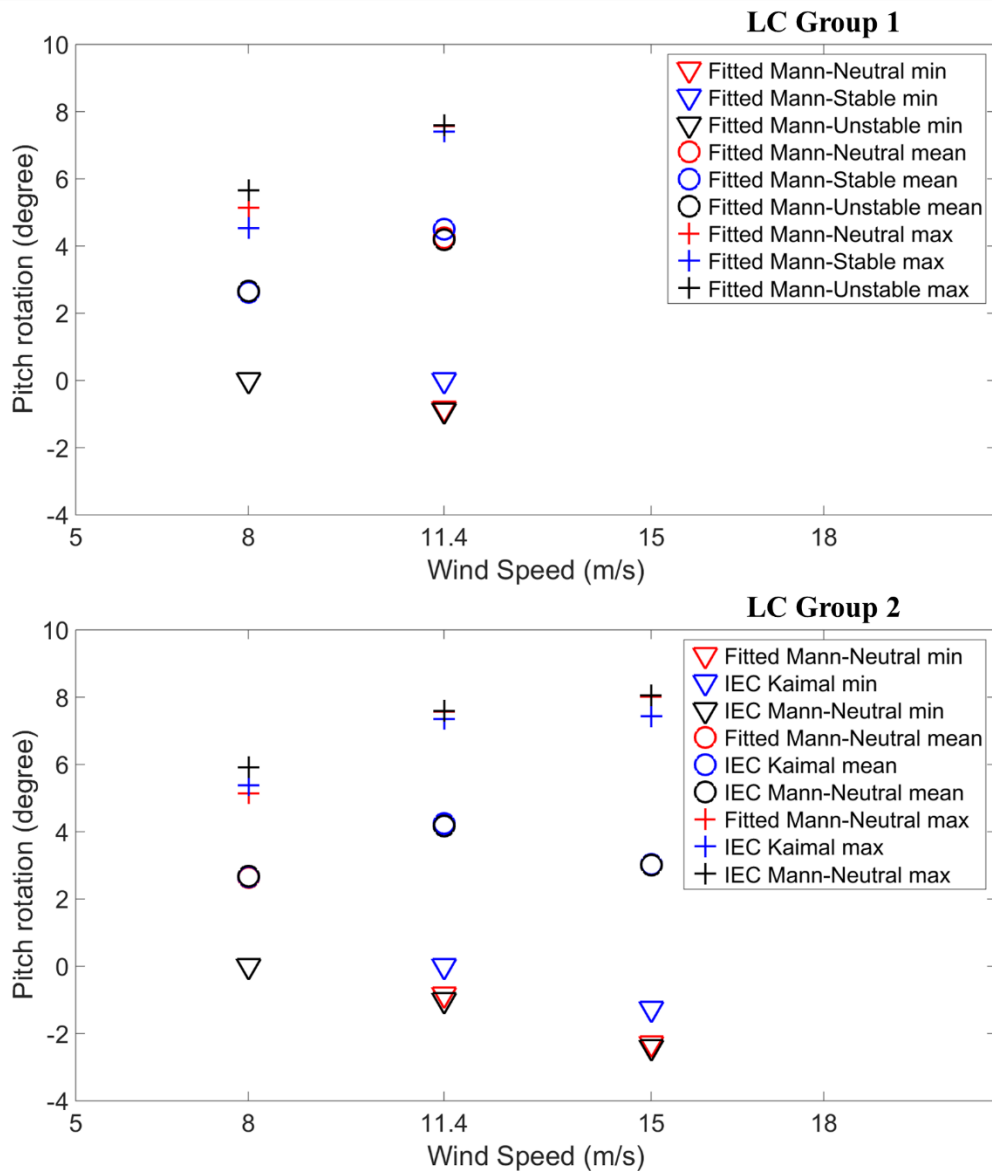


Figure 4.39 Minimum, mean and maximum pitch rotation.

At below rated wind speed, the platform pitches only in one direction (backward), while as the wind speed enters the rated, the platform starts to experience “back-and-forth” pitching. This phenomenon is indicated in *Figure 4.39* where at the rated wind speed and above, the maximum negative pitch is non-zero. Overall, the fitted-Mann unstable has the largest maximum positive & negative values for LC Group 1 and the IEC-Mann for LC Group 2. Comparing both LC Groups, the fitted-Mann (unstable) and the IEC-Mann are generating approximately equal values. The maximum difference for the pitch rotation between the load cases is seen at the level of 1.6° , which is quite low.

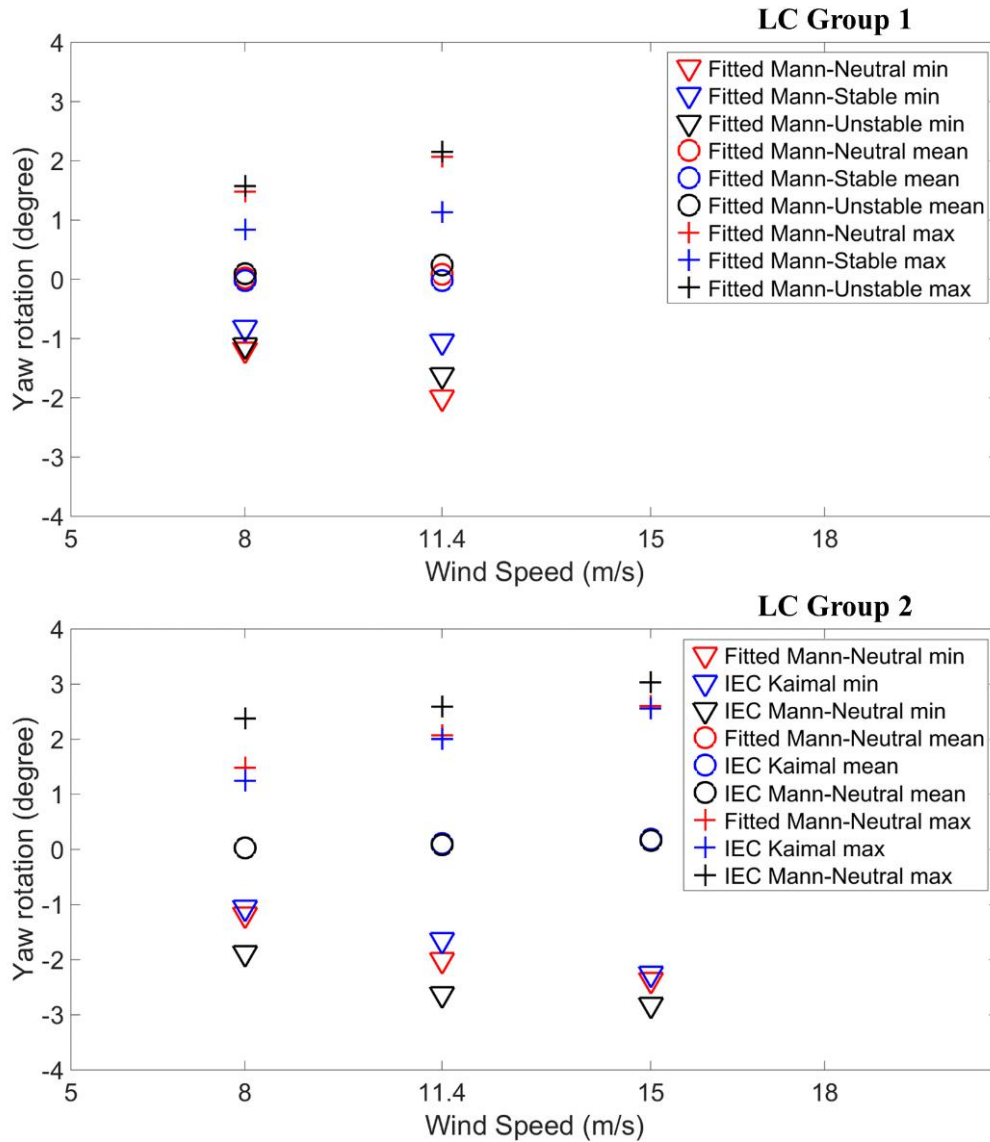


Figure 4.40 Minimum, mean and maximum yaw rotation.

The platform yaw rotation has the largest maximum positive & negative values from the IEC-Mann comparing both LC Groups at all wind speeds (*Figure 4.40*), which has the highest σ_u . For LC Group 1, the maximum positive yaw is obtained from the fitted-Mann unstable while the minimum negative yaw is obtained from the fitted-Mann neutral conditions; however, the difference between the two is very close (less than 0.5°). For LC Group 2, the IEC-Kaimal and the fitted-Mann (neutral) are having small difference with the value less than 0.5° . The maximum difference for the platform yaw between the load cases is seen at the level of 1.1° . The relatively small yaw motion observed for the OC3-Hywind might not be the case for other setup of a spar-buoy wind turbine. A change in environmental condition e.g. water depth or the wind turbine properties—the spar’s draft, mooring lines configuration or rotor diameter— might affect the motion responses of the wind turbine.

4.4 Influence of the Mean Wind Profile Variation on the OC3-Hywind Loadings and Responses

The influence of the atmospheric stability on the generated wind field can be observed in two different manners: the mean wind profile and the turbulence level. An additional study to examine the influence of mean wind profile under different atmospheric stability conditions was therefore performed. Nonetheless, it is important to note that the wind turbulence was still included in the simulations. This was done by inputting equal value of power law exponent α for LC Group 1 at all stability conditions in **Table 4.5** to 0.12 (as recommended by DNV assuming neutral atmospheric condition), while keeping the rest of the parameters the same. This modified case of LC Group 1 will be referred as LC Group 1-WP from hereafter. Originally, the input parameter α provided in **Table 4.5** generates a variation in the mean wind profile for LC Group 1 with reference rated speed at the hub as shown in **Figure 4.41**. When parameter α is inputted equally, the mean wind profile for LC Group 1-WP is as shown in **Figure 4.42**.

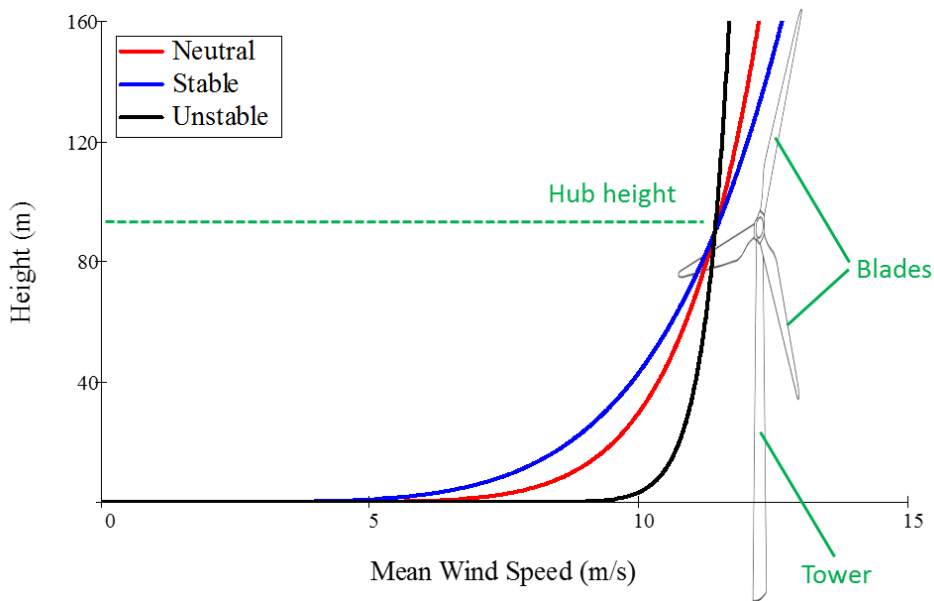


Figure 4.41 Mean wind profile input for LC Group 1 (original case).

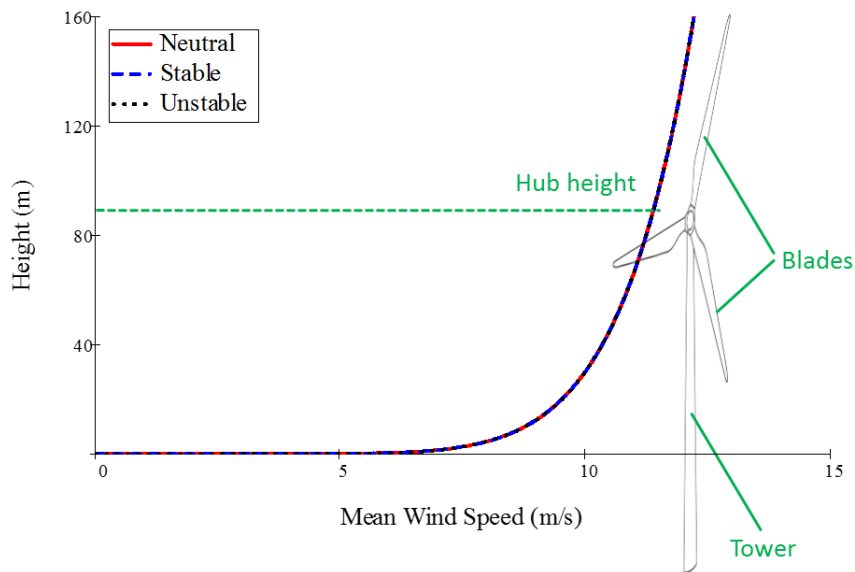


Figure 4.42 Mean wind profile input for LC Group 1-WP (modified case).

As seen from *Figure 4.41*, the influence of variation in the mean wind speed profile could have an impact on the blades and the tower. Generally, the simulations results showed *no significant impact* of the mean wind profile variation towards the loadings and motions of the OC3-Hywind. Nonetheless, the most prominent effects are observed for the tower base fore-aft moment, blade root flap-wise and edge-wise moments. In addition, the yaw motions is also slightly affected. *Figure 4.43*, *Figure 4.44*, and *Figure 4.45* show the comparison of LC Group 1 and LC Group 1-WP respectively for tower base fore-aft moment damage equivalent loads, blade root flap-wise and edge-wise moments damage equivalent loads.

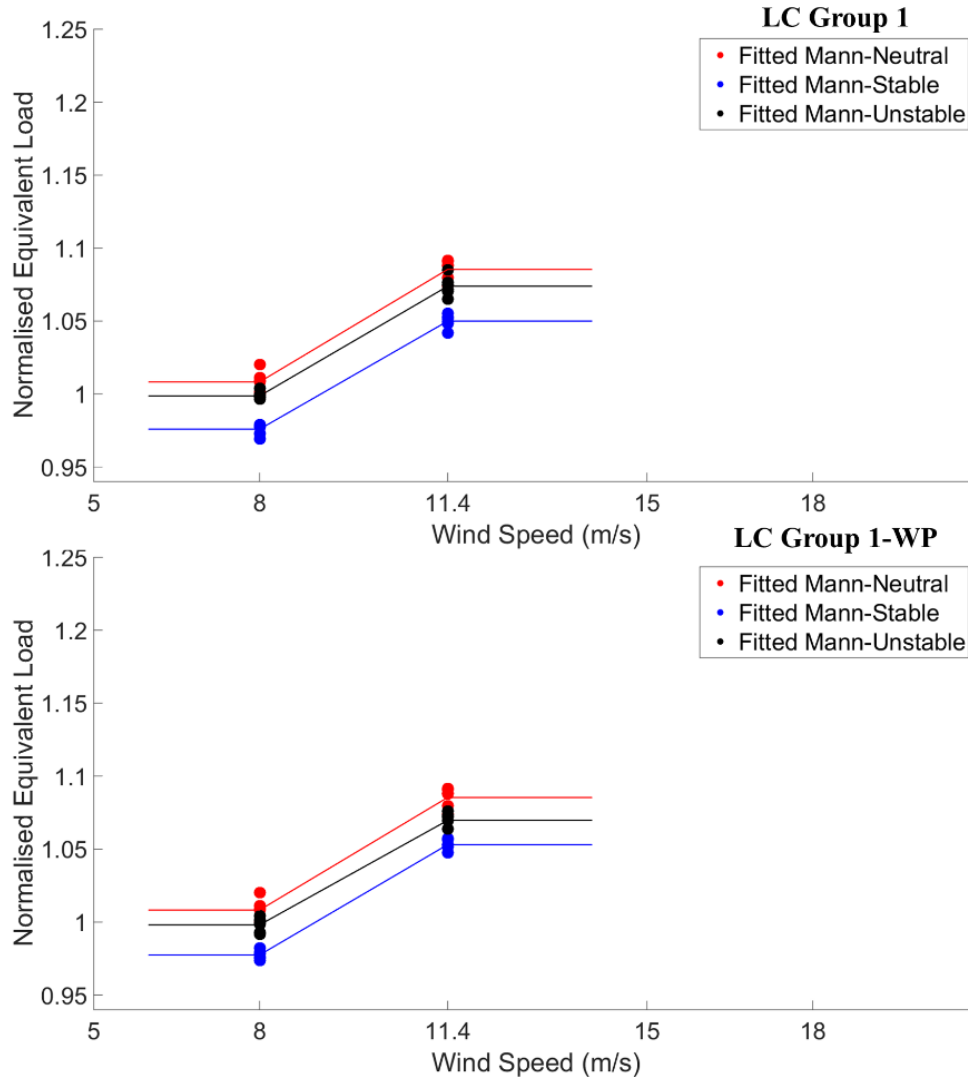


Figure 4.43 Comparison of the tower base fore-aft moment damage equivalent loads towards mean wind profile variation.

In *Figure 4.43*, it is seen that the unstable mean wind profile ($\alpha=0.04$, LC Group 1) increases the tower base fore-aft moment equivalent damage equivalent loads at the rated wind speed, by only 1%. *Figure 4.44* shows an increase in the blade root flap-wise moment damage equivalent loads under the stable condition ($\alpha=0.18$, LC Group 1) by 5% at the rated wind speed. For the blade root edge-wise moment damage equivalent loads under stable condition ($\alpha=0.18$, LC Group 1), we see an increase in the damage equivalent loads of 1.5% (*Figure 4.45*).

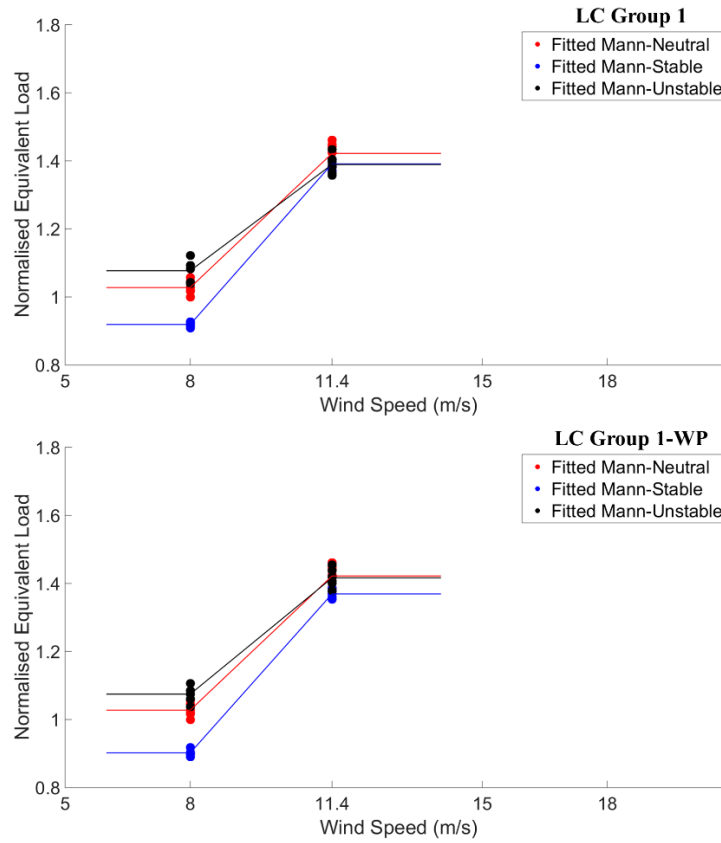


Figure 4.44 Comparison of the blade root flap-wise moment damage equivalent loads towards mean wind profile variation.

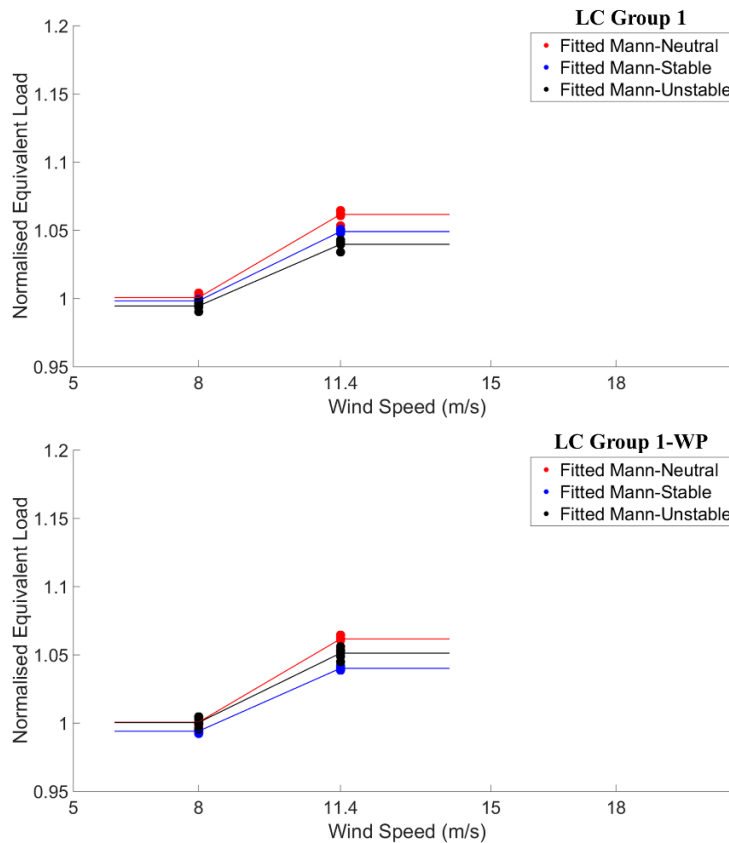


Figure 4.45 Comparison of the blade root edge-wise moment damage equivalent loads towards mean wind profile variation.

Furthermore, we only observe small changes in the platform yaw motion due to variation in the mean wind profile of around 0.4° . An equal α values for different atmospheric stability conditions results in exactly the same mean platform yaw (*Figure 4.46*, lower graph), while variation in the α values creates very low distribution in the mean yaw values by only 0.1° . The maximum and minimum spread of the platform yaw motions are more or less the same between LC Group 1 and LC Group 1-WP.

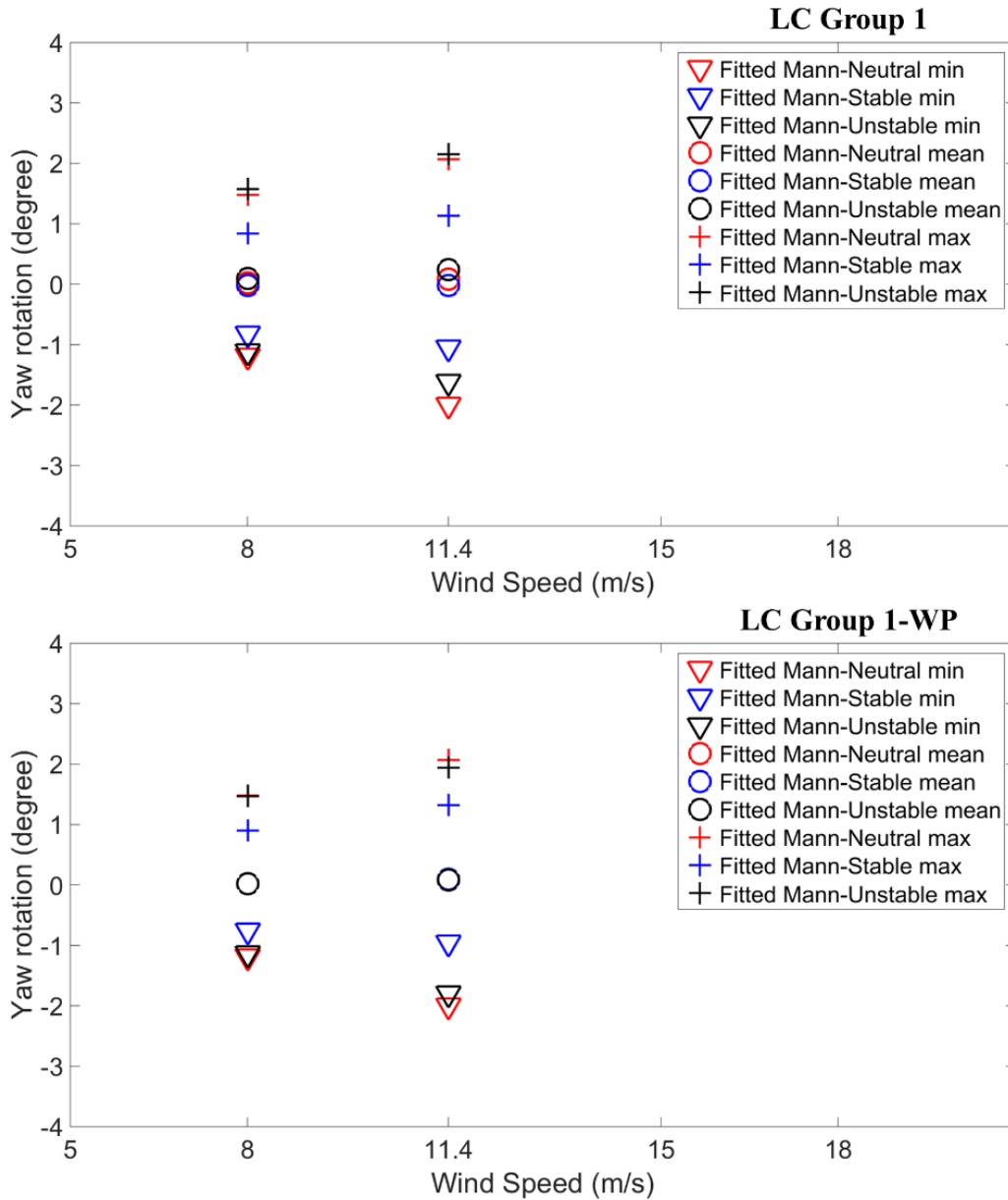


Figure 4.46 Comparison of the platform yaw towards mean wind profile variation.

5. Discussion and Conclusion

5.1 Discussion

Main discussions related to the simulations results (Chapter 4) are further discussed and studied in this subchapter. Particularly, the discussion will try to highlight the influence of the different parameters of the Mann Spectral Tensor Model using the simulation performed as part of this thesis. Nonetheless, the conclusions drawn here are based on a limited number of simulations, which should ideally be expanded as part of a more detailed parametric study. Moreover, the observation of “no influence” of some the parameters towards the OC3-Hywind responses (loads and motions) might be caused by other factors such as software limitations, data constraints and the limited numbers of simulations performed.

Furthermore, the comparison between the IEC Kaimal Spectra & Coherence Model and the Mann Model with the given parameters values from the IEC standards is presented. Several important (general) highlights from the given results in Chapter 4 are also discussed here, in particular for the pitch/fore-aft and yaw modes as well as the mooring lines. To get a better understanding about the properties of the generated coherences and wind fields, presentation of the generated coherences and wind fields characteristics and will be discussed beforehand in Subchapter 5.1.1 and Subchapter 5.1.2 respectively.

5.1.1. The Simulated Wind Coherences

The generated lateral and vertical coherences (co-coherence, real part of the cross-spectrum) from the performed load cases are presented and discussed here. The plots shown in *Figure 5.1* to *Figure 5.4* present the lateral and vertical coherences from the generated synthetic wind field (turbulence box) of the u -wind component for three separation distances: 20m, 60m, and 120m. Some of the coherences plots which are not shown here are provided in the Appendix C. From *Figure 5.1* to *Figure 5.4*, it is noted that both lateral and vertical coherences are decreasing with separation distance where at the same separation distance, the vertical coherence decays at a lower rate than the lateral coherence.

Figure 5.1 presents the coherences at below rated wind speed comparing the models from the IEC standards: the Kaimal Spectra & Coherence Model and the IEC Mann (neutral) while *Figure 5.2* gives the coherences of the two different models at the rated wind speed. From *Figure 5.1* and *Figure 5.2*, we observe that the increase from below rated to the rated wind speed slightly increases the lateral and vertical coherences. This trend is also observed when we compare the coherences for the Mann model using the fitted parameters at Høvsøre (Sathe et al., 2013). The comparison of the coherences for the Kaimal Model and the Mann Model with the given parameters from the IEC standards is further discussed in Subchapter 5.1.8.

Figure 5.3 compares the Mann Model coherences between neutral and stable conditions from the fitted parameters at Høvsøre (Sathe et al., 2013) at below rated wind speed, while *Figure 5.4* compares the coherences between neutral and unstable conditions at below rated wind speed. At the low frequencies, a tendency of the unstable conditions having the highest coherences followed by neutral and stable conditions is noted (*Figure 5.3* and *Figure 5.4*). This trend is explained by the increase in the length scale values L_M from stable to unstable conditions (*Table 5.1*) implying that the coherences are highly dependent on the length scales L_M , which was also observed by Chougule et al. (2015). Since the length scales L_M represent the eddy size in a turbulent wind field, hence a larger eddy covers a larger ‘area’ which results in higher coherences.

Table 5.1 Energy Dissipation Rate, Length Scale and Anisotropy Degree Parameters for the Load Cases

Parameter	Below rated (8m/s)				
	IEC		Fitted Parameters (Sathe et al., 2013)		
	Kaimal (Neutral)	Mann (Neutral)	Mann (Neutral)	Mann (Stable)	Mann (Unstable)
Energy dissipation $\alpha\epsilon^{2/3} (m^{4/3}s^{-2})$	-	0.0817	0.034	0.0245	0.0325
Length scale L_M (m)	340.2*	33.6	46	20	98
Anisotropy degree Γ	-	3.9	3.125	2.78	2.25
Parameter	Rated (11.4m/s)				
Energy dissipation $\alpha\epsilon^{2/3} (m^{4/3}s^{-2})$	-	0.1216	0.0685	0.048	0.051
Length scale L_M (m)	340.2*	33.6	52.5	18	107
Anisotropy degree Γ	-	3.9	3.21	2.7	2.52

*referred to L_c (coherence scale parameter)

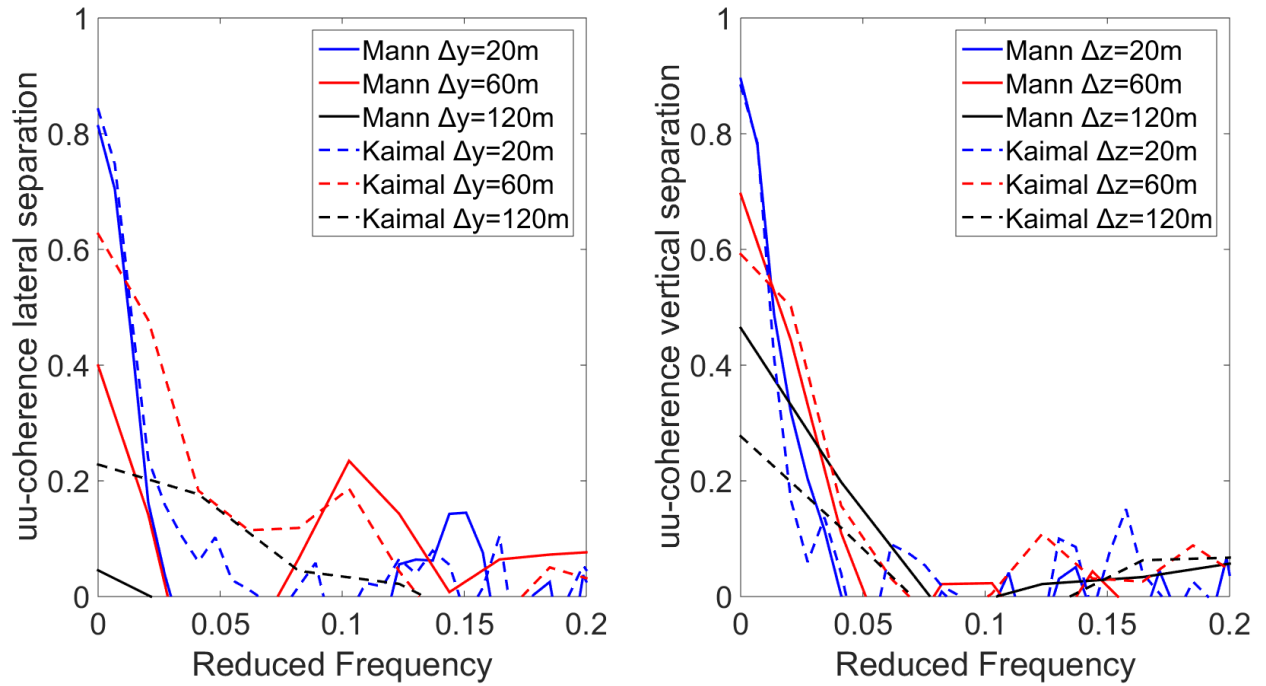


Figure 5.1 Lateral coherences of the u -component for different separations at **below rated** wind speed comparing the models given in (IEC, 2005): the Kaimal and the IEC Mann Models.

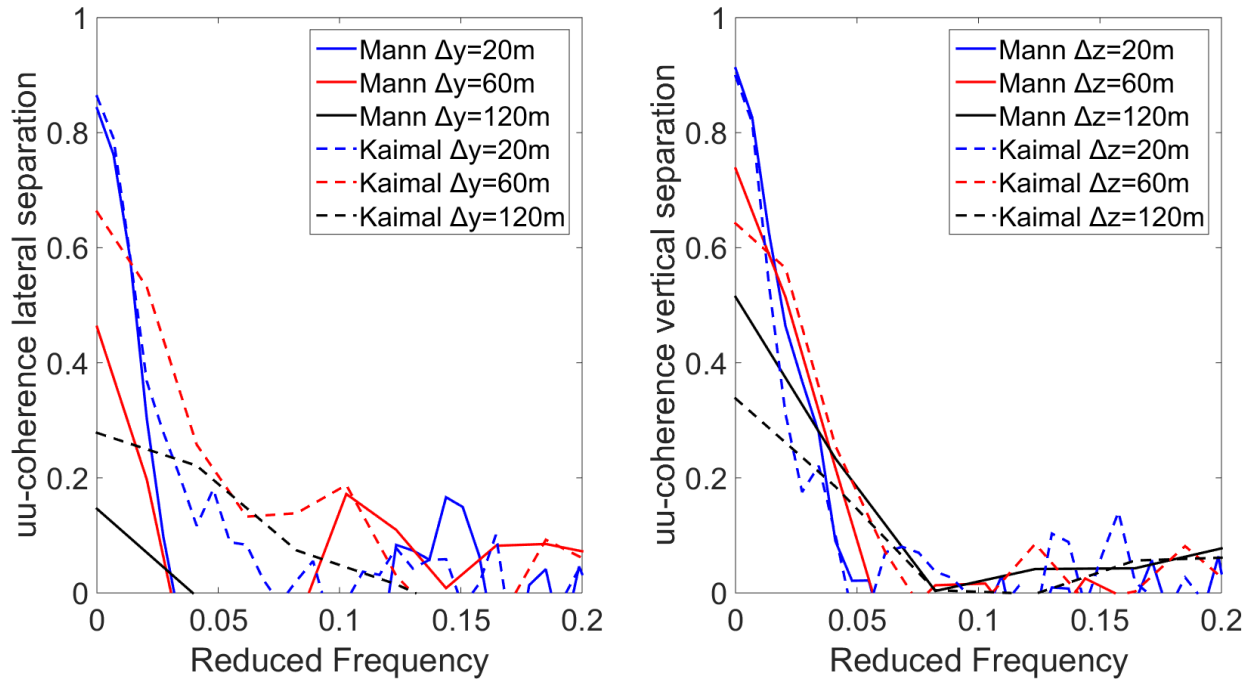


Figure 5.2 Lateral coherences of the u -component for different separations at **rated** wind speed comparing the models given in (IEC, 2005): the Kaimal and the IEC Mann Models.

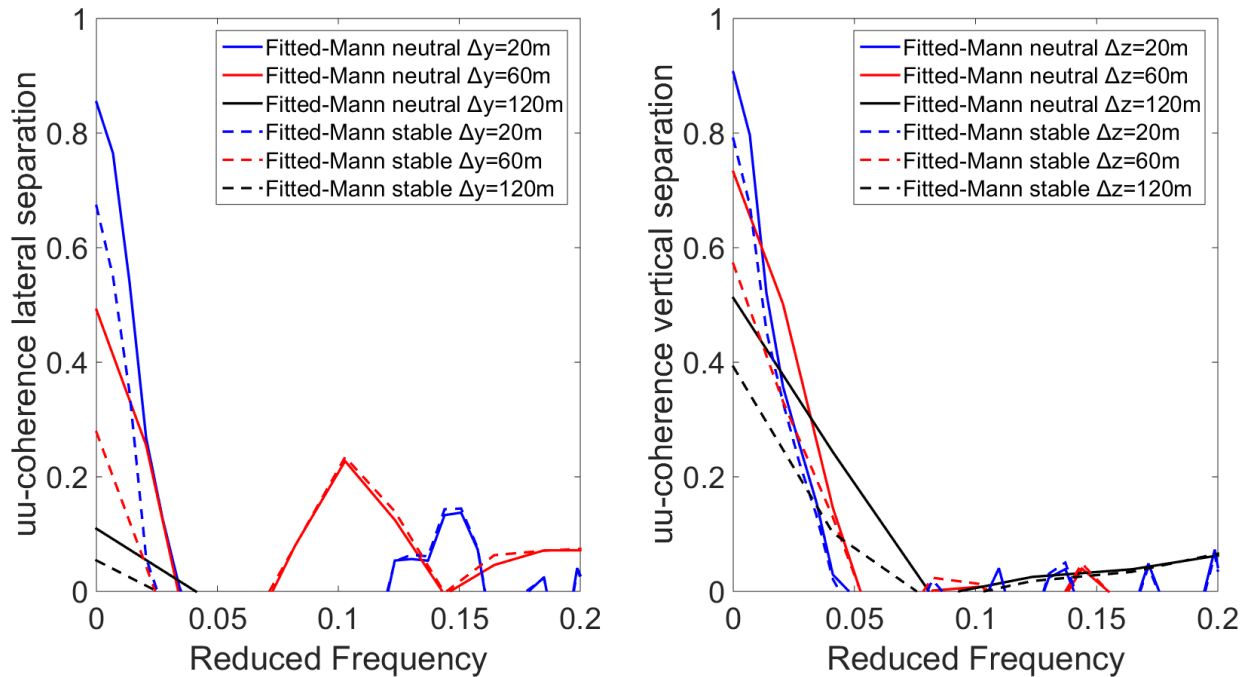


Figure 5.3 Lateral (left) and vertical (right) coherences of the u -component for different separations at **below rated** wind speed comparing the Mann Model with the fitted parameters for neutral and stable conditions.

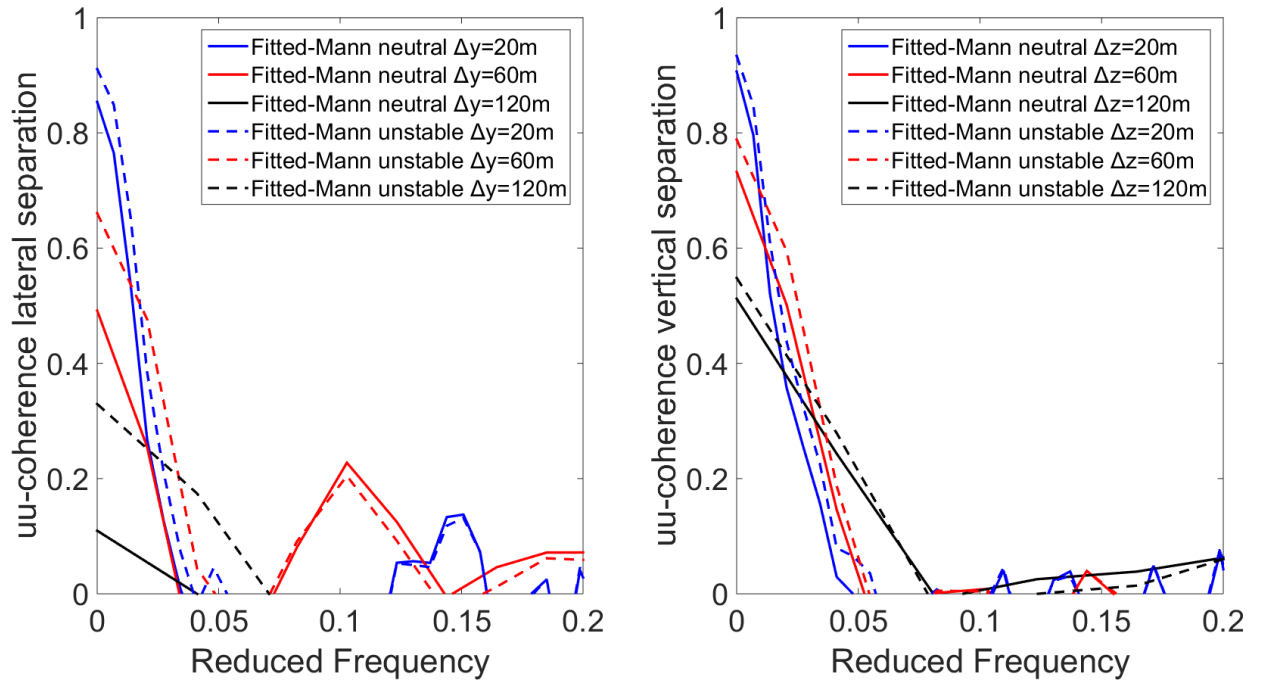


Figure 5.4 Lateral (left) and vertical (right) coherences of the u -component for different separations at **below rated** wind speed comparing the Mann Model with the fitted parameters for neutral and unstable conditions.

5.1.2. A Note on the Generated Turbulence Properties

Prior to discussing the simulation result, it is useful to have an insight regarding the generated turbulences properties. The simulated turbulence level, represented by standard deviation (σ_u) increased as the wind speeds were increasing (**Table 4.9**), which also applied for σ_v and σ_w (**Table C.1**). This increase in the standard deviation was caused by the ‘invariant’ in the turbulence intensity as the wind speed increases.

For the Mann Model, a general tendency of higher $\alpha\epsilon^{2/3}$ leading to higher σ_u was observed (**Table 4.9**). Nonetheless, this was an exception for the case where the difference between $\alpha\epsilon^{2/3}$ was very small with a relatively large difference L_M (the case of below rated wind speed comparing the fitted Mann neutral and unstable, **Table 5.1**). These suggests that:

- Since $\alpha\epsilon^{2/3}$ is the kinetic energy dissipation rate representing the mechanically generated (shear) turbulence, then higher $\alpha\epsilon^{2/3}$ will result in higher (shear) turbulence and hence the ‘total’ generated turbulence σ_u
- L_M which is a measure of eddy size and is used to reflect some of the effects of atmospheric stability. Chougule (2013) concluded that L_M could be used to simulate the effect of an increase buoyant-generated turbulence which contributes to an increased in total turbulence σ_u , however since the Mann model is valid for neutral conditions, it cannot truly model the thermal effects associated with changing atmospheric stability

Nonetheless, by comparing the fitted-Mann cases at the rated wind speed, the unstable condition which have the higher L_M than neutral condition resulted in lower value of σ_u (**Table 4.9**), in contradiction with the previously mentioned hypothesis as well as the theoretical understanding where unstable conditions should have the highest turbulence levels (σ_u) as the vertical mixing (buoyant-generated) turbulence is more significant. The reason for this is that the effect of the buoyant-generated turbulence (that varies

with atmospheric stability) *was not fully accounted* when *fitting* the wind velocity measurements data to the Mann Model (Chougule, 2013), since the Mann Spectral Tensor model was originally derived *only* for neutral conditions. According to Chougule (2013), additional parameters are required to quantify the magnitude of the buoyant-generated turbulence in the Mann Model by taking into account the gradient *Richardson number and the dissipation rate of temperature variance* in the Mann Model. This **modified Mann Model** which is currently under development (Chougule, 2013), should be able to capture a more accurate magnitude of buoyant-generated turbulence taking into account atmospheric stability corrections, but this is subject to further validation. We therefore conclude that the length scale parameter L_M obtained *from the measurement fitting* to the Mann Model does not provide the ‘complete’ representation on the quantity of the buoyant-generated turbulence under different atmospheric stability conditions.

The reasons mentioned above are a limitation of this study since the fitted-Mann parameters by Sathe et al. (2013) at Høvsøre site do not fully include the influence of buoyant-generated turbulence on the lateral and vertical coherences of the simulated ‘synthetic’ turbulent wind fields.

The general overview of the performed cases (**Table 4.9**) shows that the IEC Mann (neutral) resulted in the highest turbulence σ_u at all wind speeds, which corresponds to the highest kinetic energy dissipation rate $\alpha\epsilon^{2/3}$ (shear turbulence). The higher σ_u for neutral conditions was because $\alpha\epsilon^{2/3}$ is the measure of the mechanically generated (shear) turbulence which is the highest under neutral conditions compared to unstable and stable conditions. If the **modified Mann Model** taking into account the thermal energy dissipation rate was considered, then the ‘total’ turbulence level (σ_u) might be the highest under unstable conditions.

The generated turbulences from the IEC Kaimal Spectra & Coherence Model in this study (12% turbulence intensity) has approximately close level with the turbulences from the fitted-Mann parameter (neutral conditions) at Høvsøre Site (Sathe et al., 2013), which could be just a coincidence. This might not be the case if the fitted parameters from other sites were considered; however, due to data constraint, only one site was considered in this study.

From the power spectral density plots for the u -wind component (**Figure C.21**, **Figure 4.5**, and **Figure C.22**), in general the spectral density values for u -wind component are following the value of σ_u (**Table 4.9**) where higher σ_u generates higher u -wind component spectral density. For v -wind component (**Figure C.23**, **Figure 4.6**, and **Figure C.24**) and w -wind component (**Figure C.25**, **Figure 4.7**, and **Figure C.26**), the influence of L_M is observed where the increase of L_M implies higher turbulence energy in the low frequency range, as also outlined by Chougule et al. (2015).

Moreover, the independence of turbulence σ_u towards spatial variations was due to the homogeneity (i.e. stationary in space), especially observed in the lateral direction (**Figure C.1**, **Figure 4.8**, and **Figure C.3**). In the vertical direction, the turbulence level (σ_u) was slightly varying since homogeneity in the vertical direction is only an approximation (Mann, 1998) as noticed in (**Figure C.2**, **Figure 4.9**, and **Figure C.4**). The homogeneity is also applied for σ_v and σ_w .

5.1.3. The Case of ‘Constant’ $\alpha\epsilon^{2/3}$ with Variable L_M

This subchapter will highlight the influences of parameter L_M on the OC3-Hywind responses as it was observed to govern both lateral and vertical coherences. The analysis was done by comparing two cases selected from the Høvsøre measurements fitting (Sathe et al., 2013): the neutral and unstable conditions at below rated wind speed (**Table 5.1**). Ideally, for this analysis, two conditions with the same exact

$\alpha\epsilon^{2/3}$ should be used, however due to data constraint, the selected cases were chosen based two load cases with similar $\alpha\epsilon^{2/3}$ values. The values of the two cases are: neutral ($\alpha\epsilon^{2/3}=0.034m^{4/3}s^{-2}$, $L_M=46m$) and unstable ($\alpha\epsilon^{2/3}=0.0325m^{4/3}s^{-2}$, $L_M=98m$), with small difference in $\alpha\epsilon^{2/3}$ values.

Figure 5.4 presents the lateral and vertical coherence plots for the along wind component (u) for different separation distances comparing $L_M=46m$ (neutral) and $L_M=98m$ (unstable). It can be seen from **Figure 5.4** that *higher L_M results in higher lateral and vertical coherences*, even though the difference in the vertical coherence between the case where $L_M=46m$ and $L_M=98m$ is not as significant as the lateral coherence which is increasing with separation distance. The results presented in **Figure 5.4** are based on the simulated spatial coherences averaged for only six simulations. To reduce uncertainty in the results, ideally a larger number of simulations should be performed over a range of different L_M values.

Figure 4.34 showed that the damage equivalent loads for the tower base fore-aft moment from $L_M=46m$ was slightly higher with only 1% difference than the case where $L_M=98m$. This negligible difference suggests that in our simulations L_M *does not significantly affect the damage equivalent loads for the tower base fore-aft*. Comparing the tower top yaw moment damage equivalent loads, the case of $L_M=46m$ predicted higher damage equivalent loads compared to the case of $L_M=98m$ with the difference about 6% (**Figure 4.35**) which is slightly more significant.

The maximum platform pitch was observed to be larger for $L_M=98m$ compared to $L_M=46m$ with 0.5° difference which is not significant in our case (**Figure 4.39**). The distribution of the maximum positive & negative and the mean platform yaw motions were shifted to a more positive value for the case of $L_M=98m$ compared to the case of $L_M=46m$ (**Figure 4.40**). This result was somehow arbitrary, however, the differences between the two cases for the maximum positive are 0.09° , 0.07° for the mean, and 0.073° for the maximum negative which are negligible.

5.1.4. The Case of 'Constant' L_M and Variable $\alpha\epsilon^{2/3}$

This subchapter will highlight the influences of $\alpha\epsilon^{2/3}$ on the OC3-Hywind responses, where in this case it also indirectly implies an increase wind speed. Two cases are selected from the Høvsøre measurements fitting (Sathe et al., 2013): the stable conditions at below rated and rated wind speeds (**Table 5.1**). Again, ideally for this analysis, two conditions with the same exact L_M should be used, however due to data constraints, the selected cases were chosen based on the closest L_M difference. The values of the two cases are: at below rated wind speed ($U=8m/s$, $\alpha\epsilon^{2/3}=0.0245m^{4/3}s^{-2}$, $L_M=20m$) and at rated wind speed ($U=11.4m/s$, $\alpha\epsilon^{2/3}=0.048m^{4/3}s^{-2}$, $L_M=18m$).

The plot of the lateral and vertical coherences at different separation distances for the two load cases are presented in **Figure 5.5** from which shows that higher $\alpha\epsilon^{2/3}$ gives *higher lateral and vertical coherences*. Yet by comparing **Figure 5.4** and **Figure 5.5** we do not see a clear trend of both lateral and vertical coherences towards the value of $\alpha\epsilon^{2/3}$. Our simulations suggest that *both lateral and vertical coherences are not strongly correlated with $\alpha\epsilon^{2/3}$ but this should be further confirmed by a more extensive parametric study*.

Figure 4.34 showed that the increment of $\alpha\epsilon^{2/3}$ from $0.0245m^{4/3}s^{-2}$ to $0.048m^{4/3}s^{-2}$ increases the damage equivalent loads for the tower base fore-aft moment by 7.6%. The increase in $\alpha\epsilon^{2/3}$ also results in higher tower top yaw damage equivalent loads with 65% difference (**Figure 4.35**), which is significant.

This highlights that $\alpha\epsilon^{2/3}$ influences the tower base fore-aft and significantly affects the tower top yaw damage equivalent loads.

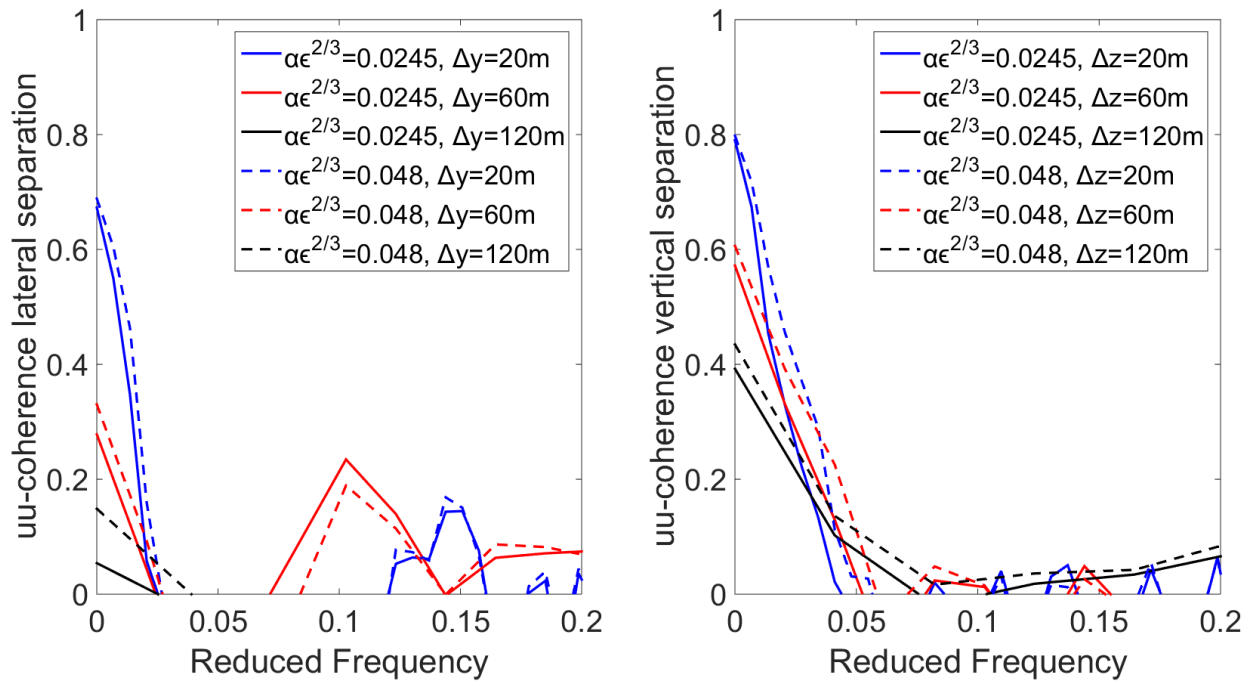


Figure 5.5 Plot of the lateral coherence (left) and vertical coherence (right) of the u-wind component comparing $\alpha\epsilon^{2/3}=0.0245\text{ m}^{4/3}\text{ s}^{-2}$ and $\alpha\epsilon^{2/3}=0.048\text{ m}^{4/3}\text{ s}^{-2}$.

From **Figure 4.39**, the case with $\alpha\epsilon^{2/3}=0.048\text{ m}^{4/3}\text{ s}^{-2}$ induces higher platform pitch mean and maximum values where the differences are 1.8° for the mean values and 2.8° for the maximum values. This indicates a *slight influence of $\alpha\epsilon^{2/3}$ on the platform pitch*. As given in **Figure 4.40**, the distribution of the maximum positive & negative of the platform yaw motions are increasing with the increment of $\alpha\epsilon^{2/3}$, although the differences are rather small, that is 0.3° for the maximum positive difference and 0.23° for the maximum negative difference. This implies a *negligible influence of $\alpha\epsilon^{2/3}$ on the platform yaw in our simulations for the OC3-Hywind setup*.

By using **the Mann Model fitted to measurements** we conclude that the fatigue damages (tower base fore-aft and the tower top yaw) are highly dependent on $\alpha\epsilon^{2/3}$. According to Dekker (1998), fatigue damages on wind turbines exposed to turbulent wind field are highly dependent on the turbulent wind field characteristics, in particular the turbulence intensity which is normally quantified as σ_u . For the fitted-Mann Model as shown in this study, σ_u is increasing with $\alpha\epsilon^{2/3}$, hence the tower base fore-aft and the tower top yaw damage equivalent loads are increasing with the increasing $\alpha\epsilon^{2/3}$. Relating this to the atmospheric stability conditions, the neutral atmospheric conditions were in general resulting in the highest damage equivalent loads as having the highest $\alpha\epsilon^{2/3}$ (**Table 4.9**) for the tower base fore-aft bending (**Figure 4.34**) and the tower top yaw (**Figure 4.35**), followed by unstable and stable conditions. This is against the theoretical understanding that under unstable conditions should result in the highest fatigue damage since the influence of the buoyant-generated turbulence dominates. Yet, as emphasised earlier that the highest σ_u for neutral conditions was due to $\alpha\epsilon^{2/3}$ which is the measure of the mechanically generated (shear) turbulence, while the buoyant-generated turbulence was not entirely accounted in the current Mann Model.

5.1.5. A Note for the Mooring Lines Tensions Results of the OC3-Hywind

From the reference (Jonkman, 2010) for the OC3-Hywind floating wind turbine definition, there are three different mooring lines models used for the OC3-Hywind: a linearized model of the complete mooring system, a non-linear model of the complete mooring system, and a non-linear model of an individual mooring line. The latter model was used in the default OC3-Hywind model from the HAWC2 (Risø DTU) which was used in this study. This method allows each individual mooring line tension calculation based on the load-displacement relationship from the Mimosa mooring analysis software (Jonkman, 2010). The computed values from the Mimosa software are presented in *Figure 3.13* and the sample input file is provided in the Appendix A. As mentioned earlier in Subchapter 3.5, each of the mooring line tensions were calculated depending only on the fairlead distance to the anchor (*Figure 3.13*) which resulted in similar values of the line tensions between the turbulence load cases. Another reason for the observed similarity in the computed mooring tensions was the fact that the same exact wave inputs and seed number were given for all load cases performed (*Table 4.3*). The same seed number used for different turbulence cases generated the exact same wave field (wave elevation time series).

Hall et al. (2014) studied the influence of the dynamic mooring line using coupled FAST-ProteusDS and the quasi-static mooring line using FAST (solving a set of analytical catenary cable equations) on the OC3-Hywind. They showed that the static mooring line model under-predicted the mooring line tension damage equivalent loads by 32% (Hall et al., 2014). This might suggest that the generated mooring line tensions from this study are under-predicted when compared to the use of dynamic mooring line model which was not performed and is a limitation of this study.

Mooring Lines Tensions Spectral Density Results

In Subchapter 4.3.3.6, the mooring lines tensions were only excited in the wave spectral peak frequency, which was also found in the study by Hall et al. (2014) for OC3-Hywind by considering similar environmental setup with this study (by considering turbulent wind and irregular JONSWAP waves), implying that the mooring tensions were highly affected by the waves. In addition, the wind turbulence excited the mooring lines tensions only in the lowest frequency range, less than 0.02Hz (*Figure 4.28* to *Figure 4.31*), yet due to the limitation in the computation of the mooring tensions, the influence of different turbulence cases in the mooring tension spectral densities was not observed.

5.1.6. A Note on the Pitch/Fore-Aft Modes of the OC3-Hywind

Coupled Platform Pitch – 1st Tower Fore-Aft

In *Figure 4.22* to *Figure 4.24* for the platform pitch motion spectral density plots, the main excitations for the platform pitch motion were shown at the wave spectral peak, 1st tower fore-aft bending, and platform pitch natural frequencies. This was also found from the study by Hall et al. (2014) who studied that the platform pitch power spectral density for the OC3-hywind ($U=11.4\text{m/s}$, 17%TI and irregular waves with JONSWAP spectrum $T_p=10\text{s}$) had three dominating peaks at the frequency of the platform pitch natural frequency, the wave spectral peak, and the tower base fore-aft. In *Figure 4.14* and *Figure 4.15*, the power spectral density plots for the tower base fore-aft moment, the main excitations for the tower base fore-aft moment peaks were also found at the frequency of the wave spectral peak, 1st tower fore-aft bending, and platform pitch natural frequencies. This indicates that the platform pitch and the 1st tower base fore-aft modes are coupled. This explains the similar behaviour of the two modes responses, especially in terms of energy content (power spectral density) results in Subchapter 4.3.3.

Influence of the Blade-Pitch Controller

The blade-pitching activity on a floating offshore wind turbine has been shown to induce negative damping (excessive back-and-forth pitching) on the spar-buoy turbine Hywind Demo (Skaare et al., 2015). The blade pitch controller is automatically activated as the wind speed enters the rated speed to maintain constant power production and to reduce thrust on the rotor due to high wind speed. In this study, the blade controller activity was influencing the OC3-Hywind pitch motion, although it was not significant. This was shown in the platform pitch plots (*Figure 4.39*) where at below rated wind speed, the minimum platform pitch was zero but as the wind speed entered the rated speed, the platform was pitching back-and-forth as the minimum platform pitch were found at negative values. This back-and-forth pitching was also noticed at the above rated wind speed, where the maximum negative values were even larger (*Figure 4.39*).

Moreover, in *Figure 4.22* to *Figure 4.24* the platform pitch spectral density plots at below rated, rated, and above rated wind speeds showed a significant increase in the peak at the platform pitch natural frequency between below rated and the rated wind speeds. On the other hand, there was no difference in the peak values at the platform pitch natural frequency between the rated and above rated wind speeds. This was also observed by Hall et al. (2014) who studied the OC3-Hywind, found that at rated and above rated wind speeds, the platform pitch spectral peak values at the platform pitch natural frequency were approximately the same. The most probable reason for this was an indication of the “activated” blade-pitch controller, which was also observed for the tower base fore-aft moment spectral densities where the peak values at the platform pitch natural frequency were increasing from below rated to the rated wind speed, but remained approximately constant at above rated wind speed (*Figure 4.13* to *Figure 4.15*). The influence of blade-pitch controller might be the cause for the decrease in the distribution of the maximum platform pitch (*Figure 4.39*) particularly at the rated wind speed and above.

Influence of a Turbulent Wind Field

Hall et al. (2014) studied the OC3-Hywind by comparing two cases a steady wind 8m/s with JONSWAP waves and turbulent wind (11.4m/s, 17% TI) with JONSWAP waves. They showed that in the latter case, the addition of stochastic wind added a peak in the platform pitch spectral density at the frequency of 1st tower base fore-aft i.e. turbulent wind triggered the 1st tower fore-aft mode, which was also observed in this study (*Figure 4.22* to *Figure 4.24*).

Karimirad & Moan (2012) studied a CMS (the same properties with OC3-Hywind but with mooring delta lines) considering two cases: (a) constant wind at below rated (8m/s and 11.2m/s) and above rated (14)m/s; and (b) 18% TI at below rated (8m/s) as well as 15% TI at 11.2m/s and 14 m/s (above rated) wind speeds. They included the delta connections in the mooring line model using DeepC code to compute the nonlinear force-displacement relationship mooring tension. They found that case (a) and (b) resulted in approximately the same mean values (based on five simulations for each wind speed) for the tower base fore-aft moment loads. This implies that in their study, the turbulent wind did not influence the bending moment loads for the tower base fore-aft mode. This study which used a simpler mooring model than Karimirad & Moan, (2012) also observed the tendency that the turbulent wind does not influence the tower base fore-aft damage equivalent loads since the maximum difference for the tower base fore-aft damage equivalent loads comparing different turbulence load cases was only 7.5% (when comparing each wind speed) as shown in *Figure 4.34*. The fact that the different turbulence load cases only slightly influenced the tower base fore-aft damage equivalent loads might be due to the excluded ‘buoyant-generated’ turbulence which would affect the pitch/fore-aft mode.

Influence of the Vertical Coherence on the Platform Pitch Motion

By using the **Mann Model fitted to measurements** we can take into account some of the effects of atmospheric stability by varying L_M . In **Figure 5.6** we compare the vertical coherences and the platform pitch spectral density at the rated wind speed. It appears that the pitch motion is not influenced by the observed differences in the vertical coherence. This may be due to the fact that at the rated wind speed, the influence of the blade-pitch controller activity is dominating. At below rated wind speed, **Figure 5.7** shows that a higher vertical coherence (unstable conditions) results in higher platform pitch energy in the lower frequencies of the OC3-Hywind which suggests that larger eddy sizes results in higher platform pitch motion. This also implies that from stable to unstable stability conditions, the pitch motion is increasing.

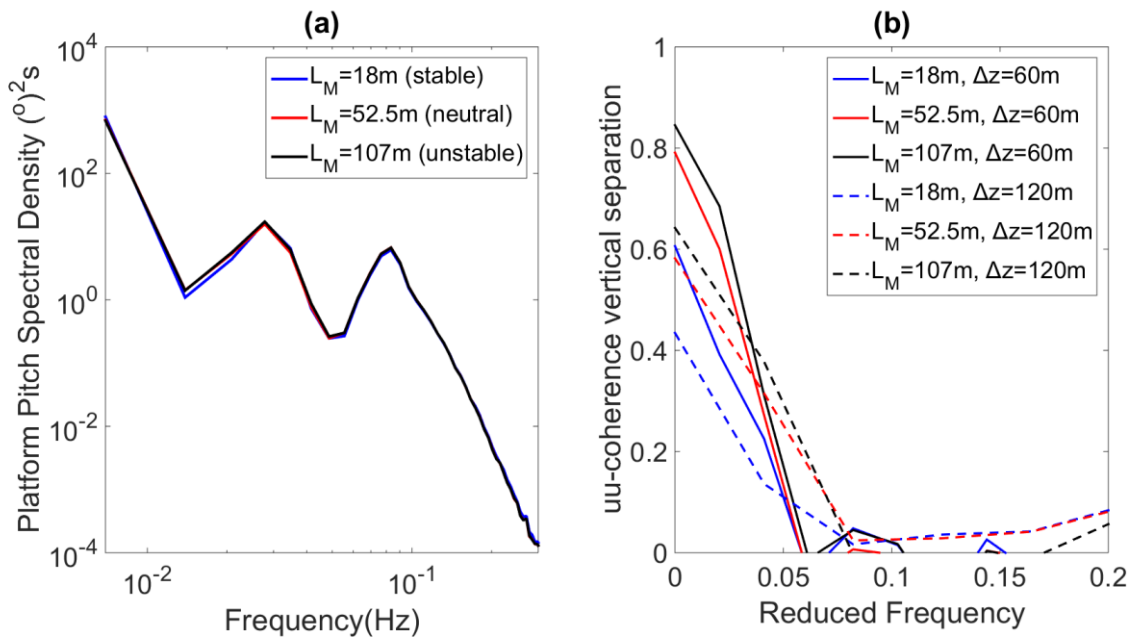


Figure 5.6 Comparison between (a) platform pitch spectral density and (b) u -component vertical coherence at different separations for different L_M at the **rated** wind speed.

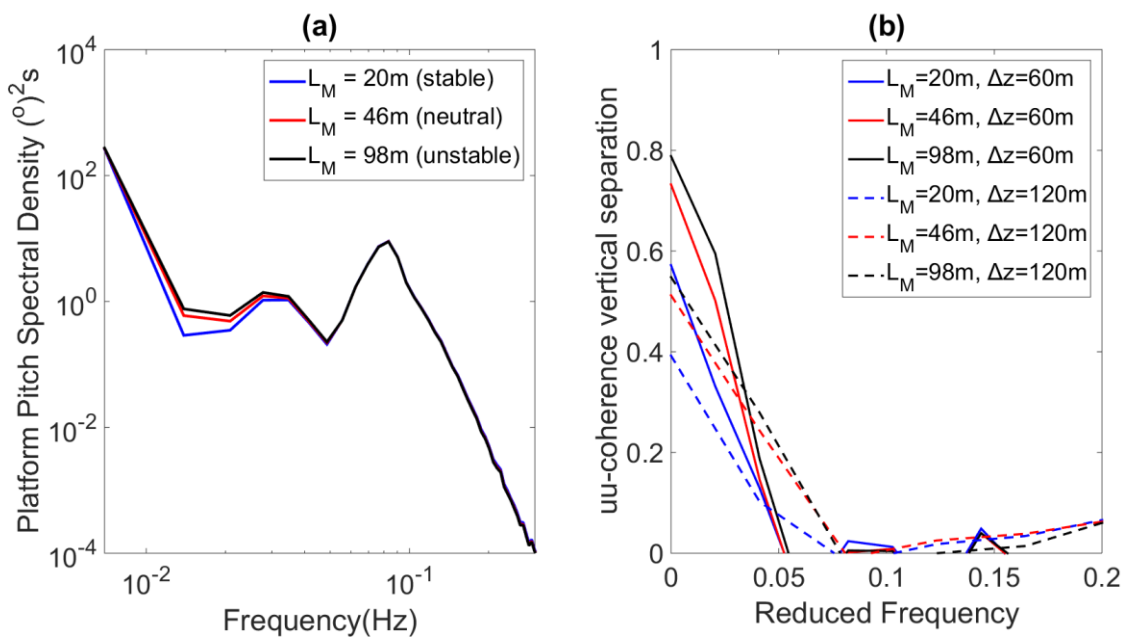


Figure 5.7 Comparison between (a) platform pitch spectral density and (b) u -component vertical coherence at different separations for different L_M at **below rated** wind speed.

5.1.7. A Note on the Yaw Modes of the OC3-Hywind

Yaw Motion of the OC3-Hywind

Figure 4.40 indicates that the platform yaw motion of the OC3-Hywind platform was not significantly affected by the different turbulence load cases. This might be due to the fact that the mooring was relatively stiff (larger water depth and draft) and the static mooring line model used in our simulations. The study by Godvik (2016) who considered a spar-buoy floating wind turbine (the Hywind Scotland) with shallower draft and larger rotor diameter than the OC3-Hywind, observed that the Hywind Scotland was yawing excessively when exposed to a turbulent wind field as generated by the IEC Mann Model when compared to the IEC Kaimal Model. This was thought to be caused by the differences in the lateral coherence from the two models particularly at large separations. The platform yaw motion of a spar-buoy floating wind turbine will be strongly influenced by the properties of the spar floater, water depth as well as the rotor size. This should be a subject for further study.

Tower Top Yaw Loadings

It was found that the tower top yaw damage equivalent loads were significantly influenced by the turbulent wind energy content, represented by parameter $\alpha\epsilon^{2/3}$. As presented in *Table 5.3*, the increase in $\alpha\epsilon^{2/3}$ clearly results in the increase of the tower top yaw damage equivalent loads whereas the influence of L_M i.e. change in spatial coherence is less obvious. Nonetheless, unless a parametric study with a constant $\alpha\epsilon^{2/3}$ and various L_M is performed (which was not done in this study due to time constraints), it is not possible to draw definitive conclusions with respect to tower top yaw loading and a change in L_M .

Table 5.2 Comparison of the Tower Top Yaw Damage Equivalent Loads for Various $\alpha\epsilon^{2/3}$

$\alpha\epsilon^{2/3}$ ($m^{4/3}s^{-2}$)	L_M (m)	Tower top yaw Damage Equivalent Load (kNm)
0.0245	20	3,169.72
0.0325	98	4,086.86
0.034	46	4,351.17
0.048	18	5,213.22
0.051	107	6,393.25
0.0685	52.5	7,603.55

Influence of a Turbulent Wind Field on the Platform Yaw Motion

From the reference (Jonkman & Musial, 2010), it was stated that the platform yawing in OC3-Hywind was caused by the rotating blades. This study also showed that the platform yaw was excited in the blade rotational frequencies of 3P and 6P (*Figure 4.25* to *Figure 4.27*). The generated turbulent wind field excites the platform yaw spectral density in the low frequency range, even though in this study the platform yaw spectral density peak at the platform yaw natural frequency (0.121Hz) was not observed due to the prominent excitation at the wave peak frequency (0.0833Hz) as shown in *Figure 4.25* to *Figure 4.27*.

Figure 5.8 shows the OC3-Hywind platform yaw power spectral density plots from (Jonkman & Musial, 2010) for the load case of $U=18m/s$, $\sigma_u=2.674m/s$ Mann Model and JONSWAP waves with $T_p=10sec$. *Figure 5.9* presents the platform yaw spectral density from the simulation result for below rated, rated, and above rated wind speeds. From *Figure 5.8* and *Figure 5.9*, it can be seen that the platform yaw spectral density values are excited in the wind turbulence (low) frequency range and as the wind speed

increases, the platform yaw energy content in the low frequency is also increasing. This means that the platform yaw motion is highly dependent on the wind speed.

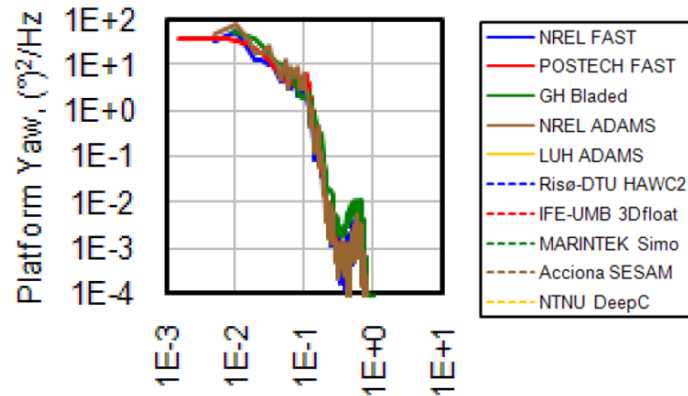


Figure 5.8 OC3-Hywind platform yaw spectral density for 18m/s wind speed (Jonkman & Musial, 2010).

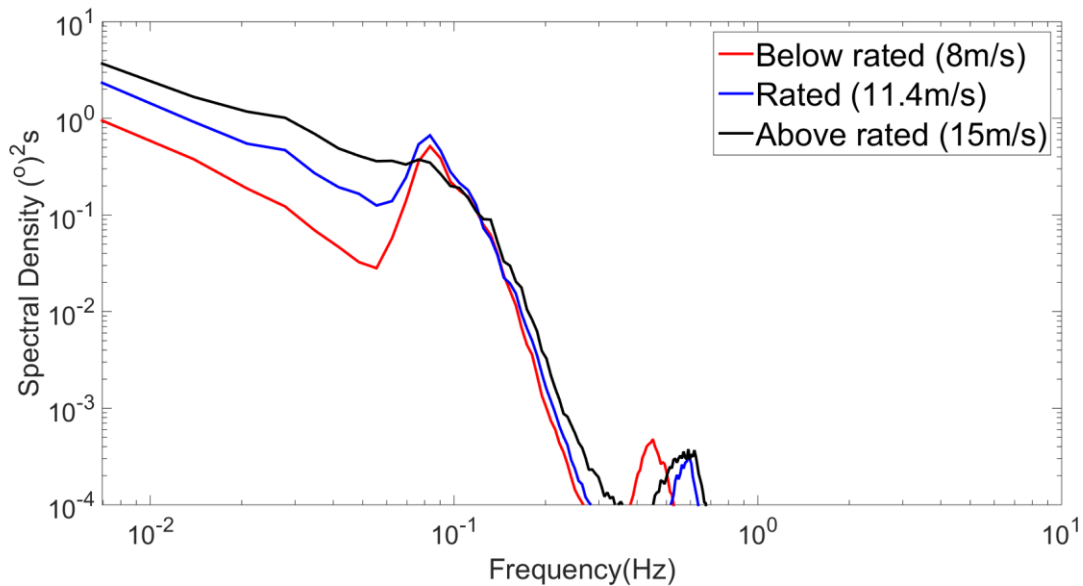


Figure 5.9 Platform yaw spectral density at different wind speed (average from all load cases).

Influence of Atmospheric Stability on the Platform Yaw Motion

By using the **Mann Model fitted to measurements** we can take into account some of the effects of atmospheric stability by varying L_M . *Figure 5.10* and *Figure 5.11* show the comparison between the platform yaw spectral densities and the lateral coherences for different L_M at below rated and rated wind speeds, respectively. At a glance, *Figure 5.10* and *Figure 5.11* suggest that a lower coherence (blue lines) resulted in lower platform yaw. It is important to note however that the cases shown here include variations in $\alpha\epsilon^{2/3}$ and L_M . As discussed in Subchapter 5.1.3 and Subchapter 5.1.4, the yaw motions appear to be more sensitive to changes in $\alpha\epsilon^{2/3}$ compared to changes in L_M . We have also discussed previously that by fitting the Mann Model which only valid for neutral condition to measurements, we do not fully include thermal effects due to changes in atmospheric stability. Therefore, it is important to determine appropriate turbulent wind models under non-neutral conditions to reduce uncertainty in offshore wind turbine designs.

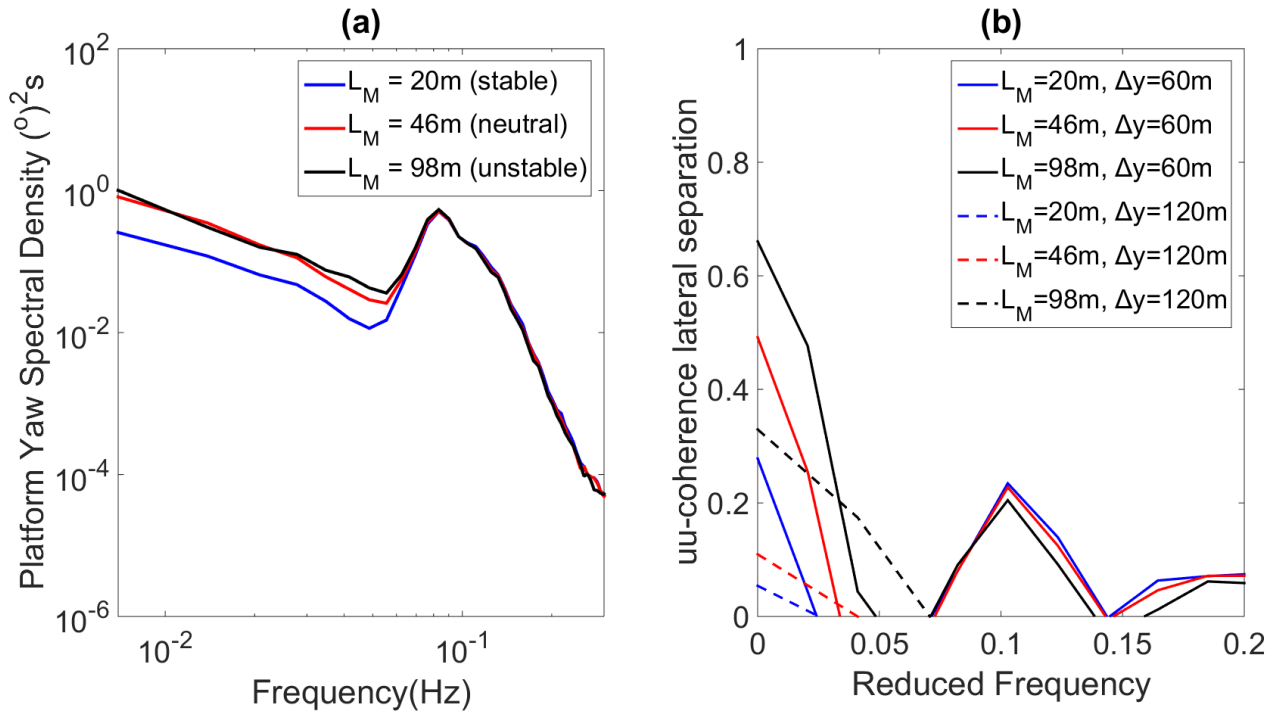


Figure 5.10 Comparison between (a) platform yaw spectral density and (b) u -component lateral coherence at different separations for different L_M at **below rated** wind speed.

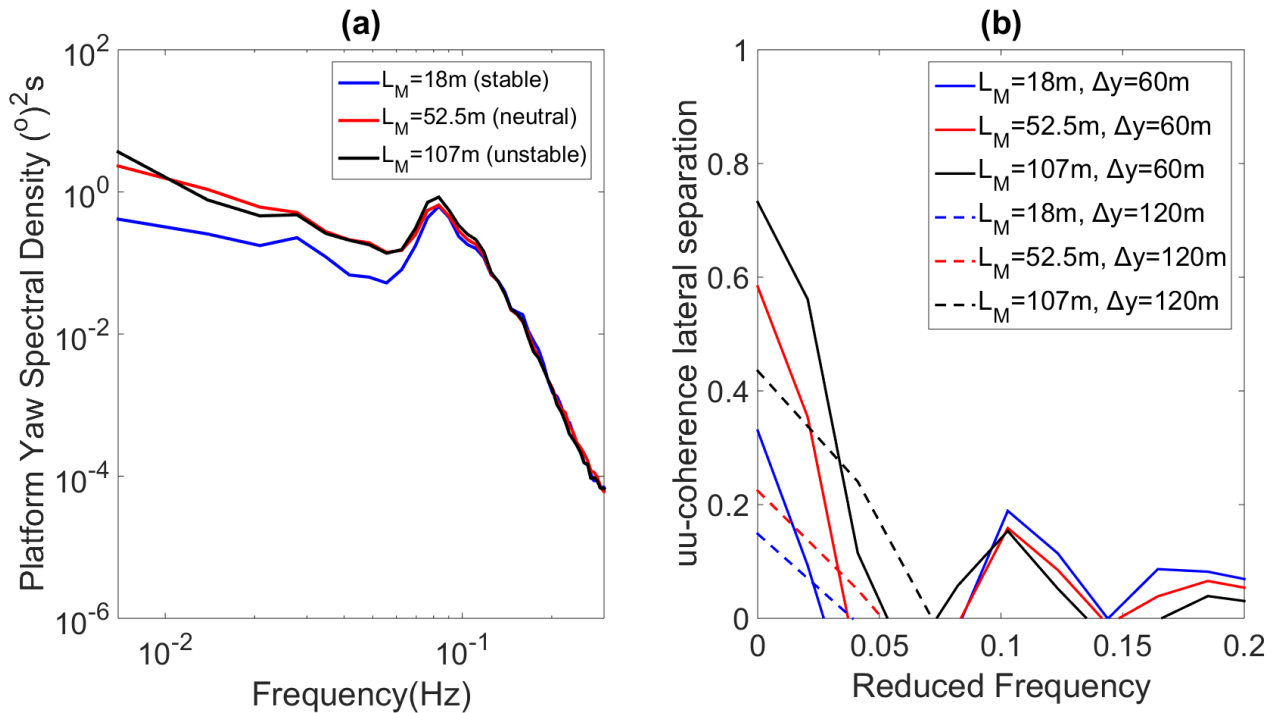


Figure 5.11 Comparison between (a) platform yaw spectral density and (b) u -component lateral coherence at different separations for different L_M at **rated** wind speed.

5.1.8. The IEC Kaimal Spectra & Coherence vs the Mann Spectral Tensor Model from the IEC Standards

This subchapter points out the main differences between the IEC Kaimal Spectra & Turbulence Model and the IEC Mann Model, by covering several aspects: the generated coherences, the generated

turbulences, and the significant influences on the OC3-Hywind loadings and motions. For theoretical insight of the two models can be found in Subchapter 2.4. It is important to notice that the term ‘IEC Mann’ refers to the Mann Model using the provided parameters values in the (IEC, 2005) under neutral stability conditions, while the term ‘IEC Kaimal’ refers to the IEC Kaimal Spectra & Turbulence Model.

The Turbulence Box (Generated) Coherences

The major difference between the IEC Kaimal Model and the IEC Mann Model *analytical* coherences is that the IEC Kaimal Model predicts the same lateral and vertical coherences at the same separation distance, while the IEC Mann Model captures different coherences for lateral and vertical separation at the same separation distance. This is also observed in the *generated* coherences (**Figure 5.1** and **Figure 5.2**). The similarity for both model is that both model predict the same *analytical* coherences for different wind speeds, while the *generated* coherences show slight increment in the coherences with wind speed (**Figure 5.1** and **Figure 5.2**). It is also noticed that the IEC Kaimal Model predicted *higher lateral coherences* for the three separations compared to the IEC Mann Model (**Figure 5.1** and **Figure 5.2**). While for the *vertical coherence*, the IEC Kaimal Model predicted *lower* coherence for the three separations than the IEC Mann Model. The tendency of the increasing difference between the two models at larger separations for both lateral and vertical coherences is also noticed (**Figure 5.1** and **Figure 5.2**).

The Generated Turbulence Box Properties

The generated turbulence standard deviations for the IEC Mann and IEC Kaimal models near the hub height from the simulations for below rated, rated, and above rated wind speeds are presented in **Table 5.3** given the same input (12% TI). **Table 5.3** shows that the generated values of σ_u , σ_v and σ_w for the IEC Mann Model were higher than the IEC Kaimal Model, except for σ_v at above rated where the IEC Kaimal Model resulted in higher value. This was caused by the difference in $\sigma_u : \sigma_v : \sigma_w$ ratio where the IEC Kaimal Model used $\sigma_u : \sigma_v : \sigma_w = 1 : 0.8 : 0.5$ while $\sigma_u : \sigma_v : \sigma_w = 1 : 0.7 : 0.5$ was used for the IEC Mann Model (IEC, 2005). The IEC Kaimal Model generates turbulences accordingly to reach the inputted target TI, while in the Mann Model, the given target TI was used to calculate the value of $\alpha \epsilon^{2/3}$ (**Table 2.10**) which resulted in higher σ_u for the Mann Model than the Kaimal Model provided the same input of TI (**Table 5.3**).

From the spectral density plots for the *u*, *v*, and *w* wind components comparing the IEC Kaimal & the IEC Mann Models (LC Group 2) at below rated (**Figure C.21**, **Figure C.23**, **Figure C.25**); rated (**Figure 4.5**, **Figure 4.6**, **Figure 4.7**); and above rated (**Figure C.22**, **Figure C.24**, **Figure C.26**); show that the IEC Mann Model resulted in higher spectral densities values than the IEC Kaimal Model for *all* mentioned wind components.

Table 5.3 Properties of the Generated Turbulence near the Hub Height

Model	σ_u (m/s)	TI _u (%)	σ_v (m/s)	σ_w (m/s)
Below Rated (8m/s)				
IEC Kaimal	0.952	11.9	0.758	0.468
IEC Mann	1.382	17.2	0.951	0.691
Rated (11.4m/s)				
IEC Kaimal	1.350	11.8	1.078	0.663
IEC Mann	1.671	14.6	1.161	0.839
Above Rated (15m/s)				
IEC Kaimal	1.770	11.8	1.416	0.866
IEC Mann	1.983	13.2	1.381	0.995

Influences on the OC3-Hywind Loadings and Motions

The IEC Mann Model predicted higher tower base fore-aft and tower top yaw damage equivalent loads than the IEC Kaimal Model at each different wind speeds (*Figure 4.34* and *Figure 4.35*). This is clear since fatigue damage is highly influenced by the turbulence level (σ_u) which in this case, the IEC Mann Model predicted higher σ_u for all wind speeds than the IEC Kaimal Model (*Table 5.3*).

Figure 4.39 showed that the simulated platform pitch motions were higher when using the IEC Mann Model compared to the IEC Kaimal Model. As mentioned earlier, the platform pitch motion is influenced by the vertical coherence, where higher vertical coherence results in higher platform pitch motions. This can be seen in *Figure 5.1* and *Figure 5.2* where the IEC Mann Model predicted higher vertical coherences—in general for all separations compared to the IEC Kaimal Model.

In *Figure 4.40*, it can be seen that the IEC Mann Model resulted in higher platform yaw motions than the IEC Kaimal Model. This finding is aligned with the study by Godvik (2016) for Hywind Scotland. By comparing the lateral coherences between the IEC Kaimal Model and the IEC Mann Model (*Figure 5.1* and *Figure 5.2*), we observe that the yaw motion is slightly affected by the lateral coherence, where lower lateral coherence (IEC Mann Model) resulted in higher platform yaw than the IEC Kaimal Model (higher lateral coherence).

It is hence can be concluded that the IEC Mann Model is *more conservative* than the IEC Kaimal Model when used to quantify the tower base fore-aft bending and tower top yaw damage equivalent loads, as well as the platform pitch and yaw motions. These results show that in order to reduce uncertainty and conservatism in the design of offshore wind turbines, it is imperative to validate these turbulence models given in the standards with offshore wind data, in particular with respect to spatial coherence. The two models given in the IEC standards are only valid under neutral conditions, and although we have tried to include some aspects of the atmospheric stability in the Mann Model by using fitted parameters, this still does not truly reflect the influence of the buoyant-generated turbulence, which is an added uncertainty. This can be seen when comparing the tower base fore-aft bending (*Figure 4.34*) and the tower top yaw damage equivalent loads (*Figure 4.35*), the cases from the Mann Model fitted to measurements (LC Group 1) predicted lower damage equivalent loads compared to the cases with given parameters from the IEC standards (LC Group 2) where atmospheric stability correction was not accounted for.

5.1.1.9 Influences of the Mean Wind Profile Accounting for Atmospheric Stability on the OC3-Hywind

The atmospheric stability condition influences the coherence as from stable to unstable conditions the coherences (lateral and vertical) are increasing. Atmospheric stability also affects the mean wind profile as well as the turbulence level. Under stable conditions, the turbulence level is the lowest but the wind shear is the highest, which is hypothesised to influence high loadings on the rotor area. On the other hand, under unstable conditions, the wind shear is the lowest yet the turbulence is significant which might contribute to an increase in fatigue on the structure.

In this study, both mean wind profile and the turbulences were varied due to different atmospheric stability conditions, and it was found that the stable mean wind profile increases damage equivalent loads for blade root flap-wise by 5% (*Figure 4.44*) compared to the uncorrected mean wind profile, which was the most significant impact observed. This value is relatively low compared to the study by Sathe & Bierbooms (2007) who found that the blade root fatigue increased by three times when the mean wind profile correction was performed. The reason could be because the turbulence was not

accounted for in their study i.e. constant wind was considered. The study done by Stava (2012) also showed that the influence of mean wind profile variations on the loadings of the wind turbine components was evident when turbulence intensity (TI) was set to 0%. The influence of mean wind profile was also the cause for the blade root edge-wise damage equivalent loads for LC Group 1 (*Figure 4.37*) which were not following the order of the generated turbulence level (σ_u). Furthermore, pitch/fore-aft modes were not influenced by the mean wind profile variation, yet the platform yaw was slightly affected in a way that the distribution of the mean, maximum positive & negative were shifted to positive values (unstable conditions) and negative value (stable conditions), as shown in *Figure 4.46*.

5.2 Conclusion

The influence of the spatial coherences in a turbulent wind field taking and varying atmospheric stability conditions on a spar-buoy FOWT (OC3-Hywind) loadings and motions was investigated in this study using HAWC2 aero-hydro-servo-elastic code. Two turbulence models given in the IEC Standards were also compared: the Mann Spectral Tensor Model and the IEC Kaimal Spectra & Exponential Coherence Model. By comparing the Mann Model cases using the fitted parameters (Sathe et al., 2013) which takes into account atmospheric stability condition through variation in L_M and $\alpha\epsilon^{2/3}$, the influence of the vertical coherence on the platform pitch motion was observed. It was seen that higher vertical coherence (unstable conditions) resulted in higher platform pitch motions, which was also observed by comparing the IEC Mann Model (neutral) and the IEC Kaimal (neutral) Model. Nonetheless, the tower base fore-aft fatigue damage was found to be relatively insensitive to the different turbulent cases and was observed the highest under neutral conditions. This may be because the buoyant-generated turbulence was not completely included in the measurement fitting as the Mann Model is valid only for neutral conditions. The OC3-Hywind pitch motion was excited in the wind turbulence (low) frequency range, and it was influenced by the blade-pitch controller activity.

It is found that the tower top yaw fatigue damage was sensitive with the turbulent wind energy content. Moreover, by comparing the Mann Model cases using the fitted parameters, the influence of the $\alpha\epsilon^{2/3}$ parameter was found to significantly influence the tower top yaw damage equivalent loads and slightly influence the platform yaw motions. Whereas the variations in the lateral coherence on the platform yaw motions and the tower top yaw damage equivalent loads were less clear. The influence of the lateral coherence on the OC3-Hywind yaw motion was observed when comparing the IEC Mann Model and the IEC Kaimal Model coherences, where lower lateral coherence (IEC Mann Model) resulted in higher platform yaw motion. In the OC3-Hywind setup, the platform was noted not to yaw excessively. Nonetheless, excessive yawing was observed in the case of Hywind Scotland which had a larger rotor and a shallower water depth (Godvik, 2016).

In general, the fatigue damage for the tower base fore-aft bending, tower top yaw, blade root flap-wise and edge-wise were the highest under neutral conditions as this case had the highest shear turbulence levels. If the buoyant-generated turbulence was properly accounted for in the turbulence models, then unstable conditions could result in the highest fatigue damage for the wind turbine components, however this was not accounted for in the turbulence models used in this study. The given values from the IEC standards are more conservative compared to the fitted parameters values even though the atmospheric stability effect was not accounted for in the IEC standards. The blade root flap-wise fatigue damage was shown to be sensitive with variation in the mean wind profile towards atmospheric stability, in particular under stable atmospheric conditions. The platform yaw motion was also slightly affected with the difference in mean wind profile. Finally, in this study the mooring line tensions were not

influenced by different turbulence load cases due to the implementation of the load-displacement relationship on the mooring tensions calculation which results in similar tension values.

5.3 Future Works & Recommendations

Given the restricted time and available data, some important aspects related to this study were not included. Thus, the following could be accounted for in further study:

- The utilisation of the *modified* Mann Spectral Tensor model to account for buoyant-generated turbulence
- A more extensive parametric study for the Mann Spectral Tensor Parameter Model can be done to confirm the impacts of each of the parameter on the generated turbulences and hence on the responses of the OC3-Hywind
- Comparing fitted-parameters from different sites for Mann Spectral Tensor model input, particularly for offshore sites, such as FINO1 platform
- A modified spar-buoy wind turbine model i.e. variation within the spar platform properties e.g. different drafts, mooring line configuration, or variation of the rotor diameter sizes can be studied to see the changes in the responses
- To accurately quantify the influence of the mean wind profile and to compare the behaviour of the wind turbine under a non-turbulent wind field, a steady/constant wind case should be performed
- To minimise uncertainty in the results, more than 6 simulations for each load cases could be considered, as well as various wind speed in the below rated and above rated region
- Accurate computation of the OC3-Hywind natural frequencies can be done with free-decay tests
- In order to validate the generated turbulence levels and spatial coherences for offshore conditions, further measurements are required to reduce uncertainty and conservatism in offshore wind turbine design.

References

- Air Pollution Training Institute. (accessed 2016). [image online] Available at: <https://www.shodor.org/os411/courses/411c/module06/unit01/page01.html> [Accessed February 2016].
- Ayee, G., Lowe, M., & Gereffi, G. (2009). *Chapter 11 – Wind Power: Generating Electricity and Employment*. [pdf online] Center on Globalization, Governance & Competitiveness (CGGC) Duke University. Available at: http://www.cggc.duke.edu/environment/climatesolutions/greeneconomy_Ch11_WindPower.pdf > [Accessed March 2016].
- Bakker, A. (2002). *Lecture 9 – Kolmogorov’s Theory: Applied Computational Fluid Dynamics*. [presentation online] Fluent Incorporation. Available at: https://www.google.no/url?sa=t&rct=j&q=&esrc=s&source=web&cd=4&cad=rja&uact=8&ved=0ahUKEwiP_-fRuIHMAhXFhiwKHRmCBwwQFgg5MAM&url=http%3A%2F%2Fwww.bakker.org%2Fdartmouth06%2Fengs150%2F09-kolm.ppt&usq=AFQjCNGbPJdrjZQPd1xZ8PixIFVCHVirw&sig2=qBHvaKcS818jesvnp-LoWQ&bvm=bv.119028448,d.bGg [Accessed April 2016].
- Blackwell, A.H., & Manar, E. *Atmosphere, Composition and Structure*. (Gale Cengage Learning) [image online] Available at: http://ic.galegroup.com/ic/scic/ImagesDetailsPage/ImagesDetailsWindow?total=5&query=OQE+%22Atmospheric+temperature%22&prodId=SCIC&>windowstate=normal&contentModules=&mode=view&limiter=&displayGroupName=Images&u=dc_demo&currPage=1&displayGroups=&source=&p=SCIC&action=e&catId=&view=docDisplay&documentId=GALE%7CCV2210008205 [Accessed February 2016].
- Burton, T., Sharpe, D., Jenkins, N., & Bossanyi, E. (2001). *Wind Energy Handbook*. John Wiley & Sons.
- Charnock, H. (1955). Wind Stress on a Water Surface. *Quarterly Journal of the Royal Meteorological Society*, [journal] 81(350), pp.639 – 640.
- Cheyne, E., Jakobsen, J.B., & Snæbjörnsson, J. (2015). Buffeting Response of a Bridge at the Inlet of a Fjord. *14th International Conference on Wind Engineering*. Porto Alegre, Brazil, 21-26 June 2015.
- Chougule, A. (2013). *Influence of Atmospheric Stability on the Spatial Structure of Turbulence*. Risø: Danmark Tekniske Universitet, PhD Dissertation.
- Chougule, A., Mann, J., & Kelly, M. (2014). Vertical Cross-Spectral Phases in Atmospheric Flow. *Journal of Physics: Conference Series*, [journal] 555(1).
- Chougule, A., Mann, J., Segalini, A., & Dellwik, E. (2015). Spectral Tensor Parameters for Wind Turbine Load Modelling from Forested and Agricultural Landscapes. *Wind Energy*, [journal] 18(3), pp. 469 – 481.

- Chougule, A. (2016). [interview]. In: NORCOWE (Norwegian Centre for Offshore Wind Energy), *Work Projects Meeting*. Grimstad, Norway, 10-11 May 2016.
- Courtney, M., & Troen, I. (1990). Wind Spectrum for One Year of Continuous 8 Hz
- Dekker, J. W. (1998). *European Wind Turbine Standards II: Executive Summary*. Netherlands: Energy Research Foundation ECN.
- DTU Wind Energy. (accessed 2016). *HAWC2 Online Course*. Danmarks Tekniske Universitet, unpublished. Available at: Danmarks Tekniske Universitet itslearning website <<https://windenergy.itslearning.com/ContentArea/ContentArea.aspx?LocationID=29&LocationType=1>> [Accessed 2016].
- DTU Wind Energy. (2013). HAWC2 Course – Wind, *HAWC2 Online Course*. Danmarks Tekniske Universitet, unpublished.
- Davenport, A.G. (1961). The Spectrum of Horizontal Gustiness near the Ground in High Winds. *Quarterly Journal of the Royal Meteorological Society*, [journal] 87(372), pp.194 – 211.
- Davenport, A.G. (1977). The Prediction of the Response of Structures to Gusty Wind. *Safety of Structures under Dynamic Loading*, 1, pp.257 – 284.
- Det Norske Veritas AS. (2010). *DNV-RP-C205: Environmental Conditions and Environmental Loads*. Oslo: Veritas Offshore Technology and Service AS, DNV.
- Diaz, A. P., Mikkelsen, T., Gryning, S. E., Hasager, C. B., Hahmann, A. N., Badger, M., Karagali, I., & Courtney, M. (2012). *Offshore Vertical Wind Shear: Final Report on NORSEWIND's Work Task 3.1*. DTU Wind Energy E, No. 0005. Danmark Tekniske Universitet: Risø, Denmark.
- Dyrbye, C., & Hansen, S.O. (1997). *Wind Loads in Structure*. West Sussex, England: John Wiley & Sons Ltd.
- Eliassen, L., Jakobsen, J. B., & Obhrai, C. (2012). The Effect of Atmospheric Stability on the Fatigue Life of Offshore Wind Turbines. In: ISOPE (International Society of Offshore and Polar Engineers), *The Twenty-second International Offshore and Polar Engineering Conference*. Rhodes, Greece, 17-22 June 2012.
- Eliassen, L. (2016). Influence of Spatial Characteristics of the Wind on a Bottom Fixed Wind Turbine. In: NORCOWE (Norwegian Centre for Offshore Wind Energy), *Science Meets Industry Stavanger*. Stavanger, Norway, 6 April 2016.
- Engineering Sciences Data Unit. (1986 & 2001). *ESDU 86010: Characteristics of Atmospheric Turbulence near the Ground. Part III: Variations in Space and Time for Strong Winds (Neutral Atmosphere)*. ESDU International.
- Gasch, R., & Tvele, J. (2011). *Wind Power Plants: Fundamentals, Design, Construction and Operation*. Springer Science & Business Media.

- Gavrilita, C., Spataru, S., Mosincat, I., Citro, C., Candela, I., & Rodriguez, P. (2012). Complete Methodology on Generating Realistic Wind Speed Profiles Based in Measurements. In: EA4EPQ (European Association for the Development of Renewable Energies, Environment and Power Quality), *International Conference on Renewable Energies and Power Quality*. Santiago de Compostela, Spain, 28-30 March 2012.
- Gipe, P. (1995). *Wind Energy Comes of Age (Vol. 4)*. John Wiley & Sons.
- Gnanasekaran, R., & Jöckel, S. (2015). Effect of Two Different Lateral and Vertical Wind Component Coherence Models on Wind Turbine Loads Using Three-Dimensional Wind Fields. In: EWEA (The European Wind Energy Association), *Europe's Premier Wind Energy Event*, [proceeding abstract]. Paris, France, 17-20 November 2015.
- Godvik, M. (2016). Influence of Wind Coherence on the Response of a Floating Wind Turbine. In: NORCOWE (Norwegian Centre for Offshore Wind Energy), *Science Meets Industry Stavanger*. Stavanger, Norway, 6 April 2016.
- Gryning, S., Batchvarova, E., Brümmner, B., Jørgensen, H., & Larsen, S. (2007). On the Extension of the Wind Profile over Homogeneous Terrain beyond the Surface Boundary Layer. *Boundary Layer Meteorology*, [journal], 124, pp.251 – 268.
- Hall, M., Buckham, B., & Crawford, C. (2014). Evaluating the Importance of Mooring Line Model Fidelity in Floating Offshore Wind Turbine Simulations. *Wind Energy*, [journal], 17(12), pp.1835 – 1853.
- Harrison, R. M. (2001). *Pollution: Causes, Effects and Control*. Royal Society of Chemistry.
- Hassan, G. (accessed 2016). *The Atmospheric Boundary Layer Shear Profile*. [image online] Available at: <<http://www.wind-energy-the-facts.org/best-practice-for-accurate-wind-speed-measurements-6.html>> [Accessed February 2016].
- Haver, S. H. (2015). Description of Ocean Waves, *OFF580 Marine Technology and Design*. Universitetet i Stavanger, unpublished.
- Holmes, J.D. (2001). *Wind Loading of Structures*. London, England: Spon Press.
- Højstrup, J., Larsen, S.E., & Madsen, P.H. (1989). Power Spectra of Horizontal Wind Components in the Neutral Atmospheric Surface Layer. *Annual Geophysicae*, [journal], special issue.
- Ingram, G. 2011. *Wind Turbine Blade Analysis using the Blade Element Momentum Method, Version 1.1*. [pdf online] Durham University: Creative Commons Attribution-ShareAlike 3.0 Unported License. Available at: <https://community.dur.ac.uk/g.l.ingram/download/wind_turbine_design.pdf> [Accessed March 2016].
- International Electrotechnical Commission. (2005). *IEC 61400-1: Wind Turbines – Part 1 Design Requirements*. Geneva: International Electrotechnical Commission, IEC.

- International Electrotechnical Commission. (2009). *IEC 61400-3: Wind Turbines – Part 3 Design Requirements for Offshore Wind Turbines*. Geneva: International Electrotechnical Commission, IEC.
- Jakobsen, J.B. (2014). Environmental Loads – Wind Load on Structures, *OFF580 Marine Technology and Design*. Universitetet i Stavanger, unpublished.
- Jonkman, J. (2007). *Dynamics Modelling and Loads Analysis of an Offshore Floating Wind Turbine*, [technical report]. Golden, CO, USA: National Renewable Energy Laboratory (NREL).
- Jonkman, J., & Buhl Jr, M.L. (2007). Loads Analysis of a Floating Offshore Wind Turbine Using Fully Coupled Simulation. In: *WindPower 2007 Conference & Exhibition*. Los Angeles, California, USA, 3-6 June 2007.
- Jonkman, J., Butterfield, S., Musial, W., & Scott, G. (2009). *Definition of a 5-MW Reference Wind Turbine for Offshore System Development*, [technical report]. Golden, CO, USA: National Renewable Energy Laboratory (NREL).
- Jonkman, J. (2010). *Definition of the Floating System for Phase IV of OC3*, [technical report]. Golden, CO, USA: National Renewable Energy Laboratory (NREL).
- Jonkman, J., & Musial, W. (2010). *Offshore Code Comparison Collaboration (OC3) for IEA Task 23 Offshore Wind Technology and Deployment*, [technical report]. Golden, CO, USA: National Renewable Energy Laboratory (NREL).
- Jonkman, J., & Matha, D. (2011). Dynamics of Offshore Wind Turbines—Analysis of the Three Concepts. *Wind Energy*, [journal], 14(4), pp.557 – 569.
- Jonkman, J. B., & Kilcher, L. (2012). *TurbSim User's Guide: Version 1.06.00*, [technical report]. Golden, CO, USA: National Renewable Energy Laboratory (NREL).
- Kaimal, J.C., Wyngaard, J.C., Izumi, Y., & Cotè, O.R. (1972). Spectral Characteristics of Surface-Layer Turbulence. *Quarterly Journal of the Royal Meteorological Society*, [journal] 81, pp.563 – 598.
- Karimirad, M., & Moan, T. (2010). Effect of Aerodynamic and Hydrodynamic Damping on Dynamic Response of Spar Type Floating Wind Turbine. In: EWEC, *European Wind Energy Conference and Exhibition*. Warsaw, Poland, 20-23 April 2010.
- Karimirad, M., & Moan, T. (2012). Wave- and Wind-Induced Dynamic Response of a Spar-Type Offshore Wind Turbine. *Journal of Waterway, Port, Coastal, and Ocean Engineering*, [journal] 138(1), pp.9 – 20.
- Kitaigorodskii, S. A., Donelan, M. A., Lumley, J. L., & Terray, E. A. (1983). Wave-Turbulence Interactions in the Upper Ocean. Part II: Statistical Characteristics of Wave and Turbulent Components of the Random Velocity Field in the Marine Surface Layer. *Journal of Physical Oceanography*, [journal] 13(11), pp.1988 – 1999.

- Krokeborg, J. (2001). Strait Crossings 2001. In: *Proceedings of the Fourth Symposium on Strait Crossings*. CRC Press.
- Lalanne, C. (2010). *Mechanical Vibration and Shock Analysis, Fatigue Damage (Vol. 4)*. New Jersey, USA: John Wiley & Sons.
- Larsen, T. J., & Hansen, A. M. (2007). *How 2 HAWC2, the User's Manual*. Risø National Laboratory, Denmark.
- Ma, Y., Hu, Z., & Xiao, L. (2015). Wind-wave Induced Dynamic Response Analysis for Motions and Mooring Loads of a Spar-Type Offshore Wind Turbine. *Journal of Hydrodynamics, Seri B [journal]* 26(6), pp.865 – 874.
- Mann, J. (1994). The Spatial Structure of Neutral Atmospheric Surface-Layer Turbulence. *Journal of fluid mechanics, [journal]* 273, pp.141 – 168.
- Mann, J. (1998). Wind Field Simulation. *Probabilistic Engineering Mechanics, [journal]*, (13)4, pp.269 – 282.
- Manwell, J. F., McGowan, J. G., & Rogers, A. L. (2010). *Wind Energy Explained: Theory, Design and Application*. John Wiley & Sons.
- Matha, D. (2009). *Model Development and Loads Analysis of an Offshore Wind Turbine on a Tension Leg Platform with a Comparison to Other Floating Turbine Concepts*. Stuttgart: Universität Stuttgart, Master Thesis.
- Monin, A. S., & Obukhov, A. (1954). Basic Laws of Turbulent Mixing in the Surface Layer of the Atmosphere. *Contrib. Geophys. Inst. Acad. Sci. USSR, [journal]* 24(151), pp.163 – 187.
- Moriarty, P.J., & Hansen, A.C. (2005). *AeroDyn Theory Manual*. Salt Lake City, Utah, USA: National Renewable Energy Laboratory (NREL).
- Motta, M., Barthelmie, R. J., & Vølund, P. (2005). The Influence of Non-Logarithmic Wind Speed Profiles on Potential Power Output at Danish Offshore Sites. *Wind Energy, [journal]* 8(2), pp.219 –236.
- Nielsen, F.G., Hanson, T.D., & Skaare, B. (2006). Integrated Dynamic Analysis of Floating Offshore Wind Turbines. In: *25th International Conference on Offshore Mechanics and Artic Engineering*. Hamburg, Germany, 4-9 June 2006.
- NORSOK Standard. (2007). *N-003: Actions and Action Effects*. Lysaker: Standards Norway AS.
- North, G. R., Pyle, J. A., & Zhang, F. (2014). *Encyclopedia of Atmospheric Sciences 2nd Edition (Volume 1)*. Elsevier.

- Obhrai, C., & Eliassen, L. (2016). Coherence of Turbulence Wind under Neutral Wind Condition at FINO1. In: EERA (European Energy Research Alliance) DeepWind'2016, *13th Deep Sea Offshore Wind R&D Conference*. Trondheim, Norway, 20-22 January 2016.
- Orcina. (Accessed April 2016). *Rayleigh Damping: Guidance*. [online OrcaFlex manual], Orcina Ltd. Available at: <<https://www.orcina.com/SoftwareProducts/OrcaFlex/Documentation/Help/Content/html/RayleighDamping,Guidance.htm>> [Accessed April 2016].
- Panofsky, H.A., & Lumley, J.L. (1964). *The Structure of Atmospheric Turbulence*. New York, USA: John Wiley & Sons Ltd.
- Panofsky, H. A., & Dutton, J. A. (1984). Atmospheric Turbulence: Models and Methods for Engineering Applications. In: *Atmospheric turbulence: Models and Methods for Engineering Applications*. John Wiley & Sons.
- Passon, P., Kühn, M., Butterfield, S., Jonkman, J., Camp, T., & Larsen, T.J. (2007). OC3—Benchmark Exercise of Aero-elastic Offshore Wind Turbine Codes. *Journal of Physics: Conference Series*, [journal], 75(1), p.012071.
- Physics Stack Exchange. (2015). [image online] Available at: < <http://physics.stackexchange.com/questions/143155/do-wind-turbines-convert-the-kinetic-energy-of-air>> [Accessed April 2016].
- Roy, S. B., & Sharp, J. (Accessed April 2016). *Why Atmospheric Stability Matters in Wind Assessment*. [online article], North American Wind Power Available at: <http://nawindpower.com/online/issues/NAW1301/FEAT_06_Why_Atmospheric.html> [Accessed April 2016].
- Saccoman, M. Y. J. (2015). *Coupled Analysis of a Spar Floating Wind Turbine Considering Both Ice and Aerodynamic Loads*. Trondheim: Norges Teknisk-Naturvitenskapelige Universitet, Master Thesis.
- Saranyasontorn, K., Manuel, L., & Veers, P.S. (2004). A Comparison of Standard Coherence Models for Inflow Turbulence with Estimates from Field Measurement. *Journal of Solar Energy Engineering*, [journal], 126(4), pp.1069 – 1082.
- Sathe, A., & Bierbooms, W. (2007). Influence of Different Wind Profiles due to Varying Atmospheric Stability on the Fatigue Life of Wind Turbines. *Journal of Physics: Conference Series* [journal], 75(1), p. 012056.
- Sathe, A., Gryning, S. E., & Peña, A. (2011). Comparison of the Atmospheric Stability and Wind Profiles at Two Wind Farm Sites over a Long Marine Fetch in the North Sea. *Wind Energy*, [journal] 14(6), pp. 767 – 780.
- Sathe, A., Mann, J., Barlas, T., Bierbooms, W.A.A.M., & van Bussel, G.J.W. (2013). Influence of Atmospheric Stability on Wind Turbine Loads. *Wind Energy*, [journal], 16(7), pp.1013 – 1032.

- Science & Technology Facilities Council (STFC). (accessed 2016). *Example of Wind Turbine Power Curve* [image online] Available at:
<http://www.elm.eri.rl.ac.uk/images/Example_Wind_Turbine_Power_Curve.png>
[Accessed February 2016].
- Simiu, E., & Scanlan, R.H. (1996). *Wind Effects on Structures*. USA: John Wiley & Sons Ltd.
- Skaare, B., Nielsen, F. G., Hanson, T. D., Yttervik, R., Havmøller, O., & Rekdal, A. (2015). Analysis of Measurements and Simulations from the Hywind Demo Floating Wind Turbine. *Wind Energy*, 18(6), pp.1105 – 1122.
- Solari, G. (1987). Turbulence Modelling for Gust Loading. *Journal of Structural Engineering*, [journal] 113(7), pp.1550 – 1569.
- Stava, O. M. (2012). *Fatigue Analysis of Offshore Wind Turbine*. Stavanger: Universitetet i Stavanger, Master Thesis.
- The Editors of Encyclopædia Britannica. (accessed 2016). *Richardson Number*. Encyclopædia Britannica [online article] Available at:
<<http://global.britannica.com/science/Richardson-number>> [Accessed April 2016].
- Tran, T., Kim, D., & Song, J. (2014). Computational Fluid Dynamic Analysis of a Floating Offshore Wind Turbine Experiencing Platform Pitching Motion. *Energies*, 7(8), pp.5011 – 5026.
- Twidell, J., & Gaudiosi, G. (2009). *Offshore Wind Power (Vol. 425)*. Multi-Science Publishing Company.
- U.S. Department of Energy. (2014). *Top 10 Things You Didn't Know About Offshore Wind Energy*. U.S. Department of Energy [online article] Available at:
<<http://energy.gov/articles/top-10-things-you-didn-t-know-about-offshore-wind-energy>>
- van der Tempel, J., & Molenaar, D. P. (2002). Wind Turbine Structural Dynamics—a Review of the Principles for Modern Power Generation, Onshore and Offshore. *Wind Engineering*, 26(4), pp.211 – 222.
- van der Tempel, J. (2006). *Design of Support Structures for Offshore Wind Turbines*. PhD Dissertation. Delft University. Available at:
<http://www.tudelft.nl/fileadmin/UD/MenC/Support/Internet/TU_Website/TU_Delft_portal/Onderzoek/Kenniscentra/Kenniscentra/DUWIND/Dissertations/doc/JvdT_final.pdf> [Accessed April 2016].
- Veers, P. S. (1988). *Three-Dimensional Wind Simulation*. [report No. SAND-88-0152C; CONF-890102-9], Sandia National Laboratories, Albuquerque, New Mexico, USA.
- Viguera-Rodríguez, A., Sørensen, P., & Viedma, A. (2006). Spectral Coherence Models for the Wind Speed in Large Wind Farms. In: *Proceedings of the 2nd Ph. D. Seminar on Wind Energy in Europe*. European Academy of Wind Energy. Roskilde, Denmark.

- Viguera-Rodríguez, A., Sørensen, P., Viedma, A., Donovan, M. H., & Lázaro, E. G. (2012). Spectral Coherence Model for Power Fluctuations in a Wind Farm. *Journal of Wind Engineering and Industrial Aerodynamics*, [journal], 102, pp.14 – 21.
- von Kármán, T. (1948). Progress in the Statistical Theory of Turbulence. *Proceedings of the National Academy of Sciences of the United States of America*, [proceeding journal], 34(11), pp.530 – 539.
- Warwick School of Engineering. (2011) [image online] Available at: <<http://www2.warwick.ac.uk/fac/sci/eng/meng/waveenergy/>> [Accessed February 2016].
- Wayman, E.N., Sclavounos, P.D., Butterfield, S., Jonkman, J., & Musial, W. (2006). Coupled Dynamic Modelling of Floating Wind Turbine Systems. In: *Offshore Technology Conference*. Houston, Texas, USA, 1-4 May 2006.
- Westerhellweg, A., Canadillas, B., & Neumann, T. (2010). Direction Dependency of Offshore Turbulence Intensity in the German Bight. In: *10th German Wind Energy Conference DEWEK 2010*. Bremen, Germany, 17-18 November 2010.
- wikiversity.org. (accessed 2016). [image online] Available at: <https://en.wikiversity.org/wiki/Fluid_Mechanics_for_MAP/Dimensional_Analysis> [Accessed April 2016].
- Wilson, R. E., & Lissaman, P. B. (1974). *Applied Aerodynamics of Wind Power Machines*. (No. PB-238595). Oregon State University, Corvallis, USA.
- Yde, A., anyd@dtu.dk. (2016). *HAWC2 – Eigenfrequencies Computations for floater (OC3-Hywind)*. [email] Message to R M. Putri (rm.putri@stud.uis.no). Sent Wednesday 1 June 2016: 11:41. Available at: <<https://outlook.office.com/owa/?realm=uis.no>> [Accessed June 2016].

A. Modelling of the OC3-Hywind in HAWC2

A.1 Basics of Modelling in HAWC2

To perform a simulation using HAWC2, a main input file and several supporting input files are required. The main input file has the extension of ‘.htc’ and known as the htc main file, whereas the supporting input files has various extensions depending on the contained information. *Table A.2* sums all input files that could be used in HAWC2 simulations. Each simulation case must have an htc file, yet the required supporting input files differ from one simulation case to another, depending on the wind turbine types and the environmental conditions considered. The supporting input files are later to be ‘called’ inside the htc main file.

An htc file contains main command blocks governing the whole simulation processes, from input processing to dll interface to writing output result. These main command blocks are listed in *Table A.3* and can be either included or omitted accordingly, with no compulsion of certain command blocks to be present. The generated outputs will be written according to the instruction given inside the htc file. Each main command blocks has its own sub-command blocks, which detail can be found in reference Larsen & Hansen (2007).

The supporting input files are in general simplification of the htc main file, that is separation of a long-detailed htc file into some different files. Examples of the supporting input files’ content includes the structural properties data and sub-command blocks.

After a simulation running is completed, the outputs generated by HAWC2 will be stored in separate files with different extensions. The main output file has the extension of ‘.sel’, known as the sel file, contains written time series result as specified in the ‘output’ main command block inside the htc file. The time series result can be visualised (plotted) by the use of Pdap, as well as Matlab or Python. Pdap is a complementary separated program from HAWC2 serving as not only result data examination but also post-processing and pre-processing, as it is capable to generate structural properties input files through Python scripting. Aside from that, the utilisation of Matlab and Python as post-processing tools is also possible.

Other outputs that are not written inside the sel file are written in separate output files with ‘.dat’ and ‘.log’ file extensions including the eigen-frequencies result, animation of the simulation, the calculated structural properties, and the log history; each is explained in *Table A.1*. In addition to Pdap, another complementary separated program from HAWC2 called Animation.exe is provided to visualise the real-time response of the simulated wind turbine by reading the animation output file.

Table A.1 Main Output Files

Output Files (extension)	Description
(sel)	The main output file, containing time series of parameters described in the ‘output’ main command block of htc file.
(log)	Log history of the simulation, giving information regarding the progress of the simulation as well as error sources during simulation.
(dat)	The computed eigen-frequencies, calculated structural properties, and animation outputs have this extension name. The calculated structural properties output contains information of the beam moment inertia, area, etc that can be accessed through notepad program, whereas for the animation and eigen-frequencies output can be accessed with Animation.exe program.

Table A.2 Input Files for HAWC2

Input Files (extension)	Description
(.htc)	Main input file containing command blocks, general information regarding the structure, environmental conditions, dlls, and outputs.
st(.txt)	Supporting input file containing the main bodies' structural data such as modulus of elasticity, shear modulus, cross section moment of inertia, stiffness, etc. Applicable for all main bodies defined.
ae(.txt)	Supporting input file containing the blades aerofoil layout as a function of radial position including thickness-to-chord ratio, chord length, twist angle, and aerodynamic profile number (which is linked to pc.txt file).
pc(.txt)	Supporting input file containing information about the blades' steady profile coefficients as a function of the angle of attack including lift, drag, and moment coefficient.
(.opt)	Supporting input file containing operational data such as wind speed, pitch angle, rotational speed, power production, and aerodynamic thrust.
(.inp)	Supporting input file containing data for wave kinematics computation such as wave theory used, wave stretching, directional spreading, wave spectrum parameters (H_s , T_p , γ) and current.
(.stc)	Supporting input file containing data for structural properties such as modulus of elasticity, shear modulus, cross section moment of inertia, stiffness, etc. Usually used for tripod or jacket substructure.
(.st)	Supporting input file containing stiffness data. Usually used for semisubmersible floating wind turbine.
(.inc)	Supporting input file containing thorough information, especially for the mooring and its related dll.
(.bin)	Supporting input file containing turbulence data for Mann method.
(.int)	Supporting input file containing turbulence data for Veers method, from Flex5.
(.hydro)	Supporting input file containing information regarding structural hydrodynamic properties such as buoyancy, drag and mass coefficients, etc. Typically used for floating substructure.
(.mbdy)	Supporting input file containing additional structural data for main bodies such as damping and sectional division. Typically used for semisubmersible floating substructure.
Input Files (extension)	Description
(.res)	Supporting input file from Mimosa Software developed by DNV-GL for mooring station keeping of spar-buoy type.
(.txt)	Supporting input file containing data as defined by user to support structural modelling (e.g. floater data).
(.dat)	Supporting input file containing data as defined by user to support structural modelling (e.g. soil data, hydrodynamic data, mooring, etc).

Table A.3 Main Command Blocks in the htc Main File

Main Command Block	Description
simulation	Setting up simulation properties including duration of the simulation, convergence limit, animation and log output files.
new_htc_structure	Specifying structural analysis output files such as the eigen-frequencies of the system, etc.
wind	Containing information regarding the wind condition such as mean wind speed, wind profile, wind turbulence, wind wakes, etc.
aero	Specifying the blades’ structural and aerodynamic properties such as aerodynamic model, tip-loss correction, induction correction, etc.
hydro	Specifying hydrodynamic-related parameters, including seawater properties, seawater level, seabed level, (floating) substructure’s hydrodynamic-related properties, etc.
dll	As a connector to the external dll for the blade & rotor controllers, mooring forces, wave kinematics, etc.
output	Defining which parameters or sensors to be written in the output file, such as the rotor thrust, rotor torque, power production, forces on towers, forces on the blades, displacement of floaters, mooring forces, the generated wave field, etc.

A.2 The OC3-Hywind Properties

The blades, hub, nacelle, and control system properties of the OC3-Hywind are given as the following.

A.2.1. Blade Structural Properties

The RNA part of OC3-Hywind adopts the NREL 5MW offshore wind turbine, which is three-bladed having the same structural and aerodynamic properties for each blade. The undistributed structural properties for each blade are given in **Table A.4** while its aerodynamic properties are presented in **Table A.5**.

Table A.4 General Properties of NREL 5MW Offshore Wind Turbine Blades (Jonkman, 2007)

Parameter	Value	Unit
Length (relative to root along pre-coned axis)	61.5	m
Mass scaling factor	4.536	%
Overall integrated mass	17,740	kg
Second mass moment of inertia (relative to root)	11,776,047	kg m ²
First mass moment of inertia (relative to root)	363,231	kg m
Centre of mass (relative to root along pre-coned axis)	20.475	m
Structural damping ratio (all modes)	0.477465	%

Table A.5 NREL 5MW Offshore Wind Turbine Blades Distributed Aerodynamic Properties (Jonkman, 2007)

Node	Radial position from root (m)	Element length (m)	Twist angle (°)	Chord length (m)	Aerofoil table
1	2.8667	2.7333	13.308	3.542	Cylinder1
2	5.6000	2.7333	13.308	3.854	Cylinder1
3	8.3333	2.7333	13.308	4.167	Cylinder2
4	11.7500	4.1000	13.308	4.557	DU40_A17
5	15.8500	4.1000	11.480	4.652	DU35_A17
6	19.9500	4.1000	10.162	4.458	DU35_A17
7	24.0500	4.1000	9.011	4.249	DU30_A17
8	28.1500	4.1000	7.795	4.007	DU25_A17

Node	Radial position from root (m)	Element length (m)	Twist angle (°)	Chord length (m)	Aerofoil table
9	32.2500	4.1000	6.544	3.748	DU25_A17
10	36.3500	4.1000	5.361	3.502	DU21_A17
11	40.4500	4.1000	4.188	3.256	DU21_A17
12	44.5500	4.1000	3.125	3.010	NACA64_A17
13	48.6500	4.1000	2.319	2.764	NACA64_A17
14	52.7500	4.1000	1.529	2.518	NACA64_A17
15	56.1667	2.7333	0.863	2.313	NACA64_A17
16	58.9000	2.7333	0.370	2.086	NACA64_A17
17	61.6333	2.7333	0.106	1.419	NACA64_A17

The aerodynamic properties for each blade are divided for 17 segments with 17 nodes, each represents the centre point of the blade segment where its radial position is counted from the rotor centre (hub), not the blade root. The total blade length (61.5m) is found by summing all the element lengths for the 17 nodes in *Table A.5*. The aerodynamic properties for each blade segment corresponds to different aerofoil type/table with different characteristic drag and lift properties that are thoroughly presented in reference Jonkman (2007).

A.2.2. Hub and Nacelle Properties

The hub and nacelle properties of the 5MW NREL offshore wind turbine properties are summarised in *Table A.6*.

Table A.6 Properties of NREL 5MW Offshore Wind Turbine Nacelle and Hub (Jonkman, 2007)

Parameter	Value	Unit
Elevation of yaw bearing above ground	87.6	m
Vertical distance along yaw axis from yaw bearing to shaft	1.96256	m
Distance along shaft from hub centre to yaw axis	5.0191	m
Distance along shaft from hub centre to main bearing	1.912	m
Hub mass	56,780	kg
Hub inertia (with respect to low-speed shaft)	115,926	kg m ²
Nacelle mass	240,000	kg
Nacelle inertia about yaw axis	2,607,890	kg m ²
Nacelle centre of mass location downwind of yaw axis	1.9	m
Nacelle centre of mass location above yaw bearing	1.75	m
Equivalent nacelle-yaw-actuator linear-spring constant	9,028,320,000	N m/rad
Equivalent nacelle-yaw-actuator linear-damping constant	19,160,000	N m/(rad/s)
Nominal nacelle-yaw rate	0.3	°/s

A.2.3. Control System Properties

The main purpose of the control system implemented in the NREL 5MW offshore wind turbine is controlling the blade pitch angle in such way to maintain constant rotor speed as the incoming wind speed exceeds the rated speed. The NREL 5MW offshore wind turbine adopts the conventional generator torque controller and full-span rotor-collective blade-pitch controller. Yet, this conventional control system has significant effect to the floating wind turbine motions and structural responses. OC3-Hywind has the modified control system of the NREL 5MW offshore wind turbine to prevent negative damping effect (Jonkman, 2010), which includes (i) gains reduction through selection of lower natural frequency of the controller response and (ii) generator-torque control strategy for wind speed above rated. *Table A.7* describes the modified NREL 5MW control system for OC3-Hywind.

Table A.7 Properties of Modified NREL 5MW for OC3-Hywind Control System (Jonkman, 2007)

Parameter	Value	Unit
Proportional gain at minimum blade-pitch setting	0.006275604	second
Integral gain at minimum blade-pitch setting	0.0008965149	-
Constant (rated) generator torque	43,093.55	Nm

A.3 Input Files

The required input files to perform simulations using HAWC2 attached in this section are the main htc file, the 64-bit Mann Turbulence Generator input file, and the Mimosa output file for mooring forces computations.

A.3.1. A Sample of the htc Main Input File

The following is a sample of an htc main input file for the case of the fitted-Mann under unstable condition at wind speed below rated.

```

;oc3_monopile_phase_1 version 5, 03-11-13, Larh
begin Simulation;
time_stop 3600.0 ;
solvertype 1 ; (newmark)
on_no_convergence continue ;
convergence_limits 5E3 1.0 1E-7 ;
logfile ./log/sparbuoy_unstable_BR_sathe_2.log ;
animation ./anim/sparbuoy_unstable_BR_sathe_2.dat;
;
begin newmark;
deltat 0.02;
end newmark;
end simulation;
;
begin new_htc_structure;
; beam_output_file_name ./log/sparbuoy_unstable_BR_sathe_2.dat; Optional - Calculated beam properties of the bodies are written to file
; body_output_file_name ./log/sparbuoy_unstable_BR_sathe_2.dat; Optional - Body initial position and orientation are written to file
; struct_inertia_output_file_name ./log/sparbuoy_unstable_BR_sathe_2.dat;
; body_eigenanalysis_file_name ./eigenfrq/sparbuoy_unstable_BR_sathe_2_eigen.dat;
; structure_eigenanalysis_file_name ./eigenfrq/sparbuoy_unstable_BR_sathe_2_strc_eigen.dat;
;-----
;
begin main_body;
name floater ;
type timoschenko ;
nbodies 1 ;
node_distribution c2_def ;
damping 0.0 0.0 0.0 1.0E-3 1.0E-3 1.0E-3 ;
begin timoschenko_input;
filename ./data/floater.txt ;
set 1 2 ;
end timoschenko_input;
begin c2_def; Definition of centerline (main_body coordinates)
nsec 8 ;
sec 1 0.0 0.0 0.00 0.0 ; Bottom of floater
sec 2 0.0 0.0 -30.00 0.0 ; COG
sec 3 0.0 0.0 -50.00 0.0 ; Anchor point (located 70.0 m below SWL)
sec 4 0.0 0.0 -60.00 0.0 ;
sec 5 0.0 0.0 -108.00 0.0 ; Start of conical section
sec 6 0.0 0.0 -116.00 0.0 ; End of cinocal section
sec 7 0.0 0.0 -120.00 0.0 ; Water line
sec 8 0.0 0.0 -130.00 0.0 ; Top of floater, interface to tower
end c2_def ;
end main_body;
;
begin main_body;
name floater_dummy ; Dummy structure with other element coordinate than the tower, for output only
type timoschenko ;
nbodies 1 ;
node_distribution c2_def ;
damping_posdef 2.00E-05 2.00E-05 2.00E-04 3.00E-06 3.00E-06 2.00E-05;
gravity 9.80665;
begin timoschenko_input;
filename ./data/NREL_5MW_st.txt ;
set 4 2 ;
end timoschenko_input;
begin c2_def; Definition of centerline (main_body coordinates)
nsec 2;
sec 1 0.0 0.0 0.0 0.0 ; x,y,z,twist
sec 2 0.0 0.0 0.1 0.0 ;
end c2_def ;
end main_body;
;
begin main_body;
name tower ;
type timoschenko ;
nbodies 1 ;
node_distribution c2_def ;
damping 0.0 0.0 0.0 2.59E-3 2.59E-3 1.0E-3 ;
begin timoschenko_input;
filename ./data/Reinforced_80m_Tower_st.txt ;
set 1 1 ;
end timoschenko_input;
begin c2_def; Definition of centerline (main_body coordinates)
nsec 11 ;
sec 1 0.0 0.0 0.00 0.0 ; Tower bottom
sec 2 0.0 0.0 -7.76 0.0 ;
sec 3 0.0 0.0 -15.52 0.0 ;
sec 4 0.0 0.0 -23.28 0.0 ;
sec 5 0.0 0.0 -31.04 0.0 ;
sec 6 0.0 0.0 -38.80 0.0 ;
sec 7 0.0 0.0 -46.56 0.0 ;
sec 8 0.0 0.0 -54.32 0.0 ;
sec 9 0.0 0.0 -62.08 0.0 ;
sec 10 0.0 0.0 -69.84 0.0 ;
sec 11 0.0 0.0 -77.60 0.0 ; Tower top
end c2_def ;
end main_body;
;
begin main_body;
name towertop ;
type timoschenko ;
nbodies 1 ;
node_distribution c2_def ;
damping_posdef 9.025E-06 9.025E-06 8.0E-05 8.3E-06 8.3E-06 8.5E-05 ;
damping_posdef 0.0 0.0 0.0 3.00E-05 3.00E-05 2.00E-04 ;
concentrated_mass 2 0.0 1.9 0.21256 2.4E5 1741490.0 1.7E5 1741490.0 ; Nacelle mass and inertia
begin timoschenko_input;
filename ./data/NREL_5MW_st.txt ;
set 2 1 ;
end timoschenko_input;

```

```

begin c2_def;          Definition of centerline (main_body coordinates)
nsec 2;
sec 1 0.0 0.0 0.0    0.0 ; x,y,z,twist
sec 2 0.0 0.0 -1.96256 0.0 ;
end c2_def ;
end main_body;
;
begin main_body;
name shaft ;
type timoschenko ;
nbodies 1 ;
node_distribution c2_def ;
damping_posdef 7.00E-3 7.00E-03 7.00E-02 3.48E-04 3.48E-04 1.156E-03 ;
damping_posdef 0.0 0.0 0.0 4.65E-04 4.65E-04 7.0725E-03 ; "tuned by Anyd 23/5/13 to 31.45 log decr. damping for free free with stiff rotor and tower"
concentrated_mass 1 0.0 0.0 0.0 0.0 0.0 5025497.444 ;generator equivalent slow shaft
concentrated_mass 5 0.0 0.0 0.0 56780 0.0 0.0 115926 ; hub mass and inertia;
begin timoschenko_input;
filename ./data/NREL_5MW_st.txt ;
set 3 1 ;
end timoschenko_input;
begin c2_def;          Definition of centerline (main_body coordinates)
nsec 5;
sec 1 0.0 0.0 0.0    0.0 ; Tower top x,y,z,twist
sec 2 0.0 0.0 1.0    0.0 ;
sec 3 0.0 0.0 2.0    0.0 ;
sec 4 0.0 0.0 3.1071 0.0 ; Main bearing
sec 5 0.0 0.0 5.0191 0.0 ; Rotor centre
end c2_def ;
end main_body;
;
begin main_body;
name hub1 ;
type timoschenko ;
nbodies 1 ;
node_distribution c2_def ;
damping_posdef 0.0 0.0 0.0 3.00E-06 3.00E-06 2.00E-05;
begin timoschenko_input;
filename ./data/NREL_5MW_st.txt ;
set 4 1 ;
end timoschenko_input;
begin c2_def;          Definition of centerline (main_body coordinates)
nsec 2;
sec 1 0.0 0.0 0.0    0.0 ; x,y,z,twist
sec 2 0.0 0.0 1.5    0.0 ;
end c2_def ;
end main_body;
;
begin main_body;
name hub2 ;
copy_main_body hub1;
end main_body;
;
begin main_body;
name hub3 ;
copy_main_body hub1 ;
end main_body;
;
begin main_body;
name blad1 ;
type timoschenko ;
nbodies 9 ;
node_distribution c2_def;
damping 3.5e-2 5.5e-4 5.0e-4 3.0e-4 0.5e-3 5.5e-3 ;
damping_posdef 0.0 0.0 0.0 1.41E-03 2.39E-03 4.5E-05 ;
begin timoschenko_input ;
filename ./data/NREL_5MW_st.txt ;
set 5 1 ;          set subset
end timoschenko_input;
begin c2_def;          Definition of centerline (main_body coordinates)
nsec 19 ;
sec 1 0.0000 0.0000 0.000 0.000 ; x.y.z. twist
sec 2 -0.0027 0.0006 1.367 -13.308 ;
sec 3 -0.1057 0.0250 4.100 -13.308 ;
sec 4 -0.2501 0.0592 6.833 -13.308 ;
sec 5 -0.4592 0.1086 10.250 -13.308 ;
sec 6 -0.5699 0.1157 14.350 -11.480 ;
sec 7 -0.5485 0.0983 18.450 -10.162 ;
sec 8 -0.5246 0.0832 22.550 -9.011 ;
sec 9 -0.4962 0.0679 26.650 -7.795 ;
sec 10 -0.4654 0.0534 30.750 -6.544 ; 50% blade radius
sec 11 -0.4358 0.0409 34.850 -5.361 ;
sec 12 -0.4059 0.0297 38.950 -4.188 ;
sec 13 -0.3757 0.0205 43.050 -3.125 ;
sec 14 -0.3452 0.0140 47.150 -2.319 ;
sec 15 -0.3146 0.0084 51.250 -1.526 ;
sec 16 -0.2891 0.0044 54.667 -0.863 ;
sec 17 -0.2607 0.0017 57.400 -0.370 ;
sec 18 -0.1774 0.0003 60.133 -0.106 ;
sec 19 -0.1201 0.0000 61.500 -0.000 ;
end c2_def ;
end main_body;
;
begin main_body;
name blade2 ;
copy_main_body blad1;
end main_body;
;
begin main_body;
name blade3 ;
copy_main_body blad1 ;
end main_body;
;

```

```

begin orientation;
;
begin base;
body floater;
inipos 0.0 0.0 120.0 ;
body_eulerang 0.0 0.0 0.0;
end base;
;
begin relative;
body1 floater 7;
body2 floater_dummy 1;
body2_eulerang 0.0 0.0 0.0;
end relative;
;
begin relative;
body1 floater last;
body2 tower 1;
body2_eulerang 0.0 0.0 0.0;
end relative;
;
begin relative;
body1 tower last;
body2 tovertop 1;
body2_eulerang 0.0 0.0 0.0;
end relative;
;
begin relative;
body1 tovertop last;
body2 shaft 1;
body2_eulerang 90.0 0.0 0.0;
body2_eulerang 5.0 0.0 0.0;    5 deg tilt angle
body2_ini_rotvec_d1 0.0 0.0 -1.0 0.5 ; body initial rotation velocity x,y,z,angle velocity[rad/s] (body 2 coordinates)
end relative;
;
begin relative;
body1 shaft last;
body2 hub1 1;
body2_eulerang -90.0 0.0 0.0;
body2_eulerang 0.0 180.0 0.0;
body2_eulerang 2.5 0.0 0.0;    2.5deg cone angle
end relative;
;
begin relative;
body1 shaft last;
body2 hub2 1;
body2_eulerang -90.0 0.0 0.0;
body2_eulerang 0.0 60.0 0.0;
body2_eulerang 2.5 0.0 0.0;    2.5deg cone angle
end relative;
;
begin relative;
body1 shaft last;
body2 hub3 1;
body2_eulerang -90.0 0.0 0.0;
body2_eulerang 0.0 -60.0 0.0;
body2_eulerang 2.5 0.0 0.0;    2.5deg cone angle
end relative;
;
begin relative;
body1 hub1 last;
body2 blade1 1;
body2_eulerang 0.0 0.0 0;
end relative;
;
begin relative;
body1 hub2 last;
body2 blade2 1;
body2_eulerang 0.0 0.0 0.0;
end relative;
;
begin relative;
body1 hub3 last;
body2 blade3 1;
body2_eulerang 0.0 0.0 0.0;
end relative;
;
end orientation;
-----
begin constraint;
;
begin fix0; fixed to ground in translation and rotation of node 1
body floater;
end fix0;
;
begin fix1; fixed relative to other body in translation and rotation
body1 floater last;
body2 tower 1;
end fix1;
;
begin fix1;
mbody1 floater 7;
mbody2 floater_dummy 1;
end fix1;
;
begin fix1;
body1 tower last ;
body2 tovertop 1;
end fix1;
;
begin bearing1; free bearing
name shaft_rot;
body1 tovertop last;
body2 shaft 1;
bearing_vector 2 0.0 0.0 -1.0;    x=coo (0=global.1=body1.2=body2) vector in body2 coordinates where the free rotation is present
end bearing1;
;
begin fix1;
body1 tovertop last ;
body2 shaft 1;
end fix1;
;

```

```

begin fix1;
    body1 shaft last ;
    body2 hub1 1;
end fix1;
;
begin fix1;
    body1 shaft last ;
    body2 hub2 1;
end fix1;
;
begin fix1;
    body1 shaft last ;
    body2 hub3 1;
end fix1;
;
begin bearing2;
    name pitch1;
    body1 hub1 last;
    body2 blade1 1;
    bearing_vector 2 0.0 0.0 -1.0;
end bearing2;
;
begin bearing2;
    name pitch2;
    body1 hub2 last;
    body2 blade2 1;
    bearing_vector 2 0.0 0.0 -1.0;
end bearing2;
;
begin bearing2;
    name pitch3;
    body1 hub3 last;
    body2 blade3 1;
    bearing_vector 2 0.0 0.0 -1.0;
end bearing2;
;
end constraint;
;
end new_htc_structure;
-----
continue_in_file ./htc/mooring.inc ;
-----
begin hydro;
begin water_properties;
    rho 1025 ; kg/m^3
    gravity 9.816 ; m/s^2
    mw1 0.0 ;
    mudlevel 320.0 ;
    water_kinematics_dll ./wkin_dll.dll ./htc_hydro/ireg_airy_h6_t12.inp ;
end water_properties;
;
begin hydro_element;
    mbody_name floater ;
    update_states 1;
    buoyancy 1;
    hydrosections auto 4 ; distribution of hydro calculation points from sec 1 to nsec
    nsec 7; z Cm Cd A Aref width dr/dz Cd_a (quad) Cm_a Cd_a_lin Aif
sec 0.000 0.969954 0.600 69.398 69.398 9.400 0.000 69.398 2.0 ;
sec 107.999 0.969954 0.600 69.398 69.398 9.400 0.000 ;
sec 108.001 0.969954 0.600 69.398 69.398 9.400 -0.181 ;
sec 115.999 0.969954 0.600 33.183 33.183 6.500 -0.181 ;
sec 116.000 0.969954 0.600 33.183 33.183 6.500 0.000 ;
sec 120.000 0.969954 0.600 33.183 33.183 6.500 0.000 ;
sec 130.000 0.969954 0.600 33.183 33.183 6.500 0.000 ;
end hydro_element;
;
end hydro;
-----
begin wind ;
density 1.225 ; to be checked
wsp 8.0 ;
tint 0.12;
horizontal_input 1 ; 0=false, 1=true
windfield_rotations 0.0 0.0 0.0 ; yaw, tilt, rotation
center_pos0 0.0 0.0 -90.00 ;
shear_format 3 0.04 ; 0=none, 1=constant, 2=log, 3=power, 4=linear
turb_format 1 ; 0=none, 1=mann, 2=flex
tower_shadow_method 3 ; 0=none, 1=potential flow, 2=jet
; scale_time_start 0 ;
; wind_ramp_factor 0.0 [t0] [wsp factor] 1.0 ;
; [gust] iec_gust [gust_type] [gust_A] [gust_phi0] [gust_t0] [gust_T] ;
;
begin mann;
;create_turb_parameters 98.0 0.0315 2.25 1027 1.0; L, alfaeps, gamma, seed, high freq compensation
filename_u ./turb/unstable_BR_sathe_2_u.bin ;
filename_v ./turb/unstable_BR_sathe_2_v.bin ;
filename_w ./turb/unstable_BR_sathe_2_w.bin ;
box_dim_u 32768 0.87890625 ;
box_dim_v 32 5;
box_dim_w 32 5;
;std_scaling 1.0 0.7 0.5 ;
dont_scale 1.0;
end mann;
;
begin tower_shadow_potential_2;
tower_mbody_link tower;
nsec 2;
radius 0.0 3.0 ;
radius 77.6 1.935 ;
end tower_shadow_potential_2;
end wind;
;
-----

```

```

;
begin aero ;
nblades 3;
hub_vec shaft -3 ;          rotor rotation vector (normally shaft composant directed from pressure to sustion side)
link 1 mbody_c2_def blade1;
link 2 mbody_c2_def blade2;
link 3 mbody_c2_def blade3;
ae_filename      ./data/NREL_5MW_ae.txt;
pc_filename      ./data/NREL_5MW_pc.txt;
induction_method 1 ;      0=none, 1=normal
aerocalc_method 1 ;      0=ingen aerodynamic, 1=med aerodynamic
aerosections     30 ;
ae_sets          1 1 1;
tiploss_method   1 ;      0=none, 1=prandtl
dynstall_method  2 ;      0=none, 1=stig øye method,2=mhh method
end aero ;

;
; begin aerodrag ; aerodynamic drag was no used in the OC3 project but should be turned on in other simulations
; begin aerodrag_element ;
; mbody name tower;
; aerodrag_sections uniform 10 ;
; nsec 2 ;
; sec 0.0 0.6 6.0 ; tower bottom
; sec 87.6 0.6 3.87 ; tower top
; end aerodrag_element;

;
; begin aerodrag_element ;          Nacelle drag side
; mbody name shaft;
; aerodrag_sections uniform 2 ;
; nsec 2 ;
; sec 0.0 0.8 10.0 ;
; sec 5.02 0.8 10.0 ;
; end aerodrag_element;
; end aerodrag

;
-----
begin dll;
begin hawc_dll;
filename ./control/bladed2hawc.dll ;
dll_subroutine regulation ;
arraysizes 15 15 ;
deltat 0.02;
begin output;
| general time ;                               1
| constraint bearing2 pitch1 1; angle and angle velocity written to dll           2,3
| constraint bearing2 pitch2 1; angle and angle velocity written to dll           4,5
| constraint bearing2 pitch3 1; angle and angle velocity written to dll           6,7
| constraint bearing2 shaft_rot 1; angle and angle velocity written to dll (slow speed shaft) 8,9
| wind free_wind 1 0.0 0.0 -90.0; local wind at fixed position: coo (1=global,2=non-rotation rotor coo.), pos x, pos y, pos z 10,11,12
| general constant 97.0 ;                      generator exchange ratio          13
end output;

;
begin actions;
| body moment_ext shaft 1 3;
end actions;
end hawc_dll;

;
begin hawc_dll;
filename ./control/pitchservo_pos.dll ;
dll_subroutine servo ;
arraysizes 15 15 ;
deltat 0.02 ;
begin output;
| general time ;                               1
| dll inpvec 1 2;                               2
| dll inpvec 1 3;                               3
| dll inpvec 1 4;                               4
| constraint bearing2 pitch1 1; angle and angle velocity written to dll           5,6
| constraint bearing2 pitch2 1; angle and angle velocity written to dll           7,8
| constraint bearing2 pitch3 1; angle and angle velocity written to dll           9,10
end output;

;
begin actions;
| body bearing_angle pitch1;
| body bearing_angle pitch2;
| body bearing_angle pitch3;
end actions;
end hawc_dll;

;
begin hawc_dll;
filename ./control/damper.dll ;
dll_subroutine damp ;
arraysizes 15 15 ;
begin output;
| general time ;                               1
| general constant 5.0;
| general constant 10.0;
| general constant -1.0E1 ;
| mbody state vel towertop 1 1.0 tower;
end output;

;
begin actions;
| mbody force_ext towertop 2 1 towertop;
end actions;
end hawc_dll;

;
begin type2_dll;
name gear;
filename ./control/hss_convert.dll ;
arraysizes_init 3 1 ;
arraysizes_update 2 2 ;
begin init;
| constant 1 1.0 ;      number of used sensors - in this case only 1
| constant 2 1000;      unit conversion factor
end init;
begin output;
| mbody momentvec shaft 1 1 shaft # only 3;
end output;
;

```

```

begin actions;
  mbdy moment_ext towertop 2 3 shaft;
end actions;
end type2_dll;
;
end dll;
-----
begin output;
  filename ./res/sparbuoy_unstable_BR_sathe_2 ;
  data_format hawc_binary;
; time 50.0 650.0 ;
  buffer 1 ;
;
general time;
aero omega;
aero thrust;
aero torque;
aero power;
mbdy momentvec tower 1 1 tower # Tower bottom tower base flange;
mbdy forcevec tower 1 1 tower # Tower bottom tower base flange;
wind free_wind 1 0.0 0.0 -90.0; local wind at fixed position: coo (1=global,2=non-rotation rotor coo.), pos x, pos y, pos z
mbdy state pos floater 1 0.0 global # Position floater bottom;
mbdy state pos floater 7 1.0 global # Position floater top;
mbdy state pos tower 1 0.0 global # Position tower bottom;
mbdy state pos towertop 1 1.0 global # tower top position ;
mbdy state vel towertop 1 1.0 global # tower top velocity;
;
;
;
mbdy forcevec towertop 1 2 towertop # yaw bearing ;
mbdy momentvec towertop 1 2 towertop # yaw bearing ;
mbdy momentvec shaft 4 1 shaft # main bearing ;
mbdy momentvec blade1 10 1 local # blade 1 50% local coordinate ;
mbdy momentvec blade2 10 1 local # blade 2 50% local coordinate ;
mbdy momentvec blade3 10 1 local # blade 3 50% local coordinate ;
mbdy forcevec hub1 1 2 hub1 # blade 1 root ;
mbdy forcevec hub2 1 2 hub2 # blade 2 root ;
mbdy forcevec hub3 1 2 hub3 # blade 3 root ;
mbdy momentvec hub1 1 2 hub1 # blade 1 root ;
mbdy momentvec hub2 1 2 hub2 # blade 2 root ;
mbdy momentvec hub3 1 2 hub3 # blade 3 root ;

mbdy state pos tower 9 1.0 global # tower top flange position ;
mbdy state pos blade1 18 1.0 hub1 # blade 1 tip position ;
mbdy state pos blade2 18 1.0 hub2 # blade 2 tip position ;
mbdy state pos blade3 18 1.0 hub3 # blade 3 tip position ;
mbdy state pos blade1 18 1.0 global # blade 1 tip position global ;
mbdy state pos blade2 18 1.0 global # blade 2 tip position global ;
mbdy state pos blade3 18 1.0 global # blade 3 tip position global ;
mbdy state_rot proj_ang blade1 18 1.0 blade1 only 3 # blade 1 tip twist;
mbdy state_rot proj_ang blade2 18 1.0 blade2 only 3 # blade 2 tip twist;
mbdy state_rot proj_ang blade3 18 1.0 blade3 only 3 # blade 3 tip twist;
hydro water_surface 0.0 0.0 ; x,y gl. pos
;
mbdy state pos floater_dummy 1 0.0 global global # platform translation in surge sway and heave ;
mbdy state_rot proj_ang floater_dummy 1 0.0 global global # platform rotation in roll pitch and yaw ;
;
;
d11 outvec 1 1 # time;
; d11 outvec 1 2 # pitch angle 1;
; d11 outvec 1 3 # pitch vel 1;
; d11 outvec 1 4 # pitch angle 2;
; d11 outvec 1 5 # pitch vel 2;
; d11 outvec 1 6 # pitch angle 3;
; d11 outvec 1 7 # pitch vel 3;
; d11 outvec 1 8 # gen. azi slow;
; d11 outvec 1 9 # gen. speed slow;
; d11 outvec 1 10 # free wind x;
; d11 outvec 1 11 # free wind y;
; d11 outvec 1 12 # free wind z;
; d11 outvec 1 13 # gear ratio;
; d11 inpvec 1 1 # Mgen slow;
; d11 inpvec 1 2 # pitchref 1;
; d11 inpvec 1 3 # pitchref 2;
; d11 inpvec 1 4 # pitchref 3;
; d11 inpvec 1 5 # Gen speed fast;
; d11 inpvec 1 6 # Mgen fast;
; d11 inpvec 1 7 # F;
; d11 inpvec 1 10 # Pitch rate [rad/s];
; d11 inpvec 2 1 # pitch 1;
; d11 inpvec 2 2 # pitch 2;
; d11 inpvec 2 3 # pitch 3;
; d11 outvec 2 1 # time;
; d11 outvec 2 2 # pitchref 1;
; d11 outvec 2 3 # pitchref 2;
; d11 outvec 2 4 # pitchref 3;
; d11 outvec 2 5 # pitch angle 1;
; d11 outvec 2 6 # pitch speed 1;
; d11 outvec 2 7 # pitch angle 2;
; d11 outvec 2 8 # pitch speed 2;
; d11 outvec 2 9 # pitch angle 3;
; d11 outvec 2 10 # pitch speed 3;
force mooring ;
mbdy forcevec towertop 1 1 towertop # tower top lower ;
mbdy momentvec towertop 1 1 towertop # tower top lower ;
mbdy forcevec hub1 1 1 hub1 # hub 1 rotor ;
mbdy forcevec hub2 1 1 hub2 # hub 2 rotor ;
mbdy forcevec hub3 1 1 hub3 # hub 3 rotor ;
mbdy momentvec hub1 1 1 hub1 # hub 1 rotor ;
mbdy momentvec hub2 1 1 hub2 # hub 2 rotor ;
mbdy momentvec hub3 1 1 hub3 # hub 3 rotor ;
constraint bearing2 pitch1 5;
constraint bearing2 pitch2 5;
constraint bearing2 pitch3 5;
constraint bearing1 shaft_rot 2;
d11 inpvec 1 8 # Mechanical power generator [kW];
d11 inpvec 1 9 # Electrical power generator [kW];
;
end output;
exit;

```


A.3.2. A Sample of the 64-bit Mann Turbulence Generator Input File

The following is a sample of an input file for the 64-bit Mann Turbulence Generator for the case of the fitted-Mann under stable condition at below rated wind speed (8m/s).

```

Information about turbulence properties for the files
stable_BR_sathe_2_u.bin
stable_BR_sathe_2_v.bin
stable_BR_sathe_2_w.bin

AlfaEpsilon: 2.450001128E-02
L_mann:      2.000000000E+01
Gamma:      2.780000091E+00
Seed nr, :   2703

Length box : 2.880000000E+04 Dx : 8.789063692E-01 Nx : 32768
Width box  : 1.600000000E+02 Dy : 5.000000000E+00 Ny : 32
Height box : 1.600000000E+02 Dz : 5.000000000E+00 Nz : 32
    
```

A.3.3. Mimosa Output File

The following is the Mimosa output file used in the simulations to compute the mooring forces for all load cases. The file contains parameters “DISTANCE”, “TENSION”, “H.TENSION”, “SUSPL”, and “TEN.ANCH”, definitions are illustrated in *Figure A.1*. Parameters “TENSION”, “H.TENSION”, “SUSPL”, and “TEN.ANCH” are a function of “DISTANCE”, where “DISTANCE” is the horizontal distance from fairlead to the anchor and “SUSPL” is the mooring un-stretched length from fairlead to the mooring line’s touch down point (Jonkman, 2010). An important note for *Figure A.1* is that it illustrates the maximum un-stretched length where the mooring line touch down point is in an infinitesimal distance with the anchor.

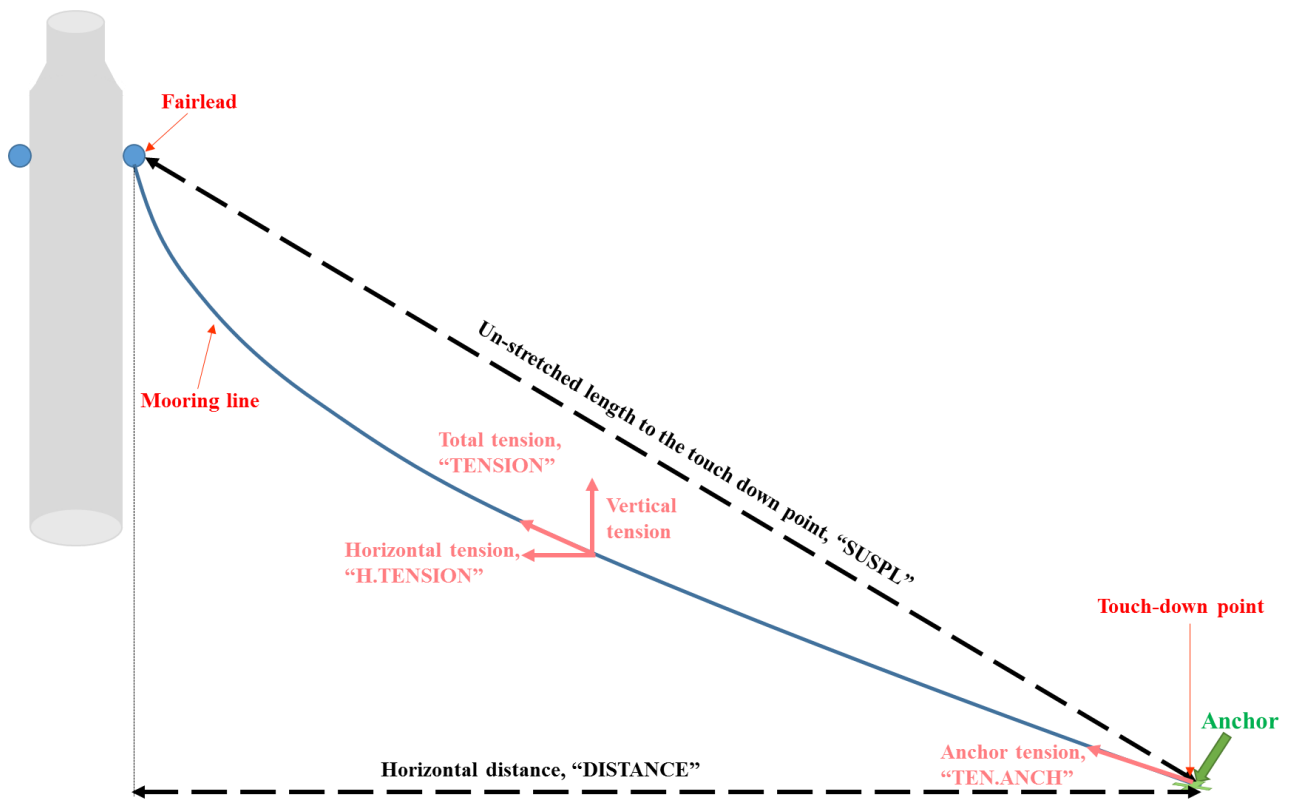


Figure A.1 Parameter definition of OC3-Hywind mooring forces from Mimosa.

1

MIMOSA Development Version 5.6-01 12-MAR-2009 11:05 MARINTEK
Page 1

Input file :
annex23_mooring.mim

* Mooring system data
Text :
3 Point Mooring System for HYWIND, no 'hanefot', fairlead at r=4.15 m

FF

MIMOSA Development Version 5.6-01 12-MAR-2009 11:05 MARINTEK
Page 2

* POSITIONING SYSTEM *

VESSEL POSITION :

X1 (Northwards) : 0.0 m
X2 (Eastwards) : 0.0 m
X3 : 0.0 m
HEADING (rel. North).... : 0.0 deg.

(DP-system has not been defined)

LINE DATA:

Line no.	Line characteristics no.	Winch may be run	Line intact/broken	Fairlead X(m)	Coordinates Y(m)
1	1	Yes	Intact	0.0	-5.2
2	1	Yes	Intact	4.5	2.6
3	1	Yes	Intact	-4.5	2.6

LINE INITIALIZING DATA:

Line no	Dir. (deg)	Tension (kN)	Horizontal distance (m)	Anchor XG(m)	coordinates YG(m)	Run length of winch (m)
1	-90.0	911.10	848.67	0.00 *)	-853.87 *)	0.00 *)
2	30.0	911.10	848.67	739.47 *)	426.93 *)	0.00 *)
3	150.0	911.10	848.67	-739.47 *)	426.93 *)	0.00 *)

*) This parameter is used in initialization

(NO THRUSTERS)

FF

* LINE CHARACTERISTICS DATA *

```

-----
Data for line characteristics number. . . : 1

Input type . . . . . : 2 (Computed by MIMOSA)
Number of values in the line
characteristics table. . . . . : 40
Number of segments . . . . . : 1
Bottom tangent option. . . . . : 1 (Bottom tangent possible)
Current forces included. . . . . : Yes
Angle from horizontal to bottom (deg). . . : 0.00
Z-coordinate of fairlead (m) . . . . . : 70.00
Z-coordinate of anchor (m) . . . . . : 320.00
Max tension in line charct. table (kN) . . : 6000.00
Friction coefficient at bottom . . . . . : 1.00
Segment  Segment  Number of  Buoy  Segment  Breaking
number  type  elements  number length (m)  load (kN)
  1      Catenary  80        0     902.20      -2.1

Segment  Diameter  Elastic  Factor of  Unit weight  Weight  Drag coeff.
number   (m)      modulus  elasticity in water  in water normal
          (kN/(m)2)  (kN/m)  and air /longitudinal
  1       0.090  0.6000E+08  1.00    0.6981     0.916  1.200 0.100
    
```

* BUOY DATA *

(No buoy data)



* LINE CHARACTERISTICS OF LINE NUMBER: 1 *

```

-----
Line characteristics number: 1

DISTANCE    TENSION    H.TENSION    SUSPL    TEN.ANCH
(m)         (kN)       (kN)         (m)      (kN)

654.26     174.7      0.2          250.3    0.0
672.50     178.5      4.0          255.7    0.0
702.05     190.0      15.5         271.3    0.0
730.16     209.2      34.7         295.5    0.0
753.94     236.0      61.5         326.4    0.0
773.34     270.4      96.0         362.3    0.0
789.03     312.6      138.2        401.9    0.0
801.80     362.4      188.0        444.1    0.0
812.31     419.8      245.4        488.3    0.0
821.08     484.9      310.6        534.0    53.2
828.48     557.7      383.4        580.8    158.6
834.79     638.1      463.8        628.6    272.3
840.24     726.2      552.0        677.1    394.1
845.00     822.0      647.8        726.1    523.9
849.20     925.4      751.2        775.7    661.7
852.93     1036.4     862.3        825.6    807.5
856.28     1155.2     981.1        875.8    961.0
    
```

859.27	1281.5	1107.5	905.0	1107.6
861.67	1415.6	1240.6	905.3	1241.7
863.61	1557.3	1380.4	905.6	1383.4
865.20	1706.7	1527.2	906.0	1532.9
866.56	1863.7	1680.9	906.4	1690.0
867.73	2028.4	1841.6	906.8	1854.7
868.77	2200.7	2009.4	907.2	2027.2
869.71	2380.7	2184.4	907.6	2207.2
870.58	2568.4	2366.5	908.0	2395.0
871.40	2763.7	2555.9	908.5	2590.4
872.17	2966.7	2752.4	909.0	2793.5
872.92	3177.4	2956.3	909.5	3004.2
873.66	3395.7	3167.4	910.0	3222.6
874.38	3621.6	3385.8	910.5	3448.7
875.09	3855.2	3611.5	911.1	3682.4
875.81	4096.5	3844.5	911.7	3923.8
876.52	4345.5	4084.9	912.2	4172.9
877.24	4602.1	4332.6	912.9	4429.6
877.97	4866.3	4587.7	913.5	4694.0
878.71	5138.3	4850.1	914.1	4966.0
879.45	5417.9	5119.9	914.8	5245.7
880.21	5705.1	5397.0	915.5	5533.1
880.98	6000.0	5681.6	916.2	5828.1

FF

MIMOSA Development Version 5.6-01 12-MAR-2009 11:05

MARINTEK
Page 5

* RESTORING MOMENT *

```

!-----!
! Rotation ! Force   in Direction ! Moment ! Max.   ! Line !
!          !         rel. North !         ! Tension ! number !
! (deg)   ! (kN)   ! (deg)   ! (kNm)  ! (kN)   !      !
!-----!
!   0.0   !   0.0   !   85.3   !-0.7611E-04!  911.1 !   1   !
!   4.5   !   0.0   !   88.7   !-908.0      !  911.5 !   2   !
!   9.0   !   0.0   !  104.1   !-1814.      !  912.8 !   1   !
!  13.5   !   0.0   !   27.5   !-2714.      !  915.0 !   2   !
!  18.0   !   0.0   !  358.5   !-3607.      !  918.0 !   1   !
!  22.5   !   0.0   !   43.7   !-4489.      !  921.8 !   1   !
!  27.0   !   0.0   !  344.7   !-5357.      !  926.5 !   1   !
!  31.5   !   0.0   !   95.0   !-6209.      !  931.9 !   1   !
!  36.0   !   0.0   !   31.3   !-7040.      !  938.1 !   2   !
!  40.5   !   0.0   !  101.0   !-7848.      !  945.2 !   1   !
!  45.0   !   0.0   !  359.9   !-8629.      !  953.0 !   1   !
!-----!

```

FF

MIMOSA Development Version 5.6-01 12-MAR-2009 11:05

MARINTEK
Page 6

* RESTORING FORCE *

Offset in Direction 0. deg. rel. North

```

!-----!
! Offset ! Force in ! Force in ! Moment ! Maximum ! Line !
! ! given ! transverse ! ! Tension ! number !
! ! direction ! direction ! ! ! !
! (m) ! (kN) ! (kN) ! (kNm) ! (kN) ! !
!-----!
! 0.0 ! 0.0 ! 0.0 !-.7611E-04 ! 911.1 ! 1 !
! 1.5 ! -61.7 ! 0.8 !0.9694E-02 ! 946.5 ! 3 !
! 3.0 ! -123.5 ! 3.8 !0.7204E-01 ! 984.2 ! 3 !
! 4.5 ! -186.0 ! 8.9 !0.2487 ! 1024.7 ! 3 !
! 6.0 ! -249.2 ! 15.6 !0.5795 ! 1067.3 ! 3 !
! 7.5 ! -313.9 ! 24.6 ! 1.139 ! 1113.3 ! 3 !
! 9.0 ! -379.6 ! 35.8 ! 1.981 ! 1162.1 ! 3 !
! 10.5 ! -446.1 ! 48.5 ! 3.127 ! 1213.1 ! 3 !
! 12.0 ! -518.9 ! 65.6 ! 4.831 ! 1272.5 ! 3 !
! 13.5 ! -596.0 ! 86.2 ! 7.138 ! 1338.2 ! 3 !
! 15.0 ! -682.9 ! 113.4 ! 10.44 ! 1416.9 ! 3 !
!-----!
    
```



MIMOSA Development Version 5.6-01 12-MAR-2009 11:05

MARINTEK
Page 7

* RESTORING FORCE *

Offset in Direction 90. deg. rel. North

```

!-----!
! Offset ! Force in ! Force in ! Moment ! Maximum ! Line !
! ! given ! transverse ! ! Tension ! number !
! ! direction ! direction ! ! ! !
! (m) ! (kN) ! (kN) ! (kNm) ! (kN) ! !
!-----!
! 0.0 ! 0.0 ! 0.0 !-.7611E-04 ! 911.1 ! 1 !
! 1.5 ! -62.6 ! 0.0 !-.7035E-04 ! 952.1 ! 1 !
! 3.0 ! -127.5 ! 0.0 !-.6445E-04 ! 996.4 ! 1 !
! 4.5 ! -195.1 ! 0.0 !0.3630E-03 ! 1044.1 ! 1 !
! 6.0 ! -265.1 ! 0.0 !-.2570E-03 ! 1095.1 ! 1 !
! 7.5 ! -339.1 ! 0.0 !0.3537E-03 ! 1150.9 ! 1 !
! 9.0 ! -414.6 ! 0.0 !-.4008E-04 ! 1208.5 ! 1 !
! 10.5 ! -499.8 ! 0.0 !-.3186E-04 ! 1276.8 ! 1 !
! 12.0 ! -593.2 ! 0.0 !-.2125E-03 ! 1354.1 ! 1 !
! 13.5 ! -702.0 ! 0.0 !0.1645E-03 ! 1447.9 ! 1 !
! 15.0 ! -830.1 ! 0.0 !0.3452E-03 ! 1562.4 ! 1 !
!-----!
    
```



MIMOSA Development Version 5.6-01 12-MAR-2009 11:05

MARINTEK
Page 8

* RESTORING FORCE *

 Offset in Direction 270. deg. rel. North

Offset (m)	Force in given direction (kN)	Force in transverse direction (kN)	Moment (kNm)	Maximum Tension (kN)	Line number
0.0	0.0	0.0	-.7611E-04	911.1	1
1.5	-60.9	0.0	0.1527E-03	931.4	2
3.0	-119.5	0.0	0.3950E-03	952.2	2
4.5	-177.0	0.0	0.1122E-03	974.1	3
6.0	-233.5	0.0	0.4117E-03	996.9	2
7.5	-288.9	0.0	0.6822E-03	1020.7	2
9.0	-343.3	0.0	0.1577E-03	1045.3	2
10.5	-397.3	0.0	-.5088E-03	1070.6	3
12.0	-451.1	0.0	-.5454E-03	1097.3	3
13.5	-504.6	0.0	0.4593E-03	1125.4	2
15.0	-558.6	0.0	-.4385E-03	1154.8	2

B. TurbSim

B.1 Inputs

The input file of TurbSim for the generation of the IEC Kaimal Spectra & Coherence Model turbulences contains several main sections: Runtime Options, Turbine/Model Specifications, Meteorological Boundary Conditions, Non-IEC Meteorological Boundary Conditions, and Coherent Turbulence Scaling Parameters. Each of the section is explained as the following.

B.1.1 TurbSim Input – Turbine/Model Specification

This input section is related to the 3D turbulence box dimensioning in the TurbSim, consisting of:

- NumGrid_Y: number of points in y-axis (N_y)
- NumGrid_Z: number of points in z-axis (N_z)
- TimeStep: time step (dt) see (3.16)
- AnalysisTime: simulation length, total duration to be written in the output (T)
- UsableTime: simulation length which value should be less than analysis time, see (3.17)
- HubHt: wind turbine hub height
- GridHeight: length of the rectangular yz-plane in z-direction ($L'_z = L_z - dz$) $< 2HubHt$
- GridWidth: length of the rectangular yz-plane in y-direction ($L'_y = L_y - dy$)
- VFlowAng: mean vertical flow angle
- HFlowAng: mean horizontal flow angle

B.1.2 TurbSim Input – Meteorological Boundary Conditions

The section of the input file defines the characteristics of turbulent wind to be generated and *only valid* for the outlined turbulence models (spectrum) in the IEC standard such as the IEC Kaimal and the IEC von Karman. Parameters contained in this section comprises of:

- TurbModel: the turbulence spectra model used, either the IEC Kaimal or the IEC von Karman
- IECstandard: the IEC 61400-x standard used, where x=1, 2, or 3
- IEcturbc: wind turbine class according to the IEC standard (**Table 2.6**) or a user-defined turbulence intensity value (manually inputted)
- IEC_WindType: turbulence type according to IEC standard, either Normal Turbulence Model (NTM), Extreme Turbulence Model (ETM), or other
- ETMc: 'c' parameter when ETM turbulence is chosen
- WindProfileType: the wind profile type either JET, logarithmic law, power law, or other
- RefHt: height of the reference wind speed
- URef: mean wind speed at the reference height RefHt
- ZJetMax: jet height when JET wind profile is chosen
- PLExp: the power law exponent when the power law wind profile is chosen
- Z0: surface roughness length z_0

B.1.3 TurbSim Input – Others

This covers the Runtime Options, Non-IEC Meteorological Boundary Conditions, and Coherent Turbulence Scaling Parameters sections. These sections are not expanded in detail as its less relevancy with the required IEC Kaimal Spectra & Coherence Model turbulent wind input for HAWC2. Detailed explanation of the three sections can be found in reference Jonkman & Kilcher (2012).

The Runtime Options section generally contains information on which type of output file to be generated and the selection of random seed number for the simulation as well as the scaling ratio for the generated turbulence standard deviation $\sigma_u : \sigma_v : \sigma_w$. This scaling option can be turned off to obtain the ‘as generated’ wind field.

The Non-IEC Meteorological Boundary Conditions section will be read by TurbSim *only if* the specified “TurbModel” in the “Meteorological Boundary Conditions” is *neither* IEC Kaimal *nor* IEC von Karman, otherwise this section must be filled to complete additional required information. Correction towards atmospheric stability and wind shear effect towards the eddies are the additional parameters to be included in this section.

Finally, the Coherent Turbulence Scaling Parameter section describing thorough inputs regarding gradient Richardson number R_i is used as a support section for the Non-IEC Meteorological Boundary Conditions section, i.e. *valid only* for non-IEC turbulence spectrum models.

B.2 Input Files

The following is a sample input file for TurbSim to generate the IEC Kaimal Spectra & Coherence Model turbulence at the rated wind speed.

```
TurbSim Input File. Valid for TurbSim v1.06.00, 21-Sep-2012

-----Runtime Options-----
2703      RandSeed1      - First random seed (-2147483648 to 2147483647)
1992      RandSeed2      - Second random seed (-2147483648 to 2147483647) for intrinsic pRNG, or an alternative pRNG: "RanLux" or "RNSNLW"
False     WrBHHTP           - Output hub-height turbulence parameters in binary form? (Generates RootName.bin)
False     WrFHHTP           - Output hub-height turbulence parameters in formatted form? (Generates RootName.dat)
False     WrADHH           - Output hub-height time-series data in AeroDyn form? (Generates RootName.hh)
True      WrADFF           - Output full-field time-series data in TurbSim/AeroDyn form? (Generates RootName.bts)
False     WrBLFF           - Output full-field time-series data in BLADED/AeroDyn form? (Generates RootName.wnd)
False     WrADTWR           - Output tower time-series data? (Generates RootName.twr)
False     WrFMTFR           - Output full-field time-series data in formatted (readable) form? (Generates RootName.u, RootName.v, RootName.w)
False     WrACT           - Output coherent turbulence time steps in AeroDyn form? (Generates RootName.cts)
True      Clockwise     - Clockwise rotation looking downwind? (Used only for full-field binary files - not necessary for AeroDyn)
0         ScaleIEC       - Scale IEC turbulence models to exact target standard deviation?
                                [0=no additional scaling; 1=use hub scale uniformly; 2=use individual scales]

-----Turbine/Model Specifications-----
32        NumGrid_Z      - Vertical grid-point matrix dimension
32        NumGrid_Y      - Horizontal grid-point matrix dimension
0.1098632813 TimeStep      - Time step [seconds]
3600     AnalysisTime    - Length of analysis time series [seconds] (program will add time if necessary:
                                AnalysisTime = MAX(AnalysisTime, UsableTime*GridWidth/MeanHHWS) )
3586.403509 UsableTime    - Usable length of output time series [seconds] (program will add GridWidth/MeanHHWS seconds)
90.00    HubHt           - Hub height [m] (should be > 0.5*GridHeight)
155.0    GridHeight      - Grid height [m]
155.0    GridWidth      - Grid width [m] (should be >= 2*(RotorRadius+ShaftLength))
0        VFlowAng       - Vertical mean flow (up) tilt angle [degrees]
0        HFlowAng       - Horizontal mean flow (skew) angle [degrees]

-----Meteorological Boundary Conditions-----
"IECKAI"  TurbModel      - Turbulence model ("IECKAI"=Kaimal, "IECVKM"=von Karman, "GP_LLJ", "NWTCPUP", "SMOOTH", "WF_UPW", "WF_07D", "WF_14D", "TIDAL", or "NONE")
"1-ED3"   IECstandard    - Number of IEC 61400-x standard (x=1,2, or 3 with optional 61400-1 edition number (i.e. "1-Ed2") )
12        IECturbc     - IEC turbulence characteristic ("A", "B", "C" or the turbulence intensity in percent)
                                ("KHTEST" option with NWTCPUP model, not used for other models)
"NTM"     IEC_WindType  - IEC turbulence type ("NTM"=normal, "xETM"=extreme turbulence, "xEWM1"=extreme 1-year wind,
                                "xEWM50"=extreme 50-year wind, where x=wind turbine class 1, 2, or 3)
default   ETMC         - IEC Extreme Turbulence Model "c" parameter [m/s]
"PL"      WindProfileType - Wind profile type ("JET";"LOG"=logarithmic;"PL"=power law;"H2L"=Log law for TIDAL spectral model;
                                "IEC"=PL on rotor disk, LOG elsewhere; or "default")
90.00     RefHt         - Height of the reference wind speed [m]
11.4      URef          - Mean (total) wind speed at the reference height [m/s] (or "default" for JET wind profile)
default   ZJetMax       - Jet height [m] (used only for JET wind profile, valid 70-490 m)
0.00      PLExp         - Power law exponent [-] (or "default")
0.01      Z0           - Surface roughness length [m] (or "default")

-----Non-IEC Meteorological Boundary Conditions-----
default   Latitude      - Site latitude [degrees] (or "default")
0.05      RICH_NO       - Gradient Richardson number
default   UStar         - Friction or shear velocity [m/s] (or "default")
default   ZI           - Mixing layer depth [m] (or "default")
default   FC_UW         - Hub mean u'w' Reynolds stress (or "default")
default   FC_UV         - Hub mean u'v' Reynolds stress (or "default")
default   FC_VW         - Hub mean v'w' Reynolds stress (or "default")
default   IncDec1       - u-component coherence parameters (e.g. "10.0 0.3e-3" in quotes) (or "default")
default   IncDec2       - v-component coherence parameters (e.g. "10.0 0.3e-3" in quotes) (or "default")
default   IncDec3       - w-component coherence parameters (e.g. "10.0 0.3e-3" in quotes) (or "default")
default   CohExp        - Coherence exponent (or "default")

-----Coherent Turbulence Scaling Parameters-----
"M:\coh_events\eventdata" CTEventPath - Name of the path where event data files are located
"Random"  CTEventFile    - Type of event files ("IES", "DNS", or "RANDOM")
true      Randomize     - Randomize the disturbance scale and locations? (true/false)
1.0       DistSc1       - Disturbance scale (ratio of wave height to rotor disk). (Ignored when Randomize = true.)
0.5       CTLy          - Fractional location of tower centerline from right (looking downwind) to left side of the dataset. (Ignored when Randomize = true.)
0.5       CTLb          - Fractional location of hub height from the bottom of the dataset. (Ignored when Randomize = true.)
30.0      CTStartTime    - Minimum start time for coherent structures in RootName.cts [seconds]

=====
NOTE: Do not add or remove any lines in this file!
=====
```


C. Simulation Results

C.1 The Generated Wind

Table C.1 The Generated Turbulence Standard Deviations

Wind Component	IEC Kaimal	IEC Mann (Neutral)	Fitted-Mann (Neutral)	Fitted-Mann (Stable)	Fitted-Mann (Unstable)
	Below Rated (8m/s)				
σ_u	0.957	1.385	0.871	0.521	0.914
σ_v	0.758	0.952	0.607	0.402	0.757
σ_w	0.468	0.691	0.519	0.332	0.676
Wind Component	Rated (11.4 m/s)				
σ_u	1.358	1.674	1.303	0.687	1.264
σ_v	1.078	1.161	0.968	0.537	1.018
σ_w	0.663	0.839	0.766	0.288	0.877
Wind Component	Above Rated (15m/s)				
σ_u	1.781	1.985	1.650	-	-
σ_v	1.416	1.381	1.223	-	-
σ_w	0.866	0.995	0.952	-	-

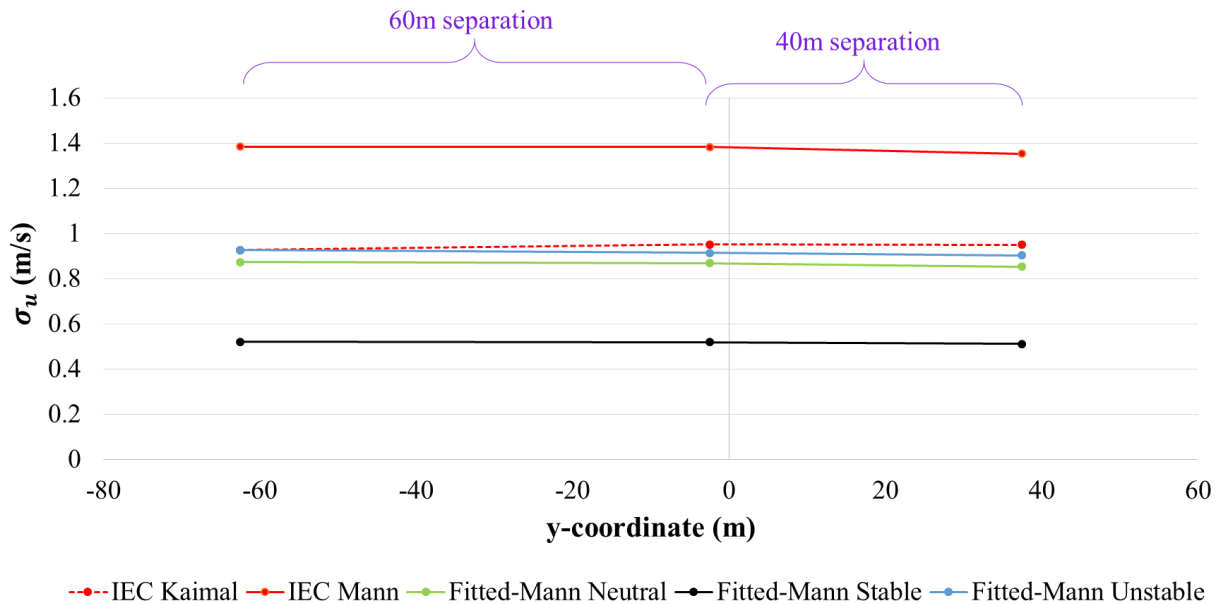


Figure C.1 Turbulence level of the u -component for 40m and 60m lateral separations (hub height elevation) at below rated wind speed.

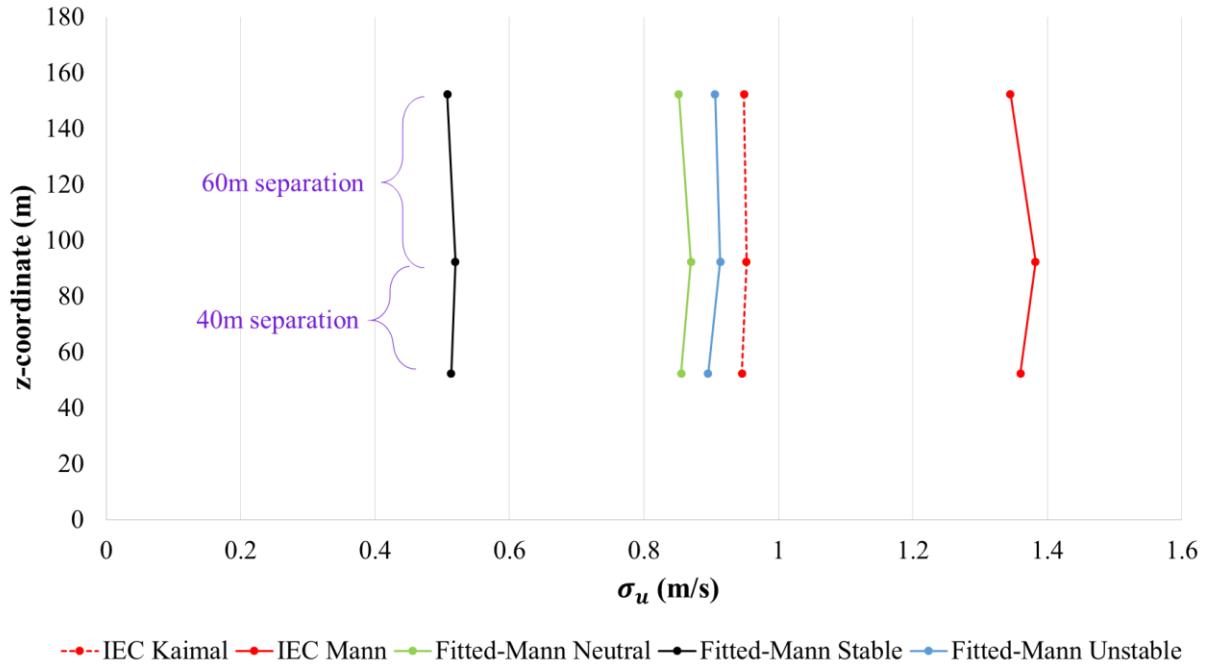


Figure C.2 Turbulence level of the u -component for 40m and 60m vertical separations (hub height elevation) at below rated wind speed.

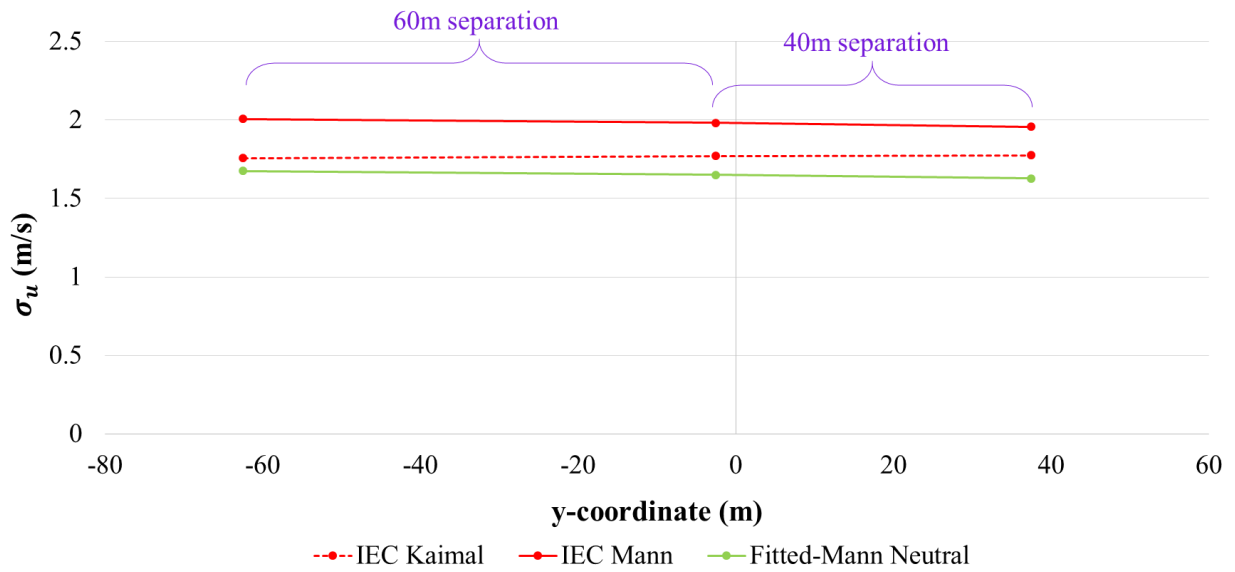


Figure C.3 Turbulence level of the u -component for 40m and 60m lateral separations at above rated wind speed.

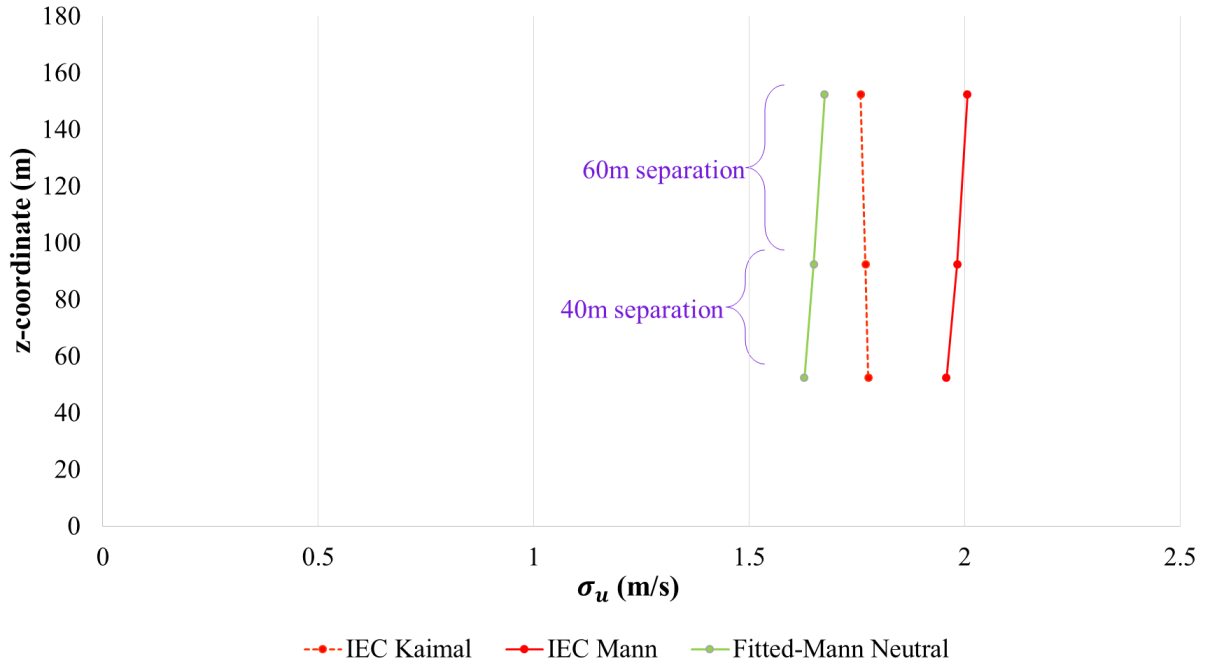


Figure C.4 Turbulence level of the u -component for 40m and 60m vertical separations at above rated wind speed.

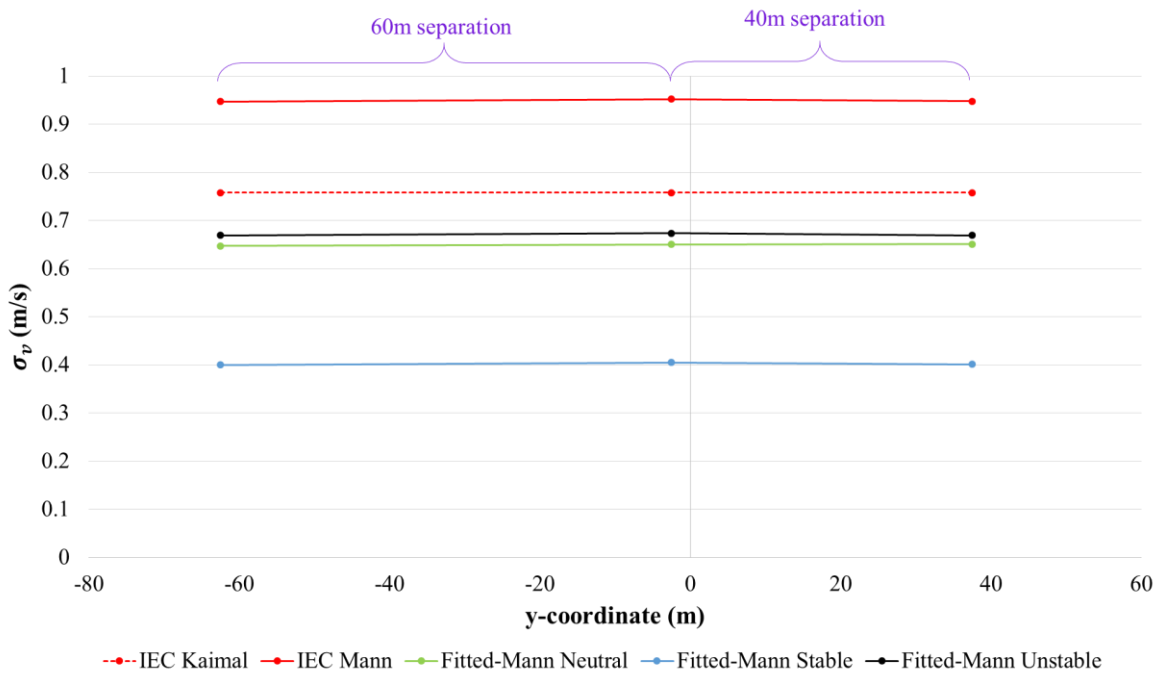


Figure C.5 Turbulence level of the v -component for 40m and 60m lateral separations (hub height elevation) at below rated wind speed.

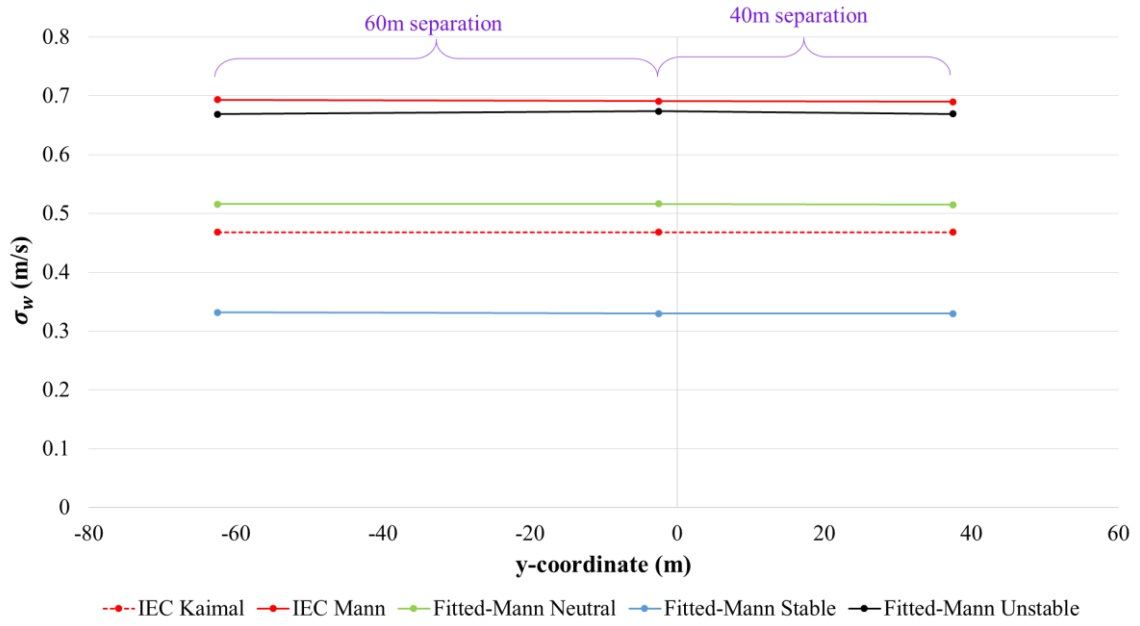


Figure C.6 Turbulence level of the w -component for 40m and 60m lateral separations (hub height elevation) at below rated wind speed.

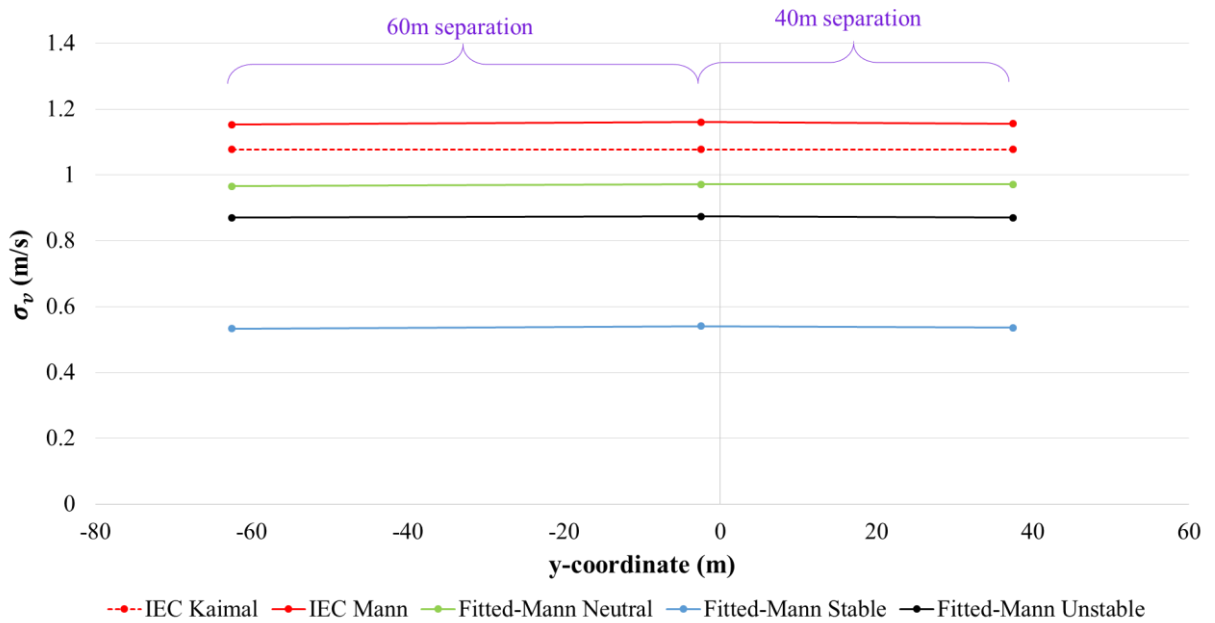


Figure C.7 Turbulence level of the v -component for 40m and 60m lateral separations (hub height elevation) at rated wind speed.

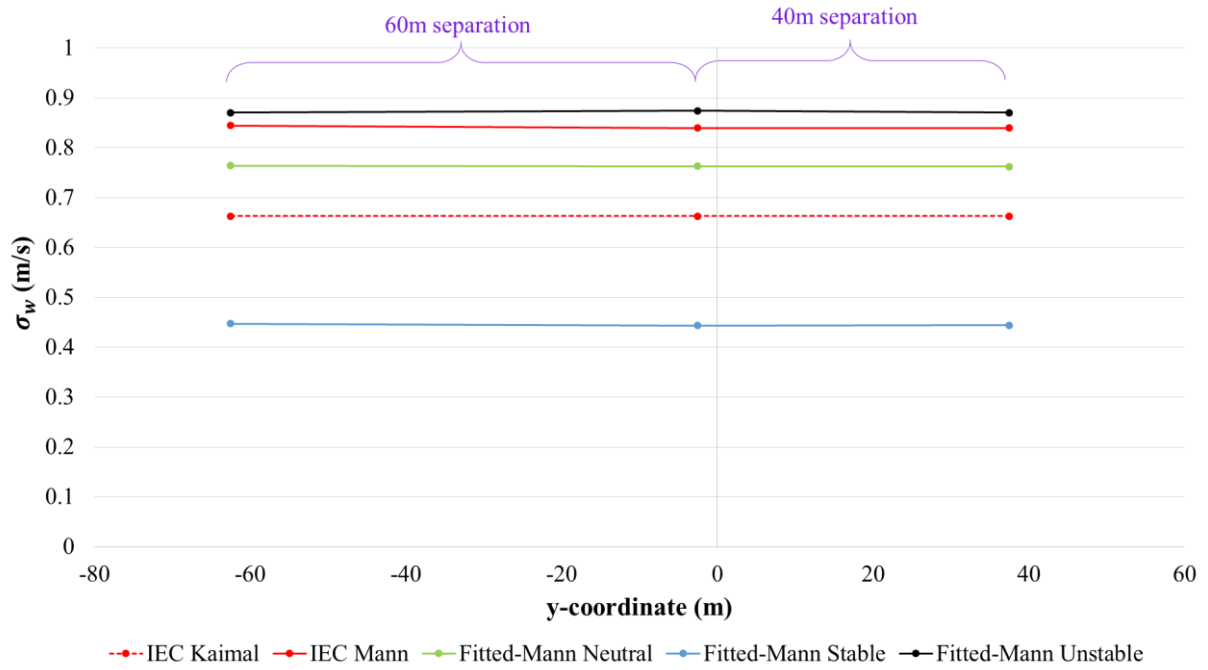


Figure C.8 Turbulence level of the w -component for 40m and 60m lateral separations (hub height elevation) at rated wind speed.

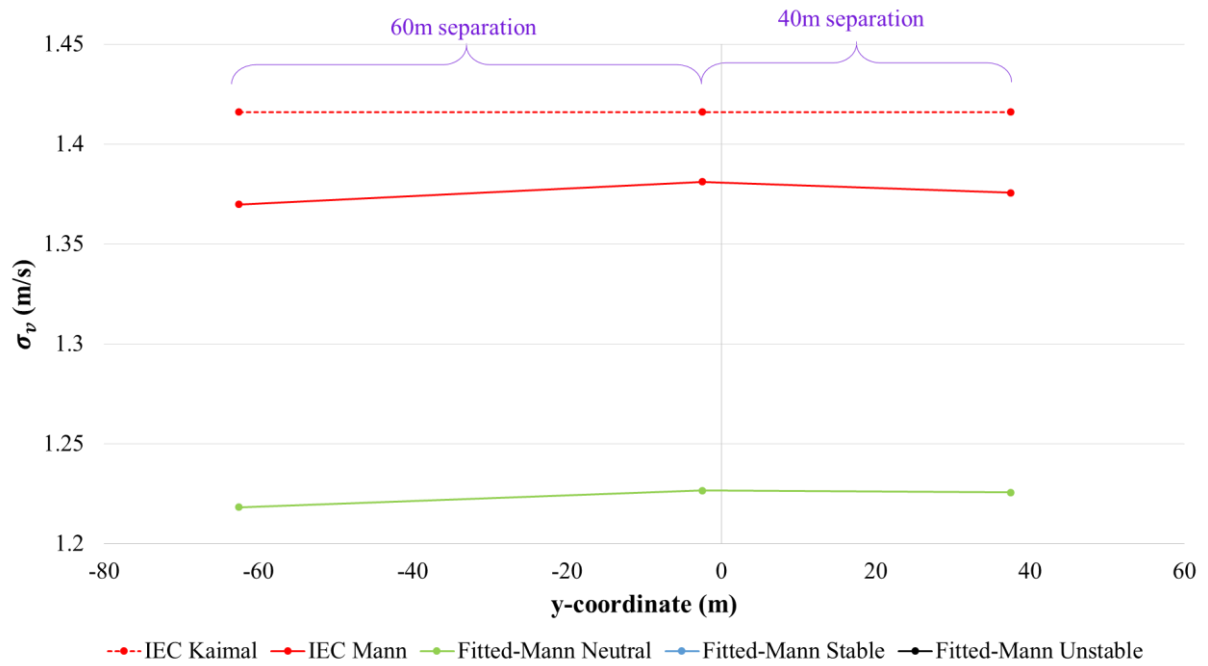


Figure C.9 Turbulence level of the v -component for 40m and 60m lateral separations (hub height elevation) at above rated wind speed.

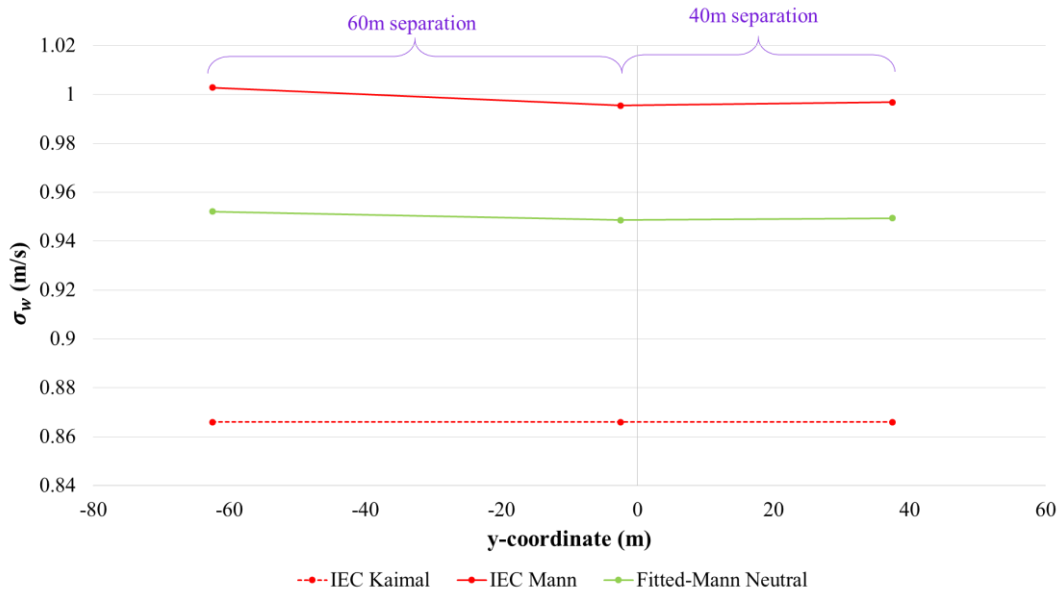


Figure C.10 Turbulence level of the w -component for 40m and 60m lateral separations (hub height elevation) at above rated wind speed.

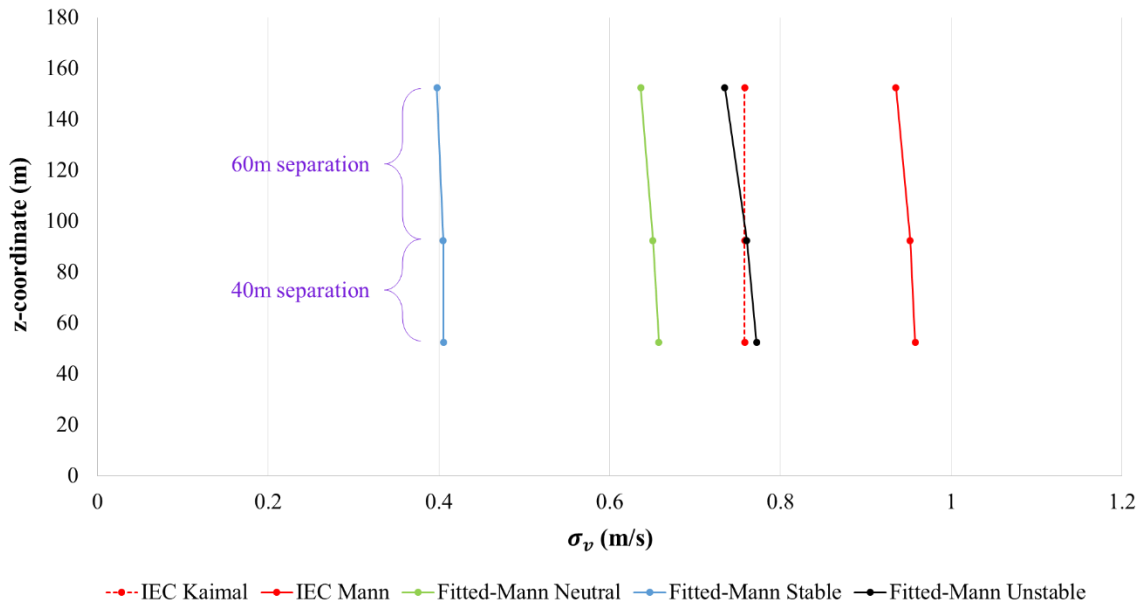


Figure C.11 Turbulence level of the v -component for 40m and 60m vertical separations (hub height elevation) at below rated wind speed.

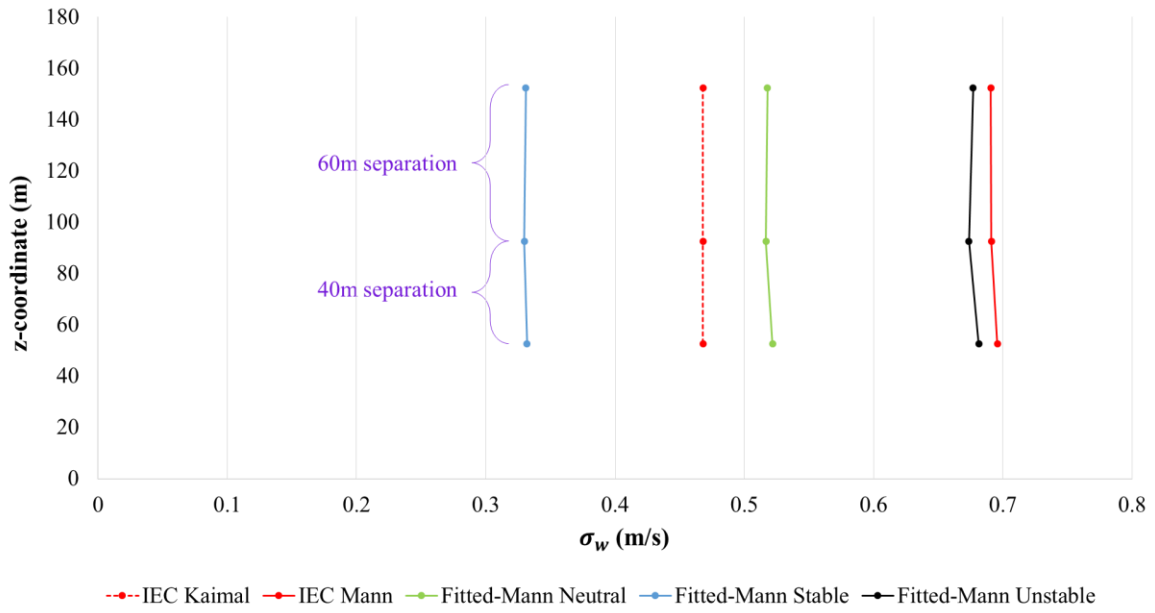


Figure C.12 Turbulence level of the w -component for 40m and 60m vertical separations (hub height elevation) at below rated wind speed.

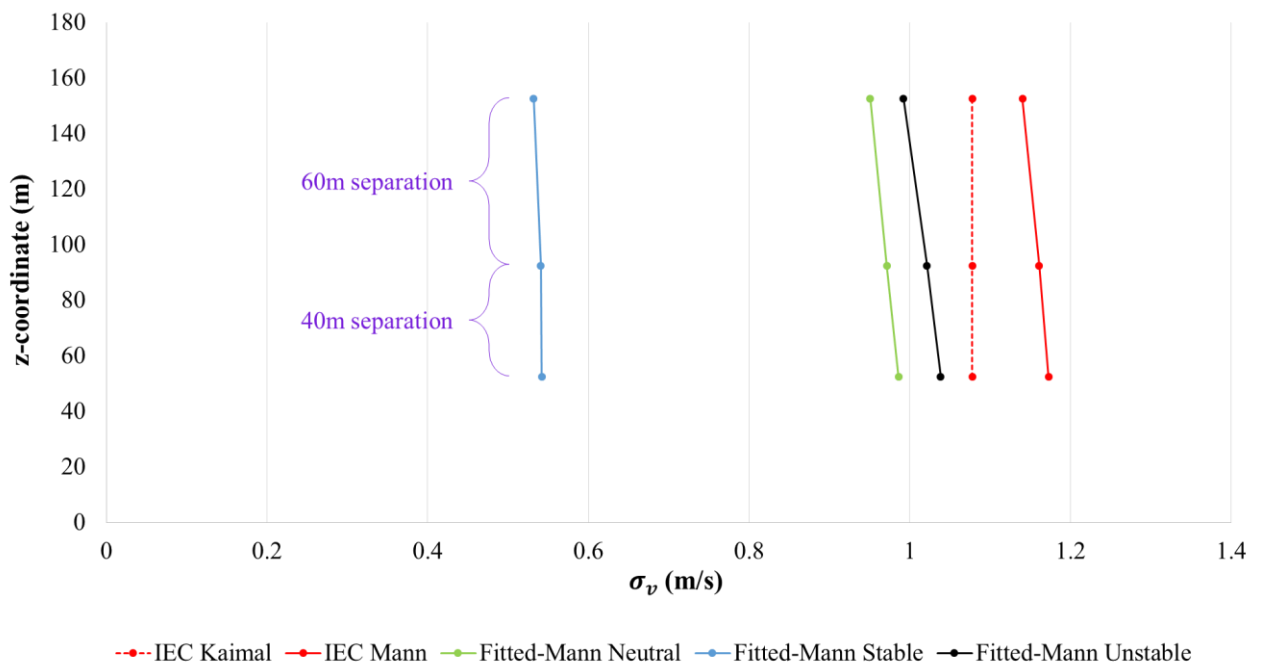


Figure C.13 Turbulence level of the v -component for 40m and 60m vertical separations (hub height elevation) at rated wind speed.

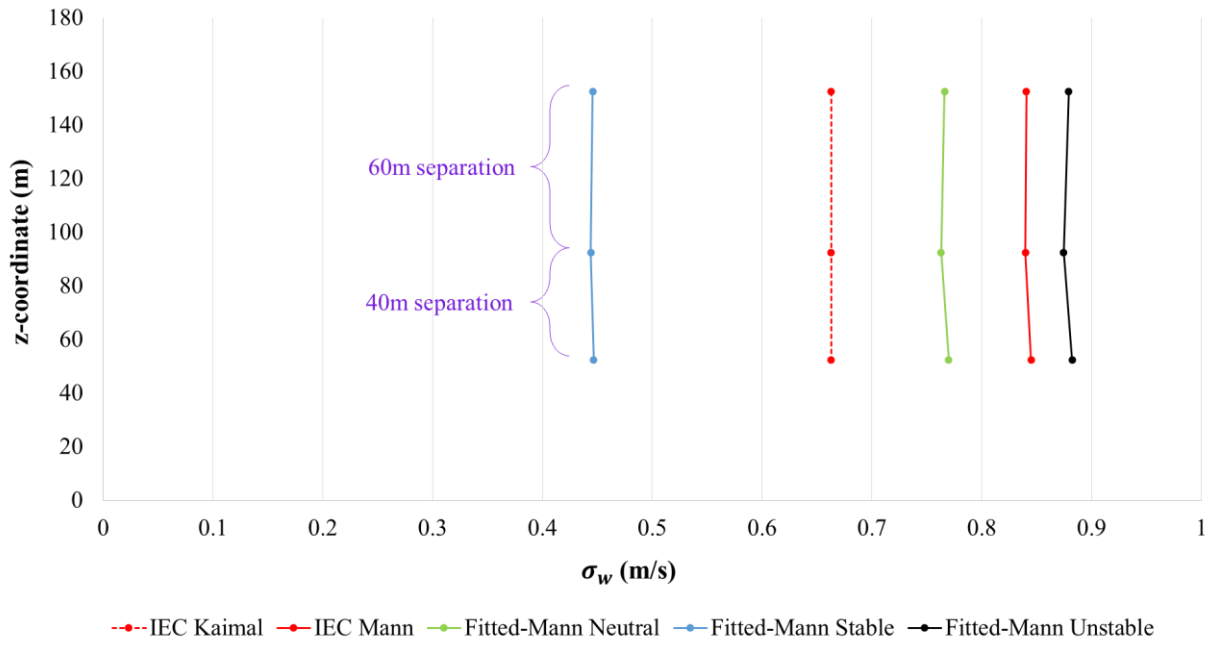


Figure C.14 Turbulence level of the w -component for 40m and 60m vertical separations (hub height elevation) at rated wind speed.

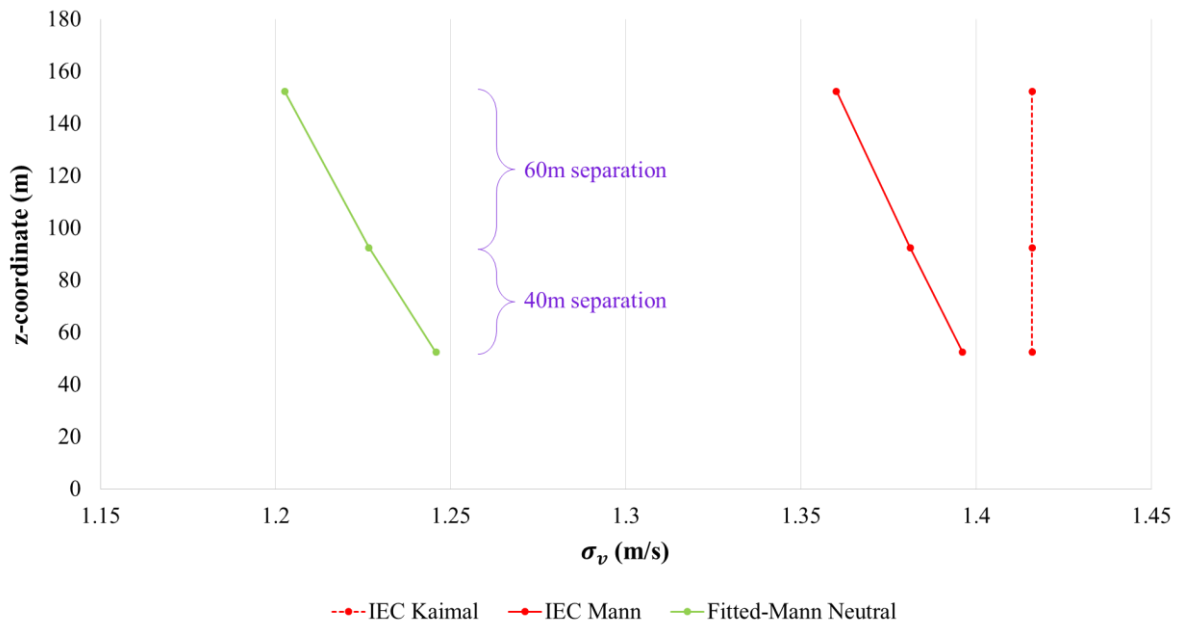


Figure C.15 Turbulence level of the v -component for 40m and 60m vertical separations (hub height elevation) at above rated wind speed.

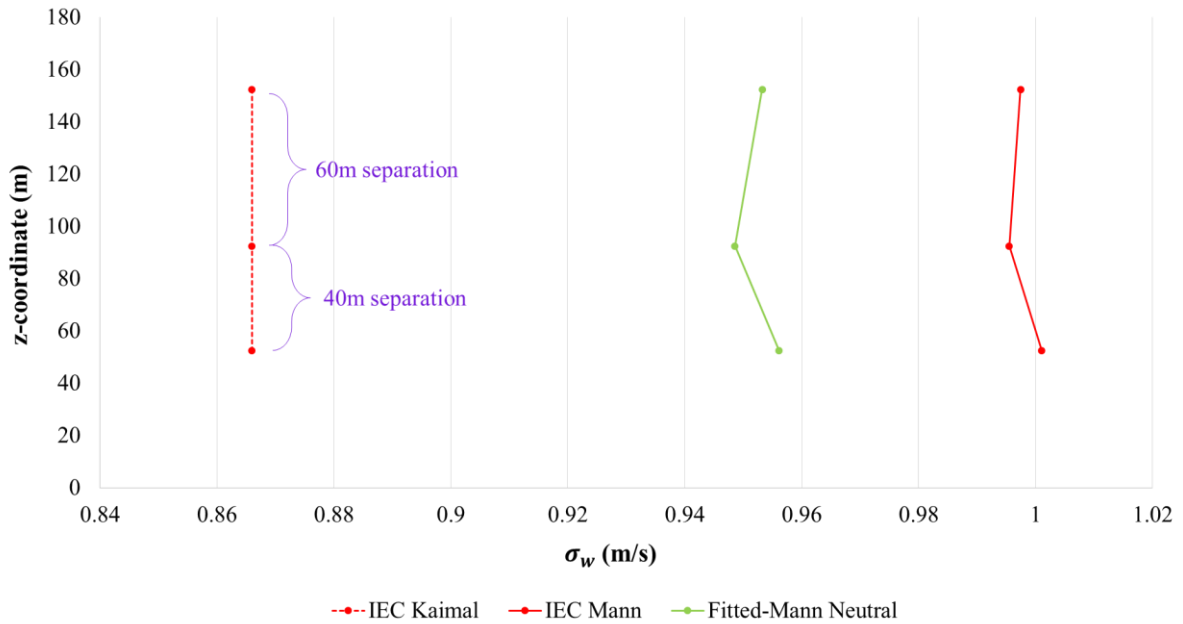


Figure C.16 Turbulence level of the w -component for 40m and 60m vertical separations (hub height elevation) at above rated wind speed.

C.2 The Coherences

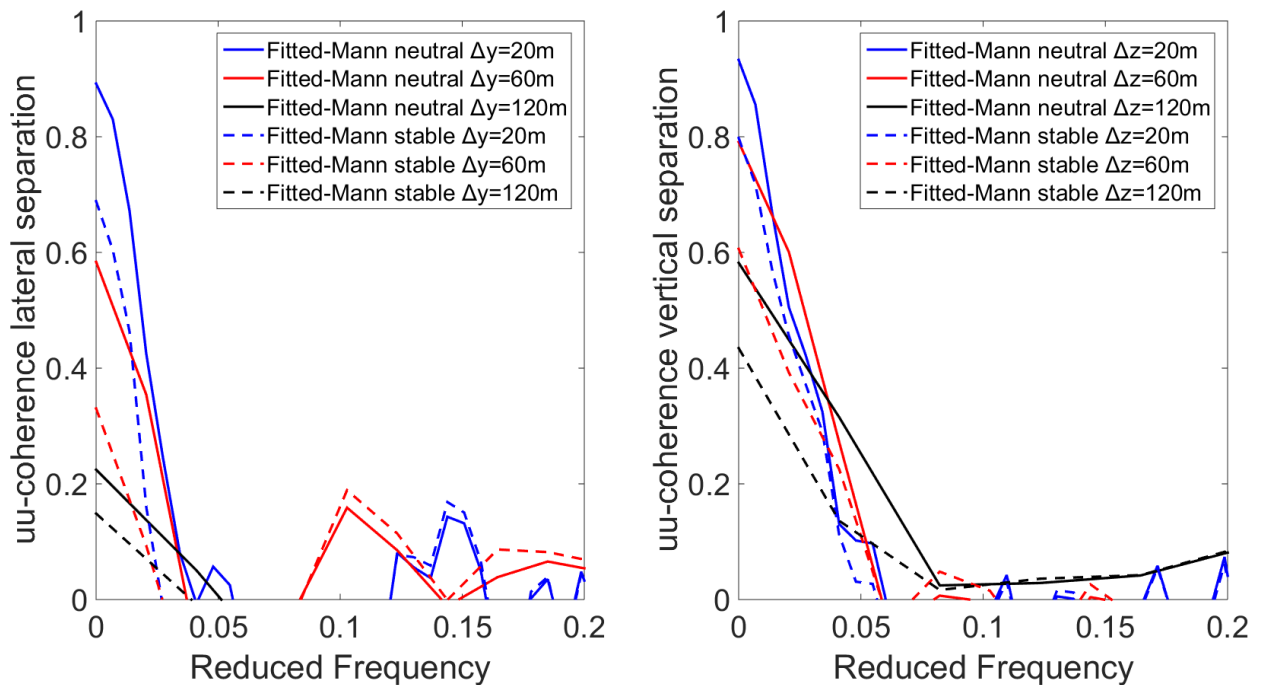


Figure C.17 Lateral (left) and vertical (right) coherences of the u -component for different separations at **rated** wind speed comparing the Mann Model with the fitted parameters for neutral and stable conditions.

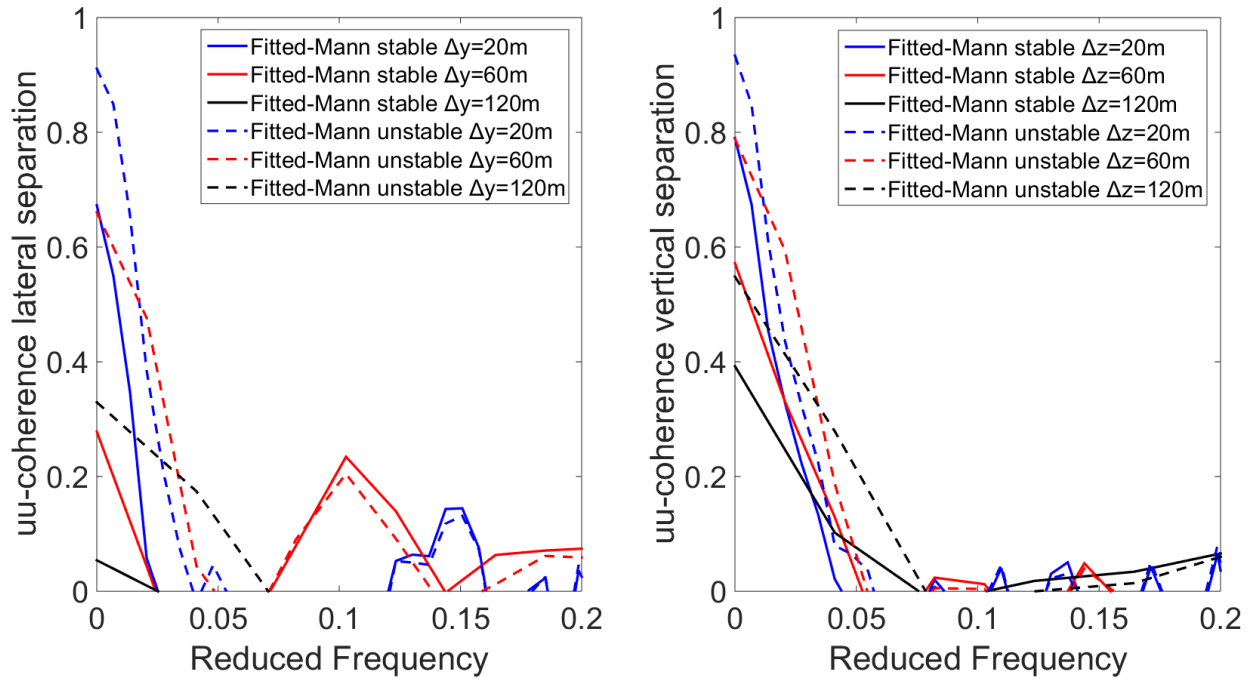


Figure C.18 Lateral (left) and vertical (right) coherences of the u -component for different separations at **below rated** wind speed comparing the Mann Model with the fitted parameters for stable and unstable conditions.

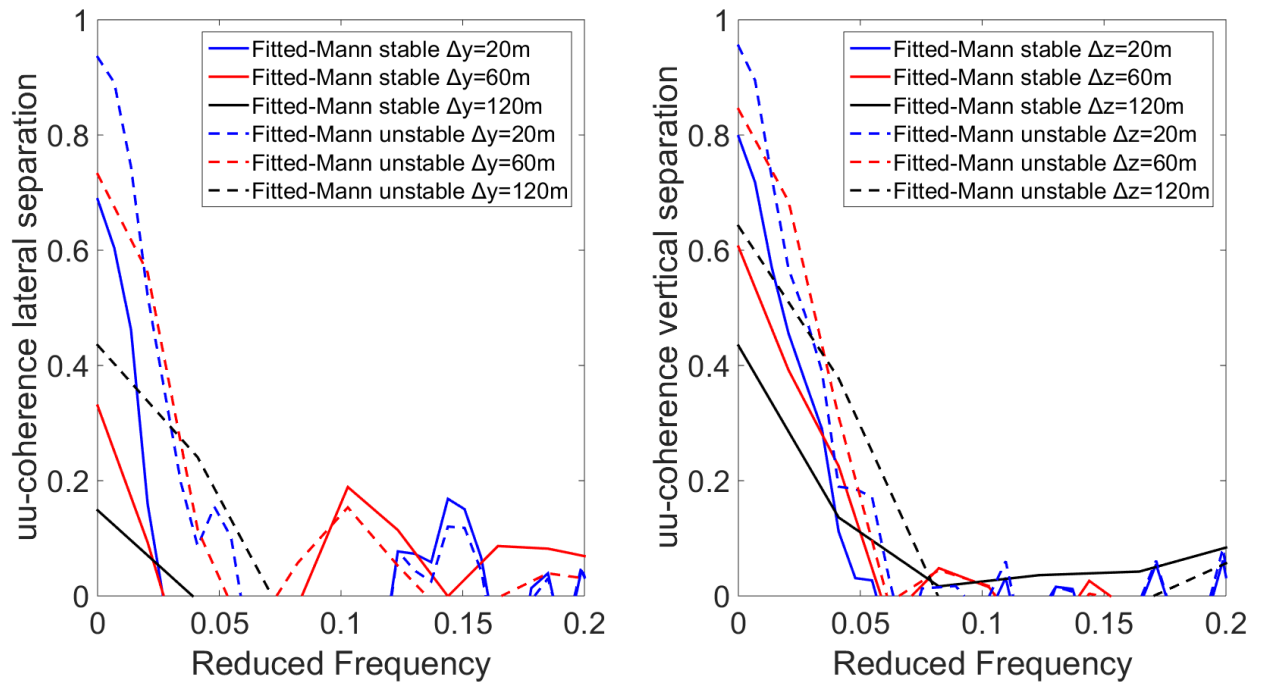


Figure C.19 Lateral (left) and vertical (right) coherences of the u -component for different separations at **rated** wind speed comparing the Mann Model with the fitted parameters for stable and unstable conditions.

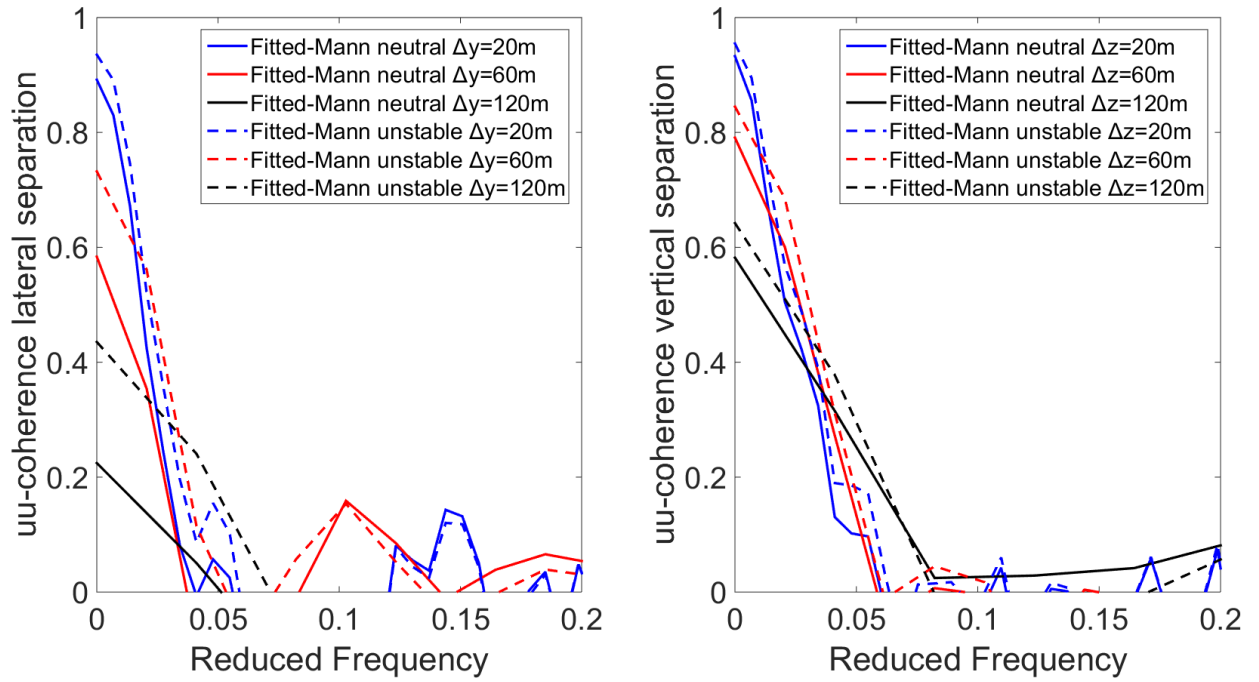


Figure C.20 Lateral (left) and vertical (right) coherences of the u -component for different separations at **rated** wind speed comparing the Mann Model with the fitted parameters for neutral and unstable conditions.

C.3 Power Spectral Densities

C.3.1 The Generated Wind Spectral Density

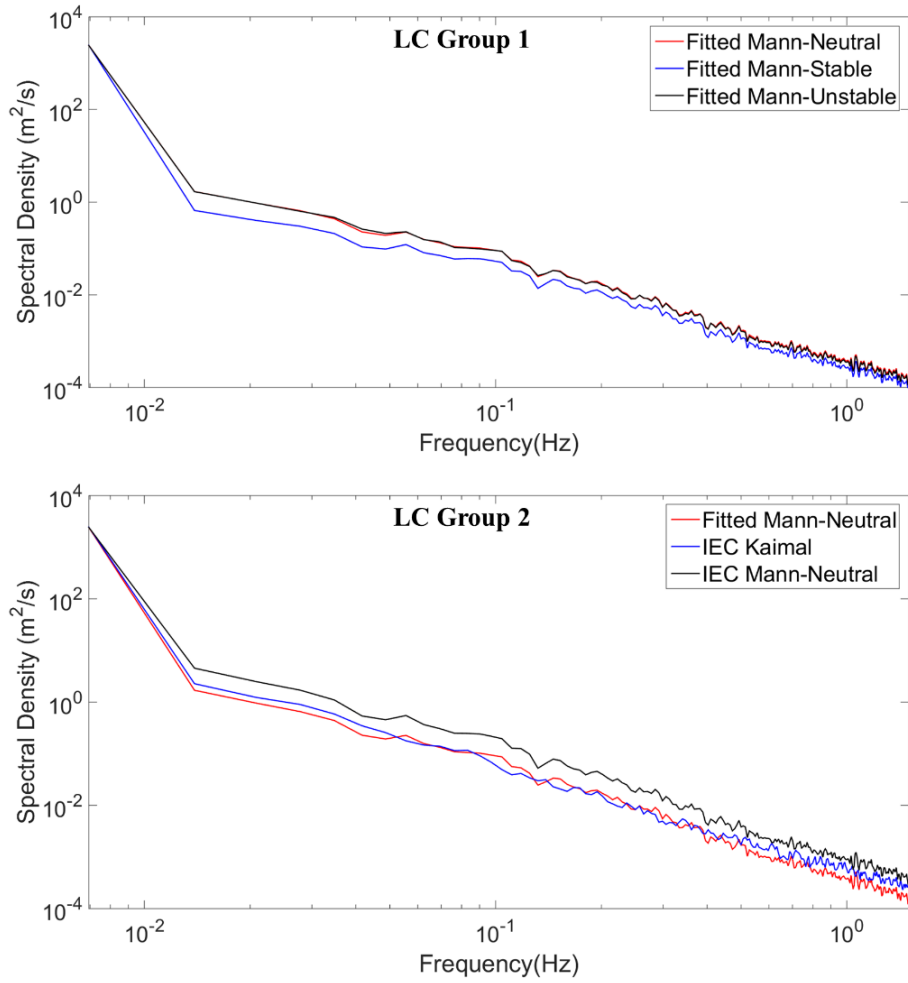


Figure C.21 Power spectral density of the along-wind component for 8 m/s wind at hub height.

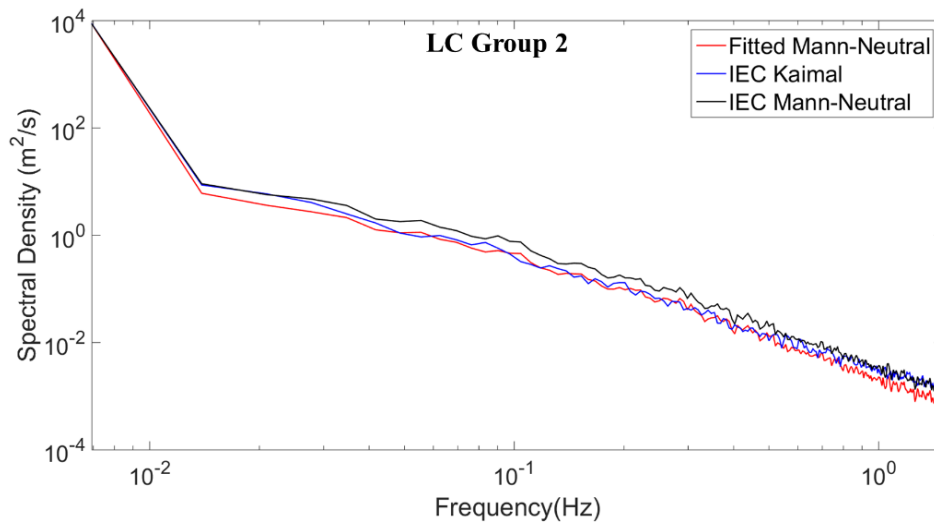


Figure C.22 Power spectral density of the along-wind component for 15 m/s wind at hub height.

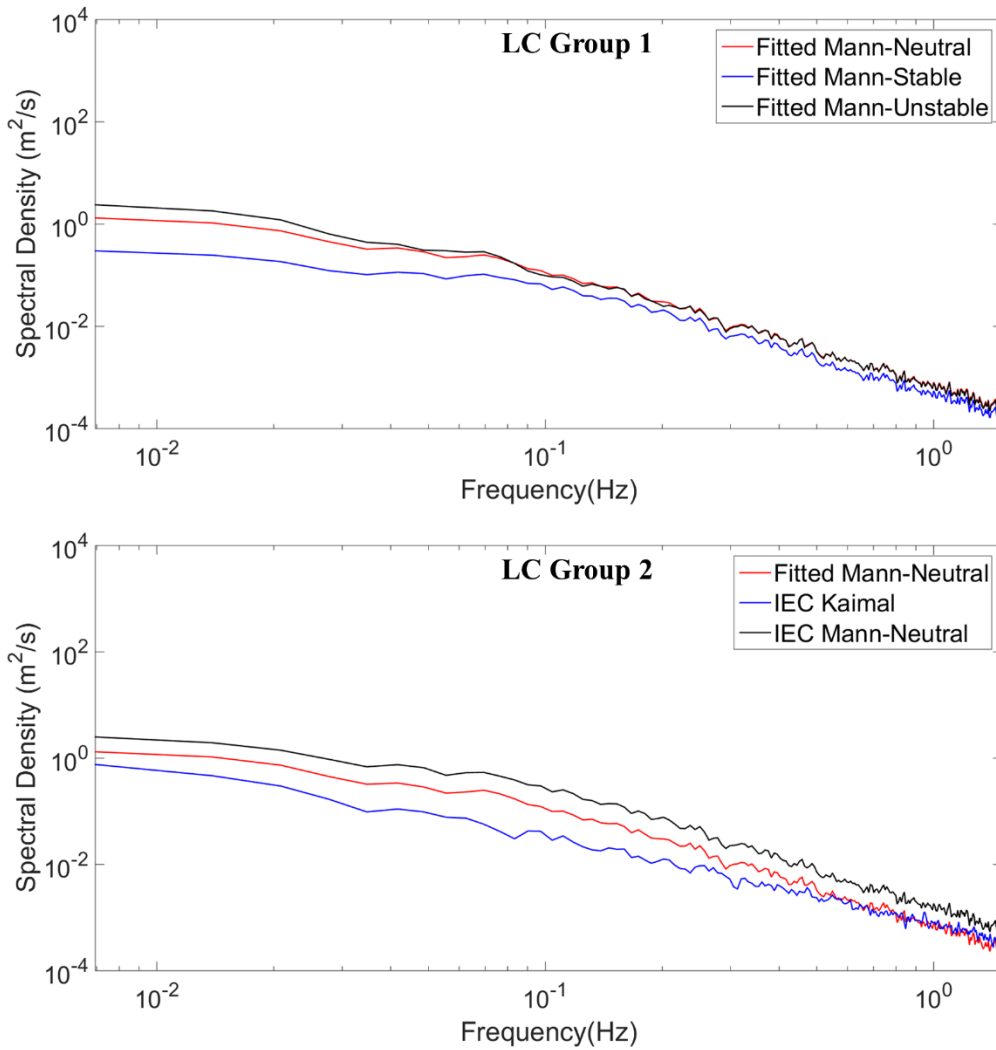


Figure C.23 Power spectral density of the cross-wind component for 8 m/s wind at hub height.

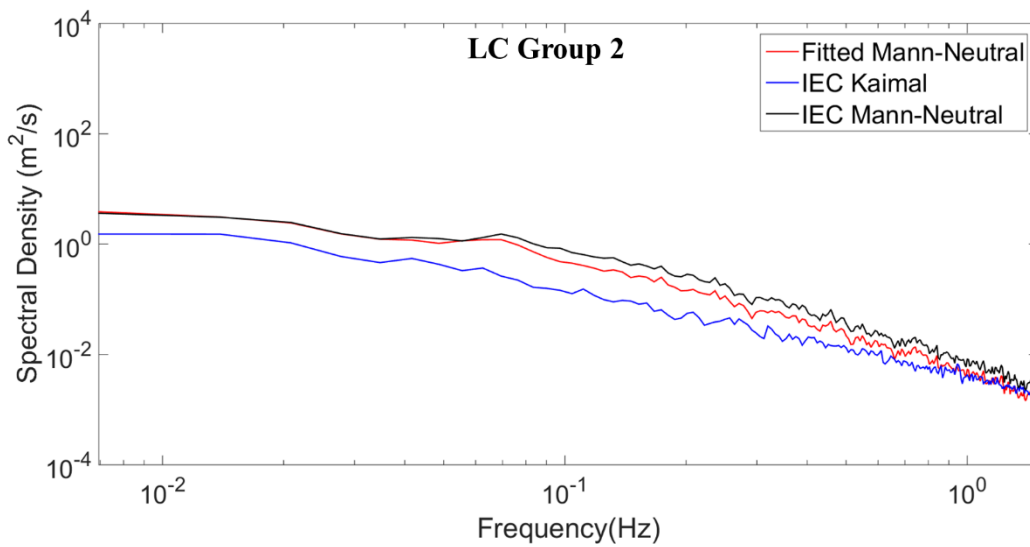


Figure C.24 Power spectral density of the cross-wind component for 15 m/s wind at hub height.

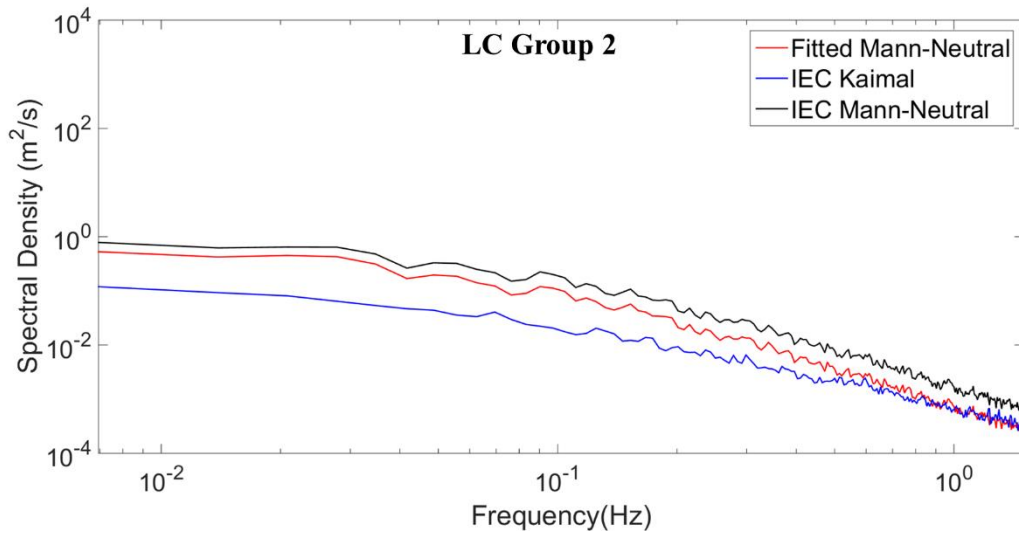
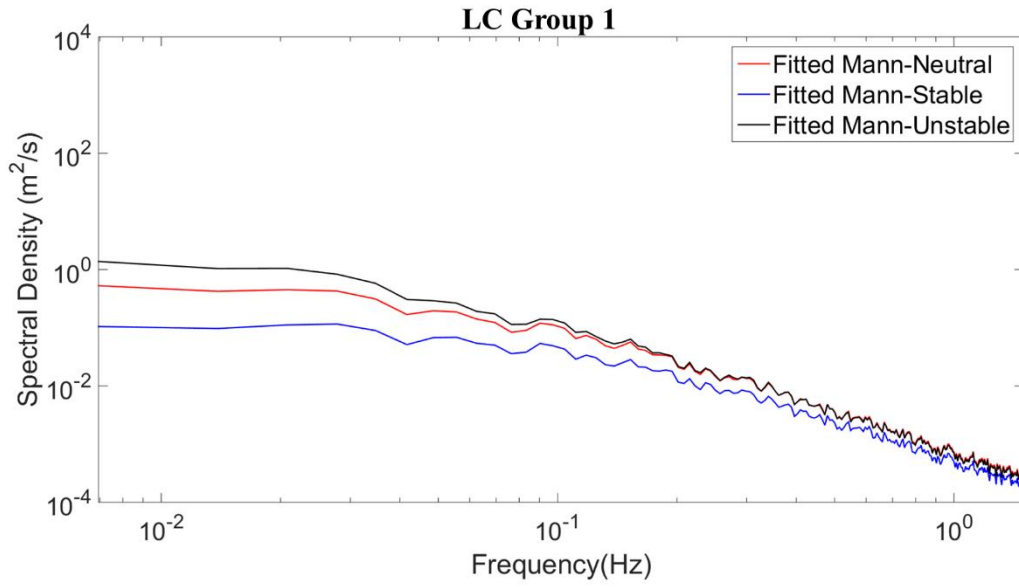


Figure C.25 Power spectral density of the vertical-wind component for 8 m/s wind at hub height.

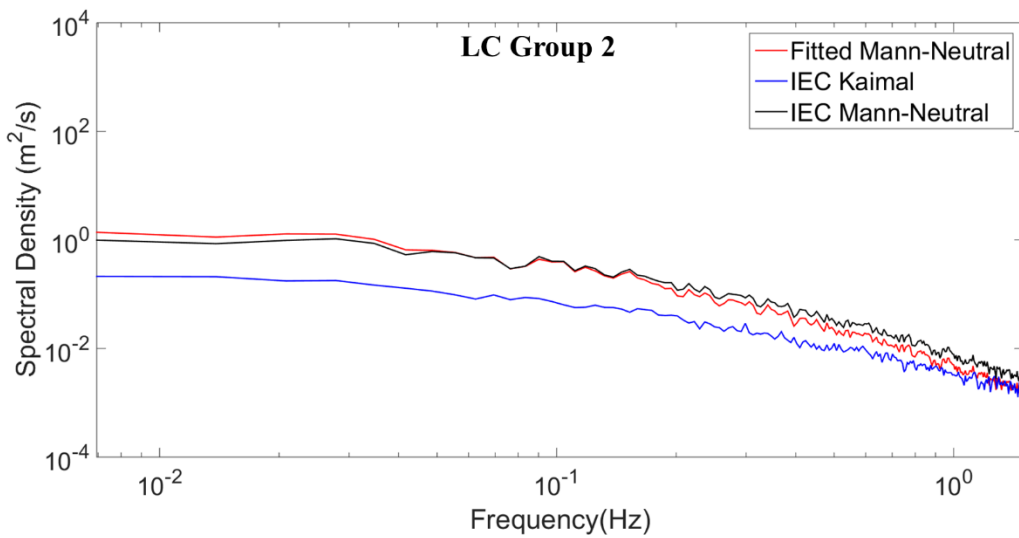


Figure C.26 Power spectral density of the vertical-wind component for 15 m/s wind at hub height.

C.3.2 The Mooring Tension Spectral Density

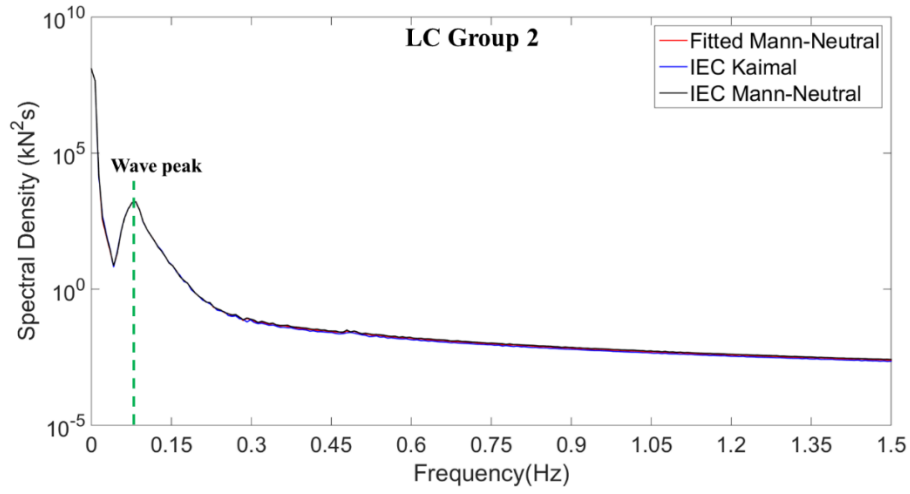


Figure C.27 Mooring line 1 tension spectral densities at above rated (15m/s) wind speed.

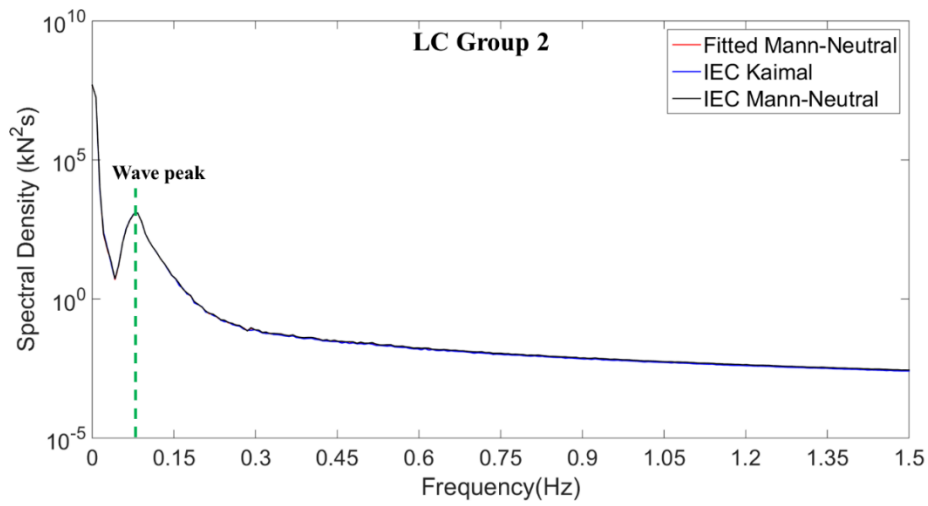


Figure C.28 Mooring line 2 tension spectral densities at above rated (15m/s) wind speed.

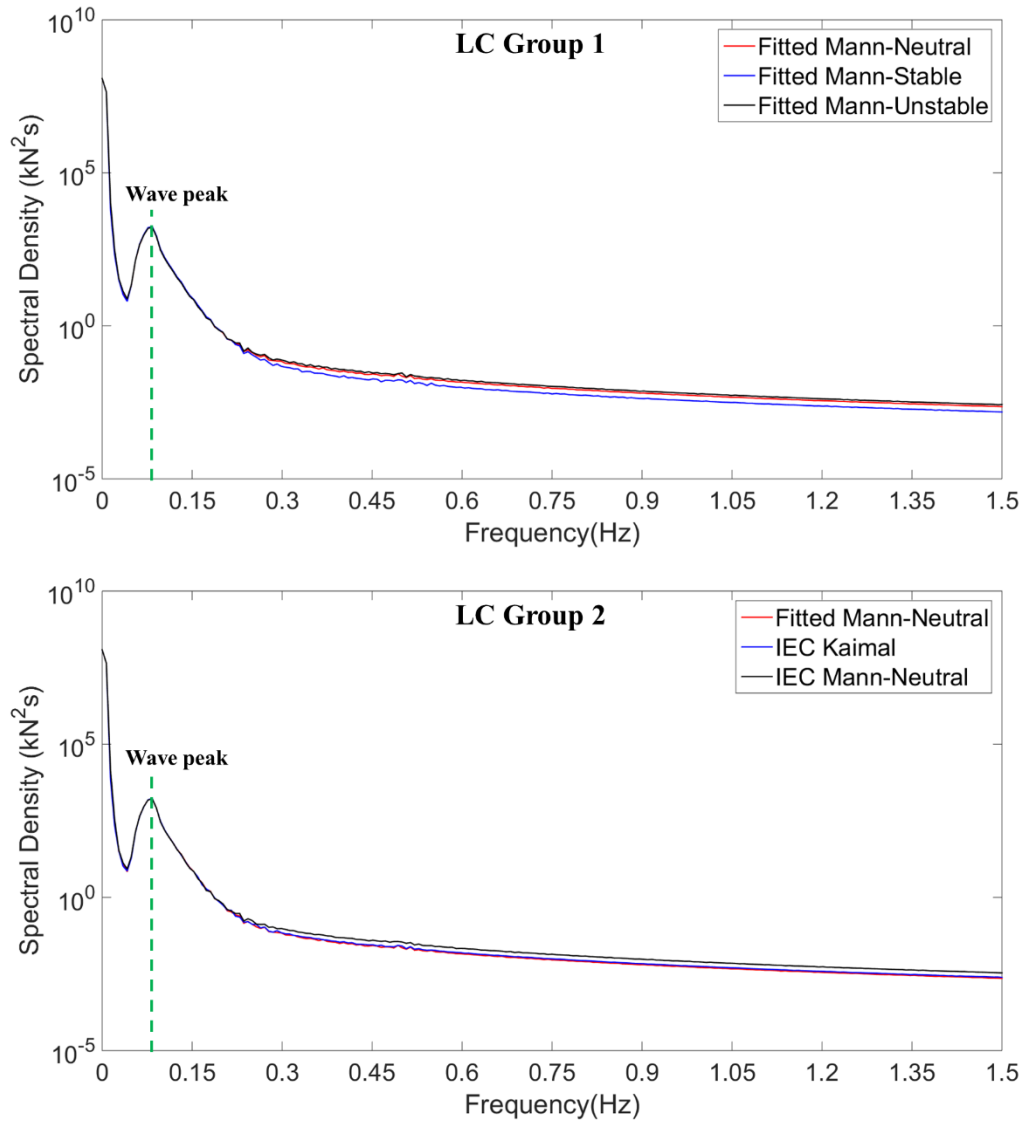


Figure C.29 Mooring line 3 tension spectral densities at below rated (8m/s) wind speed.

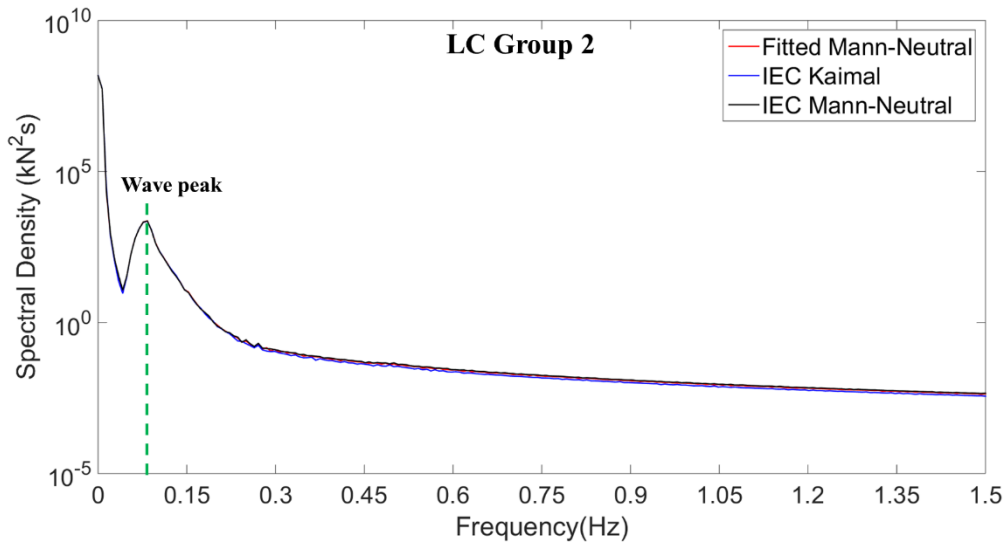
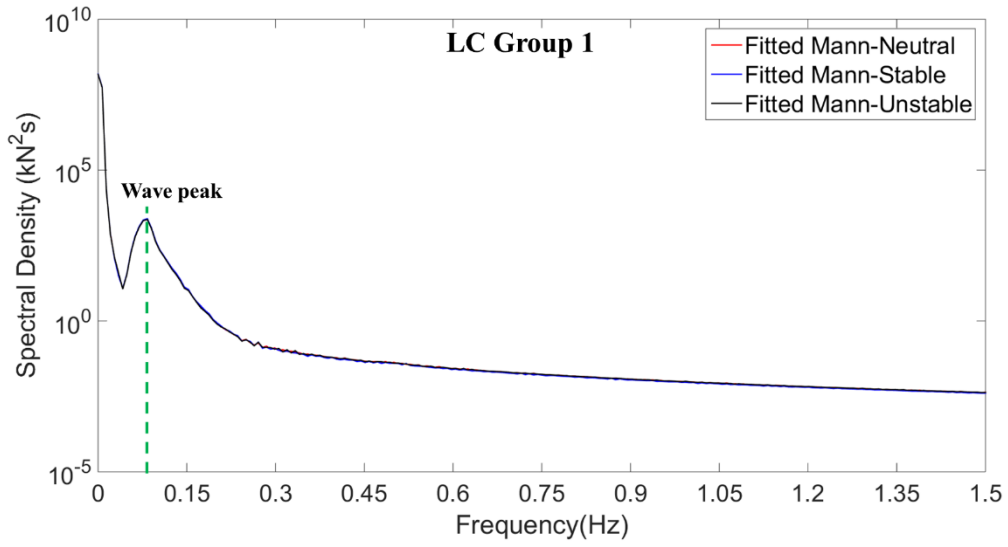


Figure C.30 Mooring line 3 tension spectral densities at rated (11.4m/s) wind speed.

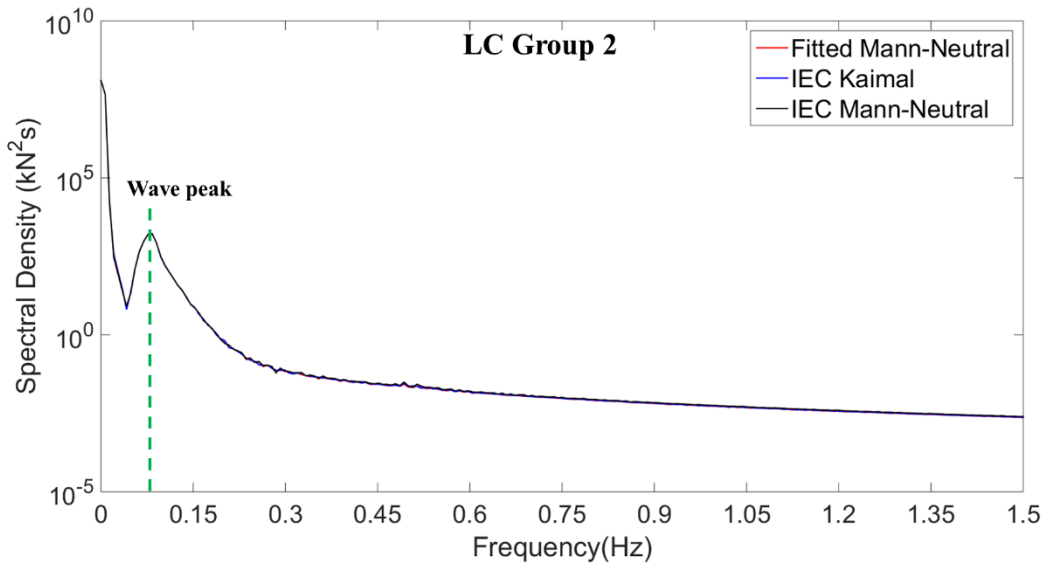


Figure C.31 Mooring line 3 tension spectral densities at above rated (15m/s) wind speed.